ARL-TR-8756 • Aug 2019

Transport in Complex Crystalline Materials Based on van der Waals Heterostructures

by Mahesh R Neupane, Dmitry Ruzmetov, A Glen Birdwell,
Robert Burke, Ryan Enck, Michael Daniel Valentin,
Edward Byrd, Matthew Chin, and Tony Ivanov

Approved for public release; distribution is unlimited.

NOTICES

Disclaimers

ARL-TR-8756 ● AUG 2019

Transport in Complex Crystalline Materials Based on van der Waals Heterostructures

by Mahesh R Neupane, Dmitry Ruzmetov, A Glen Birdwell,
Ryan Enck, Matthew Chin, and Tony Ivanov
Sensors and Electron Devices Directorate, CCDC Army Research Laboratory

Edward Byrd
Weapons and Materials Research Directorate, CCDC Army Research Laboratory

Robert Burke
General Technical Services LLC, Wall, NJ

Michael Daniel Valentin
University of California, Riverside

REPORT DOCUMENTATION PAGE

Form Approved
OMB No. 0704-0188

1. REPORT DATE *(DD-MM-YYYY)* August 2019	**2. REPORT TYPE** DSI	**3. DATES COVERED (From - To)** 1 October 2016–31 May 2019

4. TITLE AND SUBTITLE
Transport in Complex Crystalline Materials Based on van der Waals Heterostructures

5a. CONTRACT NUMBER

5b. GRANT NUMBER

5c. PROGRAM ELEMENT NUMBER

6. AUTHOR(S)
Mahesh R Neupane, Dmitry Ruzmetov, A Glen Birdwell, Robert Burke, Ryan Enck, Michael Daniel Valentin, Edward Byrd, Matthew Chin, and Tony Ivanov

5d. PROJECT NUMBER
DSI16-SE-008

5e. TASK NUMBER

5f. WORK UNIT NUMBER

7. PERFORMING ORGANIZATION NAME(S) AND ADDRESS(ES)
CCDC Army Research Laboratory
ATTN: FCDD-RLS-RE
2800 Powder Mill Rd
Adelphi, MD 20783-1138

8. PERFORMING ORGANIZATION REPORT NUMBER
ARL-TR-8756

9. SPONSORING/MONITORING AGENCY NAME(S) AND ADDRESS(ES)

10. SPONSOR/MONITOR'S ACRONYM(S)

11. SPONSOR/MONITOR'S REPORT NUMBER(S)

12. DISTRIBUTION/AVAILABILITY STATEMENT
Approved for public release; distribution is unlimited.

13. SUPPLEMENTARY NOTES
ORCID ID(s): Mahesh R Neupane, https://orcid.org/0000-0002-4806-6581; Dmitry Ruzmetov, https://orcid.org/0000-0002-0688-1908;

14. ABSTRACT

A dearth of high-quality 2-D semiconductors and the difficulty of scaling down 3-D semiconductors have severely limited the prospects for the development of next-generation energy efficient electronic devices. To overcome these challenges, we have developed a technique to integrate van der Waals 2-D and conventional 3-D semiconductors. Our resultant novel 2-D/3-D heterostructure consists of molybdenum disulfide as the 2-D component encapsulated between 3-D gallium nitride in a vertical configuration. This ultra-thin structure is a promising material system as a component of an improved heterojunction bipolar transistor (HBT). High-quality, defect-free interfaces between the 2- and 3-D systems, a critical criterion for efficient HBT device operation, was achieved through chemical powder vaporization, metal-organic chemical vapor deposition, and molecular beam epitaxy. We also synthesized a trilayer 3-D/2-D/3-D semiconductor structure (the first demonstration of its kind), validated all major critical aspects of the design, and performed a feasibility study of our design and microfabrication process for a functional HBT model. In particular, 2-D/3-D diode behavior was demonstrated for the fully synthesized heterostructures built without mechanical transfer. The outcomes of this basic research effort could pave the way for explorations into the novel physics of 2-D materials for energy-efficient electronics devices and systems.

15. SUBJECT TERMS
Director's Strategic Initiative, DSI, 2-D, 3-D, van der Waals, vdW materials, transport, density functional theory, DFT simulation, Cp2K

16. SECURITY CLASSIFICATION OF:			**17. LIMITATION OF ABSTRACT**	**18. NUMBER OF PAGES**	**19a. NAME OF RESPONSIBLE PERSON**
a. REPORT	**b. ABSTRACT**	**c. THIS PAGE**	UU	164	Mahesh R Neupane
Unclassified	Unclassified	Unclassified			**19b. TELEPHONE NUMBER (Include area code)** (301) 467-0782

Standard Form 298 (Rev. 8/98)
Prescribed by ANSI Std. Z39.18

Contents

List of Figures

List of Tables

Contributors

The following people contributed to this report:

- DeCarlos Taylor, US Army Combat Capabilities Development Command Army Research Laboratory (CCDC ARL), Weapons and Materials Research Directorate (WMRD)
- Madan Dubey, CCDC ARL, Sensors and Electron Devices Directorate (SEDD)
- Frank Crowne, CCDC ARL, SEDD
- Sina Najmaei, CCDC ARL, SEDD
- Barbara Nichols, CCDC ARL, SEDD
- Terrance O'Regan, CCDC ARL, SEDD
- Sergey Rudin, CCDC ARL, SEDD
- Pankaj Shah, CCDC ARL, SEDD
- Josh Orlicki, CCDC ARL, WMRD

Executive Summary

This Director's Strategic Initiative (DSI) project, "Transport in Complex Crystalline Materials based on van der Waals Heterostructures" was conceived and developed to investigate the electronic properties of heterogeneous van der Waals (vdW) solids. This DSI effort has contributed to the development of a technique to integrate vdW 2-D semiconductors and conventional 3-D semiconductors. The resultant novel 2-D/3-D heterostructure material consists of an atomically sharp 2-D layer sandwiched between encapsulating 3-D layers forming an ultra-thin body, which makes them a promising material system of choice as a component of an improved heterojunction bipolar transistor (HBT) technology.

To achieve a large current and faster speed vis-à-vis a lateral device geometry, we have used molybdenum disulfide as the 2-D component and gallium nitride as the 3-D component in the vertical configuration. High-quality, defect-free interfaces between the 2- and 3-D systems, a critical criterion for efficient HBT device operation, was achieved through chemical powder vaporization, metal-organic chemical vapor deposition, and molecular beam epitaxy.

Our innovative approach overcame fundamental problems limiting the use of 2-D materials in electronic devices, with far-reaching consequences for the development of energy-efficient electronic devices and systems. Consequently, our scientific discovery promises to be a key enabler for next-generation, high-frequency, high-power communication and sensing systems for battlefield needs. This work has also spurred interest in the scientific community and contributed to the advancement of fundamental knowledge and the applicability of complex crystalline materials based on vdW heterostructures.

1. Introduction/Background

The extraction of single-layer graphene from bulk graphite in 2004 by Andre Geim and Konstantin Novoselov lead to the first observation of the anomalous quantum Hall effect in graphene, which provided direct evidence of graphene's theoretically predicted Berry's phase of massless Dirac fermions.[1] Afterward, a large number of 2-D materials were discovered or revisited. Currently, there are a number of known classes of 2-D materials, including atomic crystals, transition metal dichalcogenides (TMDs), transition metal oxides, and so on.

Similar to other 2-D materials, TMDs offer chemical tunability. They have attracted much attention due to their scalability, the step-like density of states, and the absence of broken bonds at the interface. Moreover, the lack of dangling bonds at the surface of TMDs allows for fabricating material stacks with low densities of interface defects. The transition metal in a TMD determines if a material is metallic (e.g., NbX_2 or ReX_2, where X=S, Se, Te) or semiconducting (e.g., MoX_2, WX_2, where X=S, Se, Te). Various bandgap values can be selected through the choice of the chalcogenide. As proposed by Geim and Grigorieva,[2] van der Waals (vdW) materials can be stacked to form multifunctional materials. Entirely new physical phenomena can be revealed by designing tailor-made, artificial vdW solids that cannot be accessed by classical high-temperature solid-state chemistry.[3] This approach involve a rich knowledge of material science, physics, and chemistry. In addition, vdW heterostructures allow a conceptually new degree of flexibility in designing electronics, optoelectronics, and other novel devices.[4–5]

Vertical stacking of 2-D materials requires a clear understanding of the vdW gap and the force between the layers because these factors determine the interlayer tunneling between the layers.[6] The knowledge of interlayer coupling strength is also crucial for accurate material and device characterization. Similarly, as shown in multilayer graphene, chemical functionalization in the vdW gap between the 2-D layers can also tune the fundamental material and device properties.[7–8] Intercalation and the interaction with molecular adsorbates provide novel routes for chemical doping, which are unique to 2-D materials.[8] Recently, there has been an increase in understanding of the aligned growth of TMDs on near-lattice-matched substrates.[9]

2. Program Objectives

The goal of this 3-year project is to develop a unified (atomistic to macro level) understanding of the unique properties of heterogeneous vdW solids as possible next-generation materials for electronic devices. Particular attention is given to the study of *vertical charge transport in vdW structures*. We view this Director's

Strategic Initiative (DSI) program as the exploratory phase for a potential US Army Combat Capabilities Development Command Army Research Laboratory (CCDC ARL) research program in this area. Experience shows that it takes 15–20 years for new semiconductor material systems to mature from concept to industry adoption. If successful, the projected research horizon is at least 10 years past the completion date of the DSI phase. We aim to elucidate theory, synthesis, metrology, nanofabrication, and novel device concepts based on complex vdW crystals.

The following are our specific aims:

1) Develop theoretical/computational description of transport in complex heterogeneous vdW crystals.
2) Develop substrate-aligned, large-area, electronic-grade growth of complex vdW crystals.
3) Develop novel electronic device concepts based on vdW solids for the following:
    - High-speed RF front ends
    - High-power RF transmitters
    - High-efficiency digital electronics (exciton based)

Table 1 summarizes the main program objectives by year and by functional area.

Table 1 Three-year objectives of this DSI program

Year 1	Develop theory/methodology to link quantum mechanical computations with lateral and vertical charge transport to understand dominant transport mechanisms.
	Develop 2-D layer growth aligned with 3-D semiconducting substrates to enable diode fabrication.
	Characterize 2-D films grown on 3-D substrates (3-D+2-D) to explore the effects of crystallinity, orientation, morphology, defects, and such on a diode structure performance.
	Characterize the electronic properties of the structure (3-D+2-D), and analyze the junction properties to validate the theory and give insight into the performance improvement pathways.
Year 2	Develop a methodology for calculating the current transport in heterogeneous vdW crystals and ranking candidate materials in terms of electronic properties for device applications.
	Develop growth of stacked heterogeneous layers to enable transistor fabrication.
	Characterize the material and electrical properties of complex vdW crystals to validate theory and give insight into performance improvements.
Year 3	Model exciton-based transport in vdW crystals to predict the maximum operating temperature.
	Explore targeted impurity introduction in as-grown films to increase device performance.
	Develop and characterize proof-of-concept vdW solid test structures: tunneling device (speed) and n-p-n device (RF power) and excitonic device (high-efficiency digital). Judge the potential for these devices to have revolutionary performance under mission-funded 10-year plan.

3. Planned Approach

To achieve the objectives listed in Section 2 (Table 1), our planned approach includes five key steps:

1) Growth
2) Theory/modeling
3) Metrology
4) Device fabrication
5) Characterization

The tasks assigned to each step are listed in Table 2. Figure 1 shows the collaboration map for this DSI effort.

Table 2 Implemented technical steps

Growth	Theory	Metrology	Device Fab	Characterization
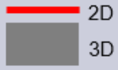	1. Growth initiation 2. 2D alignment to 3D	1. 2D quality (crystallinity, defects, impurities)	1. Area contact to 2D 2. Contact to 3D 3. Active area isolation	1. Junction studies
	1. Alignment of layers 2. vdW Gap theory 3. Charge transport	1. Films quality 2. Stacking 3. Strain	1. Contacts to all 3 layers 2. Doping	1. Tunneling 2. Access resistance 3. Barrier modulation
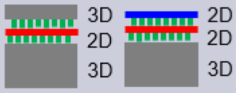	1. Defect formation 2. Defect functionalization 3. Linker types	1. Defect characterization 2. Linker metrology	1. Test structures for linker studies 2. Transistor fab	1. Current transport in linkers 2. Transistor action

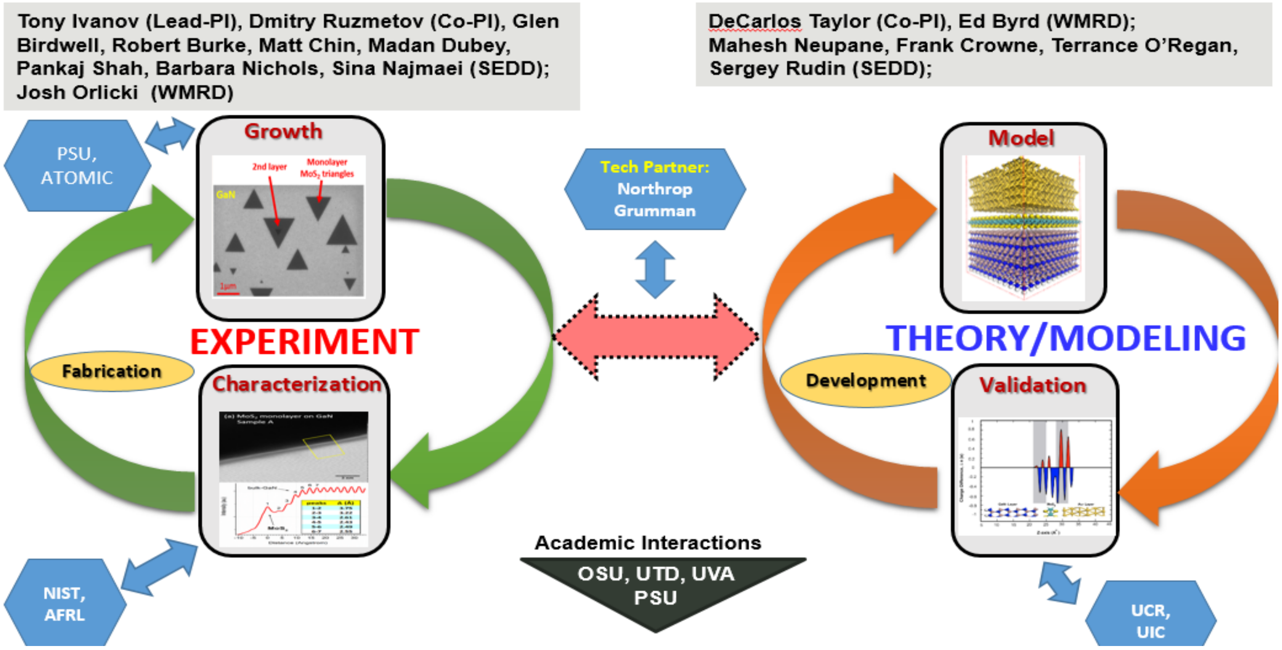

Fig. 1 Collaboration map of the DSI highlighting collaborating academic and industrial partners

4. Epitaxial Growth of 2-D Material on a 3-D Substrate

4.1 Introduction and Motivation

Two-dimensional semiconducting TMDs are promising candidates for high-performance electronic and optoelectronic devices because they exhibit atomically sharp interfaces, ultra-thin dimensions, flexibility, and large optical effects.[2,10–11] For example, molybdenum disulfide (MoS_2) is one of the most studied 2-D TMDs and has been tested in proof-of-concept, ultra-fast field-effect transistors (FETs), optical devices, and flexible electronics.[12–17] In general, however, the highest mobility 2-D MoS_2 is obtained by exfoliation of geological MoS_2 crystals that are mechanically transferred to the desired substrate. Small specimen sizes, uncertainty in placement location, and lack of control over the MoS_2 crystal composition are the main drawbacks to using the geological material source.[13,18] Attempting to overcome these limitations, many have used synthetic materials to grow 2-D semiconductors with an engineered composition. MoS_2 has been synthesized by chemical vapor deposition (CVD),[19] metal–organic chemical vapor deposition (MOCVD),[20] and pulsed laser deposition (PLD),[21] but primarily on insulating oxide substrates. Monolayer (ML) MoS_2 has been synthesized by MOCVD on oxides, but it generally results in crystals that lack alignment, resulting in grain boundaries when crystals merge.[20] While ML MoS_2 has been grown partially aligned to a sapphire substrate using CVD,[19] 2-D semiconductors grown on insulating substrates are limited to simple device architectures and generally require transfer to other substrates in order to be integrated into heterostructure devices.

On the other hand, 2-D semiconductors grown with epitaxial alignment to a conventional 3-D semiconductor substrate are of interest for use in hybrid 2-D/3-D electronic devices that employ the advantages of both the established 3-D semiconductors and the unique properties of ultra-thin 2-D crystals.[22–23] In particular, we envision that a vertical 3-D/2-D/3-D structure could enable high-frequency, high-power heterojunction bipolar transistor (HBT) devices where the atomically thin 2-D TMD base provides for high-speed operation and the vertical nature of the electronic transport allows for a large surface area and thus high current. The use of MoS_2 and gallium nitride (GaN) demonstrates an example of a 2-D/3-D combination matching the general requirements for the vertical HBT. These requirements include close lattice match and favorable electronic band structure alignment. In addition, there is evidence that MoS_2 can serve as a growth template for GaN,[24] which gives a potential pathway to produce the top 3-D component in a GaN/MoS_2/GaN stack. As an initial step toward the implementation of 3- and 2-terminal bipolar 2-D/3-D heterostructures, we investigate simple unipolar 2-D/3-D stacks to address the basic questions regarding the feasibility of epitaxial growth and vertical electron transport across the vdW gap.

In this study, we present 2-D/3-D heterostructures based on the epitaxially grown MoS_2 on GaN substrates and demonstrate vertical electrical conduction across the interface. Our GaN/MoS_2 heterostructures are a lattice-matched system, unlike most reported epitaxial 2-D/2-D and 2-D/3-D heterostructures to date.[19,25–26] The MoS_2 ML coverage is nearly 50% with ML triangles typically 1 μm along each side and ML blankets of up to 30 μm across. Photoluminescence (PL) and Raman microanalysis were employed to characterize ML MoS_2 and its interaction with the substrate. The analysis suggests that our CVD growth of epitaxial MoS_2 on GaN produces ML MoS_2 islands of superior structural quality to that of the mechanically exfoliated MoS_2 available to us for this study. Finally, we use conductive AFM (CAFM) to electrically characterize as-grown MoS_2/GaN heterostructures. It is important to note that using CAFM allows us to avoid processing the MoS_2/GaN heterostructure with microfabrication chemicals such as solvents and polymer resists. We demonstrate out-of-plane electrical conduction and estimate contact resistivity between the MoS_2 and GaN as well as current spreading in the MoS_2 ML.

4.2 Methods

4.2.1 MoS_2 Growth

MoS_2 was grown on a GaN substrate *via* a powder vaporization technique: 2 mg of molybdenum trioxide (MoO_3; 99.8%, Sigma Aldrich) is placed in the center of a single zone furnace, and 200 mg of sulfur (S) powder (99.995%, Alfa Aesar) is placed approximately 12 inches upstream of the MoO_3 crucible. To eliminate the water and organic residual in the system, 10-min vacuum (0.018 Torr) annealing at 300 °C was employed before the growth. The S was heated at 130 °C right after the annealing. The growth was set at 800 °C and 710 Torr for 15 min with 100 sccm of ultra-pure argon flow.

4.2.2 Photoluminescence and Raman Spectroscopy

The MoS_2/GaN heterostructures were characterized *via* PL and Raman spectroscopies with a WITec Alpha 300RA system using a 2.33-eV laser excitation energy. Incident laser power was adjusted in order to keep the power density at approximately 5.5 mW/μm^2 for single spectra data. Raman and PL images were developed over several square micrometer regions using a 250-nm grid spacing with integration times as large as 6 s. Regions of interest were identified from these maps for which single spectra were obtained using a 2-s integration time and 60 accumulations.

4.2.3 X-ray Photoelectron Spectroscopy

The composition of the MoS_2 structures and changes to the surface of the underlying GaN substrate were examined with X-ray photoelectron spectroscopy (XPS). The samples were analyzed in a Kratos Axis Ultra DLD instrument equipped with a spherical mirror analyzer. The X-rays were generated by a monochromated aluminum (Al) Kα source operated at 104 W. The analysis area was approximately 1 mm by 0.5 mm and the analyzer pass energy was set to 40 eV.

At least three non-overlapping spots were analyzed per sample and the quantification results shown are the arithmetic mean of these spots. For all samples measured, a low-energy electron gun was used for charge neutralization. Despite the neutralizer, differential charging was evident between surfaces with and without MoS_2 overlayers. Using the Auger parameter 3-D/$L_3M_{45}M_{45}$ for gallium (Ga; 1084.05 eV), we determined that Ga is in the 3+ oxidation state for all surfaces measured.[27] To account for differential charging, spectra from an unprocessed GaN/GaN/sapphire surface was referenced against the hydrocarbon C1s peak (C-H 284.8 eV) from adventitious carbon. For this surface, the Ga $L_3M_{45}M_{45}$ Auger transition was measured at 422.6 eV. Knowing that Ga has the same oxidation state for all surfaces measured, we used the Ga $L_3M_{45}M_{45}$ Auger transition as an internal reference for the rest of the samples: MoS_2/GaN and the GaN-S sample.

Peak fitting was carried out in the CasaXPS software using Gaussian–Lorentzian peak shapes and Shirley backgrounds. Relative sensitivity factors used for quantification were provided by Kratos Analytical, specifically for the Axis Ultra DLD instrument. Peaks that occurred as spin-orbit doublets were constrained to have equal full-width half-maximum (FWHM) values and the expected peak area ratios for each spin state (1:2 for $p_{1/2}$ and $p_{3/2}$; 2:3 for $d_{3/2}$ and $d_{5/2}$) were also constrained.

4.2.4 AFM and CAFM Measurements

The CAFM measurements were performed on a MultiMode AFM (Bruker, Santa Barbara, California) that provides nanoscale mechanical (PeakForce QNM) and electrical characterization (PeakForce Kelvin Probe Force Microscopy [PeakForce KPFM], PeakForce Tunneling Atomic Force Microscopy [PeakForce TUNA]) in addition to common topographical imaging (amplitude modulation AFM [AM-AFM]), PeakForce AFM). During mapping, over selected areas, various AFM modes were used to gather a complementary characterization of the structures of interest. The MoS_2 islands were identified in the phase contrast images of AM-AFM with the AFM operated at low set-points (reduced tapping amplitudes), in which case the repulsive response from the MoS_2 increases the phase contrast of the MoS_2 islands with respect to that of the uncovered GaN regions. The enhanced dissipative response of MoS_2 in comparison with that of GaN was confirmed also in the maps of adhesive force and dissipation acquired during PeakForce AFM over areas comprising MoS_2 islands and bare GaN.

PeakForce KPFM was used to measure the surface potential (SP) of the investigated sample.[28] PeakForce KPFM is an implementation of frequency modulation KPFM on PeakForce Tapping, which combines two cascaded lock-in amplifiers for the detection of the electrical gradient. The phase signal measured by the first lock-in amplifier at the resonance frequency of the cantilever is fed into the second lock-in amplifier that is locked at the KPFM modulation frequency. The output of the second lock-in amplifier is used for the KPFM feedback to cancel out the electric gradient at the modulation frequency. The PeakForce modulation was performed at 2 kHz and 50-nm amplitude, and the KPFM measurements were made during the second-pass of each scanning line at a 70-nm lift height. The AFM probe used for these measurements was a SCM-PIT tip (Bruker, Santa Barbara, California) with the first resonance frequency at 54.1 kHz.

In PeakForce TUNA, the tip/sample current is measured during each tap of the PeakForce Tapping by a linear amplifier. For these measurements, either a nitrogen-doped diamond coated CAFM tip (NT-MDT Co.) or a conductive platinum silicide (PtSi) tip (Nanosensors, Neuchatel, Switzerland) was used while the AFM was engaged in PeakForce Tapping (30-nm tap amplitude at 1 kHz). The PeakForce TUNA was operated at –7 V DC bias and a current sensitivity of 20 nA/V.

4.3 Results and Discussion

Epitaxial alignment between MoS_2 and GaN is predicted to exist because both GaN and MoS_2 belong to a hexagonal crystal system with in-plane lattice mismatch of less than 1% (GaN = 3.19 Å, MoS_2 = 3.16 Å).[29] We also expect the small discrepancy in the coefficients of thermal expansion between GaN and MoS_2 to allow the epitaxial alignment to remain when the stack is cooled from the growth temperature of MoS_2 to room temperature.[30–31] We note that quasi-epitaxial multilayer and ML MoS_2 films on GaN were grown by PLD.[21] Deposition of semiconductors by PLD is a straightforward method to deposit material from the target to the substrate with high deposition rates. However, PLD has inherent compositional non-uniformity issues that set limits for achieving low-defect epitaxial interfaces that are required to provide efficient carrier transport in vertical high-performance devices.

In this work, we investigate MoS_2/GaN hybrid structures on sapphire (c-plane) substrates. A stack of two GaN layers was grown on sapphire using MOCVD by NTT Advanced Technology Corp.: GaN (c-plane, silicon [Si]-doped, free electron density n = 1e16 cm^{-3}, 300 nm, top layer)/GaN(c-plane, Si-doped, n = 1e19 cm^{-3}, 700 nm)/sapphire (Fig. 2a). We grow MoS_2 in a CVD system using powder vaporization[32] (Fig. 2b). Our CVD process is described in Section 4.2. Briefly, MoO_3 is placed in the center of a single zone furnace, and S powder is placed approximately 12 inches upstream of the MoO_3 crucible. The growth occurs in ultra-pure argon at 800 °C for 15 min, with the S heated separately by a heat tape at 130 °C. Subsequently, MoS_2 domains were characterized by scanning electron microscopy (SEM) (Fig. 2c) and found to be in the form of ML equilateral triangles. A typical triangle size is 1 μm with some isolated triangles of up to 10 μm in size. Coalesced ML islands extend up to 30 μm, with no evidence of stitches when observed by SEM and AFM. There is also some trilayer and higher-order growth together with scattered 3-D crystals. The striking feature is the oriented growth of the triangles (Fig. 2c), where nearly all MoS_2 triangles are aligned with the rotational symmetry of the P63mc space group of GaN.

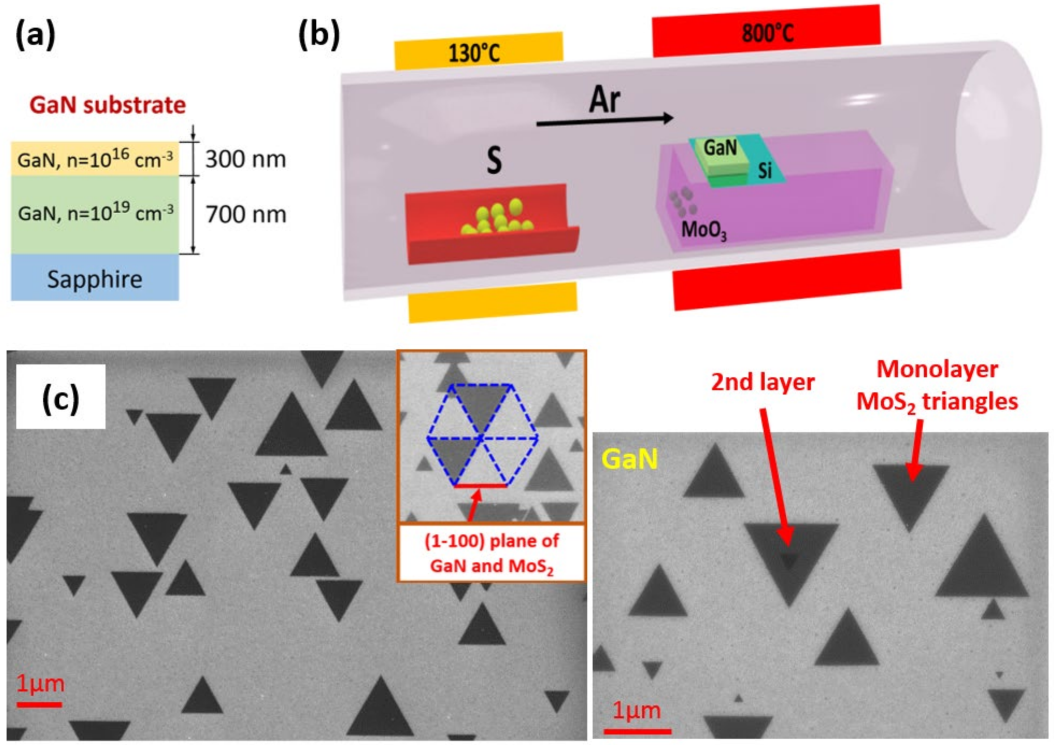

Fig. 2 a) Structure of the MOCVD GaN stack on sapphire. b) CVD system for MoS_2 growth. c) SEM of MoS_2 ML triangles on GaN epitaxial crystal. Scale bar is 1 μm and is aligned with (1-100) plane of GaN. (Inset) Orientation of the (1-100) plane of hexagonal crystals of GaN and MoS_2 is shown.

The c-plane orientation of the wurtzite lattice (hexagonal crystal system) of GaN was confirmed with electron backscatter diffraction (EBSD) analysis. The m-plane (1-100) orientation of GaN in Fig. 2c (inset) was determined by EBSD to be parallel to the horizontal axis and the scale bar. The fact that the sides of triangles of MoS_2 in Fig. 1c are aligned with the m-plane of GaN confirms the epitaxial alignment of GaN and MoS_2 lattices. Interestingly, the large ML islands (>10 μm in size) and triangles can be misaligned even though they also exhibit sharp, straight edges and 60° corners. At the same time, larger triangles of up to 8 μm that are oriented to the GaN are also observed. It is plausible that the initial growth that leads to larger structures originates on defects or 3-D crystals (often found in the center of large MoS_2 ML islands) and does not occur in an epitaxial manner. The structures that nucleate later on smaller defects or no defects progress in an epitaxial manner and are smaller in size due to shorter growth time. It is also possible that epitaxial growth happens at a slower rate than misoriented growth. SEM and AFM do not show any stitches or flake overlaps where expanding triangles merge to form larger area MLs, but high-resolution microscopy would be needed to resolve the grain boundaries if any. The merging of neighboring MoS_2 triangles without grain boundaries is a prerequisite for the large-area epitaxial growth and is a vital step for the development of the field of 2-D electronics.

The composition of the 2-D structures, layer count, and the effect of the GaN lattice on the quality of ML MoS_2 were studied with Raman and PL microspectroscopies. Raman and PL hyperspectral images generated by mapping on fundamental spectral features (e.g., peak position) provide useful information over several micrometer square regions with a lateral resolution on the order of the spot size of the laser (~340 nm in our case). Regions of interest can be readily identified and explored in more detail via single point measurements with increased integration times in order to bring out subtle details in the spectra. Figure 3a–d displays optical, Raman, and PL images obtained from a region where large isolated ML domains (~8 μm on the side) were observed. Each domain investigated exhibits a growth direction comparable to those observed for the smaller triangles that are known to have an epitaxial relationship with the GaN substrate. The ML is difficult to observe in the optical image due to the absence of interference enhancement, often used with silicon dioxide (SiO_2)/Si substrates for ML identification. To guide the reader, the domain centered in Fig. 3a is outlined by a black-dashed triangle. The red-dashed triangle is the region of enhanced MoS_2/GaN lattice interaction discussed. The material identification and ML character of MoS_2 are ascertained by the E' and A'_1 Raman peaks frequency difference of less than 20 cm^{-1}, and the strength and position of the observed PL peak (Fig. 3e–f).

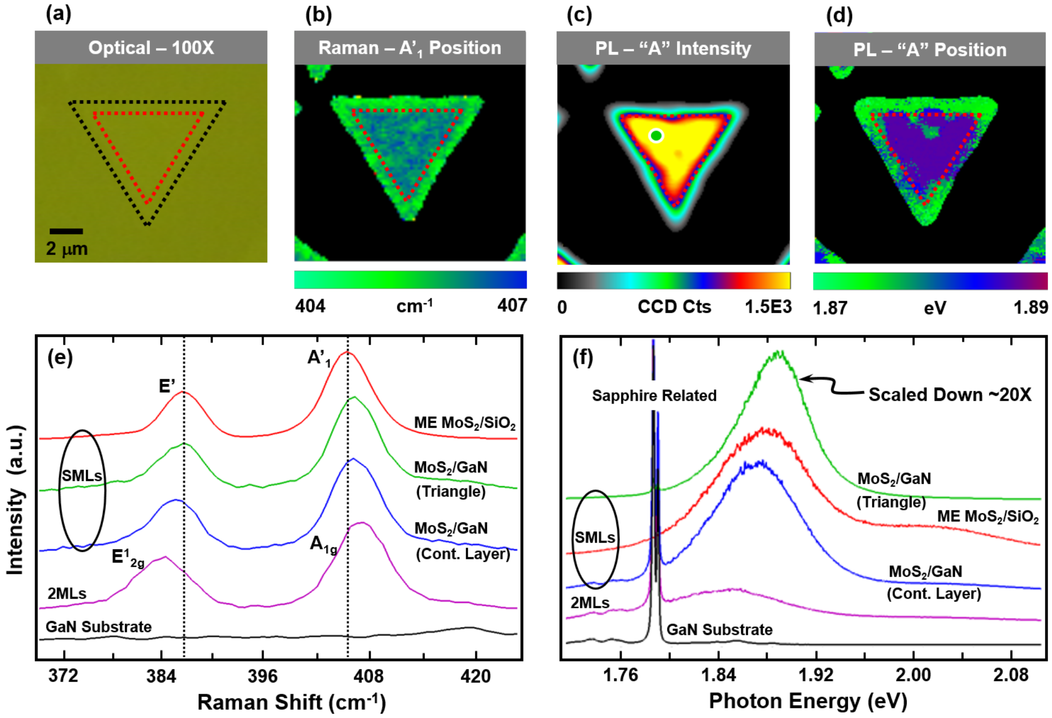

Fig. 3 a) Optical micrograph, b) Raman image of the A'$_1$ mode peak position, c) PL image of the intensity of A-exciton peak, and d) PL image of the position of A-exciton peak. The black-dashed triangle specifies the extent of the MoS_2 growth, and the red-dashed triangle indicates the region of enhanced PL signal. e) Raman spectra for mechanically exfoliated (ME) ML MoS_2/SiO_2, ML MoS_2/GaN isolated triangle, ML MoS_2/GaN continuous layers, two MLs of MoS_2/GaN, and bare GaN substrate. Vertical dashed lines indicating the peak positons for the ME reference are added for a guide to the eye. f) PL spectra taken at the same data collection points as for the Raman spectra.

The interface-sensing spectral information of the isolated triangles and their connection to light emission properties are quite interesting. We illustrate this connection by showing what can be obtained from the hyperspectral images and then focusing our attention on single spectra taken in the regions of interests revealed by imaging. Figure 3b provides a map of the position of the out-of-plane A'$_1$ peak position that reveals a blueshift of the A'$_1$ peak in a region located away from the edge of the triangle (i.e., away from the region of near-edge particles similar to those identified later in Fig. 10). Next, as shown in Fig. 3c, this region corresponds to an area of enhanced PL signal with a rapid increase starting at approximately 1 μm from the triangle's edge. As a final point to be gleaned from the images, Fig. 3d reveals that this same region also maps to that of the greatest emitted photon energy.

We now turn our attention to features in the single spectra that help us interpret the observations made available by Raman and PL images. First, the Raman spectra over a wavenumber region encompassing the in-plane and out-of-plane modes are shown in Fig. 3e. The spectra were obtained at points indicated in the PL images (see Figs. 3c and 11c) and are distinguished by the same color as the white outline circles. Additionally, results for a ME ML MoS_2[33] are represented by the red curve and provide a useful reference. Most notable is the comparison between the ME reference and the MoS_2/GaN triangle. There are three main points to be made: 1) the frequency difference between the E' and A'_1 modes of less than 20 cm^{-1} is consistent with ME MLs;[34–35] 2) peak positions for the stress sensitive in-plane mode E' are virtually the same indicating stress-free (i.e., relaxed) layer growth of the MoS_2/GaN (again, this holds for areas ~1 μm distant from the triangle's edge); and 3) as discussed in Zhou et al.,[36] the approximately 1 cm^{-1} blueshift of the A'_1 peak together with no observable change in the position of E' is suggestive of a strengthening vdW contact with the adjacent GaN substrate in this region of the triangle.[36] Continuing with the remaining spectra in Fig. 3e, the slight redshift of the E' mode observed on the MoS_2/GaN continuous ML is consistent with a similar redshift observed at the edge of the triangle (single spectra not shown) and the expected increase in the degree of edge effects in this region. Moreover, the spectra for the two MLs region aligns well with that observed for similar structures in the literature.[34–35] That is, a redshift of the E^1_{2g} mode and a blueshift of the A_{1g} mode resulting in a frequency difference of 22.6 cm^{-1}.

Figure 3f provides the PL spectra in the vicinity of the A-exciton. The data collection points on the sample and the ME MoS_2/SiO_2 reference are the same as the Raman spectra. Most remarkable is the very large (~20×) enhancement of the PL signal obtained from the triangle as compared to ME MoS_2/SiO_2 and even the continuous ML regions of the MoS_2/GaN. This enhancement may be related to a substrate charge transfer effect,[37] stoichiometry variations,[38,39] or another unknown mechanism, and will be the subject of further investigations. In addition, we see evidence of relaxed layer growth in the PL spectra. When comparing to ME MoS_2, our material has a narrower PL line width and approximately the same emitted photon peak position. The smaller linewidth (FWHM) suggests a reduction in the lower-energy charged exciton (i.e., trion) component[15] and/or an improvement in structural quality.

Next, it has been shown that relaxed ME MoS_2 MLs have a PL peak position at higher energies relative to the peak position of CVD MoS_2 on an oxide that is under tensile strain.[40] The A-exciton energy for our material is near and even at slightly higher energies than that of ME MoS_2. These observations suggest relaxed growth of our MoS_2 MLs 1 μm away from the edges of the large triangles. Interestingly, the mentioned strain in CVD grown materials is often acquired during the cool down from growth temperature due to the thermal expansion coefficient mismatch with the substrate. In contrast, for our CVD growth of MoS_2 on GaN, we have a match of the thermal expansion coefficients as well as a very close match of lattice constants that likely explains the relaxed (unstrained) state of our MoS_2 on GaN.

Continuing with the remaining spectra in Fig. 3f, the reduction of intensity and redshift of the continuous ML of MoS_2/GaN may be understood by considering the increase in the degree of edge effects as the size of the triangles are reduced and their relative numbers enlarged. All pertinent Raman and PL spectral parameters are summarized in Tables 3 and 4, respectively. Taken as a whole, the Raman and PL analysis suggests that superior material quality can be achieved by direct growth of MoS_2 on GaN compared to the ME MoS_2 available to us for this study. Technical description on PL and Raman measurement techniques is presented in Section 5.

Table 3 Raman spectral parameters corresponding to spectra shown in Fig. 2e

	E' or E^1_{2g} Mode (cm^{-1})		A'$_1$ or A_{1g} Mode (cm^{-1})	
Structure	**Peak Position**	**FWHM**	**Peak Position**	**FWHM**
ME MoS_2/SiO_2	386.5	5.5	405.4	6.4
MoS_2/GaN – Large Triangle	386.5	6.6	406.3	6.5
MoS_2/GaN – Continuous SML	385.7	6.6	406.2	6.8
MoS_2/GaN – 2-Molecular Layers	384.5	7.5	407.1	7.1

Table 4 PL spectral parameters corresponding to spectra shown in Fig. 2f. The ratio of the PL intensity (I_{lum}) and Raman intensity (I_{Raman}) is used as a measure of the intrinsic luminescence quantum efficiency as described in Splendiani et al.[51]

	"A" Exciton		
Structure	**Peak Position (eV)**	**FWHM (meV)**	I_{Lum}/I_{Raman}
ME MoS_2/SiO_2	1.875	91	16
MoS_2/GaN – Large Triangle	1.883	63	400
MoS_2/GaN – Continuous SML	1.868	82	17
MoS_2/GaN – 2-Molecular Layers	1.845	116	3

XPS analysis was employed to determine the composition of the 2-D structures and to examine possible modifications of the GaN surface as a result of the CVD process. Figure 4 shows XPS spectra for the Mo 3-D, S 2s, S 2p, and Ga 3s core levels from a MoS_2 on GaN sample. The deconvolution of the Mo 3-D region reveals Mo 3-$D_{5/2}$ and 3-$D_{3/2}$ doublets corresponding to MoS_2 (229.4 and 232.5 eV) and a weak MoO_x doublet (232.4 and 235.6 eV) related to overdeposition of MoO_x during the MoO_3 vaporization. The comparison of the areas of the S 2s and Mo 3-D peaks shown in Fig. 3a provides an estimate of the S:Mo ratio of 2.05 ± 0.1, consistent with stoichiometric MoS_2. The S 2s peak appears at 226.5 eV, which is characteristic of MoS_2. Similarly, the S 2p doublet (Δ ≈ 1.18 eV) in Fig. 3b is consistent with MoS_2. Thus, the XPS analysis corroborates the MoS_2 composition of the structures on the GaN substrate.

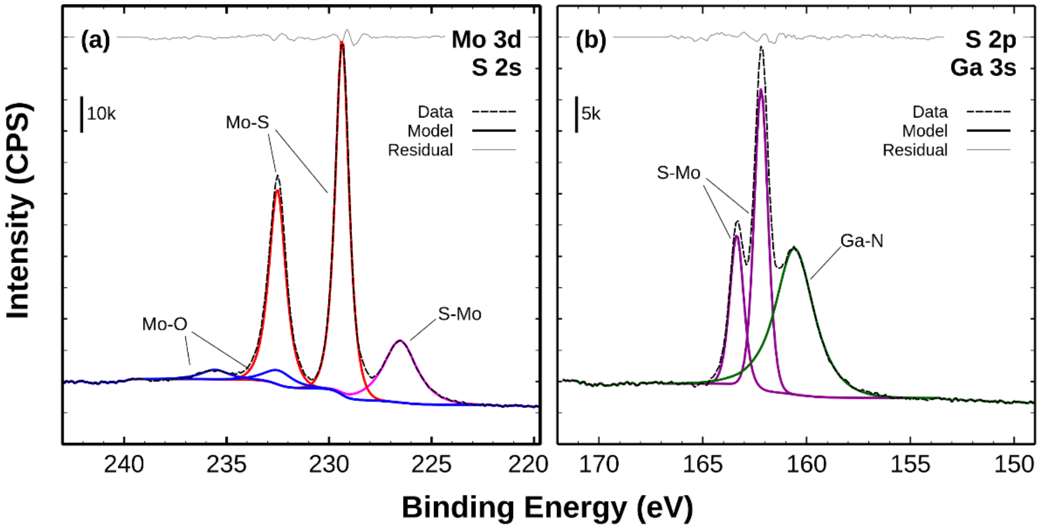

Fig. 4 Core level XPS spectra and peak fits from a) Mo 3-D and b) S 2p regions of MoS_2 on GaN. Panel a) shows components from S 2s (MoS_2), Mo 3-$D_{5/2}$, and 3-$D_{3/2}$ doublets (MoS_2 and MoO_x). In b), the S 2p doublet (MoS_2) and Ga 3s (GaN) are shown.

We investigated using XPS and an additional CVD growth whether the GaN surface is modified (i.e., sulfurized) during the CVD growth of MoS_2. A regular GaN/GaN//sapphire wafer (sample ID = GaN-S from here on) was run through the CVD process that was used to grow MoS_2 with the exception that the MoO_3 precursor was not introduced into the CVD tube. The GaN-S sample was exposed to the same S flow in the CVD tube and at the same substrate temperature and duration as the samples with MoS_2 structures. The XPS of the GaN-S sample revealed only a weak S 2s peak at BE = 226.4 eV, which corresponds to 1.3 ± 0.1 atomic percent of S on the surface. The spectral peak parameters of the Ga 2p, 3s, and 3d peaks are not modified for the pristine GaN wafer and GaN-S sample (Fig. 5c, f, and g). Furthermore, the presence of the sulfur shoulder S 2p is not detectable on the Ga 3s peak (Fig. 5f). We conclude that our GaN substrates are chemically stable in the CVD process.

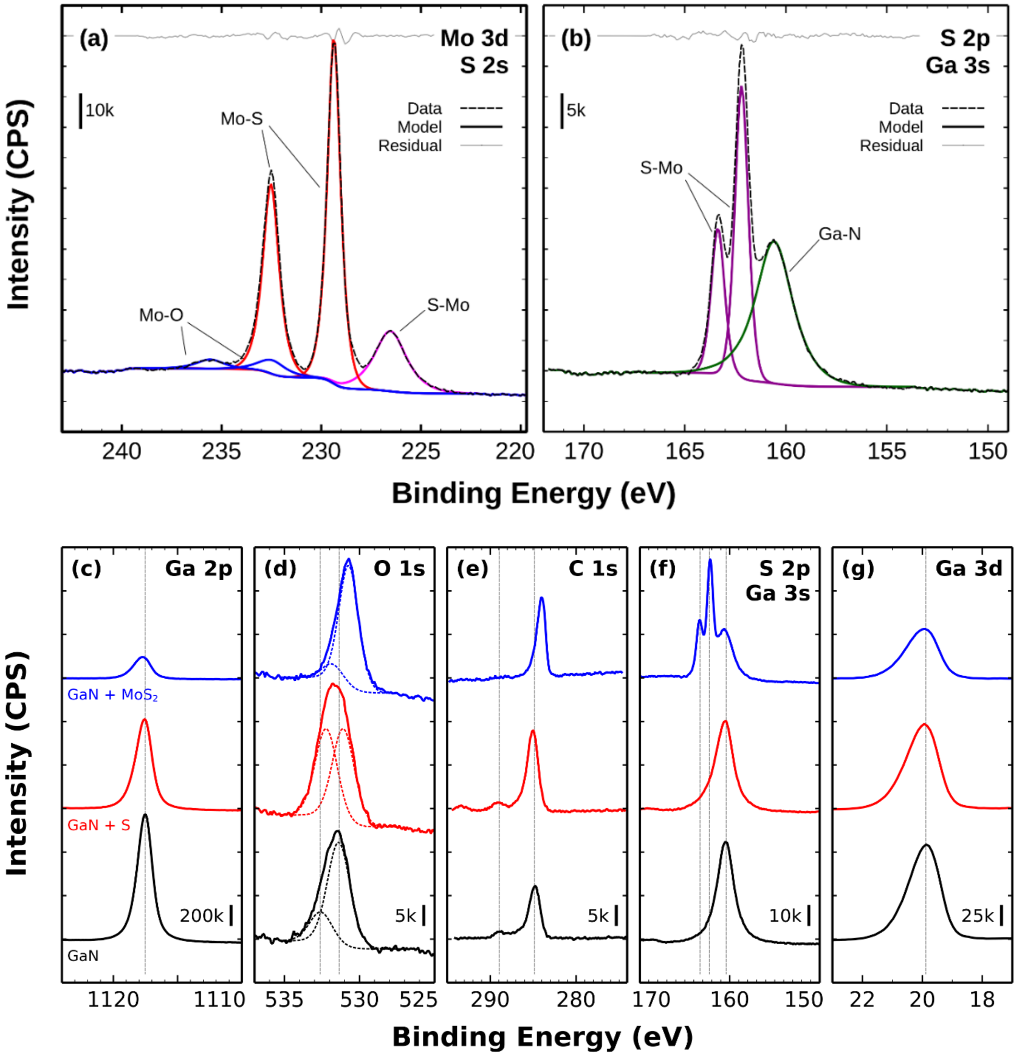

Fig. 5 Core-level spectra from a) Mo 3-D and b) S 2p regions of MoS_2 on GaN. Panel a) shows components from S 2s (MoS_2), Mo 3-$D_{5/2}$, and 3-$D_{3/2}$ doublets (MoS_2 and MoO_x). In b), the S 2p doublet (MoS_2) and Ga 3s (GaN) are shown. Panels c), d), e), f), and g) show a comparison of Ga 2p, O 1s, C 1s, S 2p, Ga 3s, and Ga 3-D regions for the unprocessed GaN surface (bottom traces, black), GaN exposed to sulfur (middle traces, red), and GaN+MoS_2 (top traces, blue).

We observe an interesting feature in the topographic and adhesion maps of the MoS_2 structures (see Fig. 7). There is enhanced density of topographic spikes near the edges of the triangles and there is lower density on the bare GaN and inside the MoS_2 triangles. The origin of this particle crowding is unclear but has been studied by other research groups. The reported increased oxygen content in the particles suggests that they are phases of MoO_x. As mentioned earlier, the presence of MoO_x was detected in our XPS measurements. It is possible that the redeposition of MoO_x phase from the MoO_3 precursor happens more frequently at the edges of the triangles since the edges offer more defects that may serve as nucleation sites. This particle crowding phenomenon could potentially limit the growth of large-area MoS_2 structures when the density of the particles is high enough to disturb the growth. Other methods of the TMD growth with a better-controlled environment that excludes oxygen may be required for large area MoS_2 growth on GaN.

We further probe the MoS_2/GaN ($n = 10^{16}$ cm^{-3}, 300 nm) heterojunction using CAFM to measure vertical charge transport. The degenerate n^+GaN ($n = 10^{19}$ cm^{-3}, 700 nm) layer served as the bottom electrode for the measurement with the AFM tip being the top nano-contact as shown in Fig. 6a. The CAFM measurements demonstrate that the MoS_2/GaN structures electrically conduct in the out-of-plane direction and across the vdW gap with typical current-voltage (I-V) characteristics shown in Fig. 6b. The conduction in the direction perpendicular to sample plane opens up the possibility to combine 2- and 3-D semiconductors in a vertical stack to create complex heterostructures with desired properties. For example, the crystalline order and epitaxy of our MoS_2/GaN stack should allow to use the top MoS_2 as a template for the consecutive epitaxial growth of next 2- or 3-D layer to build a 3-terminal device.

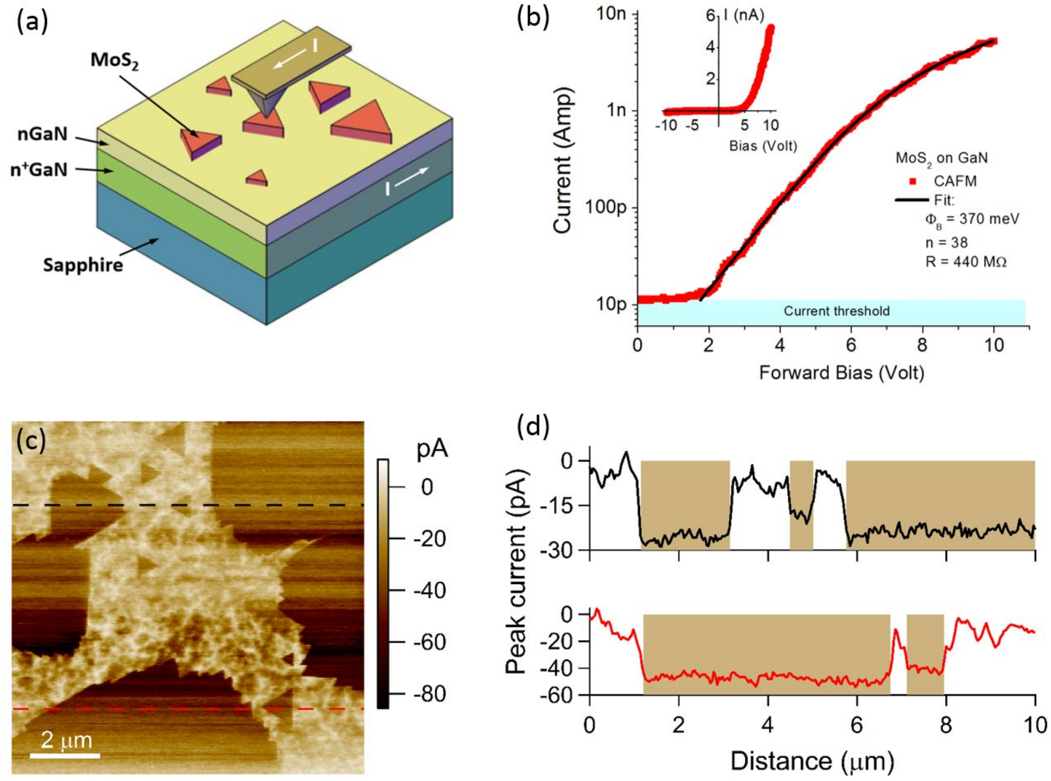

Fig. 6 CAFM of MoS_2 on GaN. a) The diagram of the measurement. b) Forward bias I-V curve on a MoS_2 ML. The fitting is described in the main text. (inset) Full I-V curve on a linear scale for MoS_2. c) Current map showing MoS_2 ML triangles. d) Line profiles across isolated triangles and large MoS_2 areas shown in c). The shaded areas in d) are ML MoS_2.

The results of CAFM local current maps are displayed in Fig. 6c and 9b. The CAFM shows enhancement of the electrical conductance on the MoS_2 monolayers versus bare GaN substrate and is also observed in the current line scans in Fig. 6d. One of the questions that we address in the CAFM study is how the current flows in the MoS_2 and across the MoS_2/GaN interface. If the sheet resistance of MoS_2 (R_{sh}) is considerably smaller than the contact resistance of the MoS_2/GaN interface over the area projected by the tip, $R_{sh} < \rho_c/A_{tip}$, then the current is expected to spread in the MoS_2 layer to minimize the contact resistance, $R_c = \rho_c/A_c$, where ρ_c is the MoS_2/GaN contact resistivity, A_{tip} is the CAFM tip contact area, and $A_c = \pi d_c^2/4$ is the effective contact area of MoS_2/GaN with the characteristic contact size d_c (which is roughly the contact transfer length commonly used to treat metal-semiconductor contacts). In this case, the CAFM conductivity in the current maps should be uniform across the MoS_2 layer within the distance d_c. If the opposite is true, $R_{sh} > \rho_c/A_{tip}$, then the current will travel vertically and will vary across the MoS_2 surface on the length scale $\sqrt{A_{tip}}$. The CAFM current maps over the MoS_2 triangles in Figs. 6c and 9b show the enhanced current level on the MoS_2 triangles and ML blankets is stable over the 1-μm size areas as compared to relatively large current fluctuations on the GaN substrate with the GaN feature sizes under 100 nm. This is indicative of large MoS_2/GaN contact areas ($d_c \geq 1\mu m$) and considerably smaller GaN/n^+GaN contact area and resistivity. To estimate d_c, the CAFM area maps were measured over large MoS_2 MLs and small triangles (Fig. 6c). In the two line scans shown in Fig. 6d, the current level on the 1-μm triangles is roughly 75% of the current level on ML islands. The higher resistance on the triangles can be explained with lower contact area limited by the triangle size, $A_{triangle} < A_c$. Since the CAFM current level does not scale with the MoS_2 area and increases only by a fraction of the current on triangles, d_c is expected to be greater than or equal to the triangle size and can be estimated as $d_c \approx 1\ \mu m$ ($A_c \approx 1\ \mu m^2$). Interestingly, the current spreading at the corners of the triangles is expected to be limited and is reflected in the measurement by a slightly lower current level at the left of both small triangles in the line scans in Fig. 6d.

Current microscopy using a CAFM tip was performed at several point locations on the MoS_2 MLs and GaN substrate. For both types of point locations, on MoS_2 and GaN, the shape of CAFM I-V curves is mostly determined by the tip-semiconductor interface that introduces the largest resistance to the current. The contribution of the MoS_2/GaN interface and the rest of the substrate is manifested only at larger currents (I > 0.5 nA) as an additional Ohmic drop, I·R. We find that the I-V curves can be fitted with the model of thermionic emission over the Schottky barrier between the tip and top semiconductor layer when the Ohmic drop I·R is included to account for the difference between the applied voltage and the voltage dropped across the Schottky barrier. An example of three-parameter fitting is displayed in Fig. 12b. Despite the unusually large ideality factor, n = 38, the Schottky barrier height Φ_B = 370 meV is near the value reported in the literature.[41] The extraction of the resistance R = 440 MΩ can be used to characterize the buried MoS_2/GaN interface which is of primary interest for this study. Using the previously estimated MoS_2/GaN contact size, $A_c = 1\ \mu m^2$, the contact resistivity can be evaluated to be below $\rho_C \leq RA_c = 4\ \Omega\ cm^2$. The fact that the constant resistance (R = 440 MΩ) fit provides an excellent match to the MoS_2 data in Fig. 12b is consistent with an ohmic MoS_2/GaN contact.

KPFM was employed to measure the electric surface potential of MoS_2 on GaN. The correct scale of the SP images was confirmed with a test scan on an Al-Si-gold (Au) calibration sample. In Fig. 7, the KPFM images of MoS_2 triangles and monolayer islands displayed a clear SP contrast between MoS_2 and GaN substrate. As shown in Fig. 7, we consistently measure a 360-mV SP difference between the GaN and MoS_2. The work function is evaluated first by calibrating the SP level on gold to the work function of 5.1 eV. Then we measure the work functions of MoS_2 and GaN to be 4.46 and 4.11 eV, respectively. This is consistent with the work function of the monolayer MoS_2 reported in the literature in the range from 4.0 to 5.1 eV.[11,42] We found the difference in SP between a monolayer and bilayer MoS_2 to be under 30 meV (see also Fig. 8).

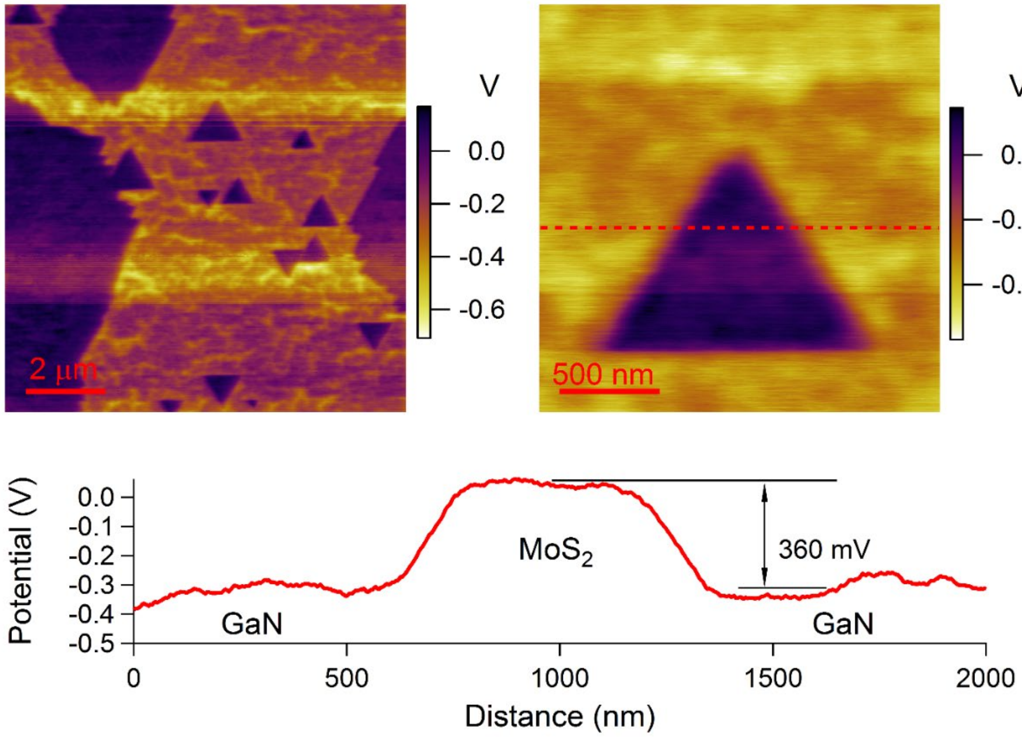

Fig. 7 **KPFM images showing the 360-mV offset of the SP of MoS_2 and GaN**

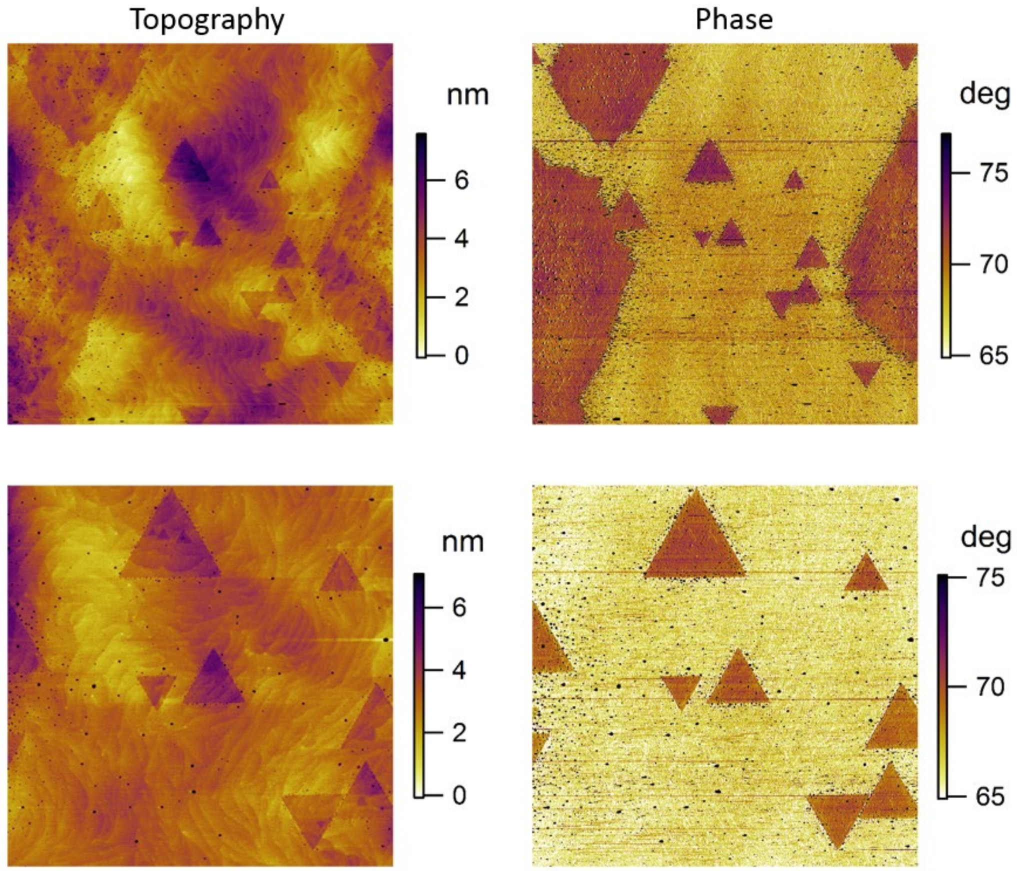

Fig. 8 AFM characterization of the MoS_2 on GaN terraced surface. (Left) Topography maps point out the higher order layer count. (Right) The phase maps distinguish between MoS_2 and GaN. (Top) Map size 10 × 10 µm. (Bottom) 5 × 5 µm.

The AFM topographical measurements of the MoS_2 MLs are strongly affected by the topography of the GaN substrate that consists of a series of terrace steps (see Figs. 6–8). The step height of a single MoS_2 ML (7 Å) is just distinguishable from the noise. Interestingly, the second-layer growth and higher-order stacking of MoS_2 MLs can be measured reliably to be near 7 Å per ML due to lower noise level of the scans on MoS_2. The phase area maps of the AM-AFM images show clear contrast of the MoS_2 MLs on the background of GaN (Fig. 9). We use the phase contrast images to simply identify the MoS_2 growth and the topography maps to readily show if the higher-order MoS_2 stacking is present (Figs. 9 and 10). Based on the contrast observed between the adhesive properties of the two materials (refer to the adhesion maps shown in Fig. 10), it is likely that the phase contrast between the two materials is due to differences between their adhesive properties.

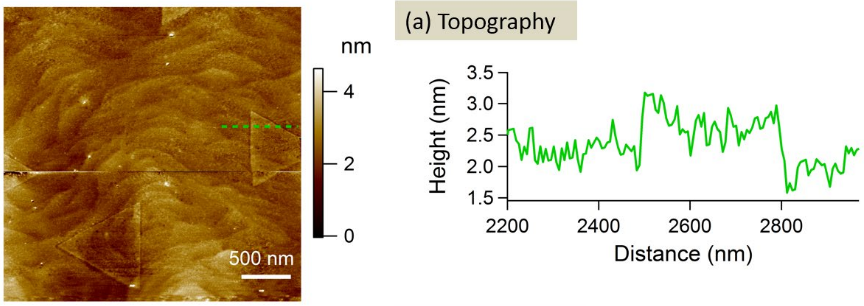

(a) Topography

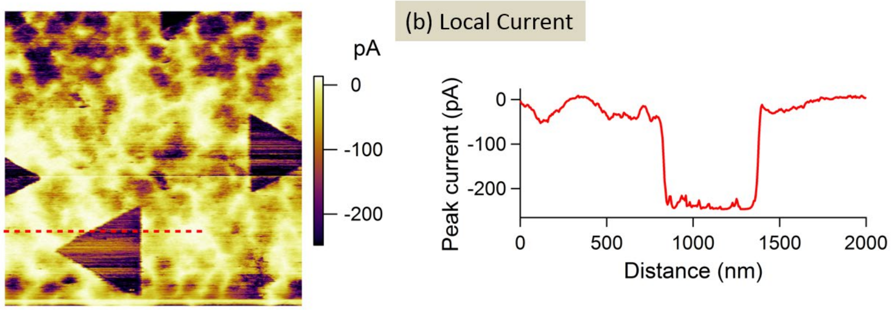

(b) Local Current

Fig. 9 CAFM measurements on MoS_2. a) Topography map and a line scan and b) local current map and a line scan across a MoS_2 triangle. The current and conductivity are enhanced on the MoS_2 ML triangles.

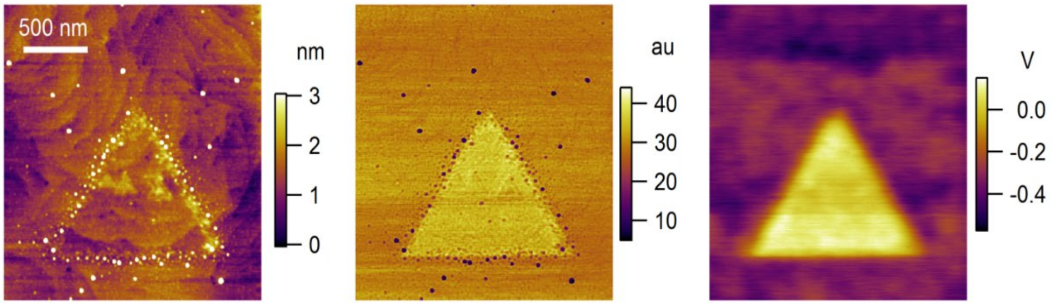

Fig. 10 Topography, adhesion, and surface potential map of a MoS_2 triangle with some bilayer and trilayer growth

4.4 Summary

We grew MoS_2 MLs epitaxially aligned to GaN substrates by means of powder vaporization. Raman spectroscopy and PL provide evidence of a high quality vdW interface between the MoS_2 and GaN substrate with 20-times PL enhancement observed in the center regions of large-area MoS_2 MLs. Measurements with CAFM showed that the MoS_2/GaN structures electrically conduct in the out-of-plane direction and across the vdW gap, which opens up a possibility to combine 2- and 3-D semiconductors in a vertical stack to create complex heterostructures with desired properties. The CAFM analysis suggests interface resistivity measured under 4 Ω cm^2 and an in-plane current spreading in the MoS_2 layer estimated to be approximately 1 μm in diameter. The KFPM measurements revealed a 360-mV contrast between MoS_2 and GaN SPs. The deduced work functions of MoS_2 and GaN were 4.46 and 4.11 eV, respectively. The CAFM current spectroscopy shows that the I-V curves on tip/MoS_2/GaN structures can be described with the thermionic emission model with unusually large ideality factor n = 38 and tip/MoS_2 Schottky barrier height of Φ_B = 370 meV. Epitaxial MoS_2/GaN heterostructures present a promising platform for the design of energy-efficient, high-speed, high-power vertical devices incorporating 2-D layered materials with 3-D semiconductors.

5. Characterization of a 2-D/3-D Heterojunction

5.1 Introduction and Motivation

In recent years, the exponential growth of research on 2-D materials such as graphene, MoS_2, and boron nitride (h-BN) has elucidated novel physics and devices.[43] However, the ability to obtain large-area, high-quality materials presents an inherent obstacle to the realization of technologies based on 2-D materials. In some cases, 2-D materials have been grown partially aligned on sapphire but require subsequent transfer to the substrate of interest, resulting in potential contamination issues.[44] Avoiding the transfer step, we previously grew MoS_2 on *n*-doped GaN via powder vaporization and provided SEM images showing evidence of epitaxial alignment[45] and others have grown MoS_2 on *p*-doped InGaN.[46] In these cases, the GaN substrate acts as a template for epitaxial growth and as an active element in the 2-D/3-D heterojunction, opening up the possibility of vertical electronic and optoelectronic devices.[45,47–49] Here we focus on the quantitative structural analysis of a 2-D/3-D heterojunction using Raman and PL measurement, cross-sectional transmission electron microscopy (XTEM), density functional theory (DFT) calculations, and electrical characterization for MoS_2 grown on *n*- and *p*-doped GaN.

5.2 Raman and PL Measurement

Raman and PL spectroscopy has been utilized extensively to investigate MoS_2 from a few molecular layers down to a single-molecular layer (SML).[34–35] Here, we provide a very brief review detailing some of the information made available by these techniques.

The Raman spectra are dominated by two characteristic Raman-active modes, noted as the in-plane E^1_{2g} and the out-of-plane A_{1g} modes in few layer systems. Since there is no center of inversion for a SML of MoS_2, E' and A'_1 are used instead of the common E^1_{2g} and A_{1g} notations when reference is made to the SML in this work. One of the most distinctive properties of confining the system to fewer layers is the redshift of the A_{1g} mode and blueshift of the E^1_{2g} phonon mode with decreasing number of layers. The blueshift of the E^1_{2g} peak was shown to be due to dielectric screening of the long-range Coulomb interaction,[50] while the redshift of the A_{1g} mode is in line with the classical picture of a harmonic potential.[51] As such, the frequency difference between E^1_{2g} and A_{1g} is often used to identify the number of MoS_2 layers. These two characteristic Raman modes have phonon frequency in the SML limit of approximately 385 cm^{-1} and approximately 405 cm^{-1}, respectively.

Other perturbations can also affect the peak positions of these characteristic phonon modes (e.g., strain and doping).[52–53] Work concerning the effect of strain shows that the in-plane E^1_{2g} mode is sensitive to strain, while the out-of-plane A_{1g} mode shows a weak strain dependence.[53] These two modes show distinct doping dependence, with the A_{1g} mode decreasing in frequency with increased electron concentration and the E^1_{2g} mode showing an overall weak dependence on electron concentration.[52] This difference is attributed to the stronger coupling to electrons of the A_{1g} mode compared with the E^1_{2g} mode. As a final point, recent work by Zhou and coworkers demonstrate that a blueshift of the A_{1g} mode is indicative of the strength of the vdW contact with the adjacent substrate.[36]

The conversion of an indirect gap material to one with a direct gap when the layer count is reduced to a SML is one of the most astonishing features of many layered vdW materials such as MoS_2.[54–55] Reduction to a SML of MoS_2 results in considerable light emission due to direct exciton recombination at a photon energy of approximately 1.8–1.9 eV. This photon energy is significantly lower than the first direct gap due to the existence of a very strong binding energy of the 2-D excitons as recently demonstrated by several research groups.[56–58] Two distinct peaks in the PL spectra may be observed near this energy range and are due to spin-orbit-induced splitting of the valence band. The most intense and lowest energy feature is known as the “A” exciton peak, whereas the much lower intensity and higher energy peak is the “B” exciton. The A-exciton peak is the PL feature of interest in this study. It should be noted that the intensity of A-exciton peak can be highly variable and is dependent upon the host substrate.[37] Furthermore, a considerable PL enhancement can result from physisorption of certain molecules that act as *p*-type dopants.[59] The energy position and width (FWHM) of this PL peak provides useful information related to the layer count, strain-state, and structural quality of the 2-D layer.

Figure 11a–c displays optical, Raman, and PL images taken at a region where small triangles have merged into continuous SMLs or layer stacks of two or more molecular layers. This region is chosen to demonstrate the high selectivity of Raman and PL dependence on the layer count. Features in the Raman image (Fig. 11b) are indicative of increased layer thickness with the greatest intensity originating from regions with the largest number of layers. Features in the PL image (Fig. 11c) corroborate those observed with Raman with regions of no-growth (black regions), SML growth (bright regions), and two or more molecular layers (gray regions) easily identifiable.

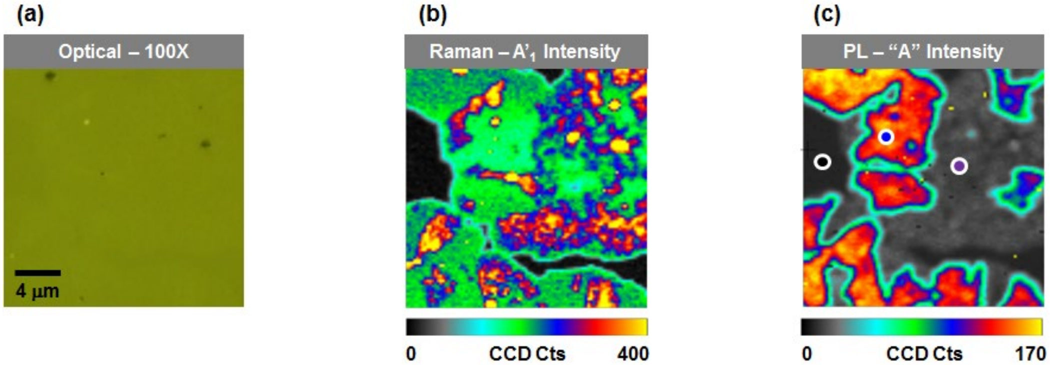

Fig. 11 a) Optical micrograph, b) Raman image of the A’$_1$ mode intensity, and c) PL image of the intensity of “A” exciton peak taken at a region where small triangles have merged into continuous SMLs or layer stacks of two or more molecular layers.

5.3 AFM (Charge Study)

CAFM, as well as other types of AFM, were used to characterize the MoS_2 structures on GaN. The details on the CAFM and AFM techniques and nanoprobes (tips) used are given in Section 4.2. During a CAFM measurement, a CAFM tip was grounded and served as the top nano-electrode while the degenerately n-doped GaN layer on the substrate was biased and served as the bottom contact to the MoS_2/GaN stacks, as depicted in the measurement diagram in Fig. 6a. Large-area (A_{back}) titanium (Ti)(bottom)/Au pads near the edges of the sample were evaporated on the top of the GaN wafer and served as the contacts to the bottom electrode, n$^+$GaN. Evaporation of the contacts with shadow masks allowed to avoid the contact of the samples with microfabrication chemicals. The Ti/Au contacts were non-ohmic but introduced only insignificant (due to large $A_{back} \gg A_c$) contact resistance ($R_{back} \propto A_{back}^{-1}$) below 1 kΩ, thus contributing negligible uncertainty (<6 µV) to the tip-to-n$^+$GaN bias at the currents measured.

In CAFM areal imaging, the substrate was biased at a constant voltage and the measured current was mapped. Topographical AFM imaging that included phase contrast imaging was usually performed over the area selected for the CAFM current mapping. A topographic map and corresponding current map of the MoS_2

structures on GaN substrate are displayed in Fig. 9. The AM-AFM maps of the topography and phase contrast are displayed in Fig. 8. Phase contrast images readily distinguish MoS_2-covered areas from GaN surface. The topographic images display a terrace-like structure of the GaN substrate with ultra-thin triangles and blankets of MoS_2 scattered on the surface. A topographic line scan across a MoS_2 triangle is shown in Fig. 9a with a vertical step in the place of the triangle just standing out from the background noise and consistent with 0.7 ± 0.5 nm height. Second layer triangles and higher-order growth can be readily seen in topographic AFM images (Fig. 8) due to lower noise level on the MoS_2 structures and measure approximately 0.7 nm per ML. Areal and line CAFM scans at –7 V substrate bias shown in Fig. 9b display the increase of conductivity on the MoS_2 triangles and the uniform current level throughout the triangles likely due to the current spreading in the MoS_2 layer. There are obvious fluctuations in the current level outside the triangles and on the GaN substrate (Fig. 9b). SEM analysis of the GaN substrate areas in between the MoS_2 triangles reveals some disordered, nanoscale growth structures in the form of clusters of nanoparticles visible only at high magnification. The topographic AFM analysis shows that those nascent, disordered growth structures, if present, must be generally no more than a MoS_2 ML in height. The nature of the observed nanoscale growth on GaN is unclear and it may be either a sub-ML of MoS_2 that later develops into ML MoS_2 or another material such as MoO_x. We speculate that those current fluctuations in the CAFM areal image (Fig. 9b) come from the enhancement of the conduction on nanoscale growth structures on the GaN substrate.

I-V spectroscopy at selected points on the sample surface was performed with the CAFM tip. Typical measured I-V curves for the MoS_2 monolayer and GaN substrate are displayed in Fig. 12. The voltage polarity on the graphs in Fig. 12 is chosen so that the positive voltage corresponds to the forward Schottky bias (i.e., electrons are injected from the semiconductor sample to the conductive tip).

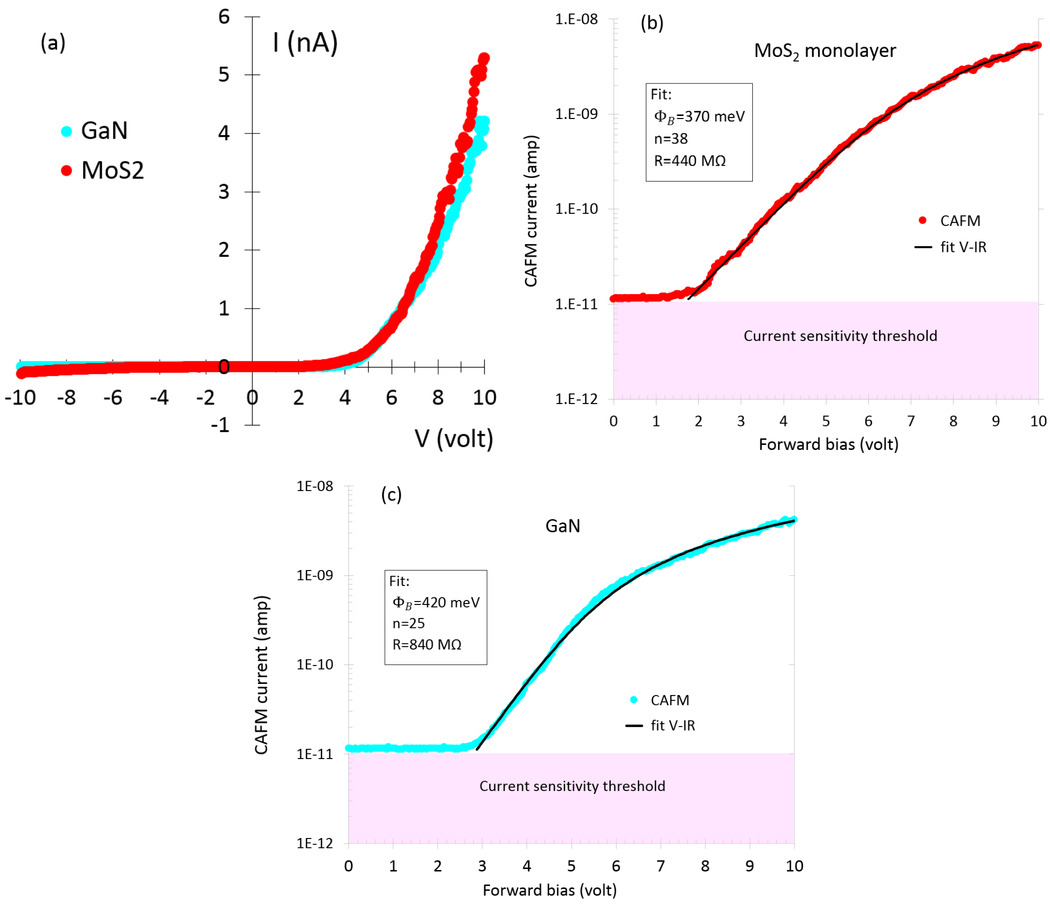

Fig. 12 Current spectroscopy of the tip/MoS$_2$/GaN and tip/GaN structures with fitting using the Eq. 1

The I-V curves for the point CAFM measurements on both MoS$_2$ and bare GaN substrate display rectifying behavior (Fig. 12a) suggesting that interfaces, not the bulk, are dominant contributors to the resistance. The similar current range and the shape of the MoS$_2$ and GaN curves and the expectation of the nGaN/n$^+$GaN contact to be close to ohmic suggest that the I-V behavior is mostly set by the non-ohmic contact between the CAFM tip and the sample. The I-V curves on MoS$_2$ locations display higher currents and narrower location-to-location variation than the I-V curves at the GaN locations. Since the I-V measurements on GaN might be affected by the nanoscale growth structures described earlier in this section and that are unresolved in the AFM images, we focus our analysis of the I-V spectroscopy on the data from MoS$_2$ MLs and show the data from the bare GaN locations only for comparison.

To de-convolute the embedded information on the MoS$_2$/GaN interface, we analyzed the I-V curves at forward bias as shown in Fig. 12b and c. At low-bias voltages, the current stays at the instrumental threshold level (~10 pA). From the threshold to 0.5 nA, the I-V follows the exponential rise that starts saturating above 1 nA. The same trend is true for the I-V curves of GaN. The current injection from a CAFM tip to a MoS_2 multilayer has been successfully described by Giannazzo et al. with the model of thermionic emission over the Schottky barrier[41]:

$$\boldsymbol{I = A_{tip}A^{*}T^{2}e^{-\frac{q\Phi_B}{kT}}e^{\frac{q(V-IR)}{nkT}}} \;, \tag{1}$$

where V is the applied bias between the tip and the sample, R is the resistance contributing to the voltage drop between the back contact to the sample and the tip-semiconductor interface, A_{tip} is the tip-sample contact area, $A^{*} = 4\pi qk^{2}m_{eff}/h^{3}$ is the Richardson constant with m_{eff} is the effective mass for electrons, h is the Planck constant, T = 293 K is the ambient temperature, q is the elementary charge, Φ_B is the height of the Schottky barrier at the tip-semiconductor interface measured from the Fermi level in the tip, k is the Boltzmann constant, and n is the ideality factor. We employed the formula (Eq. 1) to fit all the I-V curves for MoS_2 and GaN with $A_{tip} \approx 100\ nm^2$,[60] the effective masses m_{eff} of $0.47\ m_e$ for ML MoS_2,[61] and $0.20\ m_e$ for wurtzite GaN. Typical fitting results are displayed in Fig. 12b and c. For the low currents (below 0.6 nA) the curves could be fit with a simple exponent described with two fitting parameters (Φ_B, n, R=0). At larger currents, the I·R correction needed to be added to account for the discrepancy between the applied voltage and the voltage across the tip-semiconductor Schottky barrier. The extracted fitting parameters are Φ_B = 370 meV, n = 38, R = 440 MΩ for MoS_2 and Φ_B = 420 meV, n = 25, R = 840 MΩ for GaN. Large ideality factors raise a question on the applicability of the thermionic emission model for the tip-semiconductor contacts, suggesting that the extracted Schottky barrier heights need to be considered with caution. Nevertheless, our value of Φ_B = 370 meV for the barrier between ML MoS_2 and a doped diamond tip is not far from the reported Φ_B = 307 meV for the multilayer MoS_2 and Pt-coated AFM tip.[41] The larger resistance R = 840 MΩ for the GaN substrate is likely due to the smaller injection area in the top GaN and GaN/n^+GaN interface. The value of R = 440 MΩ for MoS_2 includes the contact resistance of the MoS_2/GaN interface and is used in the main text to estimate the upper bound of the interface's contact resistivity.

5.4 SEM/XTEM (Interface Study)

To understand the nature of the epitaxial MoS_2/GaN interface, we performed XTEM to extract in-plane lattice constants and characterize the vdW gap. XTEM revealed a close lattice match of 1.2% between MoS_2 and GaN with the lattice constants near their bulk material values, indicating that minimal strain is expected in the 2-D/3-D heterostructure. The latter is important for building more-complex heterostructures based on these materials in the future.

The synthesized MoS_2 is observed in the form of triangular domains on *n*- or *p*-GaN (Fig. 13). The epitaxial alignment of MoS_2 with the GaN substrate results in a high uniformity in the orientation and shape of the 2-D domains (Fig. 13a) unlike the typical in-plane randomly oriented MoS_2 domains grown on amorphous oxides.[20] Overall, our MoS_2 was observed to be of single ML thickness by Raman measurements[45] and XTEM (Fig. 13b). The average lateral size of the ML domain ranges between 1 and 3 µm depending on the growth run. There is occasional bilayer growth and higher-order stacks in the form of smaller triangles on top of the average size triangles (Fig. 13b). An interesting domain boundary in the MoS_2 ML found by XTEM as a 10-nm overlap as shown in the red insert of Fig. 13b. Terraces of atomic planes and steps are found in the GaN lattice that are “bridge” by MoS_2 MLs on top. EDX analysis done in-situ XTEM reveals the presence of Mo or S line in the surface area where the top isolated plane is visible. The Mo and S presence is not found in bulk GaN or on the surface of bare GaN, confirming that the isolated atomic plane in Fig. 13b is MoS_2.

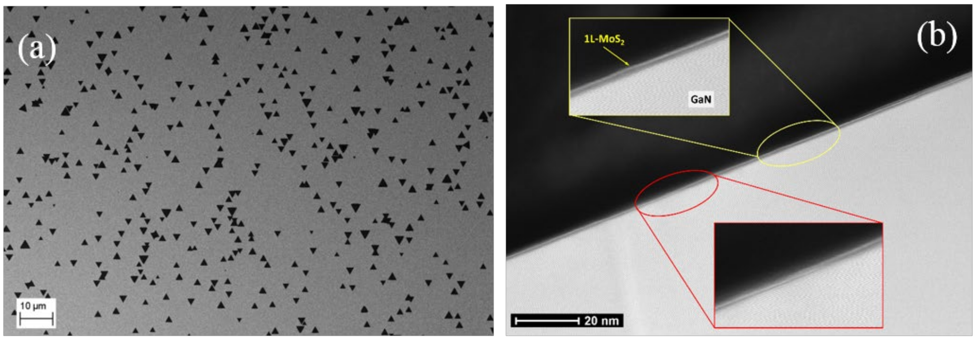

Fig. 13 MoS_2 domains on *n*-doped GaN. a) SEM image showing MoS_2 triangles aligned with the GaN lattice. b) Panoramic high-angle annular dark-field scanning transmission electron microscopy (HAADF-STEM) image showing ML and bilayer MoS_2 on GaN and the overlapping character of the MoS_2 domain boundary. The upper inset shows single-layer MoS_2 while the lower inset shows a grain boundary in the single-layer MoS_2.

Figure 14 shows XTEM images and corresponding intensity line profiles normal to the heterojunctions for Samples A and B at varying distance from the MoS_2 ML. Figure 14a and b shows ML MoS_2/GaN heterojunctions, Fig. 14c shows a bilayer MoS_2/GaN heterojunction, and Fig. 14d shows a bare GaN surface. In every case, where there is MoS_2 present, we always see two modified GaN layers of one GaN unit cell just below the MoS_2. The apparent modification of the top two GaN layers under MoS_2 could be attributed to partial oxidation[62] during the MoS_2 growth process, or some form of surface reconstruction. A detailed elemental analysis of the material composition in the vdW interfacial layer requires novel techniques such as time-of-flight secondary ion mass spectrometry (TOF-SIMS)[63] or electron energy loss spectroscopy (EELS),[64] which is beyond the scope of this study. The intensity line profiles corresponding to each XTEM image in Fig. 14 clearly show the presence of the modified GaN termination layers, even in Fig. 14a where the XTEM image is less conclusive to the eye. The MoS_2-GaN molecular layer spacing, $\Delta_{M\text{-}G}$, can be evaluated in the TEM images as the difference in the peaks 1 and 2 locations shown in the insert table in Fig. 14a and b (or peaks 2–3 in Fig. 14c) and consists of δ and half-layer thicknesses (θ_{MoS}, θ_{GaN}): $\Delta_{M\text{-}G} = \delta + \theta_{MoS}/2 + \theta_{GaN}/2$. The δ is evaluated from the center-to-center for Ga and S atoms and θ_{GaN} is omitted in our case for Ga-terminated GaN. The MoS_2-GaN spacing is measured with TEM in the range $\Delta_{M\text{-}G}$ = 3.8 to 5.7 Å. The variation of $\Delta_{M\text{-}G}$ is possibly due to the bridging of the MoS_2 ML over the GaN terraces or different conditions of the GaN termination double layer, which is more pronounced in Fig. 14b than in Fig. 14a. That said, we note a $\Delta_{M\text{-}G}$ = 4.55 Å peak-to-peak distance between the MoS_2 and the first GaN peak (peaks 2–3 in Fig 14c). This matches well to a value of 1.5 Å for the S-Mo bond distance ($\theta_{MoS}/2$) plus δ ~3.1 Å, vdW gap between S and Ga at the interface, as predicted by our theoretical calculation (details are provided in Section 5.6).

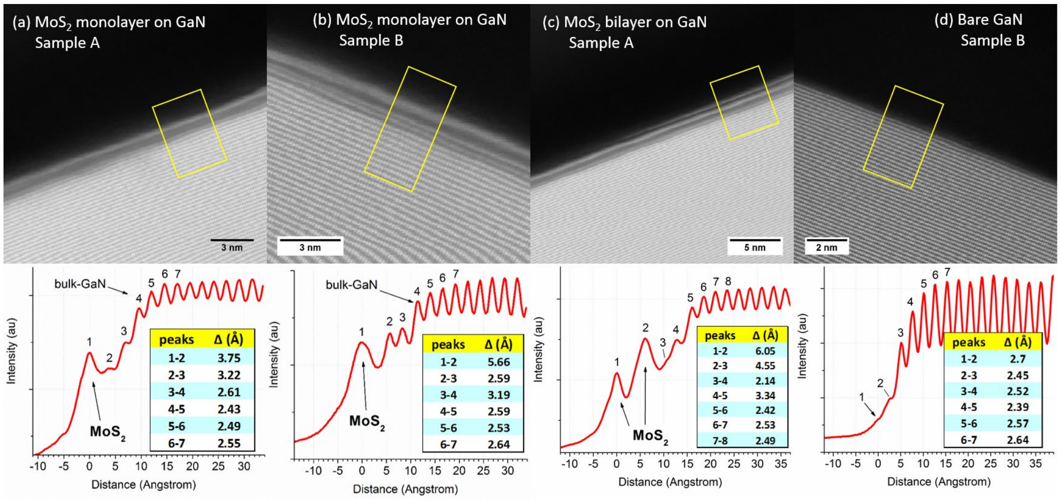

peaks	Δ (Å)
1-2	3.75
2-3	3.22
3-4	2.61
4-5	2.43
5-6	2.49
6-7	2.55

peaks	Δ (Å)
1-2	5.66
2-3	2.59
3-4	3.19
4-5	2.59
5-6	2.53
6-7	2.64

peaks	Δ (Å)
1-2	6.05
2-3	4.55
3-4	2.14
4-5	3.34
5-6	2.42
6-7	2.53
7-8	2.49

peaks	Δ (Å)
1-2	2.7
2-3	2.45
3-4	2.52
4-5	2.39
5-6	2.57
6-7	2.64

Fig. 14 XTEM images and peak intensity vs. distance from the surface for a) MoS_2 ML on GaN (Sample A), b) MoS_2 ML on GaN (Sample B), c) MoS_2 bilayer on GaN (Sample A), and d) bare GaN (Sample B). Note: The intensity of the line profiles at each point from the yellow boxes in each of the XTEM images are obtained by summing the intensities along the width of the box, perpendicular to the line profile direction.

We use in-plane intensity line profiles (not shown) to extract the in-plane lattice constants of MoS_2 and GaN. The in-plane line profiles are noisy so we performed a fast Fourier transform (FFT) to accurately extract the amplitude versus inverse distance. From the FFT, we extract in-plane lattice constants of 3.19 ± 0.13 Å for MoS_2 and 3.15 ± 0.08 Å for GaN (i.e. a lattice mismatch of 1.2%). The extracted lattice constants and mismatch align well with published results on the lattice constant *a* = 3.17 Å of unstrained MoS_2[65] as well as our calculations (refer to Section 5.6).

5.5 Vertical Transport Measurement

To analyze the electrical properties of the 2-D/3-D heterojunction, the CAFM measurements were performed using the setup illustrated in Fig. 15a. The I-V characteristics measured by CAFM for MoS_2/*n*-GaN and MoS_2/p-GaN vertical heterojunctions as well as bare *n*-GaN and *p*-GaN are shown in Fig. 15b. In these measurements, the CAFM tips are grounded and made of Pt-iridium (Ir), resulting in a Pt-Ir/MoS_2/GaN stack. The bias is applied to the substrate using a large top contact to GaN as justified previously.[45] The CAFM electrical measurements on MoS_2 show clear rectifying behavior in I-Vs for both *n*- and *p*-doped GaN substrates. The I-Vs for MoS_2/*n*-GaN are nearly exponential with the current reduction at large biases due to the ohmic voltage drop.[45] The I-Vs for MoS_2/*p*-GaN are non-exponential and show higher threshold voltages.

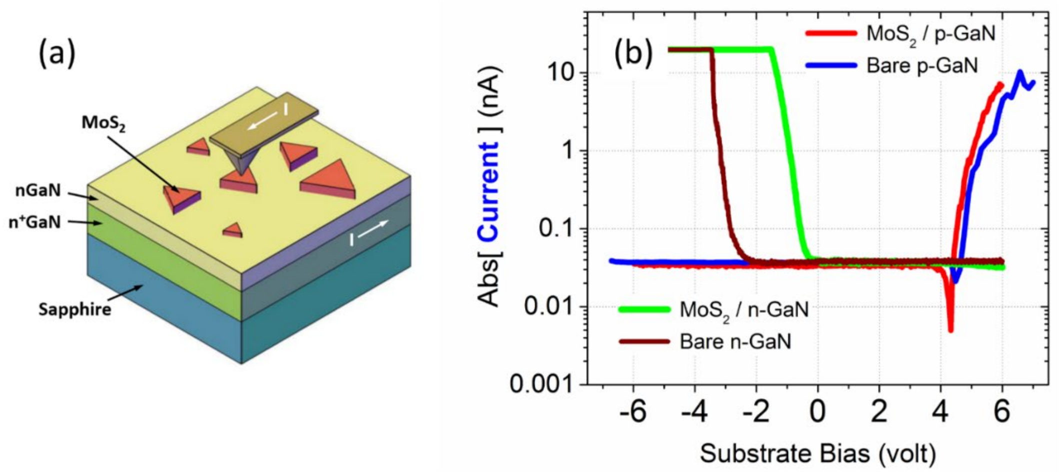

Fig. 15 a) Illustration of heterojunction sample and CAFM measurement. b) Current-voltage characteristics measured with CAFM for MoS_2/*n*-GaN and MoS_2/*p*-GaN heterojunctions and bare *n*-GaN and *p*-GaN surfaces.

The analysis of the I-V data in Fig. 15b for MoS_2 on both *n*-GaN and *p*-GaN and comparison with the measurements on bare GaN substrates provide a better understanding of the origin of the rectification behavior. There is a polarity change of the rectification when the substrate under MoS_2 changes from *n*-GaN to *p*-GaN. The rectification polarity for the MoS_2/*n*-GaN I-Vs corresponds to either the tip/MoS_2 Schottky barrier, as argued in the earlier CAFM measurements on MoS_2,[41,45] or tip/*n*-GaN Schottky barrier as supported in this study. On the other hand, the rectification polarity for the MoS_2/*p*-GaN I-Vs coincides with the expected polarity in this *p*-*n* junction with MoS_2 being the *n*-type semiconductor. Similar I-Vs and polarity were recently ascribed to the *p*-*n* junction behavior for *n*-MoS_2 on *p*-InGaN.[46] However, consideration of the I-V data for several tip-semiconductor cases in Fig. 15b indicates that the tip-GaN contact behavior governs the electrical transport rather than the MoS_2/GaN *p-n* junction. If the rectifying behavior for MoS_2/*n*-GaN is due to the tip-MoS_2 Schottky barrier, then this barrier should be present in the MoS_2/*p*-GaN I-V curves, which would zero the I-V at positive bias, which is not observed in Fig. 15b. In addition, the I-V curves for bare GaN resemble the I-V curves for the MoS_2/GaN heterojunction in polarity and shape. This data can be reconciled if we assume that the I-V curves are governed by the tip-GaN junction, which is modified by the presence of a MoS_2 monolayer. These results are important to consider when building vertical *p-n* junction heterostructures involving 2-D crystals as illustrated with the variation of I-V interpretations mentioned previously. The 2-D semiconductor components below a certain thickness in vertical bipolar heterojunctions might be electronically transparent and introduce only superficial changes to the electron transport instead of acting as independent semiconductor components.

5.6 Theoretical Verification

5.6.1 Models and Methods

To elucidate our experimental observations on the 2-D/3-D heterojunction, we calculated interface properties using DFT with the projector augmented wave (PAW) method[66] as implemented in the Vienna Ab-Initio Simulation Package (VASP) code.[67] The structure optimization, total energy, and electronic structure calculations were performed using the generalized gradient approximation (GGA) parameterized by Perdew–Burke and Ernzerhof (PBE).[68] A plane-wave basis kinetic energy cutoff of 500 and 300 eV were used and tested to reach convergence for the lattice properties of bulk GaN and MoS_2, respectively. A Γ-centered Mokhorst–Pack Brillouin zone (BZ) integration scheme was adopted to integrate over the BZ.[69] The lattice parameters were optimized individually for bulk MoS_2 and wurtzite GaN. The semi-empirical DFT-D2 dispersion correction of Grimme was implemented to include the vdW interactions in the Kohn–Sham energies.[70] The forces were calculated using the Hellmann–Feynman procedure and geometries were optimized using a conjugated gradient (CG) scheme. The atomic coordinates were optimized in all directions with a convergence criterion of 0.001 eV $Å^{-1}$ for the atomic forces. The optimized bulk MoS_2 lattice constants are a = b = 3.19 Å and c = 12.33 Å, and bulk GaN lattice constants are a = b = 3.22 Å and c = 5.25 Å. These values are in agreement with experimental data for MoS_2: a = b = 3.169 Å and c = 12.324 Å,[65] and GaN: a = 3.189 Å and c = 5.185 Å.[71]

Using the optimized lattice parameters from our bulk calculations, a single-layer MoS_2 (1L-MoS_2) and GaN (0001) surface (s-GaN) was constructed (Fig. 16), prior to forming 1L-MoS_2/s-GaN supercells (see Fig. 18). For both the systems, a vacuum spacing of 20 Å was added along the z-axis to minimize spurious interactions with the central cell and its periodic images.

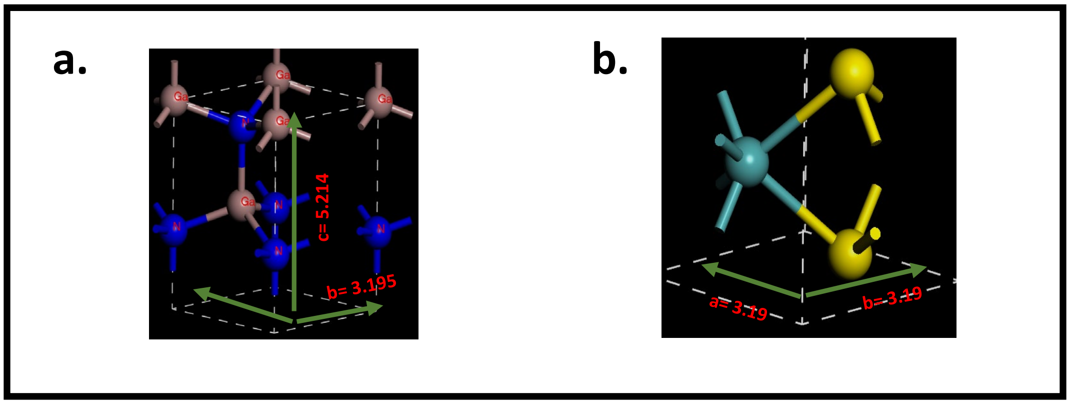

Fig. 16 a) Bulk GaN and b) MoS2 unit cells. Numeric values along the axes represent the optimized lattice parameters obtained from simulation.

To maintain a balance between accuracy and computational cost, a critical surface thickness that preserves bulk-like features was identified by varying the surface thickness in the out-of-plane direction (along z) while maintaining the periodicity of the in-plane directions (along x and y) and comparing the electronic properties, such as energy gap and edge states, to those of the bulk. The calibration models used in this study are illustrated in Fig. 17.

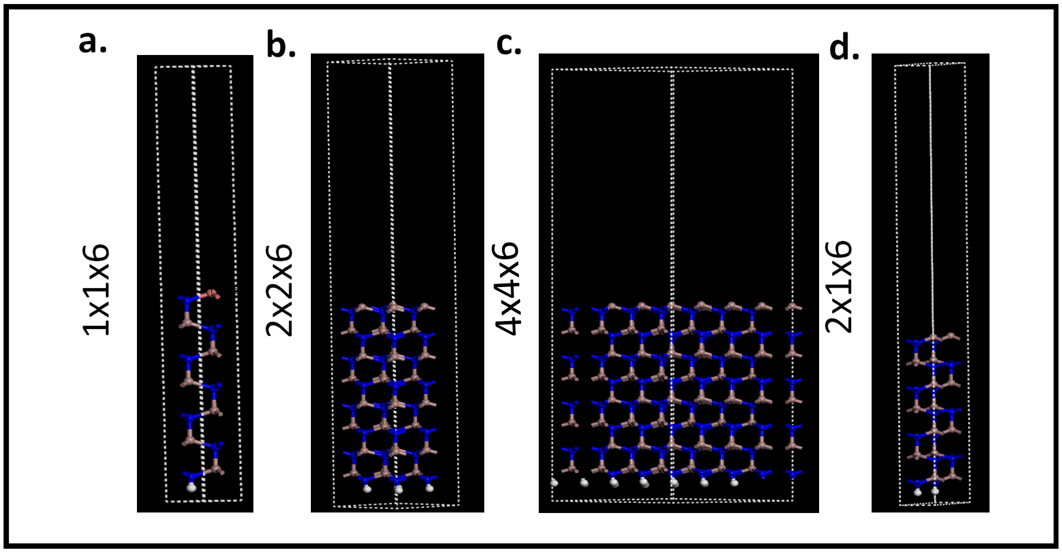

Fig. 17 Example GaN (0001)-surface models considered in the method calibration

The six Ga-N bilayers (~15 Å) were found to be a suitable representation for the bulk-like GaN surface. To simulate the laterally contracted Ga bilayer structure under Ga-rich conditions, and also allow surface relaxation, a Ga- surface consisting of a (2 × 2 × 6) supercell (Fig. 17b) with the in-plane and out-of-plane lattice constants of 6.4397 and 14.984 Å, respectively, was modeled where two Ga atoms were present in the outer laterally contracted overlayer for every one atom in the underlying layer resulting in a Ga-terminated surface. The dangling bonds at the N-terminated bottom layer were passivated by pseudo-H atoms with a charge of 0.75e in order to prevent an unphysical charge transfer between the top and the bottom slab surfaces. The upper three bilayers of s-GaN (0001) were allowed to relax, while the bottom three bilayers and saturating H atoms were fixed to mimic the bulk substrate. A vacuum spacing of 20 Å was added along the z-axis for all the structures to minimize spurious interaction due to periodicity.

5.6.2 Structural Properties

The focus of the structural properties study is to evaluate 2-D layer registry on 3-D system. Since the interface is epitaxial type, the growth of 2-D materials is governed by the weak vdW force. This force is also responsible for interlayer sliding and twisting between 2-D layer and 3-D surface at the 2-D/3-D heterojunction. To verify the structural registry between MoS_2 layer and GaN surface, we have systematically modulated the distance between MoS_2 layer and GaN surface, while varying the registry between them. Since the strain between MoS_2 and Ga-terminated GaN (0001) surface is minimal, there are mainly three different registry configurations: a) "Ga-top" (AB-like), b) "bridge", and c) "N-top" (AA-like). The top and side view of these configurations are illustrated in Fig. 18.

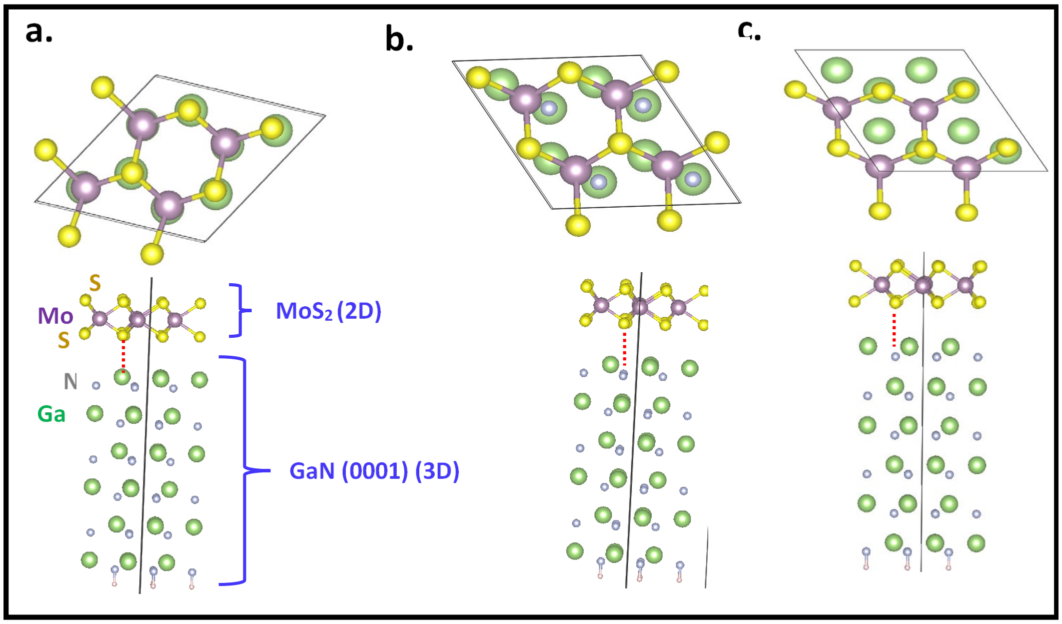

Fig. 18 Out-of-plane registries between MoS_2 and GaN (0001) surface. a) "Ga-top" configuration, b) "bridge" configuration, and c) "N-top" configuration. Dotted (red) lines indicate vertical registries between S atoms and atoms in GaN (0001) surface.

In the "Ga-top" configuration, the bottom S atoms in MoS_2 layer sit directly on top of the surface Ga atoms in the GaN (0001) surface as illustrated in Fig. 18a. As can been seen in the side view, because of the lack of intralayer symmetry, the top S atoms are not perfectly aligned with the bottom S atoms. In the case of the "bridge" configuration, the bottom S atoms in MoS_2 layer sit in between the surface Ga atoms and N atoms in the GaN (0001) surface as shown in Fig. 18b. The third and final configuration is "N-top" configuration, which is illustrated in Fig. 18c. In this configuration, the bottom S atoms in the MoS_2 layer sit directly on top of the surface N atoms in the GaN (0001) surface. Due to the hexagonal rotational symmetry of the interface between the MoS_2 layer and GaN (0001) surface, the "N-top" configuration is analogous to the in-plane rotation of MoS_2 in the "Ga-top" configuration by 60°. After establishing the possible registry configurations between the MoS_2 layer and GaN (0001) surface, we then calculate and compare total energies of these configurations and identify the stable configuration with the minimal total energies. Since the total number and type of atoms in these configurations remain constant, this approach of comparing total energies in lieu of binding energies is justifiable. The total energies for all three configurations at varying interlayer vdW distance (d_{vdW}) are illustrated in Fig. 19.

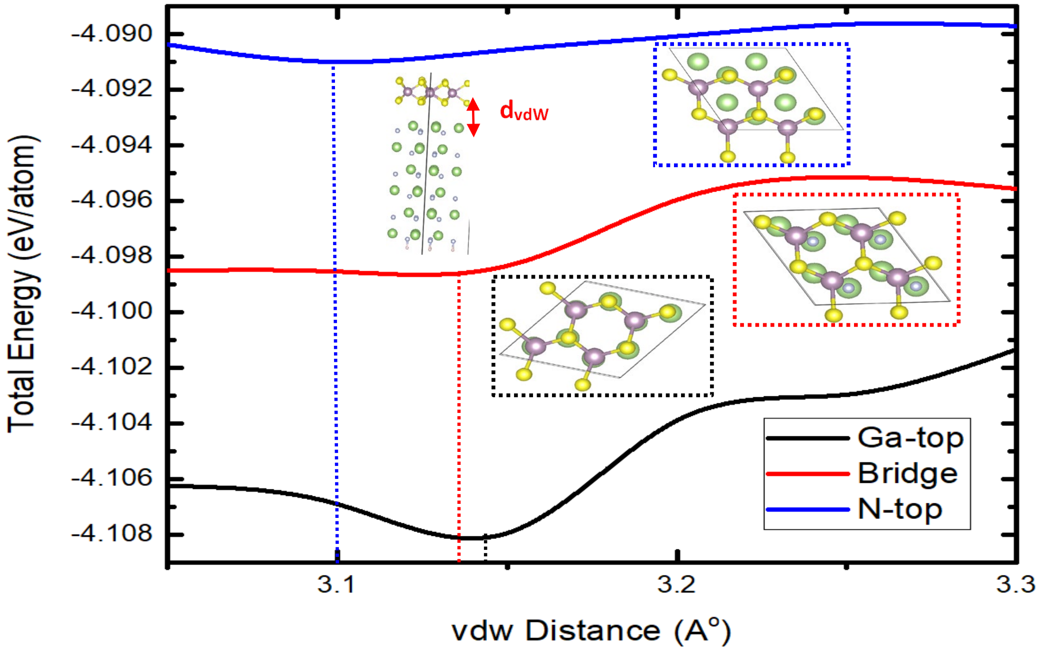

Fig. 19 Total energies for varying vdW distance (d_{vdW}) between MoS_2 on GaN (0001) surface for "Ga-top" (black), "bridge" (red), and "N-top" (blue) configurations. Insets illustrate top-down views of these registry configurations.

The "Ga-top" configurations, over the considered vdW distances, have smaller total energies as compared to "bridge" and "N-top" configurations, as can be inferred from the Fig. 19. Qualitatively, the total energy difference between the “Ga-top” and “bridge” configurations fluctuates between 5 and 8 meV. Similarly, the difference in per atom total energy between the “bridge” and “N-top” configurations varies between 4 to 8 meV throughout the considered vdW distances. Since the chemical composition in each of these configurations remains constant throughout the physical translation from “Ga-top” to “N-top” configuration, the energy contribution to that leads to the variation in the total energy mainly comes from the vdW force (energy) between surface S and Ga atoms. The MoS_2 layer encounters identical potential energy surface (PES) barriers while transitioning from “Ga-top” to “bridge” and “bridge” to “N-top” configuration on the GaN (0001) surface. This correlates well with the equidistant physical translation undergone by the MoS_2 layer while transitioning from the “Ga-top” to “bridge”, and finally, to the “N-top” configuration. This is an indication that the out-of-plane registry of MoS_2 on GaN substrate is mainly governed by the vdW-force between MoS_2 layer and GaN surface. As stated earlier, due to the hexagonal symmetry, the “N-top” configuration is thermodynamically similar to the “Ga-top” configuration when the MoS_2 layer is rotated by 60° on the GaN surface. The net per atom total energy difference of approximately 20 meV between “Ga-top” and “N-top” configuration stipulates the possibility of orientation dependent growth of MoS_2 on GaN substrate.

In conclusion, the “Ga-top” configuration in the MoS_2/GaN (0001) heterostructure is relatively stable and energetically favorable than the “bridge” and “N-top” configuration, which is consistent with our findings on the interface properties of single layer MoS_2/ GaN heterostructure using Raman and XTEM studies.

To validate and verify the vdW distance between the MoS_2 layer and GaN substrate extracted from the XTEM measurements (see Fig. 14), we further analyzed the minimal per atom total energy and corresponding vdW distance (d_{vdW}) for all the configurations. The dvdW at which the total energy is minimum represents the optimized distance between MoS_2 layer and GaN (0001) surface, which is analogous to MoS_2-GaN molecular layer spacing, ΔM-G, evaluated using the TEM images and the difference in the peaks 1 and 2 locations observed in the line profile of the XTEM measurement (refer to Section 5.4). During the layer-by-layer epitaxial growth of asymmetrical layers, the structural parameters such as lateral spacing and alignment between the layers are mainly defined by the repulsion between the interface atoms mainly caused by the vdW force between interface atoms and their cumulative covalent radii. In our MoS_2/GaN (0001) heterostructures, S, Ga, and N atoms are the interface atoms with atomic radii of 1.05, 1.22, and 0.71 Å, respectively. Since the sum of radii between S and Ga atoms is higher than the S and N atoms, d_{vdW} for the “Ga-top” configuration is expected to be higher than the "N-top" configuration. As can be seen in Fig. 19, the d_{vdW} value is slightly larger for the "Ga-top" configuration, as compared to the "bridge" and "N-top" configurations. The quantitative values of d_{vdW} for "N-top", "bridge", and "Ga-top" configurations are 3.1, 3.13, and 3.14 Å, respectively. In conclusion, the larger $d_{vdW,}$ due to the smaller repulsive forces between the interface atoms, between MoS_2 and GaN (0001) in the "Ga-top" configuration contributes to the stable MoS_2/GaN (0001) heterostructure, which is consistent with the results from the total energy calculation and experimental observations.

5.6.3 Electronic Properties

For the electronic structure calculations, a 6 × 6 × 1 k-mesh was used for both the monolayer MoS_2 and s-GaN (0001) structures. The k-mesh was reduced to a converged 3 × 3 × 1 grid for the s-GaN and SL-MoS_2/s-GaN supercell. Similarly, the energy cut-off for the plane wave basis was increased to 500 eV for the supercell calculations. The structure optimization parameters were similar to the bulk calculations mentioned previously. For the electronic properties, we have employed both the GGA with PBE and hybrid functional (HSE06) methods.

To verify the accuracy of designed models and adapted methods in our MoS_2/GaN heterostructure system, we perform electronic structure calculations for the well-established systems such as bulk MoS_2, single layer MoS_2, bulk GaN and surface GaN. The resultant electronic structures from are calculations are presented in Figs. 20 and 21. The band structure is plotted along the G-M-K-G BZ path as illustrated in the inset of Fig. 20a.

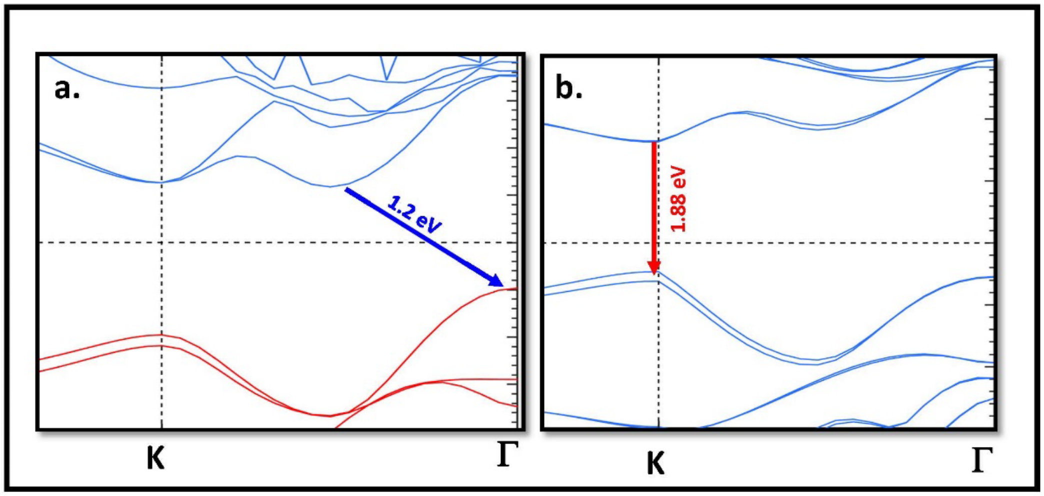

Fig. 20 Band structures of a) bulk MoS_2, and b) SML MoS_2. The number values represent fundamental energy gaps.

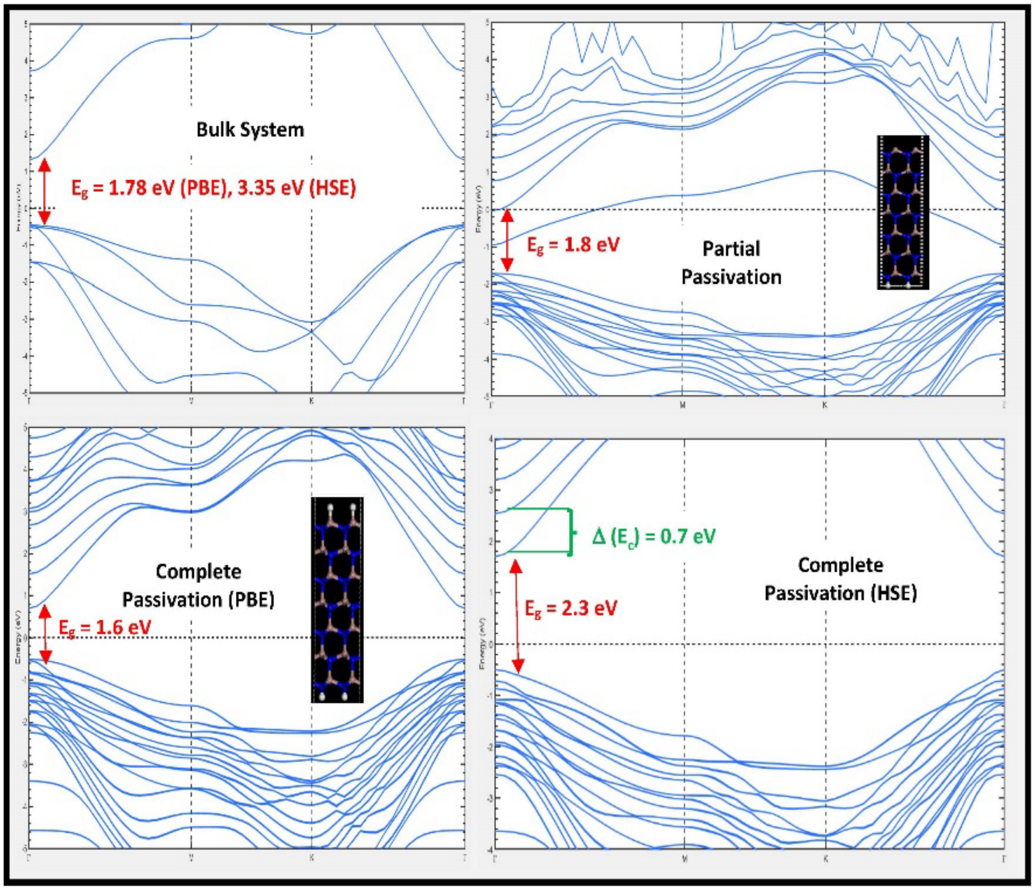

Fig. 21 Band structures of a) bulk GaN, and b) bottom passivated GaN (0001) surface, c) top and bottom passivated GaN (0001) surface with PBE level of theory, and d) similar to c) but with HSE06 level of theory. The number values represent fundamental energy gaps.

As can be seen in Fig. 20, the electronic structures of MoS_2 exhibit indirect to direct gap transition while going from bulk to the single layer system. The HSE06 functional, which incorporates electron-electron correlation, predicts values of 1.2 and 1.88 eV for the bulk and single-layer MoS_2, respectively, and these values are consistent with the published experimental as well as theoretical data. The indirect-to-direct transition of electronic structure is a consequence of the valence band (VB) sensitivity toward the interlayer vdW coupling between the layers. This is an indication that the interaction between MoS_2 and GaN in MoS_2/GaN (0001) heterostructure will influence the properties of single layer MoS_2 more than the GaN (0001).

The charge and electronics structure modeling of wurtzite (0001) surfaces like GaN (0001) surface require special convergence test on the lattice parameters, and type and thickness of the surface model because of their polar surfaces. Here, we calculated the electronic properties of bulk GaN using the optimized lattice parameters and plotted in Fig. 21a. The predicted fundamental bulk GaN energy gaps of 1.8 and 3.35 eV, with PBE and HSE06, respectively, are consistent with earlier publications. Following the bulk energy gap calculations, we performed electronic calculations for partially passivated and fully passivated GaN (0001) surfaces. As evident from the Fig. 21b, in the bottom passivated GaN (0001) surface exhibits semi-metallic characteristics. The dispersive surface states originates from the dangling Ga-N pair on the unpassivated side of the surface and extends throughout the BZ. Nevertheless, the complete passivation of GaN (0001) surfaces leads to the electronic phase transition from semi-metallic to semi-conducting system, irrespective of method or functional of choice. The HSE06 functional results in shifting of CBE toward the higher value.

Since the goal of our surface modeling is to identify the thickness and passivation mechanism that mimics the bulk-like GaN system to form experimentally observed surface, we compare the feature of the electronic structure and quantitative values of the energy gap between the bulk and surface models. Beside the degenerate and folded bands, as a consequence of a large number of atoms in the surface supercell, the dispersive characteristics of bands in the bulk GaN and fully passivated GaN (0001) surface are similar (Fig. 21c and d). The energy gap in fully passivated GaN (0001) surface is 2.3 eV, approximately 1 eV less than the bulk energy gap. The reduction in the energy gap is mainly due to finite thickness of the surface model. The contribution to the CBE states in the fully passivated GaN (0001) surface originates from the outer surface layers. The energy gap due to the inner bulk-like atoms is 3 eV. The Δ (E) = 0.7 eV between the surface and bulk CB states is analogous to the surface induced band bending observed in the similar systems in our in-house Kelvin Probe (KP) experiment. Though the quantitative value of the bulk energy gap in the fully passivated GaN (0001) surface is less than the bulk energy gap, it can be tuned using exchange-correlation parameter and thicker surface model, which is outside the scope of this study.

We have also analyzed the work-function ϕ, defined as the energy difference between the Fermi-level and vacuum energy level, of the GaN (0001) system. The vacuum level in GaN (0001) is determined by integrating self-consistent charge in the out-of-plane direction. The extracted ϕ for GaN (0001) surface is 4.21 eV, which is consistent with the recent experimental observation (4.20 eV) by Schultz et al.[72] Since the overall characteristics of the surface band structure resemble to that of the bulk system and our aim is to provide a qualitative analysis and support to the experimentally observed electronic properties, the fully passivated GaN (0001) surface models are utilized in our MoS_2/GaN (0001) heterostructure simulations.

After the verification of methods and models through electronic structure calculation of constituent systems in MoS_2/GaN (0001) heterostructure, we have conducted a detailed electronic structure calculations and analyzed orbital characteristics of the heterostructure. The resultant band structure is illustrated in Fig. 22. The inset represents the atomistic model of Ga-top MoS_2/GaN (0001) heterostructure with d_{vdW} = 3.14 Å, which is identified as the most stable configuration in the previous section.

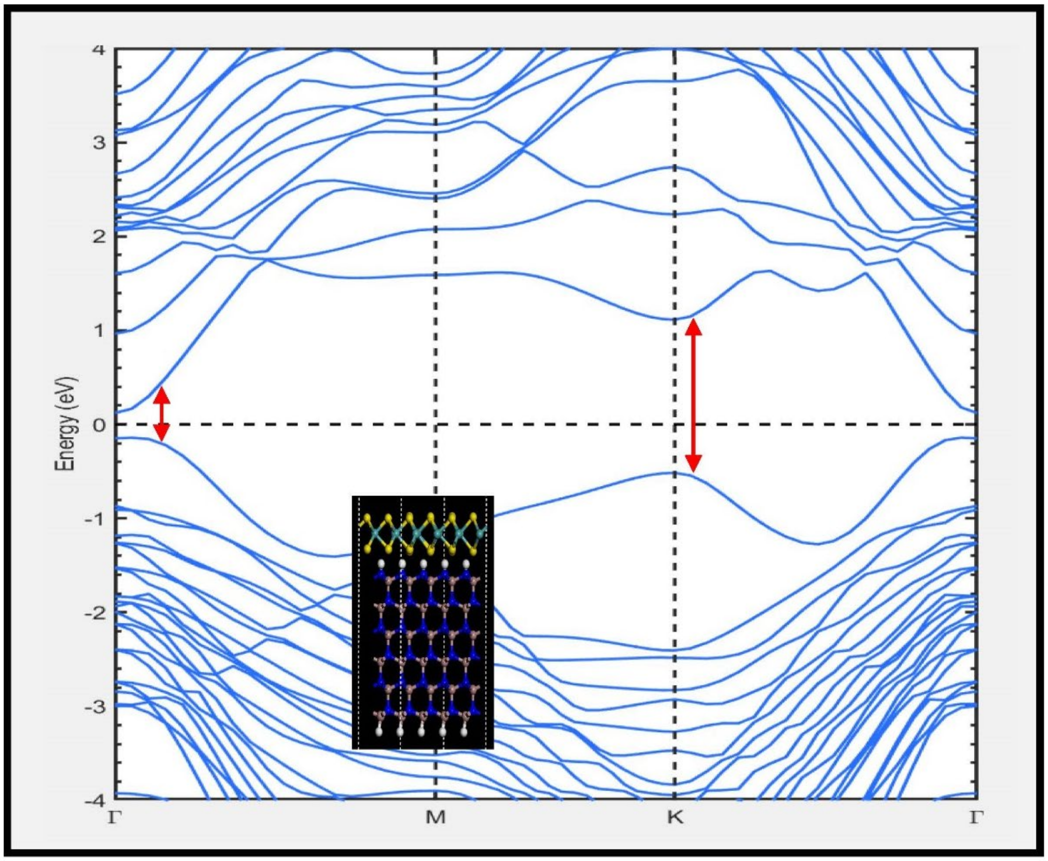

Fig. 22 Band structure of MoS_2/GaN (0001) surface with PBE level of theory. The number values represent fundamental energy gaps.

The calculated direct energy gap (E^{d}_{gap}) at Γ-point for MoS_2/GaN (0001) is 0.46 eV and indirect energy gap (E^{i}_{gap}) between K and Γ-points in the BZ is 1.21 eV, at the PBE level of theory. The energy difference between E^{i}_{gap} and E^{d}_{gap} is 0.75 eV. If we ignore the surface states and consider the bulk-like states in the GaN (0001), the resultant E^{d}_{gap} is around 1.2 eV. Even though the PBE level of theory underpredicts the fundamental energy gap, it does correctly predicts overall features of the band structure. One way to circumvent this issue is to add a computationally intensive HSE06 hybrid level of theory, which includes electron–electron interactions to the self-consistent energy and increases the fundamental gap of the system, while the overall features of the band structure remains same. This is also confirmed by our single layer MoS_2 band structures presented in the Fig. 20. The HSE06 predicted bandgap, ignoring the surface states, is 1.86 eV.

In the vertical HBT devices, the current across the base 2-D material sandwiched between 3-D layers (see Fig. 14) is defined by the charge transfer due to the interlayer coupling between the 2- and 3-D layers. At the atomistic scale, the charge transfer between the layers is characterized by the degree of electronic states hybridization between them. To analyze the charge transfer process, we have analyzed the atomistic projected density of states of the MoS_2/GaN (0001) heterostructure. A closer look at the projected density of states reveals that the valence band edge (VBE) energy states are mainly consist of Mo and S states from the MoS_2 layer, with weak hybridization with the surface Ga and N states. On the contrary, surface Ga and N states from the GaN (0001) surface dominate the conduction band edge (CBE) energy states. As can be seen in the Fig. 22, the states around the K point in the BZ are composed of states from MoS_2 layers and the dispersion resembles that of a single MoS_2. The unperturbed nature of the states suggest for an asymmetric hybridization of the energy states across the BZ in MoS_2/GaN (0001) heterostructure. This is also an indication that the electronic properties of the MoS_2/GaN (0001) heterostructure can be modulated by modulating structural and electronic properties of the MoS_2 layer alone.

On a passing note, there is a common consensus in the research community about the low-quality GaN surface due to the dangling bonds and resultant structural relaxation. Many experimental as well as theoretical attempts have been made to identify a suitable passivation mechanism to mitigate this issue. Motivated by this, we have also calculated electronic properties of MoS_2/unpassivated GaN (0001) heterostructure. One key finding from our study is that the presence of MoS_2 layer on the unpassivated GaN (0001) surface minimizes the surface states within the bandgap, suggesting the use of 2-D materials as an alternative passivating layer to GaN surface.

In addition to the detailed analysis of electronic properties, we have made an attempt to establish a correlation between the calculated electronics properties to that of observed threshold voltage shift and decrease in on current observed in or experiment mainly due to charge migration from the MoS_2 layer to GaN surface. In our experiment, for both types of GaN layers, the insertion of the MoS_2 layer reduces the magnitude of the turn-on voltage, which is especially pronounced for the MoS_2/*n*-GaN case. In order to understand how the single MoS_2 layer modifies the electrical properties of the PtIr/*n*-GaN junction, we performed a DFT calculation of the work function and conduction and valence band offsets of the MoS_2/GaN (0001) heterostructure as well as the bulk Pt and GaN (0001) surface, using the methods and parameters described earlier in the method section. The theoretical band-alignment between the metal, GaN, MoS_2 and MoS_2/GaN systems is presented in Fig. 23. The band offsets between bands on these systems are determined by aligning their vacuum levels to zero energy.

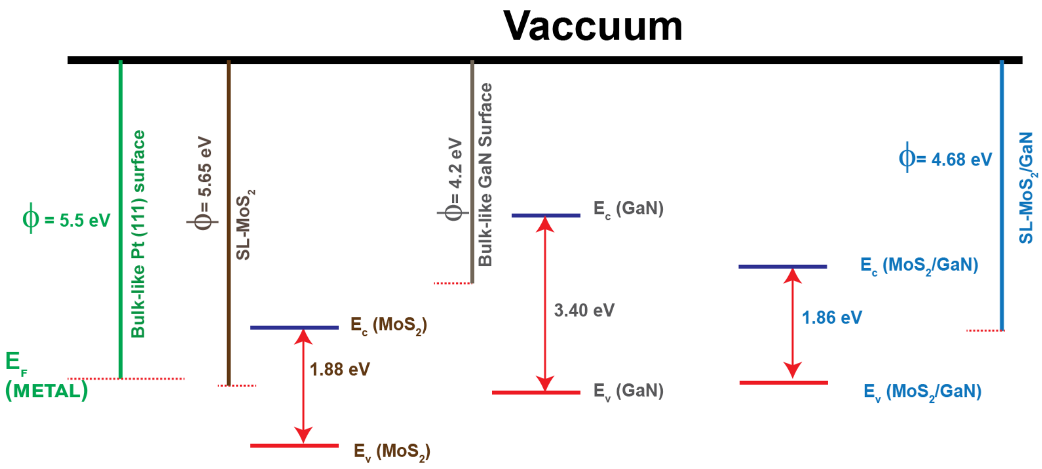

Fig. 23 DFT-calculated band alignment of Pt (111) surface, bulk GaN (0001) surface, single layer MoS_2, and MoS_2/GaN (0001) heterostructure

For the electronic transport across the metal-semiconductor (MS) heterojunction, the energy offset, known as Schottky barriers heights (SBHs), presents itself as an energy barrier that leads to rectifying behavior between the metal and the semiconductor. Since the vertical current flow across the MS interface depends exponentially on the magnitude of the SBH at the applied voltages, the SBH is clearly the crucial property of MS interface that determines its electrical characteristics.[73] In our case, the *n*-type (*p*-type) SBHs between the Pt and single layer MoS_2 is determined by determining energy difference between the Fermi level of Pt and CBE (VBE) of the MoS_2 layer, a method commonly known as Schottky–Mott approximation. Quantitatively, the *n*- and *p*-type SBHs, when Pt metal is used as the contact on the single layer MoS_2, are predicted to be 0.84 and 1.09 eV, respectively. Though the *n*-type SBH is lower than the experimentally predicted value of 1.7 ± 0.5 eV,[74] it is consistent with the previously published theoretical value (0.84 eV) using the similar approach.[75] The SBHs for the bulk-like GaN (0001) surface are 3 eV (*n*-type) and 0.4 eV (*p*-type).

The bandgap 1.86 eV of MoS_2/GaN (0001) heterostructures is found to be close to that of the single-layer MoS_2. Moreover, because of the ultra-thin dimension of the MoS_2 layer in the MoS_2/GaN (0001) heterostructure, it will be susceptible to increased electron tunneling and larger currents. The difference in the electron affinity of 0.2 eV between the MoS_2/GaN (0001) and bulk-GaN contributes to the formation of a secondary barrier, where MoS_2/GaN (0001) forms a graded junction. Hence, the reduction of the SBH and the formation of a secondary potential barrier due to the introduction of single layer MoS_2 collectively contribute to the overall increase in the current and reduce the turn-on voltages as observed in Fig. 13b. Small thickness of the interfacial MoS_2/GaN (0001) layer must be the reason of the similarity of the I-V curves with and without single layer MoS_2 especially for the case of *p*-GaN where the electrical data indicate no apparent *p*-*n* junction. Though the simple band alignment of the individual components in the heterostructure results in the qualitative agreement, the quantitative determination of SBH values requires electronic calculation of computationally demanding, lattice-matched metal/2-D heterostructures.

5.7 Summary

In conclusion, we performed XTEM of monolayer MoS_2 on GaN vertical heterojunctions that were grown by the powder vaporization technique. The extracted in-plane lattice constants of GaN and MoS_2 were similar to that of bulk unstrained values, indicating an epitaxial, nearly lattice-matched growth of MoS_2 on GaN. We have performed systematic theoretical study of GaN (0001) surfaces, single layer and bulk MoS_2, and MoS_2/GaN (0001) heterostructure, while making an attempt to correlated theoretically observed structural and electronics properties with the experimentally characterized structural and electrical data. The theoretically predicted lattice parameters for the single layer MoS_2, bulk GaN and MoS_2/GaN (0001) heterostructure are consistent with the STEM and XTEM data from the experiment. Most notably, the predicted vdW gap of 3.14 Å between the single layer MoS_2 and GaN (0001) surface in the MoS_2/GaN (0001) was within the experimental error margin range (i.e., 3.1 ± 0.5 Å between GaN and monolayer MoS_2 that we extracted from XTEM images). We used CAFM to measure vertical current across the MoS_2/*n*-GaN and MoS_2/*p*-GaN heterojunctions and observed rectification of the current in both cases as well as a switch of the polarity of the rectification for *n*- and *p*-doped GaN. There is a larger turn-on voltage shift due to the insertion of MoS_2 for the *n*-GaN case that may be explained by Schottky barrier lowering and the formation of a graded junction. Similarly, the predicted electronic properties for the MoS_2/GaN (0001) heterostructure provide insight into the shift in the V_{th} and turn-on current in the AFM measurement. Despite the fact that an unperturbed single layer MoS_2 is distinctly observed on the GaN surface by XTEM, our electrical measurements and theoretical analysis indicate that the ML does not demonstrate bulk semiconductor properties and can be viewed as a modified nanoscale interface in the vertical metal/GaN junction. This may open up new possibilities for the engineering 2-D/3-D heterojunction for the future technologies. This work stipulates that multiple 2-D layers will be required for the construction of the proposed vertical bipolar device.

6. Epitaxial Growth of Metal on a 2-D Material/3-D Substrate

6.1 Introduction and Motivation

Vertical devices based on 2-D semiconductor heterostructures are of interest since they promise high-speed and large-power performance due to short current paths and large current cross sections.[45] The integration of novel 2-D semiconductors with established conventional materials in 2-D/3-D heterostructures has the potential to take advantage of both the unique properties of atomically sharp 2-D crystals and time-tested, mainstream 3-D materials.[76] MoS_2 and GaN are suitable candidates for 2-D/3-D heterostructures. MoS_2 is one of the most studied 2-D semiconductors since it is chemically stable and has desirable electronic and optical properties including an energy bandgap of 1.3 to 2.2 eV depending on the layer count.[77–78] Suitable bandgaps and small mismatch in electron affinities of MoS_2 and GaN make it possible to envision their function in a vertical HBT. In this case, an ultrathin 2-D base would provide for short minority carrier diffusion times and thus fast performance.[79–80] GaN is an important semiconductor for high-speed and power devices, and is currently used in wireless communications, radars, guided missiles, and electronic warfare system.[81] Matching in-plane lattice constants and similar thermal expansion coefficients of MoS_2 and GaN promise low-defect epitaxial alignment between the two materials that is preserved upon the cooling of the sample from the growth to room temperature.[45,82] The epitaxial nature of the growth of MoS_2 on GaN is important for the study of the vertical transport since the registry of the lattices of the two materials will provide an ordered, intimate, and reproducible interface desired for the low-scattering vertical charge transport.

There has been interest in the scientific community in MoS_2/GaN heterostructures as a model 2-D/3-D platform with a potential for applications in electronics technology. Lee et al.[83] have demonstrated that a multilayer stack of *p*-MoS_2 grown by CVD and transferred onto an *n*-GaN substrate works as a bipolar semiconductor diode with high degree of rectification. Concurrently, epitaxial 1L-MoS_2 domains on *n*-doped GaN were grown by powder vaporization and electrical properties of such as-grown vertical 2-D/3-D heterojunctions were tested with CAFM.[45] The close lattice match of GaN and some 2-D transition metal dichalcogenides inspired using MoS_2 as a near-lattice-matched substrate for nitride growth.[24] Growing GaN on top of a 2-D structure is very relevant for the development of a vertical 3-D/2-D/3-D heterostructure system, such as an HBT, where the emitter layer of GaN would be needed to be grown on the 2-D layer. Along this direction, Tangi et al.[84] performed successful growth of GaN on top of 1L-MoS_2 when GaN was grown by MBE and 1L-MoS_2 was CVD-grown on sapphire. Soon thereafter, MoS_2/GaN Esaki tunnel diodes capable of large current density were fabricated with transferred multilayer p^+ MoS_2 on n^+ GaN grown by MBE.[85] In our recent work, the nanostructure of the heterojunction of epitaxial monolayer and bilayer MoS_2 on *n*-GaN was analyzed with TEM and good monolayer quality and close in-plane lattice match of MoS_2 and GaN were established.[84] Electrical characterization with CAFM of epitaxial 1L-MoS_2 grown directly on both *n*- and *p*-doped GaN and the comparison of the I-Vs with bare GaN response for each type of doping were made. A switch of the rectification polarity depending on the GaN substrate doping was found. The consideration as a whole of the electrical behavior of several different tip-semiconductor combinations indicated that the charge transport across the CAFM-tip/1L-MoS_2/GaN interface was dominated by the character of the tip/GaN interface implying the 2-D monolayer was electronically semi-transparent.[84] A couple of years ago, Henck et al.[86] investigated the electronic band structure of 1L-MoS_2/p-GaN heterostructure using angle resolved photoemission spectroscopy and high resolution XPS. The 0.32-eV shift of the valence band in GaN toward the Fermi level was observed after the addition of the 1L-MoS_2 to the surface, indicating the reduction of band bending in the 2-D/3-D heterostructure. We find a similar trend in our work as detailed in Section 6.3. Recently, successful CVD growth of epitaxial 1L-MoS_2 on GaN was reported by other groups and interesting electron-phonon interaction effects were seen in their PL data.[87]

The objective of this study is to explore how 2-D semiconductors can be integrated with conventional components of RF electronic devices such as III-V semiconductors and metals. To this end, a 2-D semiconductor is chosen in the form of SML thickness as the most basic case and to emphasize the novel effects that might arise due to the unique properties of 2-D materials, such as ultra-thin dimensions. We fabricate epitaxial Au/2-D/3-D and Au/3-D semiconductor heterostructures in a similar process and analyze their properties.

The first question that we explore is whether the 2-D monolayer remains a distinct unperturbed component inside the heterostructure rather than alloys with the neighbor material layers or is disrupted by the physical and chemical interactions during the fabrication process. This issue is especially critical for a device of a vertical charge transport geometry. We address this question with cross-sectional TEM imaging of Au/1L-MoS_2/GaN and Au/GaN heterojunctions and obtain quantitative nanostructural information on the heterojunctions supported with first principles DFT calculations.

Our next test investigates the effect of the 2-D ML on the electrical properties of the host Au/3-D heterojunction. The I-V characteristics are measured with nanoprobes inside an SEM and a comparison of the electrical properties of the heterojunctions is made. Interestingly, the 2-D ML appears as a distinct layer in TEM images but behaves as an electronically semitransparent component inside

Au/3-D heterojunctions. An analysis of the I-V data was employed to draw band alignment diagrams of the heterojunctions. Finally, our first principles calculations, which are validated with the agreement with the TEM data, provide further insight into the physics of these heterojunctions. The calculations of the atom-projected density of states of Au/1L-MoS_2/GaN elucidate how the energy band of the interface states is formed inside the band gaps of MoS_2 and GaN. These calculated gap states support the presence of Fermi level pinning effect deduced from the electrical data.

Furthermore, we address the notorious question on how the charge depletion regions in a bipolar 2-D/3-D junction can form when its 2-D component is thinner than a typical depletion width in a conventional bipolar junction under zero bias. To do so, we calculate the nanoscale charge density distribution in the Au/1L-MoS_2/GaN heterojunction and show that the depletion region extends beyond the 2-D layer into the vdW gaps and that the charge exchange mainly occurs across the MoS_2/Au interface while the GaN layer is effectively screened by the larger vdW gap. The results of this study improve the understanding of the interaction of 2-D crystals with the components of traditional electronic devices, which is important for developing successful vertical 2-D/3-D heterostructure devices.

6.2 Methods

6.2.1 2-D Semiconductor Growth

The domains of MoS_2 were grown on GaN substrates by a powder vaporization method, which has been described previously.[45] Briefly, MoO_3 is placed in the center of a single zone furnace along with the GaN substrate, and S powder is placed approximately 12 inches upstream of the MoO_3 crucible. The growth occurs in ultra-pure argon at 800 °C and 710 Torr for 15 min, with the S heated separately by a heat tape at 130 °C. The GaN substrates were purchased from NTT-AT[*] and consisted of a GaN film that was grown epitaxially by MOCVD on *c*-plane sapphire substrates. The GaN film is of 1.2 μm thickness and is *p*-doped with Mg dopants of 10^{19} cm^{-3} concentration. The resultant free-hole carrier density of *p*-GaN is $p \approx 10^{17}$ cm^{-3} as confirmed by NTT-AT.

---

[*] Disclaimer: Certain commercial equipment, instruments, or materials are identified in this document. Such identification does not imply recommendation or endorsement by the National Institute of Standards and Technology, nor does it imply that the products identified are necessarily the best available for the purpose.

6.2.2 Gold Nanocontacts

Au nanocontacts on MoS_2/GaN samples were fabricated by electron beam lithography and PVD. The arrays of circular nanodots of 600- and 400-nm diameter were patterned in poly(methyl methacrylate) (PMMA) resist using a 100-kV beam with a dosage of approximately 850 to 1,000 μC/cm^2 using a Vistec EBPG5000+ES electron beam lithography (EBL) system. The dosed sample was then developed using a 1:2.5 ratio of methyl isobutyl ketone (MIBK) to isopropyl alcohol (IPA) followed by an IPA rinse. No descum or any other plasma clean was used to prevent ion damage to the 2-D MLs. The deposition of a 60-nm Au layer was achieved in an e-beam evaporator (CHA Industries) at room temperature with a chamber pressure of 1 μTorr and a deposition rate of 2 Å/s. Lift-off was performed in an acetone bath for 4 h at room temperature.

6.2.3 TEM Sample Preparation

This was done using a FEI Helios NanoLab 660 dual-beam focused ion beam (FIB) and SEM system equipped with focused electron and ion beam induced deposition (EBID and IBID) capabilities. The focused EBID (or IBID) allows deposition of Pt or carbon (C) in the areas patterned by the SEM electron beam (or FIB) with the help of a precursor gas injection system. A region of interest was in situ capped with C and Pt protection layers using EBID and IBID. A lamella slice containing an Au/MoS_2/GaN interface was ion milled with the FIB and extracted using an Oxford Omniprobe 300 manipulator and Pt welds by EBID. The lamella was EBID-welded to a TEM copper grid and consequently thinned by FIB to electron transparency.

6.2.4 Scanning Transmission Electron Microscopy

This was carried out using a spherical-aberration corrected FEI Titan 80-300 operating with a primary beam energy of 300 keV. HAADF images were collected using a detector inner collection angle of 70 mrad. The convergence angle of 13 mrads was achieved with a 40-μm probe forming aperture. Additionally, XEDS was carried out using a probe current of 0.3 nA and a side-entry Si drift detector. Structural characterization was performed using electron nanobeam diffraction using a primary beam energy of 300 keV in a spherical aberration-corrected STEM. The convergence angle of approximately 3 mrad was achieved with an aperture size of 10 μm. The probe was positioned on the area of interest using the scan coils of the STEM and the resulting convergent-beam electron diffraction (CBED) pattern was collected using a charge-coupled device (CCD) camera. The scales in the TEM line profile graphs were calibrated to the c lattice constant of GaN assuming its bulk value $c = 5.185$ Å based on our independent measurements and the literature.[88]

6.2.5 Electrical Measurements

These were performed inside a field emission SEM from Zeiss where the Au nanocontacts were accessed with Kleindiek Nanotechnik piezo-actuated nanomanipulators. Circular Au nanocontacts and MoS_2 monolayer domains were appraised with SEM. The selected nanocontacts were contacted with W nanoprobe of tip radius 150 nm and I-V characteristics were measured with a Keithley 238 programmable source-measure unit. Generally, no noticeable damage was observed on the Au nanocontacts after tungsten (W) nanoprobe contact. The bottom contact to the MoS_2/*p*-GaN heterojunctions was enabled with large Ti/Au top contacts to *p*-GaN as warranted previously.[44,84]

6.2.6 Kelvin Probe Measurement

This was performed at room temperature in air on a Kelvin probe system by KP Technology Ltd. The stainless steel tip radius is approximately 2 mm. The measurement was performed in an enclosed dark chamber with no background illumination. A Au contact on the sample served as a calibration material.

6.3 Results and Discussion

MoS_2 domains were grown on *p*-GaN substrates (*c*-plane GaN, thickness $th = 1.2$ μm, free-hole density $p \approx 10^{17}$ cm^{-3}; host substrate, *c*-plane sapphire, $th = 0.5$ mm) by powder vaporization as described in Section 6.2 and elsewhere.[45] Our XPS studies indicate that the as-grown MoS_2 is an *n*-type semiconductor.[89] Thus the synthesized MoS_2/*p*-GaN heterojunctions represent a case of a 2-D/3-D *np*-structure. The as-grown MoS_2 domains on *p*-GaN substrates underwent thorough structural characterization with SEM, AFM, XPS, PL, and Raman spectroscopy as described elsewhere[45,84] and were proven to be of good quality MoS_2. The MoS_2 domains covered approximately 40% of the GaN surface. The MoS_2 consisted of single, isolated triangles, predominantly of ML thickness (1L-MoS_2), as well as merged areas, second layer, and higher-order stacks. An SEM image of 1L-MoS_2 domains is shown in Fig. 24a. Isolated MoS_2 domains were in the shape of equilateral triangles with its side typically of 1 to 3 μm in length. The triangle sides are found to be parallel to the *m*-plane of the GaN substrate lattice in approximately 99% of the time. The growth of MoS_2 aligned with respect to the underlying GaN lattice is evidence of epitaxy.

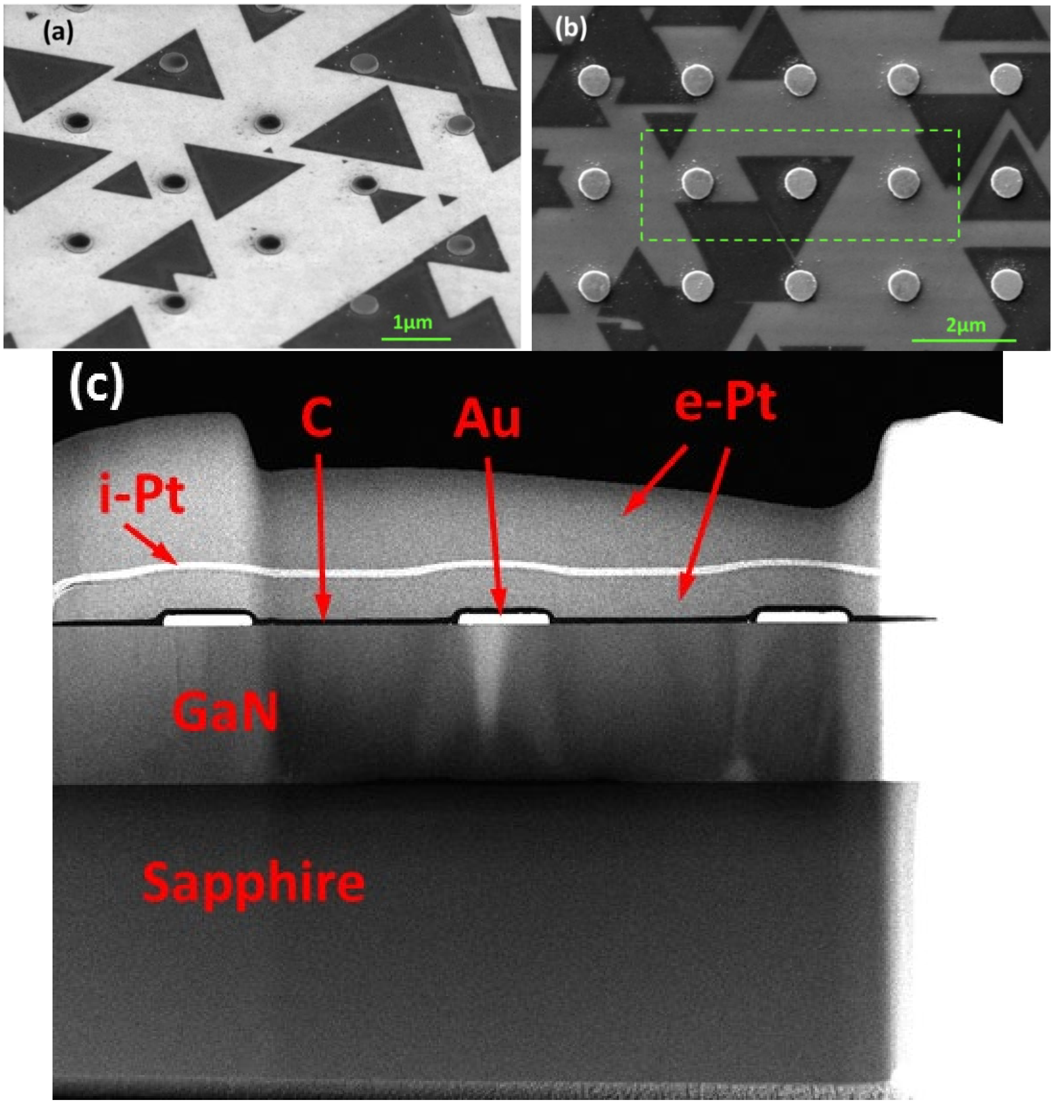

Fig. 24 Top and side views of the Au/2-D/3-D and Au/3-D junctions. a) and b) SEM images of triangular 1L-MoS$_2$ domains on a GaN substrate with circular Au nanocontacts. The green rectangle shows the area that was selected for TEM characterization

To form metal/2-D/3-D and metal/3-D junctions, arrays of Au nanodots (600- and 400-nm diameter, 60-nm thickness, 2-µm period) were fabricated on the MoS$_2$/GaN/Sapp structures (Fig. 24). Au nanodots were only evaluated if they were either entirely on a MoS$_2$ triangle or entirely on bare GaN substrate to represent Au/1L- MoS$_2$/GaN or Au/GaN junctions, respectively. The fine specks around the Au nanodots that are visible in SEM (Fig. 24b) were determined by TEM to be Au nanoparticles scattered on top of the MoS$_2$, GaN, and nanodots from the final dot fabrication step and did not affect the conclusions of this study.

Cross-sectional characterization of the 2-D/3-D heterostructures was performed with scanning TEM. The sample area selected for TEM is shown with the green rectangle on the SEM image in Fig. 24b and consists of three Au nanocontacts on a MoS_2 domain and bare *p*-GaN. The TEM image of the prepared cross section is shown in Fig. 24c. The central Au nanocontact in Fig. 22c lies on a MoS_2 domain, while the two side nanocontacts lie on bare *p*-GaN substrate as seen in Fig. 24b.

The TEM of the interface under the central Au dot (see Fig. 24b and c) that lies on a MoS_2 domain is shown in Fig. 25a. The TEM image shows the atomic planes in Au nanocontact 1L-MoS_2, and GaN substrate parallel to the interface. The TEM of the interface near the edge of the Au nanodot illustrates that GaN/MoS_2 structure remains unperturbed when the Au nanodot is added (Fig. 25b). For comparison, the Au/semiconductor interface of the Au nanodot on bare GaN is shown in Fig. 25c. The TEM analysis proves the monolayer nature of the MoS_2 domain extending throughout the whole undersurface of the central Au nanodot.

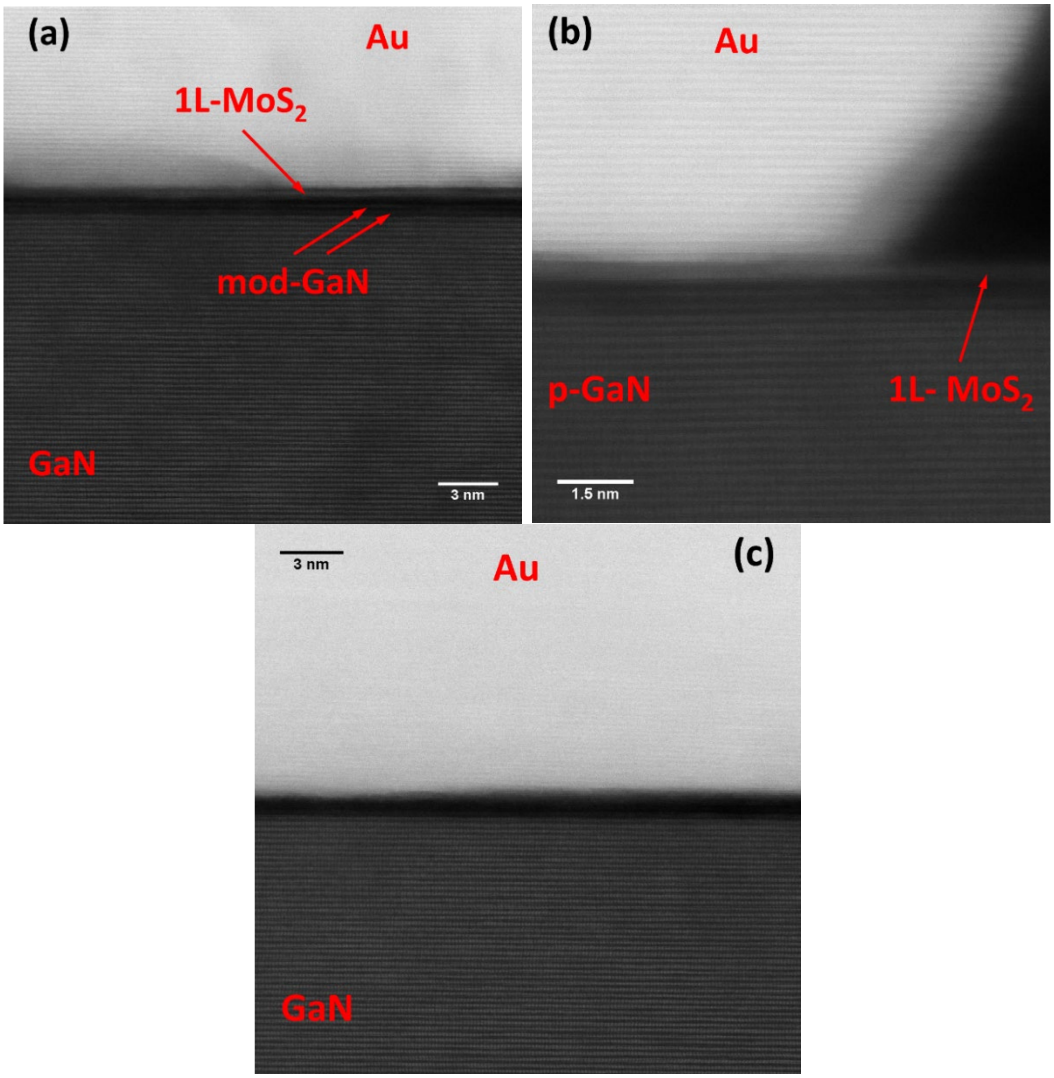

Fig. 25 Cross-sectional TEM images of a) and b) the Au/1L-MoS_2/*p*-GaN heterojunction and c) the Au/*p*-GaN junction

We used high-magnification TEM images (e.g., Fig. 26a) to extract the lattice constants of the materials in the vertical structure. The in-plane lattice constants of GaN and 1L-MoS_2 were calculated from the TEM images using FFT of the averaged line intensities and were found to be $a = 3.175$ and 3.188 Å, respectively, which constitutes only a 0.4% lattice mismatch. The value of the measured in-plane atomic period 3.175/2 Å is within 0.4% of the literature value of the lattice constant of GaN ($a = 3.189$ Å) (Sze 1981) and confirms the orientation of the cross-sectional plane in the GaN substrate which is m-plane $(1\bar{1}00)$, as intended. The central Au nanodot in Fig. 22b, which lies on 1L-MoS_2, is found to have distinct uninterrupted atomic planes throughout the Au dot. The only small grains observed inside the nanodot are found near the edges away from the substrate. The vertical period of the atomic planes in the central Au dot is measured to be 2.26 Å, which corresponds to the Au lattice $a_{Au} = 3.91$ Å oriented with $[111]$ direction along the c-axis $[0001]$ of GaN. The measured Au lattice parameter $a_{Au} = 3.91$ Å is within 4 % of the literature value of 4.065 Å for bulk Au. The in-plane atomic period of the Au nanodot was calculated with FFT from the TEM images to be 2.91 Å. This value corresponds to the viewing direction in the TEM images (GaN $[10\bar{1}0]$) to be along the Au $[\bar{1}\bar{1}2]$ direction. These data indicate epitaxial alignment of the central Au nanodot to GaN. The epitaxy was confirmed with the CBED measurements in TEM. The CBED images of the central Au nanodot on GaN/1L-MoS_2 showed alignment of the Au lattice to the GaN substrate, while the single crystal nanodot on bare GaN produced a misaligned diffraction pattern (Fig. 27). The peak simulation and assignment for the GaN substrate and epitaxial Au nanodot were performed (Fig. 27) using SingleCrystal from CrystalMaker Software Ltd, which determined the following epitaxial alignment: Au $[111]$ aligns with GaN $[0001]$; Au $[2\bar{2}0]$ aligns with GaN $[1\bar{2}10]$ with a -8 % lattice mismatch. Interestingly, the left (in Fig. 24b and c) non-epitaxial Au nanodot on bare GaN is found to be of multigrain nature with different grain orientations whereas the right nanodot on bare GaN is predominantly a single crystal but of misaligned orientation as shown in Fig 27c.

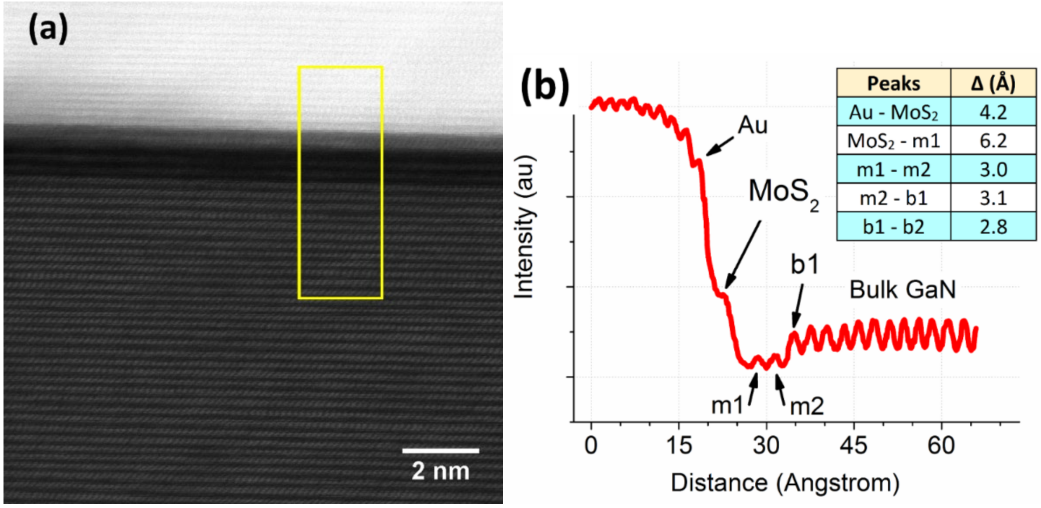

Peaks	Δ (Å)
Au - MoS$_2$	4.2
MoS$_2$ - m1	6.2
m1 - m2	3.0
m2 - b1	3.1
b1 - b2	2.8

Fig. 26 Cross-sectional TEM image analysis of the Au/1L-MoS$_2$/p-GaN interface. a) A micrograph of the interface that includes the MoS$_2$ layer and two modified GaN layers. The yellow rectangle specifies the area used for the line profile in b). b) An averaged line profile of the TEM image intensity perpendicular to the interface and averaged along the interface within the yellow rectangle.

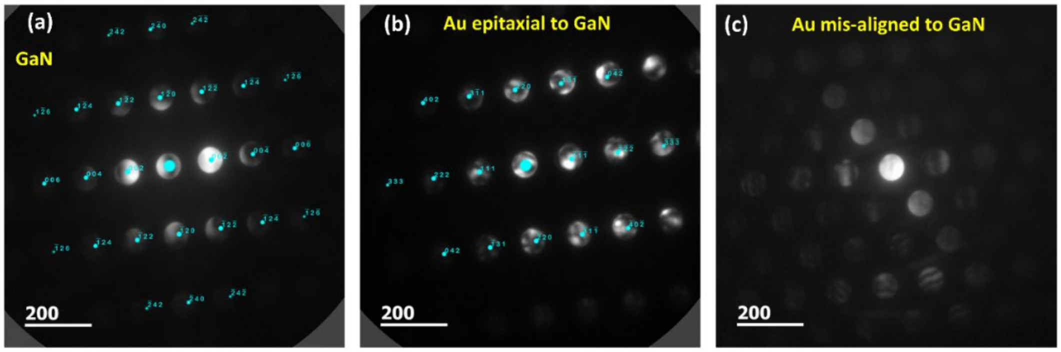

Fig. 27 Electron diffraction images of a) GaN substrate under the Au nanocontact on MoS$_2$, b) Au nanocontact on GaN/MoS$_2$, c) Au nanocontact directly on GaN with no MoS$_2$. Epitaxial alignment is evident for a) and b), but not c).

All three materials in Fig. 25a, Au 1L-MoS$_2$, and GaN, have atomically sharp interfaces that do not intermix. The ability to fabricate metal contacts to a single 2-D semiconductor ML without disrupting its structural integrity is important for the development of functional electronic devices based on 2-D crystals, especially for the case of devices with vertical charge transport. Yet, to our knowledge, there has been little direct evidence (such as high-resolution TEM) before this work that such metal/2-D interfaces were possible. Generally, various semiconductor processing steps, such as plasma treatments, high impinging energies of PVD-deposited metal atoms, diffusion, and chemical reactions are expected to pose risks to the integrity of the 2-D ML. As an example, last year Kim et al.[90] provided rare cross-sectional TEM images of metal/1L-MoS$_2$ contacts and found that Pd and Ti contacts to 1L-MoS$_2$ on a SiO$_2$ layer resulted in a distortion of the 1L-MoS$_2$. A disrupted metal/2-D interface can be tolerated in lateral devices or stacks of several 2-D layers, but is unacceptable for vertical devices comprising a single ML when direct shorts of the surrounding materials through the ML would negate the function of the 2-D material.

To avoid physical ion damage to the 2-D layer, we eliminated the plasma clean steps in our nanodot fabrication process and chose a low impinging energy PVD process such as evaporation (vis-à-vis sputtering). To mitigate chemical interaction and inter-diffusion of the metal into the 2-D layer, we chose Au as the contact material. Au is believed to create a less intimate contact to 2-D MoS$_2$ than high adhesion materials (such as Ti and chromium [Cr]), which are likely to disturb a single ML. In the computational study of Kang et al.,[91] vdW gaps between several metal contacts and MoS$_2$ were investigated. The authors predicted Au contacts to have larger physical separation and lower level of hybridization with the 2-D material as compared to some other common contact metals, such as Ti, Mo, and palladium (Pd). Au has been used by the 2-D scientific community to deposit contacts to MoS$_2$, but there are scarce data published on the nanostructure of the Au/MoS$_2$ interface. In the study of Gong et al.,[92] ultrathin (2 nm) Au films were deposited by PVD onto MoS$_2$ and were reported to be of a discontinuous and granular nature, unlike what we see in our case. We speculate that the epitaxial growth of Au, dictated by the alignment of the MoS$_2$ and the whole heterojunction to the GaN lattice, is essential for the continuity of the Au film and order at the Au/MoS$_2$ interface seen in our system.

The top two atomic layers of the GaN, which represent the height of one unit cell of the GaN lattice, appear to be modified in the areas beneath the MoS$_2$ ML. As was previously reported for *n*-doped GaN,[84] the modification in *p*-GaN is purely restricted to areas where MoS$_2$ is present and is not observed on the bare GaN. These two modified layers at the interface are labeled “mod-GaN” in Fig. 25a. In a separate TEM/EDS study, the modified atomic layers are determined to be a GaN crystal diluted with S and Mo. Details concerning these findings will be published in a future article by R Burke et al.[93] The modified layer is ultra-thin, and we do not expect S and Mo to be efficient dopants in GaN.[94] Therefore, the superficial layer in GaN is not expected to significantly affect the electrical properties of the GaN side of the heterojunction.

We performed quantitative TEM characterization of the Au/2-D/3-D interface in order to evaluate the vdW gap and other parameters of the heterojunction. Averaged TEM intensity line scans were extracted from the images, as shown in Fig. 26, where a yellow rectangle on the TEM image denotes the area examined. The line intensity profile was plotted perpendicular to the interface (i.e., along the long edge of the rectangle). The intensity at each point of the plotted line scan is an average along the line parallel to the interface within the rectangle. The first Au layer, MoS_2 ML, modified GaN layers (m1, m2), and first bulk GaN layer (b1) are denoted in the line profile of Fig. 26b. Atomic plane spacings Δ were determined from the line profile and summarized in the inset table. The atomic spacings Δ were measured this way in over 20 locations at the interface of the epitaxial nanodot. For the distance between the MoS_2 and the first atomic Au layer above MoS_2 ($a1$), we get the value averaged over multiple locations $\Delta(a1 - MoS_2) = 4.5 \pm 0.4$ Å, where the uncertainty is the standard deviation for different measurements and represents the variation of the actual spacing and error of the measurement. The distance Δ is measured from the peak of the TEM intensity (i.e., between the centers of Mo and Au atom rows). Similarly, the MoS_2-GaN spacing is $\Delta(MoS_2 - m1) = 6.1 \pm 0.3$ Å. Assuming $\Delta(Mo - S) = 1.5$ Å as the Mo-S bond distance and keeping in mind that our GaN is Ga-terminated, the MoS_2-GaN vdW gap can be estimated as $\delta(S - Ga) = \Delta(MoS_2 - m1) - \Delta(Mo - S) = 4.6 \pm 0.3$ Å. This δ value is larger than the one measured previously for the GaN/MoS_2 system without the Au capping layer, 3.1 Å.[84]

We speculate that the presence of the top Au layer above MoS_2 could be reducing the adhesion strength of the MoS_2 and GaN. A precise measurement of δ in the absence of the Au capping layer for the sample studied in this work could not be done because of the ion damage to the MoS_2 during the FIB sample preparation (see the surface area outside the nanodot in Fig. 27). The Au nanodot served, in part, as a protective mask during the TEM sample preparation. Next, the distance between the atomic layers in the modified GaN layers is measured to be $\Delta(m1 - m2) = 3.1 \pm 0.2$ Å, which is larger than the spacing between bulk GaN layers that varies within $\Delta(b2 - b3) = 2.6 \pm 0.2$ Å.

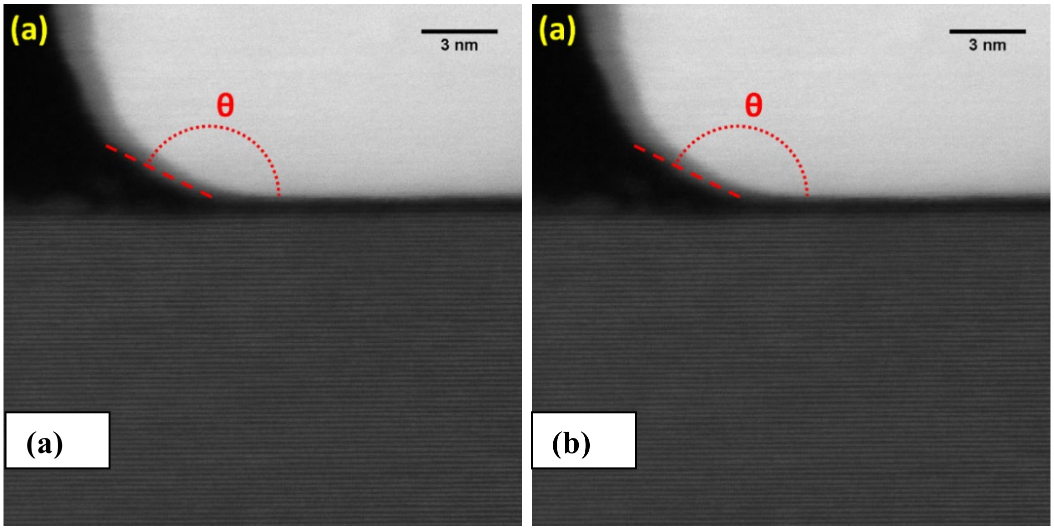

Fig. 27 TEM images of the edges of an Au nanodot at the Au/GaN interface a) without MoS_2 and b) with a MoS_2 ML. The Au wets the sample surface at a smaller contact angle ϑ when a MoS_2 ML is present.

It was noted in the TEM images that the wetting of the Au nanodot of the substrate changes depending on whether the dot is on MoS_2 or bare GaN, per Fig. 27. The contact angle of the Au nanodot on bare GaN was measured to be $\vartheta = 152°$ and the contact angles on the left and right sides of the central nanodot on MoS_2/GaN are $\vartheta = 112°$ and $130°$. Thus we observe an improved adhesion of Au to the GaN substrate when it is covered with 1L-MoS_2. Figure 27a shows a SEM image of a Au/(1L-MoS_2)/ *p*-GaN heterojunction contacted with a W nanoprobe. Au nanodots that lay entirely inside a single isolated 1L-MoS_2 triangle were selected for the *I-V* measurements, and over a dozen of such Au/(1L-MoS_2)/*p*-GaN heterojunctions were measured and analyzed.

The I-V characteristics of several representative Au/(1L-MoS_2)/ *p*-GaN vertical heterojunctions are displayed in Fig. 28b. The I-V measurements show rectification behavior. We attribute the electrical characteristics of the heterojunctions to be primarily determined by the nanodot/GaN junction which is perturbed by the insertion of a 1L-MoS_2. This physical picture was proposed in our earlier study after the analysis of the metal/1L-MoS_2/GaN electrical characteristics measured by CAFM on both *p*- and *n*-doped GaN and bare metal/GaN junctions.[84] This is in contrast to the picture for a thick MoS_2 layer where the MoS_2 acts as an independent semiconductor in the heterojunction forming two separate junctions on the Au and GaN interfaces.

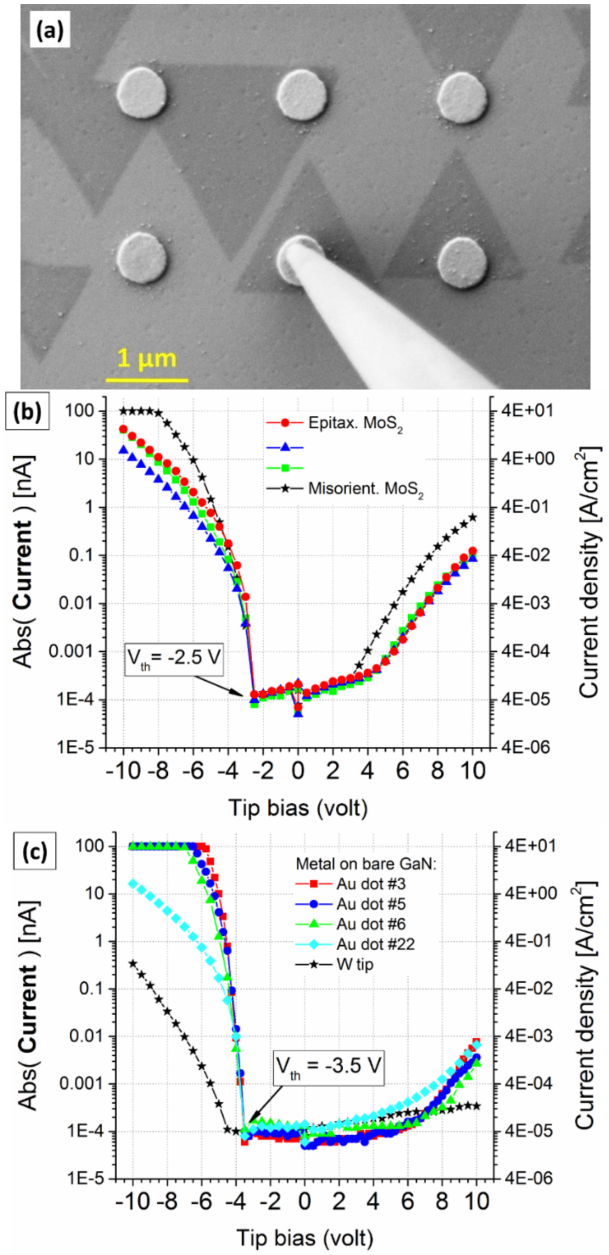

Fig. 28 a) SEM of an isolated ML MoS_2 triangle under an Au nanodot that was contacted and electrically tested with a W nanoprobe tip. b) Electrical data on Au/MoS_2/GaN. c) Electrical data on Au/GaN.

The electrical data involving permanent Au contacts on MoS_2/*p*-GaN are considerably more reproducible and less noisy than our earlier CAFM data;[45,84] therefore, the fine details of the I-V characteristics can be extracted and analyzed. The rectification polarity in Fig. 28b and c is consistent with a *p*-type Schottky barrier (SB). The forward bias on the Au/*p*-GaN SB corresponds to the negative bias on the W nanoprobe (i.e., the Au nanodot). A striking feature in the I-V curves is that all Au/(1L-MoS_2)/*p*-GaN heterojunctions show the same distinct turn on (threshold) voltage at $V_{th} = -2.5\ V$ applied to the Au contact and the same slope near V_{th}. No deviations from the $V_{th} = -2.5\ V$ turn on voltages on the forward Schottky bias were observed for over a dozen nanodots tested, including nanodots on isolated MoS_2 triangles and on merged triangle clusters that are believed to be of ML thickness as well. For comparison, the I-V curves for the nanodots on bare GaN are plotted in Fig. 28c. A similar distinct value of the turn on voltage is measured for Au/p-GaN junctions with $V_{th} = -3.5\ V$. Again, approximately 10 dots (measurements) were tested and all of them displayed the –3.5 V turn-on voltage (V_{th}).

The high reproducibility of the V_{th} value and the I-V slope near V_{th} indicate that those parameters are determined mainly by the materials involved (Au/MoS_2/ p-GaN or Au/p-GaN) and are not affected by the 2-D domain sizes, quality of the probe/dot contacts, or various uncertainties of the measurements. The slope of the I-V curve near V_{th} was used to evaluate the effective SBs (Φ_B) assuming a thermionic emission model,[95–96]

$$I = A_{dot} A^* T^2 e^{-\frac{q\Phi_B}{kT}} e^{\frac{qV}{nkT}}, \qquad (2)$$

where $A_{dot} = 0.3\ \mu m^2$ is the area of the Schottky contact ($\emptyset 600\ nm$), $A^* = 120 \cdot (m^*/m_e)\ A/cm^2K^2 = 260\ A/cm^2K^2$ is the Richardson constant[95] of GaN based on an effective hole mass of $m_h^* = 2.2 m_e$,[97–98] T is the absolute temperature, n is the ideality factor, $q = 1.6 \times 10^{-19}\ C$, and k is the Boltzmann constant. Examples of the exponential curve fitting near the forward bias threshold are shown in Fig. 28. The extracted fitting parameters are $\Phi_B = 1.3\ eV$ and $n = 4.5$ for Au/MoS_2/p-GaN and $\Phi_B = 1.5\ eV$ and $n = 4.5$ for Au/p-GaN. Therefore the analysis of the I-V characteristics within the model of thermionic emission over an Au/GaN SB yields that the insertion of a 1L-MoS_2 on the Au-GaN interface effectively reduces the SB by 0.2 eV.

The large value of the extracted ideality factor n indicates that there might be other physical mechanisms present behind the electron transport in addition to, or instead of, the thermionic emission. There are scarce electrical data in the literature for the metal/(1L-MoS_2)/GaN system. For thick (~10 nm) MoS_2 flakes contacted by metals, a significant contribution from tunneling across the metal/MoS_2 Schottky and tunnel barriers in addition to the thermionic emission has been demonstrated.[99] Even though the system with 1L-MoS_2 is different, a similar tunneling mechanism could be present in our case as well. Since the electrical behavior of the Au/(1L-MoS_2)/GaN heterojunctions is governed by the Au/GaN contact, we can compare our results with the literature data on Au/GaN and other metal/(3-D semiconductor) junctions. A model based on Eq. 1 was successfully used to characterize Pt/n-GaN macroscopic Schottky diodes and a large number of nanoscale Schottky contacts created with a CAFM tip.[96] Further insight can be gained from a thorough study by Card and Rhoderick,[100] where metal/semiconductor contacts were explored and insulating SiO_2 films of various thicknesses were introduced at the interface. It was found that with the presence of an oxide layer, the general formula of Eq. 2 still held for the forward bias with increased parameters n and Φ_B. The increase in the oxide thickness resulted in a continuous increase in the ideality factor n and the oxide barrier height. The latter effectively increased the coefficient Φ_B in Eq. 2 with respect to the true metal/semiconductor SB.

Additionally, the deviation of the I-V curves from the exponential was progressively more pronounced in the same manner as in the I-V curves in the Fig. 28b and c (i.e., the decrease of the slope at a larger forward bias on a semilog I-V plot). It is reasonable to conclude that the large values of the ideality factors extracted from our I-V plots and the deviation from the exponential behavior are the result of the presence of an insulating layer at the Au/GaN and 1L-MoS_2/GaN interfaces. For the case of p-doped semiconductors, the presence of an interfacial oxide layer between a metal contact and p-GaN was suggested as well using capacitance-voltage (C-V) characteristics analysis.[101]

To summarize, the absolute values of the effective SBs ($\Phi_B = 1.3\ 1.5\ eV$) extracted using Eq. 1 may be overestimates if a significant insulating layer is present at the interface with GaN. A more secure result of the analysis of the measured I-V data displayed in Fig. 27 is the 0.2 eV relative decrease of Φ_B upon the insertion of a 1L-MoS_2 on the Au/p-GaN interface. To illustrate these results, we plot a band diagram of the Au/p-GaN and Au/MoS_2/p-GaN heterojunctions in Fig. 28 based on the SB values available to us from the above I-V analysis.

The band diagram in Fig. 29 assumes literature values for the basic parameters of bulk Au and GaN and matches them with the measured SBs on the interface. The work function (WF) of the Au is assumed to be *5.1 eV*,[94] and the bandgap of GaN is $E_g = 3.4\ eV$.[102] The reported values for electron affinity of GaN vary between $\chi = 2.6$ *to* $4.1\ eV$[102–107] with the lower values of affinities generally measured for surfaces prepared in ultra-clean conditions. An $\chi = 3.8\ eV$[104] is assumed in Fig. 28. The free-hole carrier density of p-GaN used in this study is $p \approx 10^{17}$ cm^{-3}. The position of the Fermi level (E_F) with respect to the top of the valence band (E_V) in bulk p-GaN can be estimated with the formula[88] $E_F - E_V = kT \cdot ln\, N_V/p = 0.17\ eV$, where $N_V = 8 \times 10^{19}\ cm^{-3}$ is the effective density of states in the valence band of GaN calculated with an effective hole mass of $m_h^* = 2.2 m_e$.[97–98] Within the Schottky–Mott approximation,[95] the SB height for Au/p-GaN is expected to be $E_g + \chi - WF_{Au} = 2.1\ eV$, which exceeds the measured value $\Phi_B \approx 1.5\ eV$. We propose that there is Fermi level pinning at the

Au/GaN interface that is reflected in Fig. 28 as a discontinuity in the vacuum level at the interface due to the presence of trapped charges on it. The insertion of a MoS_2 ML modifies the pinning and reduces the SB by 0.2 eV.

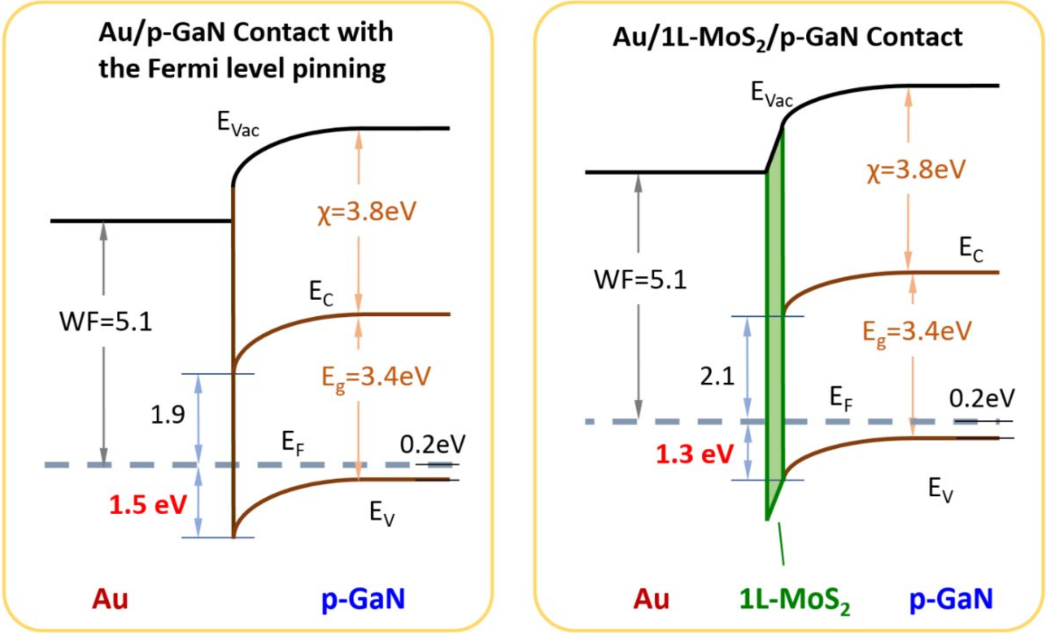

Fig. 29 Band alignment of Au and *p*-GaN at the contact and with an interfacial single monolayer MoS_2. The monolayer 2-D represents a modified Au/GaN interface, and the 1L-MoS_2 internal band structure is not plotted.

The SB heights extracted from our electrical measurements ($\Phi_B = 1.3\ 1.5\ eV$) are substantially lower than the Schottky–Mott approximation value (2.1 eV). This is in contrast to the Ni/p-GaN system reported in the literature, where a large $\Phi_B \approx 2.8\, eV$ extracted from the electrical testing appears to be close and even above their Schottky–Mott values.[101] To validate our SB numbers, we made independent measurements of the band bending (BB*)* at the surface of our GaN substrates. We performed Kelvin probe (KP) measurements with a macroscopic tip (Ø 2 mm) of the WF of a bare p-GaN wafer under atmospheric conditions relative to an Au contact. The measured WF at the surface of p-GaN is $6.20 \pm 0.05\, eV$, which is relative to the Au standard of 5.1 eV. The BB on the bare p-GaN surface can be calculated as the difference of the surface WF from the bulk value ($E_g + \chi - 0.17\, eV \approx 7.0\, eV$): $BB = 7.0 - 6.2\, eV = 0.8\, eV$. The Kelvin probe result for the BB in our p-GaN agrees with the literature values for the surface BB of bare p-GaN of 0.8 eV when measured with photoelectron spectroscopies.[102,107] On the other hand, for the Au/GaN contact the electrically measured SB height yields BB of 1.3 eV (as shown in Fig. 29). The larger BB of 1.3 eV extracted from our I-V analysis is likely due to the presence of the Au capping layer. The insertion of 1L-MoS_2 in between GaN and Au effectively increases the separation between the metal and 3-D semiconductor and relaxes the BB in GaN toward its bare surface value. The reduced BB measured with KP is in accord with our I-V analysis results (i.e., the reduced SB heights) and can be explained with the presence of trap states on the interface resulting in the Fermi level pinning as illustrated in Fig. 29.

It is instructive to compare our electrical results with a recent study by Henck et al.[86] involving characterization of the 1L-MoS_2/*p*-GaN band structure via ARPES/XPS. The BB in GaN was found to decrease from 1.9 to 1.6 eV after the transfer of a 1L-MoS_2 on *p*-GaN. Thus, the researchers found a 0.3 eV decrease of the BB in GaN as compared to a 0.2-eV decrease for our case of epitaxial Au/MoS_2/GaN. However, their absolute values of the GaN BB (1.9 to 1.6 eV) deviate from our numbers (1.3 to 1.1 eV) and from the results for bare *p*-GaN (BB=0.8 eV) reported earlier. The electron affinity of GaN 4.4 eV in the study of Henck et al.[86] is rather large when compared to the values in other reports in the literature of 2.6 to 4.1 eV.[102–107] These discrepancies, as well as the spread in the literature of the electron affinities and BB, indicate that there is large variation (of several tenths of an electron volt) of the energy band parameters that depend on the materials state and measurement methods used. The presence of the Au layer in our case, and the different choice of the 2-D monolayer (epitaxial vs. transferred MoS_2) might also explain the differences with the ARPES results. Regardless, the tendencies and relative changes, as compared to absolute values, in the band values sustain better for different measurement techniques.

The I-V curves at a forward bias above the threshold voltage exhibit some deviation from one measurement (nanodot/domain system) to another (see Fig. 27). We observed a tendency that larger MoS_2 domain triangles, and especially clusters of connected triangles, show larger currents at high biases than smaller domains. This is likely to be the manifestation of the current spreading inside a MoS_2 domain. When the current spreads away from the junction boundary, which is defined by the nanodot, and flows in the in-plane direction inside the MoS_2 domain, an effective increase in the MoS_2/GaN contact area is made accessible by the MoS_2 domain size. The current spreading in the MoS_2/GaN system was shown to exist in our previous study, where we demonstrated via CAFM imaging that larger triangles resulted in more current at the same bias than smaller triangles. Furthermore, it was shown that within one triangle, the current diminished in the corners.[45] This study suggests that the current spreading manifests itself mainly at larger biases and is negligible near the threshold voltages.

While approximately 99% of the MoS_2 domain triangles are oriented with the GaN lattice, there are occasional ML triangles that are misoriented with respect to the substrate lattice. These misoriented triangular domains often exceed by a factor of 2 to 4 the average size of oriented (epitaxial) MoS_2 triangles. The larger size implies that they grow faster than the epitaxial MoS_2 or nucleate earlier. An example of a MoS_2 triangle that is rotated by 24° with respect to the rest of the epitaxial MoS_2 domains is observed in SEM measurement and the I-V plot for this triangle is given in Fig. 27b, and shows the same threshold voltage $V_{th} = -2.5\ V$ as for the epitaxial MoS_2, but with higher current levels above V_{th}. The latter could be due to the larger size of misoriented MoS_2 and the current spreading effect described previously. Currently, the dearth of misoriented MoS_2 domains precludes a detailed study of such systems.

Another result that comes from the analysis of the I-V curves is that the current at larger biases gradually decreases from measurement-to-measurement on different nanodots. This trend is illustrated in Fig. 28c, where the I-Vs of several Au nanodots on bare GaN are presented. The nanodot numbers in the legend correspond to the sequence of the measurements. During the first few measurements of Au dots 3, 5, and 6 the current magnitude gradually decreases from measurement-to-measurement. At dot 22, the current is substantially smaller above V_{th} (Fig. 27c). This effect is negligible near the threshold voltage $V_{th} = -3.5\ V$, indicating again that the value of V_{th} and the I-V slope near V_{th} are the intrinsic parameters of the metal–semiconductor junction. Since different independent Au/GaN junctions (Au dots 3, 5, 6, and 22) are measured, the trend must be due to the nanoprobe itself. The degradation (possibly oxidation induced by the current heating) of the W nanoprobe is believed to be the root cause behind this time-dependent observation of the larger contact resistance of the W tip/Au nanodot junction. Additionally, we contacted the GaN substrate with a W nanoprobe (tip) directly, and obtained the I-V of the W/GaN junction (Fig. 28c). Clear rectification was observed for the W/GaN junction corresponding to the p-type SB. The threshold voltage shifted to –4.5 V, and the current level and the slope near V_{th} were substantially reduced. Bare W nanoprobe measurements on MoS_2 triangles were not performed because of possible damage to the MLs.

6.4 Theoretical Verification

6.4.1 Method

The calculations were performed using a first-principles method with the projector augmented wave (PAW) basis set,[66] as implemented in the VASP[67] code. The GGA parameterized by PBE[68] exchange-correlation (XC) functional was employed to calculate the structural and electronic properties of 2-D/3-D, metal/2-D, metal/3-D and metal/2-D/3-D heterojunctions. Prior to forming heterostructures, bulk lattice properties of the constituent systems (Au, GaN, and MoS_2) were calculated using the kinetic energy cut-off of 500 eV for electronic wave functions. A Γ-centered

Monkhorst–Pack BZ integration scheme was adopted to integrate over the BZ.[69] To include vdW type interaction in the Kohn–Sham energies during structure and energy minimizations, the semi-empirical DFT-D2 dispersion correction of Grimme was used.[70] The forces were calculated using the Hellmann–Feynman procedure and geometries were optimized using a conjugated gradient (CG) scheme with a convergence criterion of 0.001 eV Å^{-1} for the atomic forces. The optimized bulk MoS_2 lattice constants are $a = b = 3.19$ Å and $c = 12.33$ Å, and bulk GaN lattice constants are $a = b = 3.22$ Å and $c = 5.25$ Å, consistent with Petkov et al.[65] and O'Regan et al.[108]. The slab model for Au (111) surface was constructed using six MLs of Au atoms with optimized in-plane bulk lattice parameters of 2.88 Å. This is similar to the model used in our previous study[109] to construct 1L-MoS_2/GaN heterostructures.

Unlike in the 1L-MoS_2/GaN heterostructure where the lattice mismatch is less than 1%, the lattice mismatch between Au (111)/1L-MoS_2 and Au (111)/GaN heterostructures is relatively large (<8%). To compensate for the strain between 1L-MoS_2 or GaN and Au (111), we have strained the Au layer to match the underlying 1L-MoS_2 or GaN layers. The commensurate 2-D/metal, 3-D/metal, and 2-D/3-D/metal heterostructures are created using CellMatch tool.[110] To maintain a tradeoff among the supercell size, accuracy, and computational cost, the smallest supercells with strained Au-layer (approximately +4%) were selected for this study. The resultant supercells possessed in-plane commensurate lattice vectors of (2.72 × 2.55), (2.31 × 2.25), and (2.32 × 2.25) nm for Au/1L-MoS_2, Au/GaN, and Au/1L-MoS_2/GaN heterostructures, respectively. Periodic boundary conditions were applied in the lateral directions, and the atomic positions in the interface were allowed to relax. To avoid surface to surface interactions, a vacuum region of at least 20 Å was added in the out-of-plane direction. In addition, to mitigate the charge fluctuation due to surface dipoles and avoid spurious dipole–dipole interactions between repeated slabs, a dipole correction was applied along the direction normal to the surface. All the generated models used in this study are illustrated in Fig. 30.

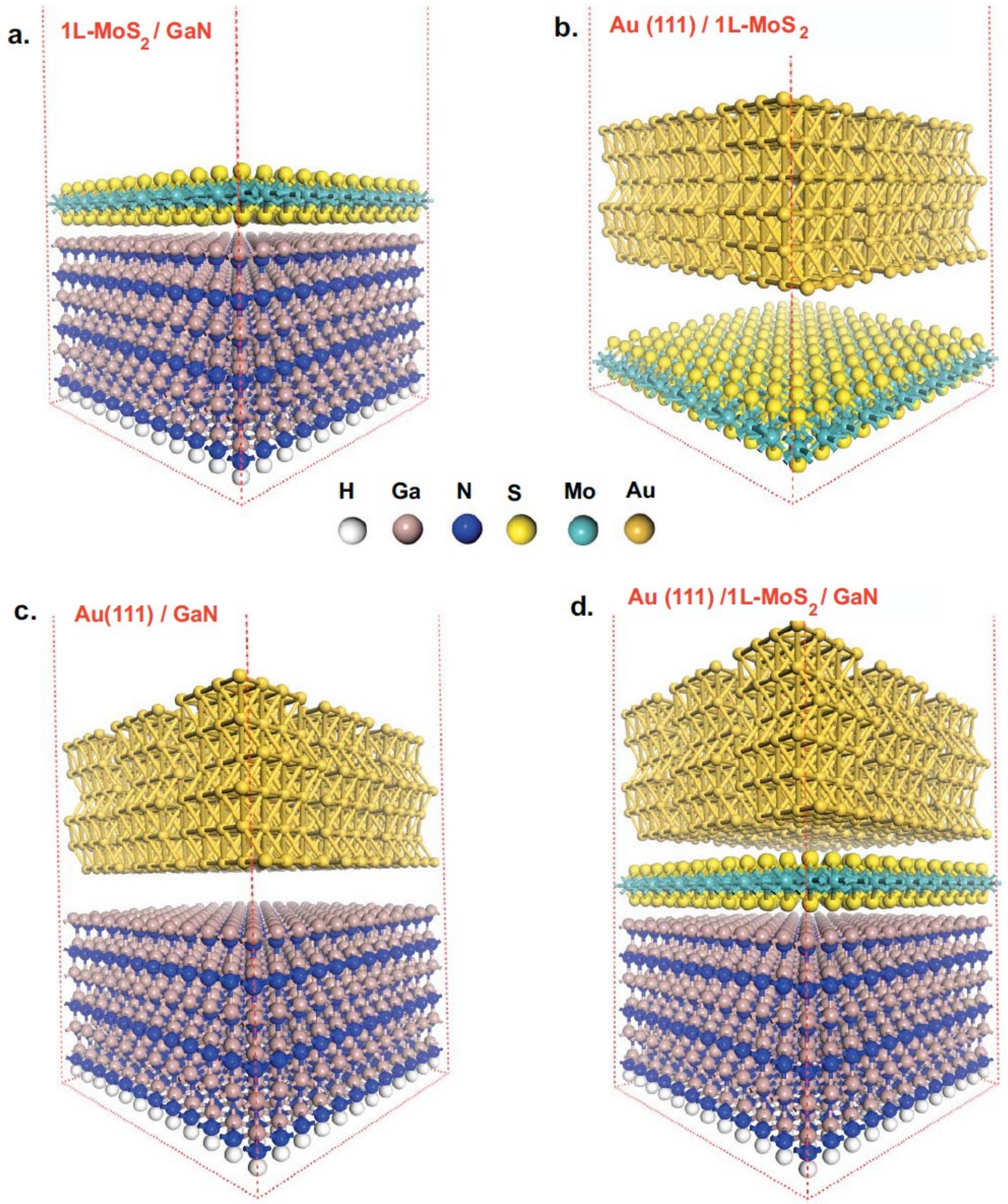

Fig. 30 Atomistic representations of modeled heterostructures a) 1L-MoS_2/GaN, b) Au (111)/1L-MoS_2, c) Au (111)/GaN, and d) Au (111)/1L-MoS_2/GaN. For the heterostructures with an Au (111) surface, the Au (111) surface is formed by straining the Au lattice constants by approximately 4.5% to form commensurate heterostructures. The lattice vectors are asymmetrically replicated to match the underlying semiconducting surfaces.

For the electronic properties calculations, we have analyzed parameters such as total and partial density of states (DOS), charge and potential profiles across the junction, and WF. Using these vdW-optimized heterostructures, the total energies and DOSs were recalculated with the denser k-point grids (6 × 6 × 1). Since we have consistently used strained Au (111) layers in self-consistent charge calculations, strain induced effects in the electronic properties of Au(111)/

1L-MoS_2, Au(111)/GaN, and Au(111)/GaN/1L-MoS_2 heterostructures were intrinsically normalized. By integrating the electrostatic potential on a real space grid in the heterostructures along the direction normal to the surface, vacuum levels, and WFs were identified. Charge accumulation and depletion characteristics at the heterojunctions were analyzed by integrating charges normal to the junctions.

6.4.2 Structural Properties

To gain further insight into the structural properties of the studied Au/2-D/3-D heterostructure system, we performed a systematic theoretical study of 2-D/3-D, Au/2-D, Au/3-D, and Au/2-D/3-D heterojunctions. To create 2-D/3-D and metal/ 2-D/3-D heterostructures with desired in-plane periodicity and minimal surface induced features in the structural and electronic properties, we have used a slab-model of both the metal and 3-D surfaces by checking their thickness convergence against their bulk properties, as described in our earlier study.[84] The details concerning implemented methods and parameters used to design commensurate, strain-compensated Au/2-D, Au/3-D, and Au/2-D/3-D heterostructures are presented in the in Section 6.2, and the simulated heterostructures are shown in Fig. 30. The observed equilibrium gaps are summarized in the Table 5.

Table 5 vdW-optimized vdW gaps. d_{12} is the optimized distance between metal/2-D or metal/3-D or 2-D/3-D layers, and d_{23} is the optimized distance between 2-D/3-D layers in the metal/2-D/3-D system.

System	d_{12} (Å)	d_{23} (Å)
1L-MoS_2/GaN	3.1	…
Au(111)/1L-MoS_2	3.3	…
Au(111)/GaN	3.25	…
Au(111)/1L-MoS_2/GaN	3.3	4.0

The column d_{12} refers to the distance between the atomic planes on both sides of the interface between the first and second material layers. For example, d_{12} for 1L-MoS_2/GaN is the center-to-center S-Ga atomic plane distance for Ga-terminated GaN. Similarly, d_{23} refers to the distance between the interfacial atomic planes of the second and third layers (refer to Fig. 30). The vdW distance between the GaN/1L-MoS_2 is defined as the distance between the surface Ga atoms and the bottom S atoms in the 1L-MoS_2. Here, one interesting observation we would like to highlight is the approximately 29% increase in the distance between GaN/1L-MoS_2 in the Au(111)/1L-MoS_2 /GaN heterostructure as compared to the standalone

GaN/1L-MoS_2 system. This observation is cross-validated with our TEM data that follows.

The vdW-spacing between the 2-D and 3-D layers was optimized, and an equilibrium vdW-gap of 3.1 Å between the 1L-MoS_2 and GaN surface was calculated, which is consistent with our previous TEM observations.[84] Prior to designing a metal/2-D/3-D heterostructure, metal/2-D and metal/3-D heterostructures are individually optimized. The optimized vdW gaps for Au/1L-MoS_2 (see Fig. 26b) and Au/GaN (see Fig. 26c) heterostructures are 3.3 and 3.25 Å, respectively, indicating physisorbed nature of the metal/2-D and metal/3-D interfaces. We can compare the calculated Au/MoS_2 vdW gap $\delta_{theor}^{met/2D} = 3.3$ Å with our TEM measurement result $\Delta(a1 - MoS_2) = 4.5 \pm 0.4$ Å. The vdW gap will be Δ minus the Mo-S bond length 1.5 Å, which yields $\delta_{TEM}^{met/2D} = 3.0 \pm 0.4$ Å consistent with the calculated value. Using these optimized geometries and vdW gaps, we designed an Au/1L-MoS_2/GaN heterostructure, as shown in Fig. 26d, and further optimized the vdW gap between 1L-MoS_2 and GaN layer in Au/1L-MoS_2/GaN heterostructure, by fixing the Au/1L-MoS_2 gap. The resultant equilibrium vdW gap for 1L-MoS_2/GaN interface in Au/1L-MoS_2/GaN is $\delta_{theor}^{2D/3D} = 4.0$ Å, an approximately 30% increment in vdW gap as compared to isolated 1L-MoS_2/GaN system reported earlier.[84] Quantitatively, the difference in observed (see above) and predicted $\delta^{2D/3D}$ with the Au contact is 0.6 ± 0.3 Å, a difference of approximately 13%. Though the increase caused by the Au contact of the vdW gap between 1L-MoS_2 and GaN layers observed in experiment is correctly captured in simulation, a quantitative agreement between observed and calculated vdW gaps demands for a comprehensive relaxation of Au/1L-MoS_2/GaN, which is outside the scope of this study.

It was noted in the TEM images that the wetting of the Au nanodot of the substrate changes depending on whether the dot is on MoS_2 or bare GaN. The contact angle of the Au nanodot on bare GaN was measured to be $\vartheta = 152°$ and the contact angles on the left and right sides of the central nanodot on MoS_2/GaN are $\vartheta = 112°$ and $130°$. Thus we observe an improved adhesion of Au to the GaN substrate when it is covered with 1L-MoS_2.

To understand this enhanced binding characteristics of Au contact with and without MoS_2 on GaN during fabrication, we performed first-principle calculations of Au on MoS_2 and Au on MoS_2/GaN heterostructures and compared their formation /adsorption energies, which is defined as the total energy difference between the heterostructure and the sum of its constituent layers. To rule out any method and simulation parameters dependent effect on the total energy calculation, we performed a static energy calculation by using similar first-principles-related parameters, such as k-point grids cutoff energies and smearing parameters, and by maintaining equilibrium vdW gaps between the Au-MoS_2, MoS_2-GaN, and Au-GaN layers at 3.3, 3.1, and 3.25 Å, respectively. The calculated adsorption energy difference of –4.5 eV (–0.56 eV/surface atom) between Au/1L-MoS_2/GaN and Au/GaN heterostructures indicates stronger binding of the Au 1L-MoS_2, and GaN surfaces in Au/1L-MoS_2/GaN heterostructure as compared to Au and GaN surfaces in an Au/GaN heterostructure. This is expected, because the dangling Ga bonds on a GaN surface introduce a polarization force at the surface, which in turn contributes to the repulsion of Au layer. In contrast, adding MoS_2 layer in between GaN and Au surface passivates the dangling Ga bonds while suppressing polarizability of the surface, resulting in relatively stronger binding between the GaN and Au surfaces. A further study on the effect of metal and insertion layer types in order to improve adhesion of the Au contact to the GaN substrate may be of interest for metal contact engineering in 2-D/3-D heterostructures.

6.4.3 Electronic Properties

The shift in the threshold voltage (V_{th}) in metal/2-D/3-D vertical device configuration is quantitatively related to the shift in the Fermi-level or intrinsic doping concentration and potential drop across the metal/2-D and 2-D/3-D junctions. To understand the potential drop across the heterojunctions in Au (111)/GaN heterostructure, pre and post MoS_2 layer insertion, the potentials obtained from the electronic structure calculations are integrated along the direction normal to the interface and plotted in Fig. 31. Since the stable configurations Au (111)/GaN, Au (111)/MoS_2, and MoS_2/GaN layers are physio-absorbed, vdW-optimized distances (gaps) (see Table 5) between the layers are used during electronic structure calculations. The effective potential drop at the Au (111)/GaN interface without the MoS_2 layer is 7.2 eV. Insertion of the MoS_2 layer in between Au (111) and GaN layers leads to formation of graded potential profile along the Au (111)/MoS_2/GaN interface. Quantitatively, the effective potential drops by 2.4 eV between the GaN and MoS_2 layers and by 4.7 eV between the MoS_2 and Au (111) layers, which is a cumulative potential drop of 7.1 eV. Large potential drops across Au (111)/GaN, with or without MoS_2, suggests that a lower carrier injection barrier exists at the interface, resulting in a larger current density across the interface. Moreover, the resultant potential drop difference of 0.1 eV between the Au (111)/GaN and Au (111)/MoS_2/GaN heterostructures indicates a further reduction in the barrier at the Au (111)/GaN interface due to the inserted MoS_2 layer. The observed graded-like junction formation due to the inserted MoS_2 layer is an indication that, with proper insertion layer type and thickness selection, the interface potential between the semiconducting, 3-D-like system and metal contact can be modulated. In addition, the net shift in the macroscopic average potential across the GaN layers in Au (111)/GaN heterostructure after MoS_2 layer insertion is approximately 0.75 eV. This shift in potential also implies an increase in intrinsic doping concentration and a stronger binding between the GaN and Au (111) layers prompted by the inserted MoS_2 layer, which is consistent with our experimental and theoretical observations discussed earlier. A noticeable shift of Δ (V) = 0.5 eV in the vacuum level before and after MoS_2 layer insertion was also observed, mainly due to the suppression of interface dipoles, which qualitatively agrees well with the change in threshold voltage observed in our experiment.

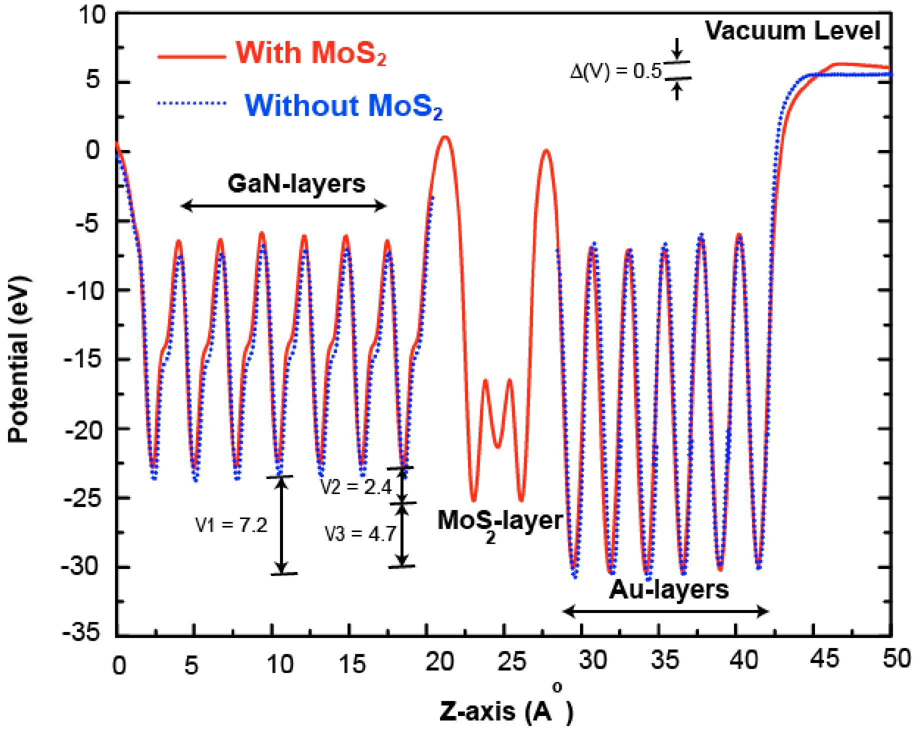

Fig. 31 Effective potential profile of the Au (111)/GaN heterostructures before and after MoS_2 layer insertion along the out-of-plane axis (Z-axis). The spatial location of each layer are marked accordingly. To illustrate effective potential drops across the interface, potential profile for the Au (111)/GaN heterostructure over the Au (111) layers are shifted and superimposed on top of potential profile of the Au (111)/MoS_2/GaN heterostructure. Δ(V) represents shift in vacuum potential due to the MoS_2 layer insertion. V1, V2, and V3 represent potential difference between the GaN and Au, MoS_2 and GaN, and MoS_2 and Au layers, respectively.

In the physio-absorbed interface with vdW-gap, the interlayer gap or vdW-gap also plays a significant role in defining the magnitude of the charge transport across the interface. To garner further understanding of the role of the inserted MoS_2 layer on charge transfer and rule out any proximity-induced effect due to the reduced vdW-gap between the Au (111) and GaN layers in the optimized geometry, we have performed an additional electronic structure calculation of an Au (111)/GaN heterostructure by fixing the distance between the Au (111) and GaN layers to the distance between the Au (111) and GaN layers in the optimized Au (111)/MoS_2/GaN heterostructure. The potential profile comparison between the Au (111)/GaN heterostructure with a fixed gap of 10.47 Å and Au (111)/MoS_2/GaN is presented in Fig. 32. Compared to the Au (111)/GaN heterostructure with equilibrium (optimized distance), the effective average potential shift of approximately 1 eV in the GaN layers due to the MoS_2 layer insertion in Au (111)/GaN heterostructure is also observed. Furthermore, without the MoS_2 layer and with an Au (111)–GaN separation distance of d = 10.47 Å, the potential at the Au (111) and GaN interface approaches the vacuum level, an indication of minimal interaction and charge transfer between the Au (111) and GaN layers due to layer decoupling.

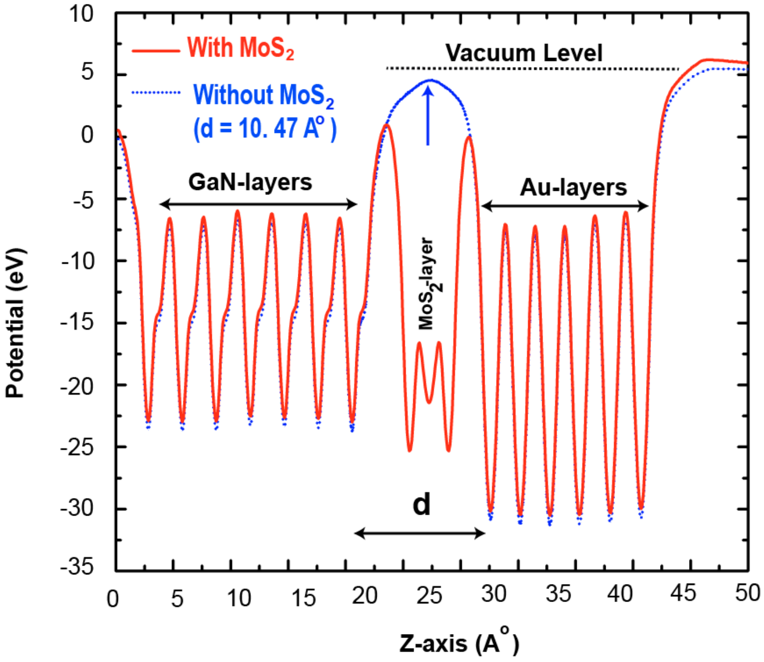

Fig. 32 Effective potential profile of the Au(111)/GaN heterostructures before and after MoS_2 layer insertion. The spatial location of each layer are marked accordingly. In the Au (111)/GaN heterostructure without the MoS_2 layer, the Au(111) and GaN distance (d) was fixed to 10.47 Å. Vertical arrow indicates the interface region where the potential reaches the vacuum potential level for the Au(111)/GaN heterostructure without the MoS_2 layer, indicating minimal charge transfer between the Au(111) and GaN layers.

Bipolar semiconductor junctions formed with 2-D materials are expected to exhibit new physics as compared to conventional *pn*-junctions. For example, depletion widths are critical parameters of conventional bipolar devices, but it is not clear how the depletion regions are formed in a heterojunction with a 2-D component that may only be one monolayer thick. Knowing the charge density distribution across the 2-D/3-D heterojunction can shed light on the origin of the I-V behavior and the Fermi level pinning. The magnitude of the charge depletion width across the metal/2-D and 2-D/3-D junctions and the Fermi-level pinning (FLP) energy window are the two major effects that define the I-V characteristics in the metal/2-D/3-D heterostructure. The FLP effect is mainly caused by interface induced dipole formation due to charge redistribution across the metal/2-D/3-D interface. To address these issues, we have calculated the plane-averaged charge density difference along the out-of-plane direction in the Au/GaN heterostructure with and without 1L-MoS$_2$ using the converged charges from our electronic structure calculations. The charge density difference (Δn) along the out-of-plane direction is defined as $\Delta n = n(het) - n(Au_{111}) - n(GaN)$ and is plotted in Fig. 32. Here, $n(het)$ is the plane averaged charge density of the Au(111)/MoS$_2$/GaN heterostructure, $n(Au_{111})$ and $n(GaN)$ are the plane averaged charge densities of Au(111) and GaN layers separated by a 10.47-Å vacuum gap (see Fig. 31). We have established (see Fig. 32) that the interaction between the Au and GaN layers in the absence of the 2-D layer is negligible. The charge density distribution in the heterostructure is shown in Fig. 33 relative to the baseline individual $n(Au_{111})$ and $n(GaN)$ to highlight the changes brought about by the 2-D ML. The degree of charge redistribution provides an insight into the effect of the MoS$_2$ ML insertion on dipole formation at vdW interfaces.

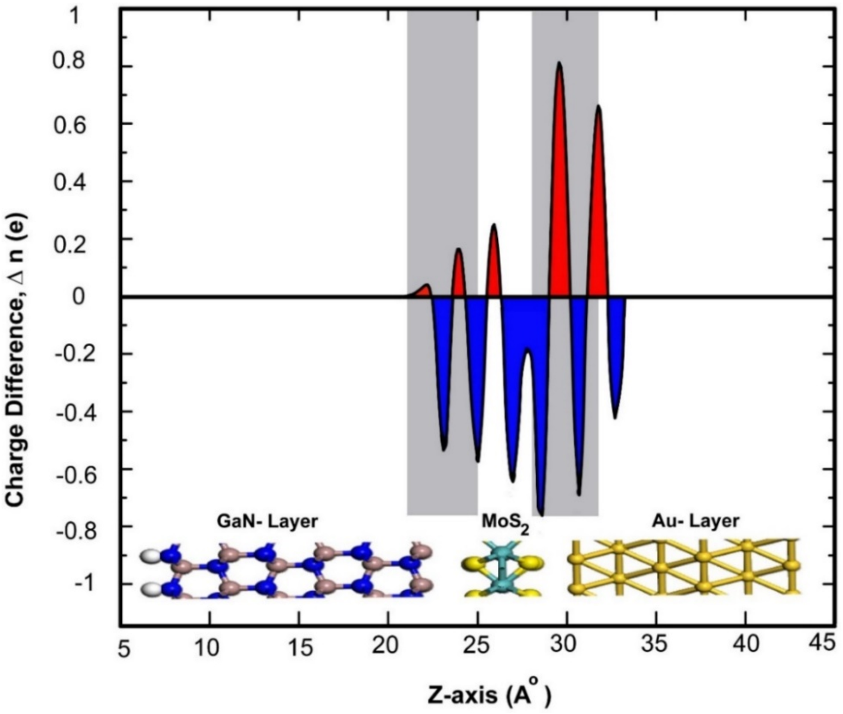

Fig. 33 Plane-averaged charge density difference (Δn) of the Au (111)/GaN heterostructures before and after MoS$_2$ layer insertion. Refer to text for the definition of Δn. The spatial location of each layer are marked accordingly. The interface regions are shaded with gray boxes. Blue and red regions indicate the charge depletion and accumulation, respectively. Inset illustrates the atomistic representation of the Au, MoS$_2$, and GaN layers in an Au (111)/MoS$_2$/GaN heterostructure.

It is evident from Fig. 33 that the charge fluctuations around the interfaces are significant in the Au (111)/MoS_2/GaN heterostructure, mainly due to the interactions between the GaN and Au (111) layers with the MoS_2 layer. The depletion areas in Fig. 33 are plotted in blue and have positive net charge due to the withdrawal of electrons. The charge depletion and accumulation at the GaN/MoS_2 interface is asymmetric compared to Au (111)/MoS_2. In addition, the depletion width is larger in the Au (111)/MoS_2 interface as compared to the GaN/MoS_2 interface, signifying strong interaction through higher DOS hybridization between the surface Au states and MoS_2 states, mainly d-states from the Mo-atoms. At the GaN/MoS_2 interface, the depletion area of positive charges is higher than the accumulation of the negative charges, indicating larger charge withdrawal by the GaN layer, which results in a larger potential drop across the GaN/MoS_2 interface. However, the depletion width in the GaN layer is minimal because of the weak interaction between the GaN and MoS_2 layers, which resulted from the larger vdW-gap (4 Å), as compared to 3.3 Å between the Au (111) and MoS_2 layers. Due to the strong interaction and states hybridization, the charge from the Au (111) layer extends through the MoS_2 layer into the GaN layer, which is evident by the extension of positive charges throughout the MoS_2 layer. The asymmetric charge accumulation and depletion widths in the GaN/MoS_2 and Au (111)/MoS_2 interfaces are likely one of the causes of the asymmetric threshold voltage V_{th} observed when the polarity of the applied bias is changed.

The charge redistribution across the interfaces also results in the formation of interface dipoles, which strongly influences the band alignment and SB height. As discussed earlier, the charge fluctuation is conspicuous across the Au (111)/ MoS_2/GaN heterojunction, contributing to interface dipole formation, and hence the FLP at the interface. The observed charge fluctuation characteristics are a consequence of the interactions between the energy states of the constituent layers at the heterojunctions. For example, in the Au (111)/MoS_2 heterostructure, the gap states are dominated by the hybridized Au and Mo d-states that results in the FLP, which can be further minimized by surface functionalization of the Au surface.[110] The complexity of the hybridization of the states near the Fermi-level increases significantly in the 3-D/2-D/metal heterostructure as compared to the cases of the metal/2-D and metal/3-D heterostructures. In particular, for the GaN/MoS_2/Au (111) heterostructure, the MoS_2 states hybridize with both the surface states of GaN and Au. To illustrate this, we plot in Fig. 34 the atom-projected density of states (PDOS) of Au (111)/GaN heterostructure after MoS_2 layer insertion.

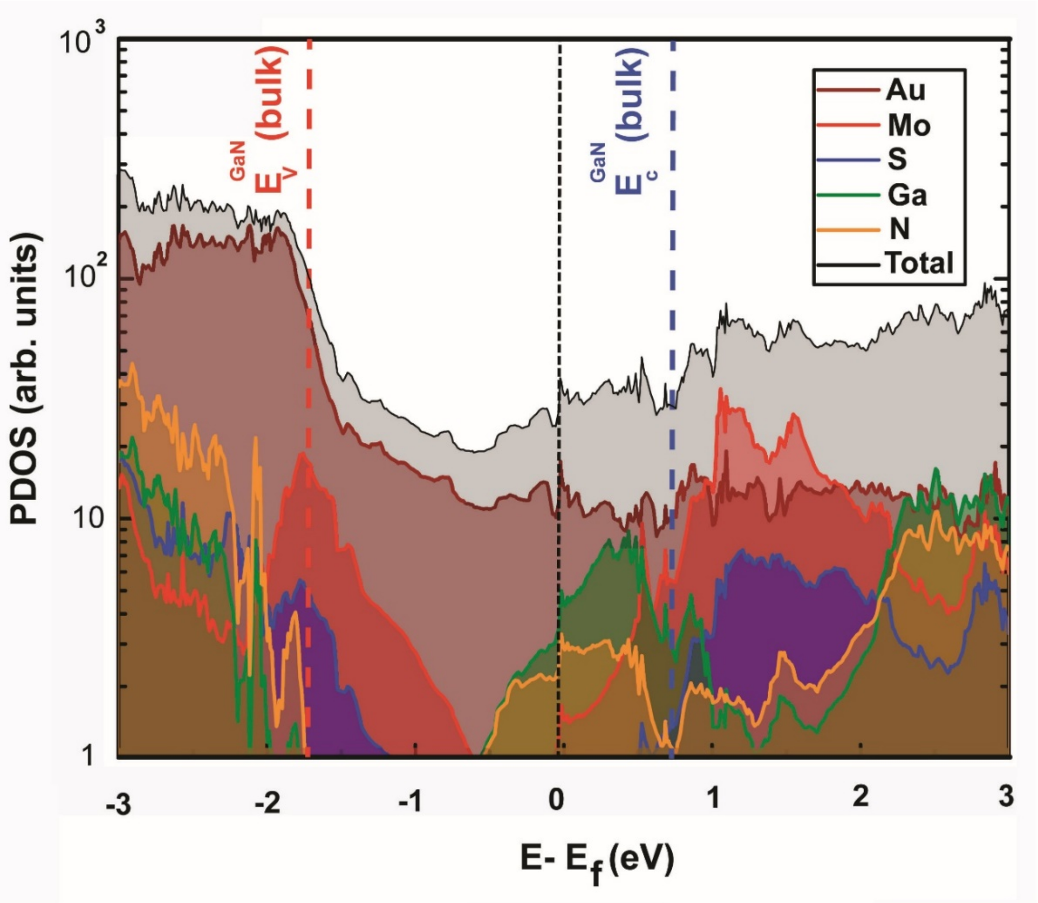

Fig. 34 Atom-PDOS of Au(111)/GaN heterostructures after MoS_2 layer insertion. The energy scale in the *x*-axis is referenced to the Fermi energy level (E_f), which is illustrated by the broken vertical line. The GaN bulk valence and conduction band states are marked as E_V^{GaN}(bulk) and E_C^{GaN}(bulk) with red and blue vertical lines, respectively.

Figure 34 shows in detail how the gap states arise from the overlap of the Mo, S, Ga, and Au atomic states, which consequently leads to the FLP. The bulk conduction band and valence band edges of GaN extracted from a separate calculation are marked to illustrate the gap states originating from the MoS_2-GaN and Au-GaN states hybridizations. The observed conduction band offset (CBO) and valence band offset (VBO) between MoS_2 and bulk GaN in GaN/MoS_2/Au(111) are 0.7 and 1.3 eV, respectively. It can be seen that the band offsets (or band alignment) between MoS and GaN deviates from the bulk values when we consider the GaN surface states. Undoped GaN was used in the PDOS calculation that explains the Fermi level position in GaN that differs from the experimental system (compare to Fig. 29). The observation of the gap states throughout GaN and MoS_2 bandgaps is consistent with the substantial band bending due to the FLP observed in the KP measurement, which in turn reduces the effect of the SB and complicates the device design. The functionalization or surface passivation of both the Au and

GaN surfaces might be one of the possible solutions to minimize the FLP and improve the control on the SB.

6.5 Summary

The integration of a monolayer 2-D semiconductor with conventional (3-D) semiconductors and metals was explored in order to build the scientific framework needed to develop hybrid 2-D/3-D heterostructure electronic devices. All-epitaxial Au/1L-MoS_2/GaN heterostructures were fabricated with MOCVD, powder vaporization, and e-beam evaporation and compared to Au/GaN junctions. Nanostructures consisting of Au/GaN with and without 1L-MoS_2 present at the interface were evaluated with cross-sectional TEM. The atomic plane spacing between the Mo and Ga planes (2-D to 3-D distance) and Au to Mo planes were measured to be 6.1 ± 0.3 and 4.5 ± 0.4 Å, respectively, which are consistent with first-principles calculated values.

The I-V characteristics of the vertical heterojunctions were measured and show that the charge transport was dominated by the Au/GaN interface with the vdW 2-D material acting as a perturbation. The site-resolved charge density and potential profiles calculated using the first-principles method elucidated the role of the 2-D layer in the formation of the potential barrier and showed the depletion regions within the mixed-dimensional bipolar junction. The SBHs extracted from I-V curves are 1.3 eV for the Au/MoS_2/p-GaN heterostructure and 1.5 eV for the Au/*p*-GaN heterostructure, indicating a reduction in the barrier height by 0.2 eV when MoS_2 is present. The reduced SB values suggest FLP and substantial BB in GaN at the interface. The formation of gap states leading to FLP was supported by our first-principles calculations of the atom-PDOS in the heterojunction. This study provides quantitative information and insight on the nanostructural and electrical aspects of the interactions of a semiconductor 2-D ML with III-V semiconductors, a mainstay of modern high-speed electronics and metals.

7. Growth and Characterization of a Multilayer 2-D Material on a 3-D Substrate

7.1 Introduction and Motivation

We have shown in the previous sections that a single molecular layer 2-D semiconductor (1L-2-D) grown on a conventional (3-D) semiconductor represents a convenient system to study the unique properties of 2-D materials. However we have found that 1L-2-D is electronically semi-transparent (see Section 5) and cannot be used in vertical bipolar junctions as an independent component forming a *pn*-junction. Therefore, 1L-2-D is unsuitable as a bipolar component in a 3-D/2-D/3-D HBT that we aim to create. We need a thicker semiconductor in place of the base of the HBT, so that the base exhibits the properties of the semiconductor whose doping polarity (*n* or *p*) is opposite to the polarity of the emitter and collector of the HBT. We set an objective to grow an approximately five-layer stack of a 2-D material, such as MoS_2 and WSe_2. We expected a five-layer stack of 2-D to exhibit its bulk semiconductor properties in a 2-D/3-D junction and yet be thin enough to give the speed advantage over the conventional all-3-D HBTs.

Our attempts to grow multilayer 2-D semiconductors by powder vaporization process described in the Section 6 were unsuccessful in the sense that the longer growth times resulted in nonuniform 3-D structures (such as MoS_2 in the shape of grains, flakes, and rods) rather than a uniform, layered material. A nonuniform semiconductor could not be used in our microelectronic devices. We considered other ways to synthesize electronic grade 2-D materials of multilayer thickness and had success with the MOCVD growth developed at the Penn State University (PSU).

In this work, we utilize MOCVD to synthesize few layer MoS_2 and WSe_2 on *p*- and *n*-type GaN, respectively, to probe the 2-D/3-D electrical properties. MOCVD enables large area, uniform TMD films via layer-by-layer growth as identified by AFM and Raman spectroscopy, where the layer number is tuned via growth time. XPS characterization confirms that stoichiometric MoS_2 (Mo:S=1:1.95) and WSe_2 (W:Se = 1:2.03) layers are grown with negligible metal-oxide bonding compared to powder-vaporized TMDs. Furthermore, there is no degradation or structural change of the GaN substrate. Importantly, we demonstrate that the vertical transport in the 2-D/3-D hybrids vary with 2-D thickness and the choice of the heterostructure. ML TMDs on GaN exhibit clear direct tunneling, and few layer (FL) 2-D layers (>2 layers) lead to *p-n* junction behavior. While *p-n* diodes based on FL MoS_2/*p*-GaN and WSe_2/*n*-GaN exhibit similar turn-on voltages under forward bias, FL MoS_2/*p*-GaN exhibits 100 times higher current under reversed bias due to strong charge transfer, and an intrinsic dipole between the MoS_2/*p*-GaN interface. As a result, we hypothesize that the few layer WSe_2/*n*-GaN is an appropriate choice for high-quality synthetic 2-D/3-D *p-n* heterostructures. Finally, we demonstrate MoS_2/WSe_2/*n*-GaN hybrids with atomically sharp interfaces, and unlike the resonant tunneling observed on MoS_2/WSe_2/epitaxial graphene (EG), single-layer MoS_2/WSe_2 on *n*-GaN exhibits ohmic behavior, while FL MoS_2/WSe_2 on *n*-GaN is dominated by SB transport.

7.2 Method: MOCVD Growth

TMD films are directly deposited on (*p*- or *n*-)GaN/c-sapphire substrates via MOCVD. The doping concentration for *n*-type GaN is 1017 cm^{-3} and hole concentration for *p*-GaN is 1018 cm^{-3}. The MoS_2 films are grown in a hot wall reactor at 650 °C using molybdenum hexacarbonyl (Mo(CO)6) and diethyl sulfide (DES) precursors, with sodium chloride (NaCl) powder placed upstream from the reactor hot zone for nucleation control and carbon sequestration.

7.2.1 MoS_2 Growth

The $Mo(CO)_6$ and DES precursors are sealed in two individual bubblers as shown in Fig. 35a. The GaN samples are put in the center of the furnace together with 1 mg of NaCl powder. Before the growth, the chamber is first annealed in vacuum (18 mTorr) at 300 °C for 5 min to remove the moisture and contaminants, followed by pressurizing the chamber to 10 Torr with 565 sccm of argon as the carrier gas. During the growth, a 2-min nucleation step with 2 sccm of H_2 from the $Mo(CO)_6$ bubbler and 45 sccm of H_2 from the DES bubbler is applied, followed by increasing the H_2 flow rate to 5 sccm for $Mo(CO)_6$. The entire growth takes 30, 60, and 120 min, respectively, to grow 1L 2L and approximately 5L MoS_2 on *p*-GaN.

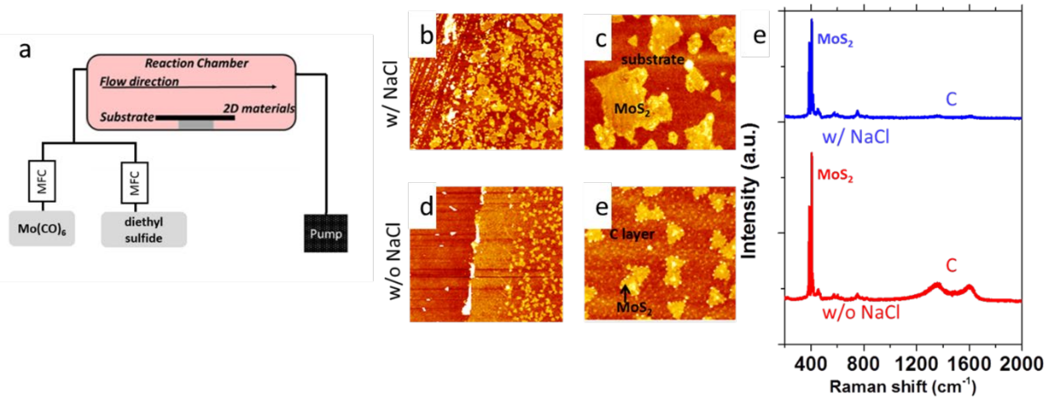

Fig. 35 The growth and fundamental characterization: a) the schematic of MOCVD reactor of MoS_2; b) and c) the large-scale (10 µm) and small-scale (2 µm) AFM scan of MoS_2 grown with NaCl; d) and e) the large-scale (10 µm) and small-scale (2 µm) AFM scan of MoS_2 grown without NaCl; a clear carbon film is observed after the growth without NaCl; e) the Raman spectra of the MoS_2 grown with and without NaCl (blue) and without NaCl (red); clear carbon peaks are observed without NaCl.

It is noticed that the NaCl is getting popular in the MOCVD growth of MoS_2 to eliminate the moisture and suppress the nucleation.[20,111] Here we notice that the other impact of NaCl in the MOCVD growth is removing the carbon residuals caused by the metal organic precursors. Nanocrystalline MoS_2 flakes are observed by AFM (Fig. 35b and c) when the NaCl is applied, while a uniform layer with 0.3-nm thickness is underneath the triangular MoS_2 film without NaCl (Fig. 35d and e). The Raman spectra shown in Fig. 35e suggest that although the MoS_2 can be synthesized either with or without NaCl, the growth without NaCl shows significant amount of carbon, correlating to the thin layer underneath the MoS_2. More theoretical calculation is motivated to understand the reaction between the NaCl and the precursors in depth.

7.2.2 WSe_2 Growth

The WSe_2 films are prepared using a cold wall reactor at 650 °C with tungsten hexacarbonyl ($W(CO)_6$) and hydrogen selenide (H_2Se). Growing 2-D vdW layer material on 3-D substrates would not be the same as traditional epitaxy due to the absence of dangling bonds on the surface. Here, epitaxial WSe_2 on 3-D substrate, *n*- and *p*-type GaN, with uniform coverage achieved successfully through optimized growth condition without any degradation of GaN substrate. Growths performed at atmospheric pressure (700 Torr) using H_2 as a carrier gas, by following the growth profile as seen in Fig. 36. A reactive precursors—$W(CO)_6$ at the transition metal side and H_2Se at the chalcogenide side—started flowing simultaneously just after temperature reached at 650 °C, in order to avoid roughening of GaN surface through degradation under H_2 environment. A controlled 2L-WSe_2 epitaxial and controlled layered film was obtained for the partial pressure of $W(CO)_6$ of 5.8×10^{-4} Torr and H_2Se of 11 Torr in a 30-min growth period. Post-growth annealing of 5 min under H_2Se environment was performed in continuation of growth process to reduce the chalcogenide-based defects in the film, which were directly evidenced in our previous study. A sharp and abrupt interface at GaN surface (based on cross-sectional TEM), presented a control layer-by-layer growth with vdW epitaxy of WSe_2 at 3-D substrate surface. We believe that passivation of the surface dangling bonds on the 3-D substrate would be a key to achieve vdW epitaxial growth of the 2-D vdW layers on ordinary 3-D substrates.

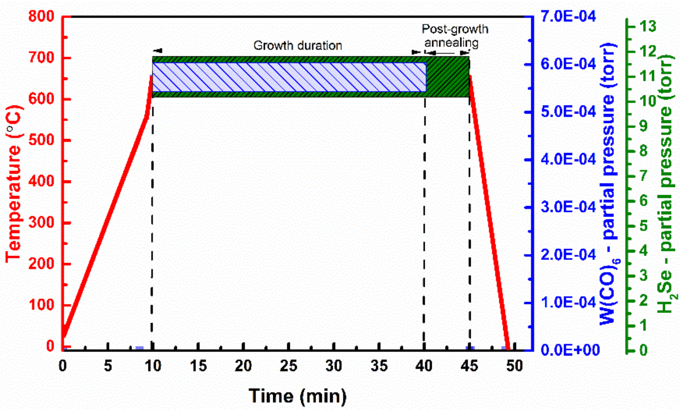

Fig. 36 Growth temperature/flow/pressure profile of MOCVD growth of WSe_2 on *n*-GaN

7.3 Characterization

7.3.1 AFM, Raman, and XPS

AFM (Fig. 37a–c) demonstrates controlled formation of 1L 2L, and FL (3.5 nm) MoS_2 as growth time is increased from 30 to 60 to 120 min, where the topography of ML MoS_2 (Fig. 37a) closely matches the natural roughness of GaN substrate.[45] An additional adhesion map (inset of Fig. 37a) is provided to visualize the distinction between 1L MoS_2 and p-GaN. ML, 2L, and FL (4.7 nm) WSe_2 (Fig. 37d–f, respectively) is realized using growth times of 5, 10, and 30 min. Raman spectra of MoS_2 (Fig. 37g) exhibits the typical 384 cm^{-1} (E^1_{2g}) and 403 cm^{-1} (A_{1g}) vibration modes for 1L MoS_2, 384 cm^{-1} (E^1_{2g}) and 405 cm^{-1} (A_{1g}) for 2L MoS_2, and 383 cm^{-1} (E^1_{2g}) and 407 cm^{-1} (A_{1g}) for FL MoS_2, confirming the thickness difference.[35] Similar Raman shift trend is also observed on WSe_2 (Fig. 3h) from 250 cm^{-1} (1L) and 249 cm^{-1} (6L) for the E^1_{2g} peak, agreeing with previous reports.[112]

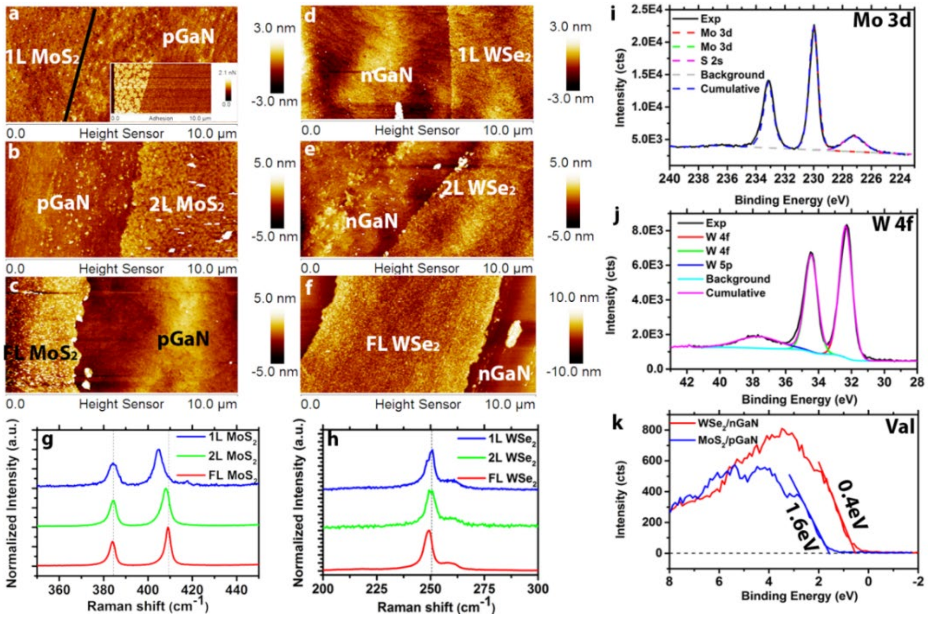

Fig. 37 Thickness controlled growth of TMDs: a)–c) AFM image of 1L–FL MoS_2 grown on *p*-GaN. To identify the thickness, the film is intentionally scratched. The height profile in b) and c) clearly show 2L (1.3 nm) and approximately 5L (3.5 nm) of MoS_2 on *p*-GaN. The height ML in a) is difficult to visualize due to the roughness of *p*-GaN, but the adhesion map (inset) demonstrates the sub-ML flakes on *p*-GaN; d)–f) AFM image of 1L–FL WSe_2 grown on *n*-GaN, the height profile indicates the different thicknesses of WSe_2; g) Raman spectra for 1L–FL MoS_2, the A_{1g} peak exhibits a significant red shift as thickness decreases, while the E^1_{2g} peak remains nearly the same, confirming the thickness reduction; h) Raman spectra of 1L–FL WSe_2, the observed E^1_{2g} peak shows a slight red shift as thickness increases; i) XPS spectrum of Mo 3-D core level, clear Mo–S bonding is detected and the Mo-O bonding is below the detection limit; j) XPS spectrum of W 4f core level, W-Se bonding is identified and the W 5p is also observed; k) valence band edge of the FL MoS_2/*p*-GaN (blue) and FL WSe_2/*n*-GaN (red). The Fermi level is 1.6 and 0.4 eV above the valence band maxima of MoS_2 and WSe_2, respectively, indicating that the MoS_2 is *n*-type and WSe_2 is *p*-type.

Synthetic MoS_2 and WSe_2 are nearly stoichiometric (Mo:S = 1:1.95; W:Se = 1:2.03) with negligible metal-oxygen bonding and no structural degradation is observed on GaN after the growth. In the case of MoS_2, the Mo 3-D doublet peaks in XPS are observed at 230.0 and 233.1 eV together with an S 2s peak at 227.2 eV (Fig. 37i). Following peak fitting, the only detected bonding is between Mo and S. Importantly, Mo-O bonding is significantly reduced for MoS_2 grown by MOCVD compared to PV.[45] This is likely the result of the elimination of the oxygen precursor MoO_3 often used for Mo in the PV method. Tungsten diselenide XPS (Fig. 37j) exhibits three W peaks at 32.3 eV (W 4f7/2), 34.4 eV (W 4f5/2), and 37.7 eV (W 5p3/2) only, indicating no W-O bonding or other impurities within the detection limits of XPS.[113] Finally, valence band edge measurements (Fig. 37k) of MoS_2 and WSe_2 indicate the valence band maximum (VBM) of MoS_2 is 1.6 eV below the Fermi level, suggesting that MoS_2 is electron doped (*n*-type). In contrast, the VBM of WSe_2 is 0.4 eV below the Fermi level, indicating hole doping (*p*-type) behavior of WSe_2.[114] This is typical of MoS_2 and WSe_2, and is attributed to chalcogen vacancies in the TMD layer.[20,115–116] Further XPS characterization of the GaN before and after the growth also indicates no detectable structural degradation of GaN after the growth.

7.3.2 Electronic Properties of TMDs/GaN Heterostructure

Vertical charge transport through the 2-D/3-D hybrid is highly sensitive to the 2-D layer properties. Here, we use CAFM with a Pt/Ir tip to probe the nanoscale vertical transport of *p*-*n* junction TMD/GaN heterostructures. Based on fitting the local I-V characteristics with the Fowler–Nordheim tunneling equations,[117–118] the carrier transport can be described to be dominated by direct tunneling for 1L MoS_2/*p*-GaN and 1L WSe_2/*n*-GaN. Thus, ML TMDs are considered nearly electrically transparent due to the full depletion region overlap. Additionally, the TMD layer between the Pt/Ir metal tip and GaN surface leads to a reduction in the transport barrier due to FLP at the tip/TMD interface, thereby reducing the contact resistance.[45,108,119] As the 2-D layer thickness increases, the carrier transport becomes dominated by the barrier at the 2-D/GaN interface. This is evident when analyzing the I-V characteristics of FL *n*-MoS_2/*p*-GaN and *p*-WSe_2/*n*-GaN (Fig. 4a). For simplicity, (*p*-GaN or WSe_2) positive bias is applied on the *p*-type semiconductor. The two heterostructures show slightly different turn-on voltage at approximately 1 V for WSe_2/*n*-GaN and 1.4 V for MoS_2/*p*-GaN under forward bias, with an ideality factor (n) of 30 for MoS_2/*p*-GaN and 15 for WSe_2/*n*-GaN. The high ideality factor is likely due to the SB between the tip and TMDs,[41,45] leading to a combination of *p*-*n* and SB transport. Improved ohmic contacts to the TMDs will enable lower ideality factors.

We note that under reverse bias, the MoS_2/*p*-GaN structure exhibits significant levels of current, even at low voltages. To understand this behavior, KPFM and Low Energy Electron Microscopy/Reflectivity (LEEM/LEER) measurements are employed. KPFM measurements of FL MoS_2 (Fig. 38b) and FL WSe_2 (Fig. 38c) reveal distinct work function differences between the TMDs and (*p*- or *n*-)GaN. The work function of WSe_2 is measured to be approximately 300 meV higher than *n*-GaN, and MoS_2 is approximately 150 meV higher than *p*-GaN. This work function difference is confirmed by LEEM/LEER measurements, where multiple spots are evaluated on FL MoS_2/*p*-GaN (LEEM, Fig. 38d) and FL WSe_2/*n*-GaN (LEEM, Fig. 38e). The corresponding LEER spectra (Fig. 38f) suggests that the work function difference between FL MoS_2 and *p*-GaN is approximately 220 meV and between FL WSe_2 and *n*-GaN is approximately 250 meV. Based on the measured work function ($\Phi_{WSe2} = 4.8$ eV; $\Phi_{GaN} = 4.5$ eV), XPS measurements[120] and reported electron affinity ($\chi_{WSe2} = 3.9$ eV;[121] $\chi_{GaN} = 4.1$ eV,[41] the band diagram of WSe_2/*n*-GaN can be established (Fig. 38g), which agrees with literature values for WSe_2/GaN.[120] However, counter to the reported values,[10,122] KPFM and LEER in this work both demonstrate that the work function of MoS_2 is higher than that of *p*-GaN (Fig. 38b and d). We hypothesize that this could be due to modification of the GaN Mg dopant properties: 1) the degradation of Mg-doped GaN during the H_2 involved growth that results from the Mg dopant, leading to a reduced hole concentration of *p*-GaN[123–126] or 2) the strong intrinsic dipole and charge transfer at the semiconductor/semiconductor interface.[127] In either case, this would shift the Fermi level (and hence work function) toward higher values in the GaN bandgap, leading to a modification of the MoS_2/*p*-GaN behavior.

The XPS measurements reveal the type I band alignment between MoS_2 and *p*-GaN (Fig. 38h). Combining with the aforementioned KPFM and LEEM/LEER measurement, the band bending under different bias is shown in Fig. 38h. Conventional electron conduction is responsible for the forward biased current, but unlike WSe_2, the hole conduction due to the tunneling can introduce reversed bias current.[10] Furthermore, material modifications (below the detection limits of XPS) in the GaN due to high temperature synthesis of the MoS_2 could also be the source of high leakage currents in reverse bias observed in Fig. 38a;[128] however, additional theoretical work is needed to understand the aforementioned scenario in depth.

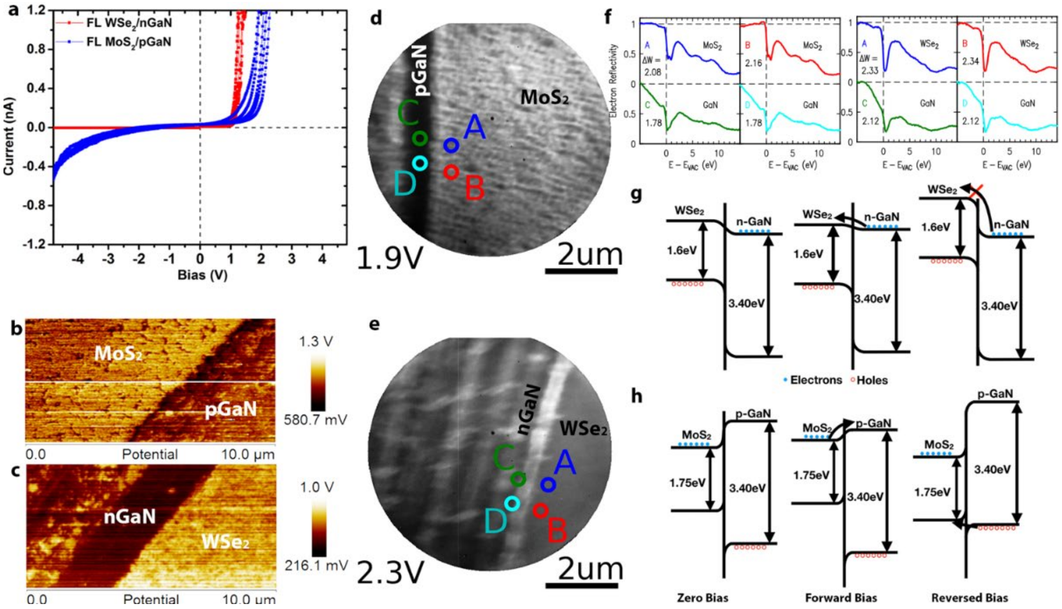

Fig. 38 The electronic properties of the TMDs/GaN heterostructure: a) the I-V measurement of FL MoS$_2$/*p*-GaN and WSe$_2$/*n*-GaN. Both heterostructures are turned on at approximately 1.4 V under forward bias. However, FL MoS$_2$/*p*-GaN exhibits a higher leaking current. b) and c) KPFM characterization of FL WSe$_2$/*n*-GaN and FL MoS$_2$/*p*-GaN, the WF of WSe$_2$ and MoS$_2$ is 300 and 150 meV higher than *n*-GaN and *p*-GaN, respectively. d) and e) LEEM micrographs of FL MoS$_2$/*p*-GaN (V = 1.9 eV) and FL WSe$_2$/*n*-GaN (V=2.3 eV). The scratch of GaN is clearly visualized by LEEM and the LEER check point is labeled with different color in Fig. 36d and e. f) The LEER spectra of FL MoS$_2$/*p*-GaN (top) and FL WSe$_2$/*n*-GaN (bottom), which quantifies the electrostatic surface variation and hence the variation of vacuum level. g) The band alignment of WSe$_2$/*n*-GaN. h) The band alignment of MoS$_2$/*p*-GaN. It is clear that the hole conduction can be responsible for the reversed bias current.

7.3.3 2-D/2-D/3-D Trilayer Stacks of MoS$_2$/WSe$_2$/GaN

Utilizing the same synthesis techniques, it is possible to realize more complex 2-D/3-D hybrids such as MoS$_2$/WSe$_2$/*n*-GaN (MWnG). Here, WSe$_2$ films are deposited on *n*-GaN, and subsequently MoS$_2$ films are deposited on WSe$_2$/*n*-GaN to form the MWnG hybrid. The MoS$_2$ is grown at 650 °C, resulting in nanocrystalline sub-MLs on the 1L WSe$_2$ (Fig. 39a) and uniform FL MoS$_2$/FL WSe$_2$ (Fig. 39b). Raman spectroscopy (Fig. 39c) confirms the presence of MoS$_2$ and WSe$_2$, with no evidence of intermediated phases (WS$_2$, MoSe$_2$, etc.). Cross-sectional HR(S)TEM and EDS (Fig. 39d) reveal that the FL hybrid structure is 6–7 layers, evenly split between MoS$_2$ and WSe$_2$. The EDS mapping (Fig. 39e) indicates that the layers of MoS$_2$ and WSe$_2$ are well defined with a sharp interface, and no evidence of alloying.

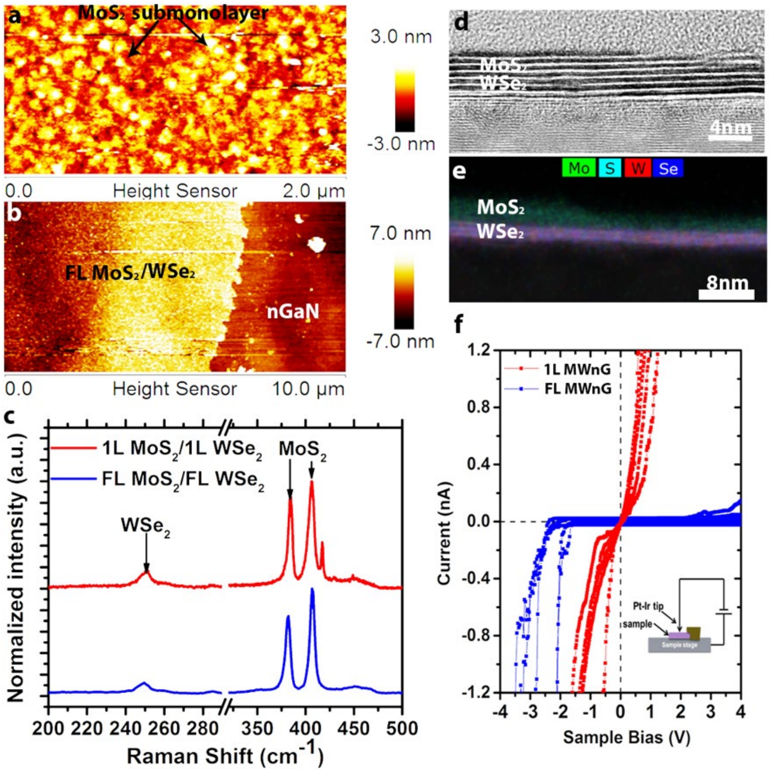

Fig. 39 The 2-D/2-D/3-D heterostructure of TMDs/GaN: a) and b) AFM images of 1L MoS$_2$/1L WSe$_2$/*n*-GaN and FL MoS$_2$/FL WSe$_2$/*n*-GaN. The sub-monolayer domains can be seen on the top of WSe$_2$ and the uniform FL heterostructure exhibits an approximately 4.6 nm total thickness. The Raman spectra c) confirms the co-existence of MoS$_2$ and WSe$_2$. d) and e) the HRTEM image of the FL MoS$_2$/WSe$_2$/*n*-GaN heterostructure, approximately 7 atomic layers is clearly observed, and the HRSTEM image colored by EDS mapping shows a sharp interface between MoS$_2$/WSe$_2$. f) The I-V curve of 1L MoS$_2$/WSe$_2$/*n*-GaN and FL MoS$_2$/WSe$_2$/*n*-GaN. Unlike the Schottky-dominant rectifying characteristic shown on FL sample 1L sample exhibits nearly linear tunneling characteristic without negative differential resistance.

7.3.4 Conductive AFM: Vertical Electron Transport Measurement

The electrical properties characterized by CAFM (Fig. 39f) vary greatly between ML heterostructures and FL heterostructures. When the film contains FL MoS$_2$ and FL WSe$_2$, a rectifying conductivity is observed. This rectifying feature is attributed to the forward-biased SB between the Pt/Ir tip and MoS$_2$.[41,45] Interestingly, unlike the reported resonant tunneling of 1L MoS$_2$/1L WSe$_2$ heterostructures on graphene, we find nearly ohmic behavior *n*-GaN, with no negative differential resistance (NDR) observed at room temperature. Such behavior is likely due to the thermionic emission at room temperature and nondegenerated doping concentration of our MoS$_2$ and WSe$_2$ films.[129–130]

7.4 Summary

This work demonstrates the scalable growth of TMD/GaN hybrid structures, where film thickness is controlled by tuning the growth time. The process results in high-quality MoS_2 and WSe_2, as well as enables a route to 2-D heterostructures on GaN for next-generation electronics. Vertical transport through the hybrid structures is affected by the 2-D layer thickness, where ML films exhibit strong direct tunneling characteristics and few layer 2-D enables p-n junction formation at the 2-D/3-D interface. Compared to FL WSe_2, the FL MoS_2 films exhibit high leaking current in reversed bias. Our KPFM and LEEM/LEER characterization reveals a counterintuitive work function difference between MoS_2 and *p*-GaN, potentially due to the strong interface charge transfer and possible nonstructural degradation (Mg passivation) in *p*-GaN. Furthermore, FL MoS_2/WSe_2 heterostructures on *n*-GaN exhibits rectifying behavior due to the presence of the metal/MoS_2 SB. In contrast, we find ohmic behavior when the thickness of the film is reduced to one atomic layer. This study elucidates that the thickness and materials choice are critical toward high-quality 2-D/3-D heterostructures.

Importantly, our results demonstrate that multilayer 2-D semiconductors grown by MOCVD function as bipolar semiconductor components in 2-D/3-D junctions with GaN and form bipolar *pn*-diodes (see Fig. 38a). This is in contrast to our results on the single layer 2-D semiconductors grown by PV described in Section 7.2. Therefore, we can utilize multilayer 2-D semiconductors grown by MOCVD at PSU as a 2-D base component in our targeted device: a 3-D/2-D/3-D HBT.

8. Growth and Characterization of a 3-D/2-D/3-D Heterostructure

8.1 Introduction and Motivation

To implement a functioning HBT based on the 2-D semiconductor base, we need to be able to fabricate trilayer bipolar 2-D/3-D heterostructures and electrically access individually all three transistor components: collector, base, and emitter. Between the choice of the 3-D/2-D/2-D heterostructures described in Section 7.3.3 and 3-D/2-D/3-D to be described in this section, we made our choice to use the latter for the following reasons. To access individually the base (middle layer) and collector (bottom layer), we need to perform some lithographic patterning after the collector (GaN) growth, which essentially implements bipolar diodes formed by the base and collector. Then the synthesis of the top layer (emitter) should be gentle enough to preserve the prefabricated diode devices. Therefore, the MOCVD process for the top layer is considered to be too harsh, in terms of chemicals and temperature. While a PVD process, such as MBE, can be gentle enough to synthesize the top layer and preserve the devices on the substrate. Next, the synthesis of a conventional (3-D) semiconductor is more established and reliable than the synthesis of new 2-D materials. Lastly, the MOCVD process described in the Section 7.3.3 is worked out to produce only ultra-thin layers of the top 2-D layers, while the HBT needs the emitter layer of approximately 100 nm thickness in order to supply sufficient amount of carriers during the transistor operation. Our MOCVD method is not suitable for the deposition of such thick layers (100 nm) of 2-D materials. For these reasons, we chose the MBE process of a 3-D semiconductor as a route to fabricate the last, top layer in the trilayer structure of an HBT. Thus, we focus further on the 3-D/2-D/3-D heterostructures.

8.2 Top 3-D Layer Deposition Method: MBE Growth

The growths of the top layer of GaN in the trilayer 3-D/2-D/3-D heterostructure were conducted in a Varian Gen II plasma assisted molecular beam epitaxy (PA-MBE) reactor in the CCDC ARL's Electro-Optics & Photonics Division (Fig. 40). The Al source is a Veeco 400-g Al SUMO effusion cell with a pyrolytic h-BN crucible. The Ga source is an E-Science extended capacity Titan source with a graphite crucible. The N source is a Veeco Uni-bulb plasma source with an aperture designed for growth of small sample sizes less than 6 cm^2. The group III metal sources evaporate their respective atomic sources through evaporation of a liquid metal, whereas the N source uses N_2 gas. The Gen II design includes a load-lock for loading and unloading substrates, a buffer chamber with a wagon wheel style sample holder with two substrate heaters for thermal cleaning, and a growth chamber where the sources, substrate heater and manipulator (continuous azimuthal rotation [CAR]), and primary vacuum pumps reside. The minimum load-lock vacuum pressure is 5E-9 Torr, the buffer chamber vacuum pressure is 3E-10 Torr, and the growth chamber pressure is approximately 4E-11 Torr.

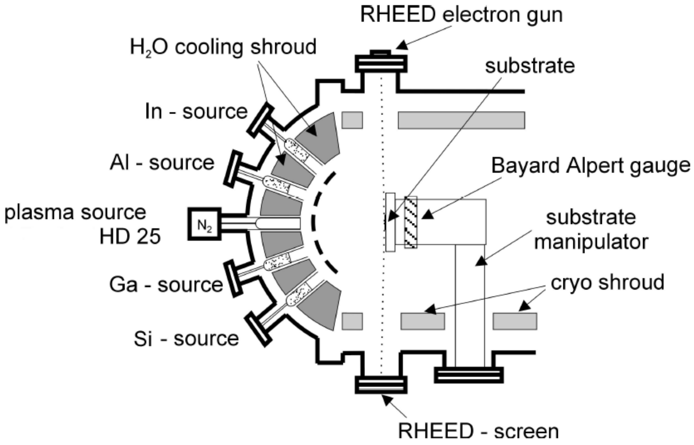

Fig. 40 Diagram of the MBE deposition system used for the GaN growth

We began our investigation of the growth of GaN on MoS_2 by PA-MBE by using conditions that have been shown to be effective for growing low-temperature GaN on silicon carbide (SiC). A low growth temperature in this case was chosen to limit the thermal decomposition of MoS_2 prior to the commencement of epitaxial growth. An initial Ga beam equivalent pressure (BEP) of 1.6E-7 Torr was chosen, which provides an atomic flux of 2.6E14 atoms/cm^2/s, or approximately 180 nm/h. This flux was chosen to provide a stoichiometric flux, equivalent to the arrival rate of active N provided by the N plasma source. The N plasma source flow was 0.40 sccm and RF power 300 W, which provides an N limited growth rate of 180 nm/h.

The ratio of Ga to N atomic fluxes and the substrate temperature were found to be critical parameters for the successful growths of GaN on top of MoS_2. In conventional MBE growths of GaN on 3-D substrates, the preferred substrate temperatures are usually above 600 °C and the Ga/N flux ratio is kept to be above 1 in order to achieve a high-quality GaN crystal. In our first experimental growths using these conventional parameters, we found out that the MoS_2 layer was completely etched away as determined by Raman imaging. Also, the GaN film was of poor texture and poor crystallinity. To overcome these problems, we have invested a considerable effort into the development of a nonstandard GaN growth method that is compatible with MoS_2 substrates that we used.

We have established a collaboration with the group of Prof Siddharth Rajan at the Ohio State University who had experience with the MBE growth of GaN on top of MoS_2 (specifically, sapphire/MoS_2). Since sapphire is not a semiconductor, Rajan's group had achieved the synthesis of 3-D/2-D semiconductor heterostructures and still were working, in parallel to our project, toward the synthesis of trilayer 3-D/2-D/3-D structures. It has been pointed out to us by the Rajan's group that, in order to prevent Ga atoms from etching away the MoS_2 layer, one needs to keep the Ga/N atomic flux ratio below 1. Additionally, the substrate temperature needs to be kept at or below 550 °C. The results of Rajan's experimental growths of GaN on MoS_2 are summarized in Fig. 41. These results are in agreement with the successful growth of GaN on MoS_2 reported in the literature by Tangi et al.,[84] where a 500 °C substrate temperature and N-rich flux ratio were used (Ga BEP 2.1e-8 Torr).

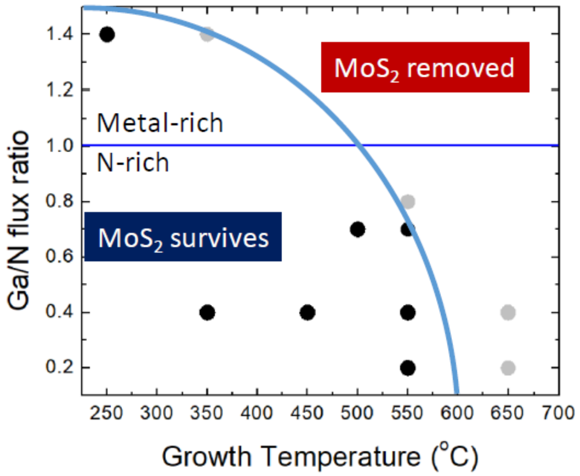

Fig. 41 MBE growth results of GaN on sapphire/MoS_2 substrates. Black dots depict the growths where MoS_2 survived and gray dots are the growths where MoS_2 got etched away. The line shows the parameter area of successful growths. (Courtesy of the Prof Siddharth Rajan group at the Ohio State Univ. [2017].)

Guided by these experimental data, we have developed an MBE growth process at 550 °C substrate temperature and with a N-rich flux ratio. The growth conditions corresponding to the best morphology were using a BEP of 3.5E-8 Torr, which is equivalent to 5.4E13 atoms/cm^2/s, or 45 nm/h. These conditions were surprising given that excess N typically leads to very rough, 3-D growth on traditional substrates. More work needs to be done to explain how such conditions lead to smooth 2-D GaN films when grown on MoS_2. We have demonstrated first successful growths of GaN on GaN/MoS_2 substrates. Figure 42 shows the SEM and AFM images of the GaN surface in the sapphire/GaN/MoS_2/GaN heterostructure as well as a cross-sectional view of the GaN/MoS_2/GaN trilayer covered with a protective Pt coating. Due to the ultra-thin dimensions, the MoS_2 is not visible on this cross-SEM image. The Raman measurements in the following section prove the presence of the MoS_2 layer and the crystalline GaN nature of the top MBE layer. The AFM-measured RMS roughness of the top GaN surface is 1.0 nm. Some porosity and elevated roughness are observed in the SEM and AFM characterization. These GaN film properties are somewhat inferior to the properties of GaN crystals MBE-grown by standard high-temperature, Ga-rich techniques that work for sapphire and 3-D semiconductor substrates. Further optimization of the

MBE process on 2-D semiconductors might improve the GaN film structure. Nevertheless, our results of the first, wafer-scale synthesis of a GaN/MoS_2/GaN trilayer structure with ultra-thin 2-D semiconductor embedded in it represent an important step forward toward the utilization of 2-D semiconductors in high-performance electronic devices. More characterization of these trilayer heterostructures follows.

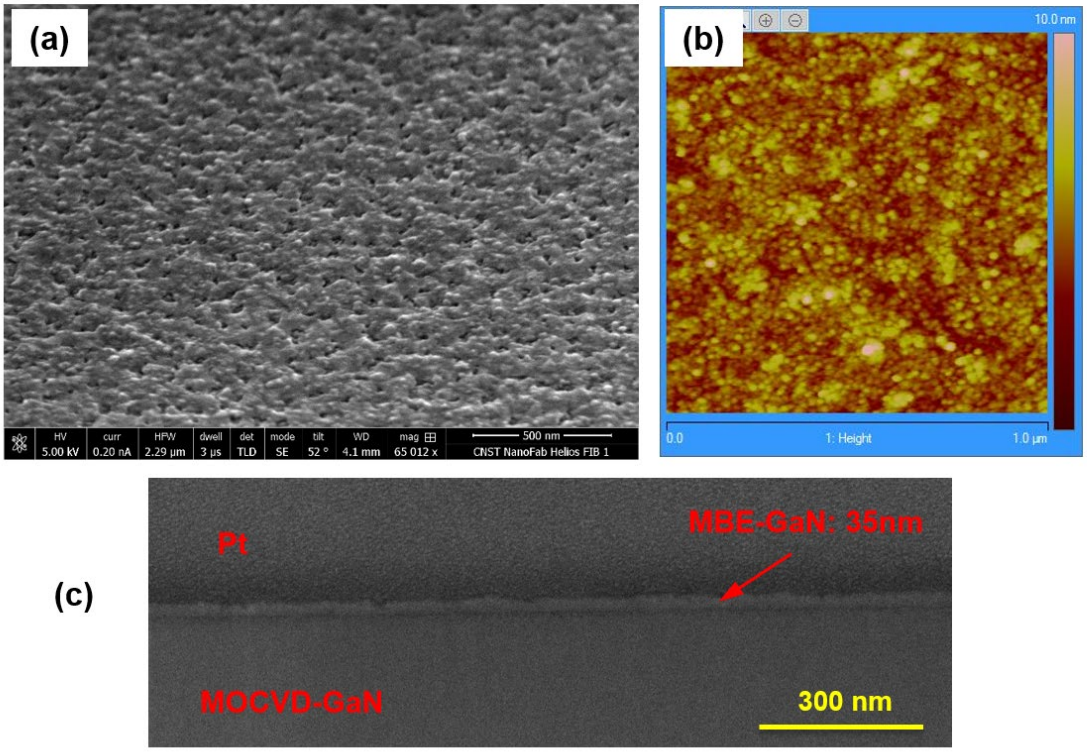

Fig. 42 Primary nano-characterization of the MBE growth of GaN on top of the GaN/MoS_2 substrate. a) SEM and b) AFM images of the top GaN surface. Roughness RMS = 1.0 nm. c) Cross-sectional SEM.

8.3 Characterization

8.3.1 Raman Measurement

GaN layers were grown by MBE on top of GaN (MOCVD substrate)/MoS_2 structures and the quality of the resulting trilayer stack was first checked with Raman spectroscopy. It was found that the GaN layers grown by Ga-rich MBE result in the removal of the MoS_2 layer and poor-quality GaN layer. The removal of the MoS_2 was deduced from the disappearance of the characteristic MoS_2 spectral lines shown in Fig. 43a as the “pre-top GaN” curve. The disappearance of the MoS_2 modes reflected the fact that the MoS_2 was etched away during the Ga-rich GaN growth. The Raman GaN mode of the GaN (MOCVD substrate)/MoS_2 structure is shown in Fig. 43b as the "pre-top GaN" curve. After the Ga-rich GaN growth the Raman GaN mode showed the presence of the weaker broadened peak. The new peak was due to the new GaN material and the broadening was the evidence of the deteriorated crystal quality.

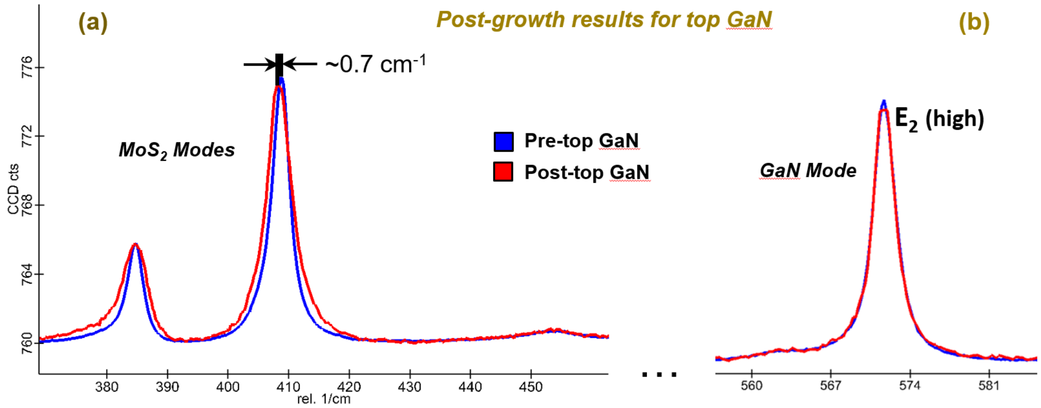

Fig. 43 Raman spectra of the GaN/MoS_2 substrate with and without the top MBE N-rich GaN. a) The MoS_2 Raman lines prove that the MoS_2 layer is preserved in the MBE process. b) The Raman GaN line is unchanged after the MBE GaN growth. The quality of the top MBE GaN appears in Raman spectra the same as the quality of the MOCVD GaN substrate.

After we worked out the N-rich MBE growth process for GaN, the aforementioned problems with the MoS_2 etch and GaN line broadening were overcome. Figure 43 demonstrates the Raman lines for the GaN/MoS_2 substrate and GaN/MoS_2/GaN trilayer when the top layer was grown by the N-rich MBE process. The MoS_2 modes are clearly present in the trilayer stack ("post-top GaN" curve). Some broadening of the MoS_2 peaks is present meaning that the MoS_2 quality is slightly affected in the growth process, but the presence of the robust MoS_2 layer stack is undisputable. The GaN mode of the trilayer stack (Fig. 43b, "post-top GaN" curve) is apparently unaffected by the MBE growth meaning that no deterioration of the top GaN layer is detectable by Raman.

8.3.2 TEM: Cross-sectional Study of GaN/ML-MoS2/GaN

The quality of the 3-D/2-D/3-D trilayer structure was studied with cross-sectional STEM. The STEM images are shown in Fig. 44. The bottom substrate is an *n*-GaN wafer grown by MOCVD by the NTT-AT company. Four molecular layers of MoS_2 are seen in the center of the TEM images. The crystal planes right above the MoS_2 stack are the GaN, which was deposited by a N-rich MBE process at CCDC ARL. The dark amorphous layer below the MoS_2 and above the GaN substrate was determined by EDX to be S. The presence of an amorphous S layer is an obstacle for the electron transport. The layer thickness is near 1.5 nm. It is thin enough for an HBT device to operate and show amplification. This S layer will need to be reduced or eliminated in the future as a part of the optimization of the performance of the HBT device.

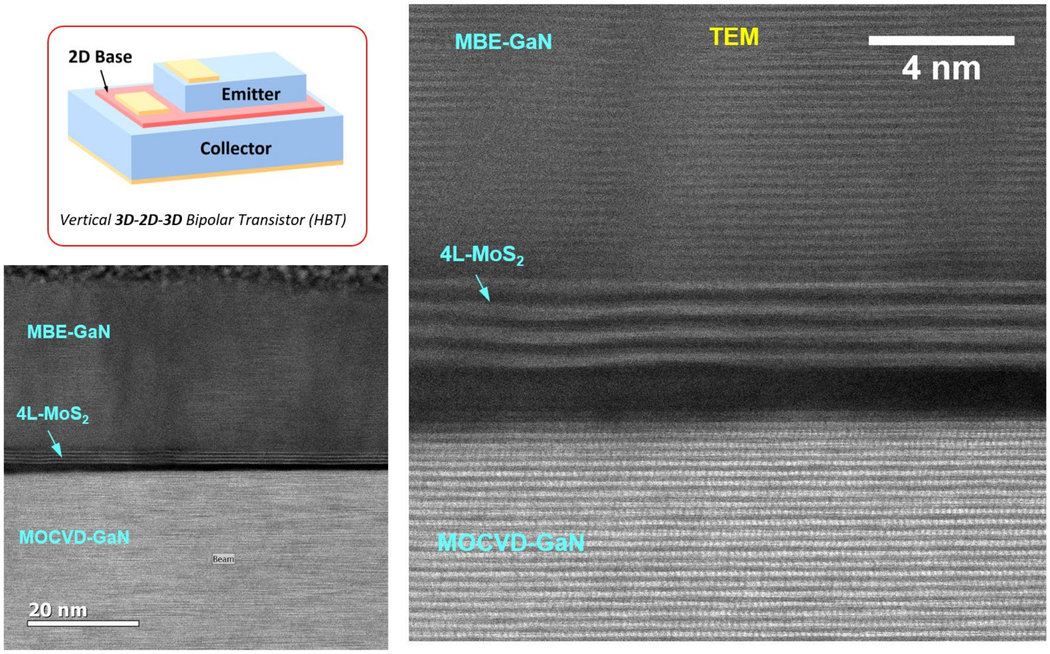

Fig. 44 The trilayer 3-D/2-D/3-D structure for HBT. (Top): The bipolar transistor schematic. (Bottom, right): TEM of the GaN/MoS_2/GaN heterojunction.

8.4 Summary

The STEM and other microstructural analyses confirm that we have synthesized the trilayer 3-D/2-D/3-D semiconductor structure, which can be used for the fabrication of a vertical 2-D/3-D HBT. We believe this is the first demonstration of a 3-D/2-D/3-D semiconductor heterostructure. This is an important step toward the implementation of 2-D crystals in high-speed electronic devices.

9. 2-D/3-D Bipolar Devices

9.1 The Microfabrication of the Devices

Our objective is to fabricate 2- and 3-terminal bipolar semiconductor devices. Specifically, we aim to make GaN/MoS_2 bipolar diodes and GaN/MoS_2/GaN HBT. The MoS_2 has to be of a few layer thickness in order for MoS_2 to sustain its bulk semiconductor properties in the device. To make an electrical contact to the base (MoS_2) of the HBT without applying the same potential to the collector (bottom GaN), we place SiO_2 insulating pads on the bottom GaN. In the Fig. 45, the metal pad M1 makes a contact to the bottom GaN substrate, the ring-shaped pad M2 is separated by SiO_2 from the bottom GaN and contacts the MoS_2 layer. In the HBT design in Fig. 45a, the pad M3 contacts the top MBE-grown GaN, which serves as an emitter.

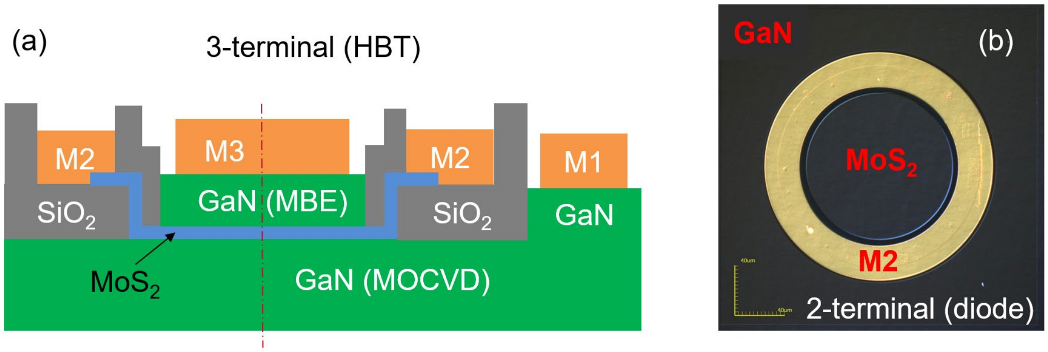

Fig. 45 a) Diagram of the cross section of the GaN/MoS_2/GaN HBT. b) Optical image of a fabricated GaN/MoS_2 diode. The scale bars are 40 µm.

After the SiO_2 pads are fabricated on GaN, we grow the MoS_2 by MOCVD as a blanket on all the substrate and let it go over the GaN substrate and SiO_2 pads. The metal contacts M2 to the MoS_2 will be placed at the locations where the SiO_2 pads are under the MoS_2. Thus, the collector is isolated from the base in the location where the contact to the base is made. For the 2-terminal devices, the fabrication is stopped at M2, and the top GaN and M3 are not made (Fig. 45b). M1 pads are made as large-area contacts to the GaN substrate at the corners of the wafer. The large area (>1 mm^2) of the M1 contact provides low contact resistance, which is negligible even if the contact is non-ohmic.

The microfabrication of devices starts with a 3-inch wafer of GaN (1-µm-thick, doped *n*/*n*+ via Si or *p* via Mg) deposited via MOCVD by NTT-AT (Japan) atop 500-µm *c*-plane SSP sapphire. The wafer is coated with protective layer of photoresist (AZ5214) soft baked at 110 °C for 2 min. Once the wafer has been diced into 10- × 10-mm pieces, the photoresist is washed away with acetone. A layer of approximately 200 nm of PMMA A4 is spun at 2000 rpm and baked at 180 °C. EBL (Vistec EBPG5000+ES) is used to create a marker layer defined in AutoCAD 2018LT. The pattern is developed in a 1:3 MIBK/IPA solution for 75 s. Blanket Ti metal is deposited at room temperature via electron beam evaporation (CHA) with a base minimum pressure of 1E-6 Torr. A liftoff process in a hot acetone bath at 50 °C for 1 h is used to remove the excess metal. Ti is used over other metals for two processing purposes. First, Ti metal has high contrast in the SEM/EBL to our GaN surface, which is essential to the marker layer. Secondly, Ti creates a thick oxide layer effectively making the metal inert for the later growth process.

A rigorous cleaning procedure is then performed. Substrate pieces are placed in a PRS3000 (Transene Company, Inc.) bath at 80 °C for 15 min followed by a new room temperature PRS3000 bath, which is sonicated for 5 min. Each piece is rinsed in a water bath followed by 5-min room temperature baths in acetone then IPA. AFM confirms the cleanliness of the GaN surface showing little to no photoresist residue and a clear picture of the GaN surface.

Once the substrates are cleaned, a plasma enhanced chemical vapor deposition (PECVD) process is used to deposit 100 nm SiO_2 at 250 °C (Plasma Therm 790+) with a deposition rate approximately 50 nm/min. We use 100-nm thickness for sufficient electrical separation from the MoS_2/GaN terminals and refraction of that thickness is useful for tools like Raman spectroscopy. Once deposited and cooled a layer of approximately 200 nm of PMMA A4 is spun at 2000 rpm and baked at 180 °C. EBL is used to define the SiO_2 mesa area, developed the same as described previously, then etched using a wet buffered oxide etch (6:1 hydrofluoric acid [HF]/ammonium fluoride [NH_4F]) with an etch rate of approximately 70 nm/min for 2 min and rinsed in water multiple times to halt the etch. The PMMA is removed with a hot acetone bath at 50 °C for 1 h. AFM confirms the height of the SiO_2 ring structure, as well as the roughness of the SiO_2 and GaN surfaces.

To assure a clean surface for MoS_2 deposition, the sample is boiled in Remover PG at 80 °C for 3 h and inspected with an optical microscope. Multiple rounds of Remover PG may be used if the surface is not clean. To confirm the quality of the surface, AFM is used to see the terraces of the GaN substrate and confirm no resist residues.

The samples are then sent to Kehao Zhang in the Prof Josh Robinson's group at PSU for MoS_2 growth via MOCVD as described in Section 7.2. Once the samples with the blanket MoS_2 layer are received back from PSU, we use the Ti alignment marks to pattern MoS_2 into circles and fabricate M2 ring metal contacts (see Fig. 42). Specifically, a layer of PMMA is deposited by methods mentioned previously. EBL is again used to define the mesa of the MoS_2, which is then etched using a reactive ion etch (RIE) (on Ulvac NE550e) using 30 sccm of chlorine (Cl_2) + 5 sccm of O_2 followed by a subsequent O_2 etch step to descum the resist top layer. In Chipara et al.,[131] this Cl_2 etch is developed to etch MoS_2 in a more clean manner than an O_2 etch alone or a CH_4+O_2 chemistry, which effects SiO_2, critical to device reliability.

The PMMA is then washed away with acetone and another layer of PMMA is deposited for the contact layer. EBL defines the contact layer and a blanket 15-nm Ti/85-nm Au metal (M2 in Fig. 42) is deposited via e-beam evaporation. In the work of Mazzoni et. al.,[132] they show the Ti/Au contact to MoS_2 to have the least contact resistance when performing transfer length measurements. A liftoff process of heated acetone removed excess metal from the pattern.

Considering the contact to the GaN substrate, ideally, metal–semiconductor contacts should be ohmic contacts; however, due to SBs/p-n junctions most contacts to semiconductors are non-ohmic. Using the resistance for a regular 3-D semiconductor, such as GaN, we can make a low-resistance non-ohmic contact by increasing the area A of the contact:

$$R_C = \frac{\rho_C}{A}, \tag{3}$$

where ρ_C is, likely non-ohmic, contact resistivity. For n-GaN wafers making the contact area A larger than 1 mm^2 is sufficient for the voltage drop on the M1 contact resistance to be negligible with respect to the voltage drop on the MoS_2/GaN diode. Thus, the M1 contact resistance can be neglected. For the p-GaN wafers, the electron energy band misalignment between p-GaN and metal resulted in larger contact resistance unless a specific recipe is used to produce the p-GaN "ohmic" contacts.[133] We note here that all our contacts to GaN wafers were strictly speaking non-ohmic. The "ohmic" recipe yielded contacts to p-GaN with greatly reduced resistances, which allowed us to neglect the back contact resistance in the analysis of the electrical properties of the devices. The "ohmic" recipe involved a nickel (Ni)(15 nm)/Au(85 nm) stack for the contact followed by a specific anneal. Additionally, the p-type carrier density was reduced in the p-GaN wafer during the MoS_2 MOCVD process due to the presence of the H_2 in the process. The lower carrier density resulted in higher back contact resistance (the resistance between M1 and the pGaN/MoS_2 interface of the diodes). Therefore, we used the Ni(15 nm)/Au(85 nm) structure for "ohmic" (low resistance) M1 and employed the anneal process described to reactivate p-carriers in the p-GaN wafer.

The first step to fabricate a low-resistance corner contact to GaN was to place a drop of photoresist (AZ5245) cured overnight on the device area. The resist is used as a mask for the device area. The same Cl_2 RIE etch is used on the outside of the device area to etch away and clean the GaN surface. Once the photoresist is removed, an Al foil mask is created to deposit large-area Ni/Au contacts on the corners of the device substrate. Ni/Au contacts were deposited following the recipe for the ohmic contacts to GaN.[133] The n-type GaN/p-type MoS_2 device can be tested as is and the p-type GaN/MoS_2 is annealed in an argon environment at 650 °C for 20 min to finish the ohmic contact fabrication and reactivate the p-carriers (Mg dopant) in the GaN lattice in the same anneal. Both p-GaN and n-GaN diode devices are ready now for testing.

9.2 Two-terminal Devices

MoS2/GaN diodes were microfabricated on GaN wafers of 1 × 1 cm size. Figure 46 shows optical images of the whole GaN wafer with 50 devices and an enlarged view of several devices. The blue circles represent working devices and black circles are corrupted devices due to the microfabrication problems. The gold ring is the top metal contact M2. The large M1 contacts to the GaN substrate are not imaged since they were placed in the corners of the wafer after the optical imaging.

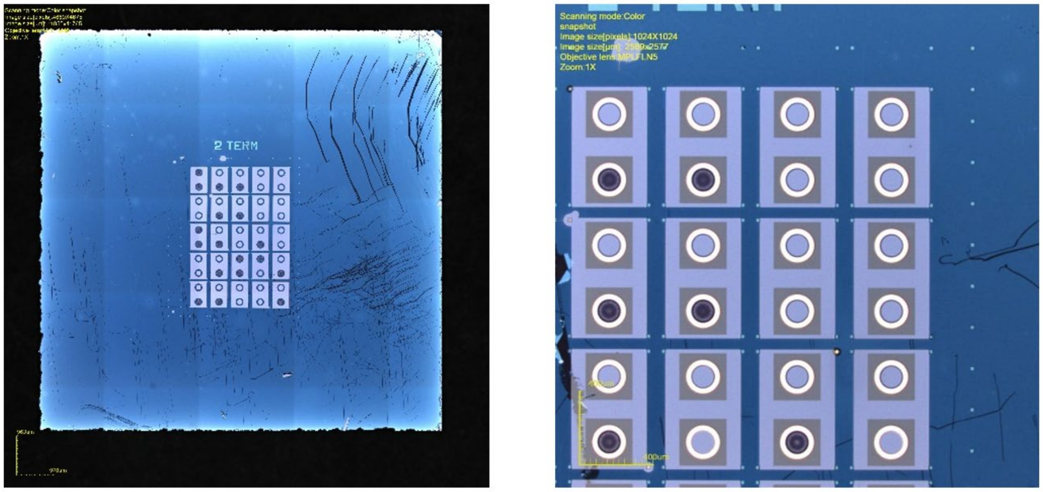

Fig. 46 Optical images of a *n*-GaN wafer with fabricated GaN/MoS$_2$ diode devices. (Left) Whole wafer (1 × 1 cm) with 50 diodes. (Right) Zoom-in on several devices. The horizontal spacing between the centers of circles is 500 µm.

Electrical testing of the diodes was done between the M1 and M2 contacts, denoted in Fig. 45. Representative I-V curves are shown in Fig. 47. The diodes of both polarities (*pn* and *np*) were fabricated using *n*-GaN and *p*-GaN wafers. As-grown MoS$_2$ is naturally *n*-doped, so that undoped MoS$_2$ was used on a *p*-GaN wafer. To create a *pn*-junction with *n*-GaN, p-doping of MoS$_2$ was required. To achieve the *p*-doping of MoS$_2$, a Mg precursor was added to the MOCVD system during the MoS$_2$ growth, as described previously.

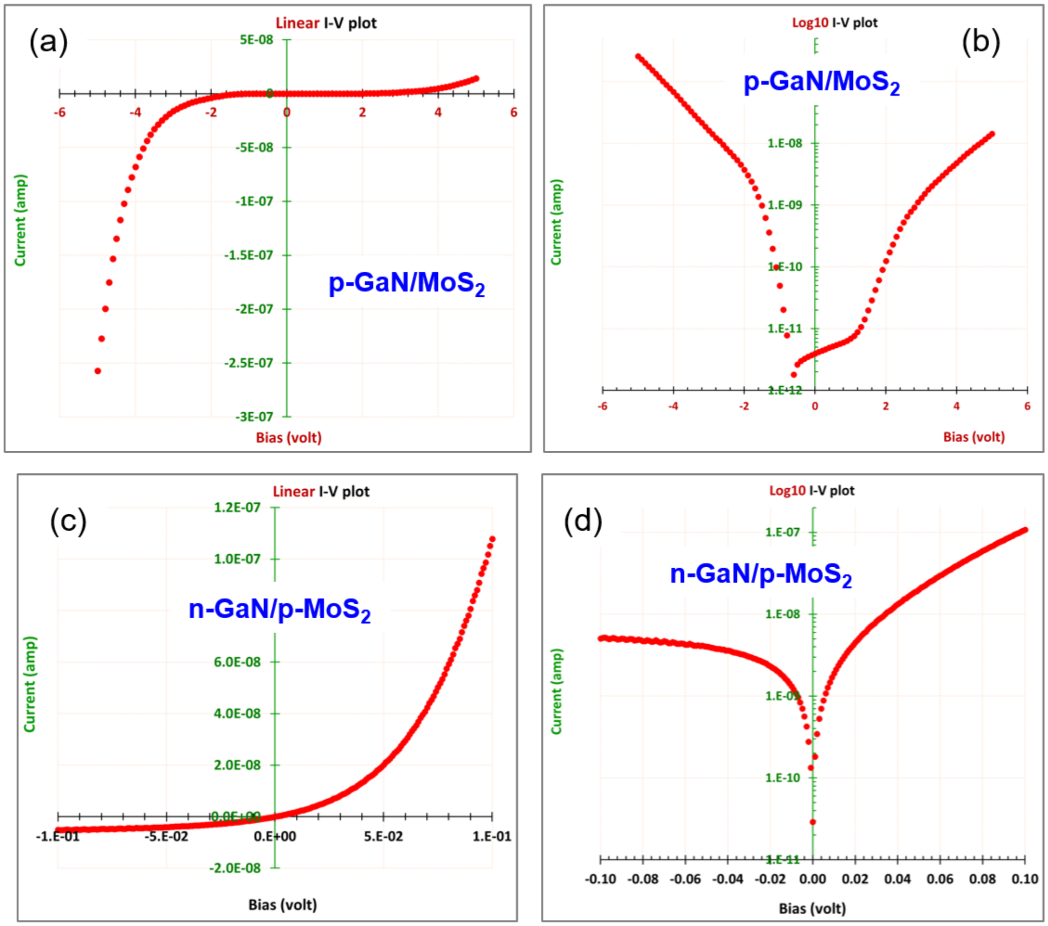

Fig. 47 I-V characteristics of the GaN/MoS$_2$ diodes. a) and b) *p*-GaN/MoS$_2$ diodes with unintentionally *n*-doped MoS$_2$. c) and d) *n*-GaN/*p*-MoS$_2$ with niobium (Nb)-doped MoS$_2$. a) and c) are linear I-V and b) and d) are log I-V.

The I-V curves for the *p*-GaN/MoS$_2$ diodes plotted on linear (Fig. 47a) and Log (Fig. 47b) scales show clear rectification. The bias axis corresponds to the electrical potential applied to the M2 ring electrode, thus the MoS$_2$ side of the *pn*-junction. Therefore, the observed rectification polarity corresponds to the negative potential on MoS$_2$ for the forward bias, as expected for the fabricated *p*-GaN/MoS$_2$ diode. The linear Log(I)-V segment on the forward bias (i.e., the stretch between –2 and –5 V on Fig. 47b), a relatively high degree of rectification, and low activation voltage indicate the *pn*-junction behavior as opposed to other physical mechanisms, such as SB rectification. The reason of the change of slope at –2 V on the log scale is not confirmed yet, but believed to be due to the non-ohmic back contact to *p*-GaN. The latter assumption is based on the thorough electrical characterization of the diodes made in the previous batches where the poor, non-ohmic contacts to *p*-GaN were making a considerable contribution to the I-Vs up to –5 V. Our efforts to decrease the resistivity of the M1/*p*-GaN contacts and bulk resistivity of *p*-GaN (described in the previous section) led to the decrease of this undesirable influence of the back contact down to –2 V, as shown in Fig. 47b.

The I-V curves for the *n*-GaN/*p*-MoS_2 diodes are plotted on linear and log scales in Fig. 47c and d. The *n*-GaN wafer consists of two GaN layers, where the top layer is doped n=1E16 cm^{-3} to create a *pn*-junction, and the bottom layer is doped n=1E19 cm^{-3} to provide low voltage drop on the substrate from M1 to the diode. The highly conducting GaN layer also provides low contact resistance M1/*n*-GaN. As the result, the distortions from the exponential behavior start only below 0.04 V for the *n*-GaN diodes and the distortions are less dramatic (compare Fig. 47d and Fig. 47b). Overall, the I-V displays rectifying behavior with the rectification direction characteristic to pn-junction, also displaying low activation voltage and exponential behavior above 0.04 V. These observations indicate again that our fabricated devices operate as *pn*-junction diodes. However, more testing is needed to ascertain this conclusion.

The importance of these results on 2-terminal 2-D/3-D bipolar devices is the following:

- These are the first (to our knowledge) working vertical bipolar 2-D/3-D diodes made from synthesized materials. Synthesized materials (as opposed to geological materials) allow for precise control on impurities needed for high-performance devices.
- The bilayer 2-D/3-D structures are grown as a stack, so that no mechanical transfer was involved. The mechanical transfer of 2-D crystals is commonly used in the scientific community to make devices from 2-D materials and results in contaminations, structural defects, and small sizes of the 2-D material available for devices. These drawbacks are currently a major obstacle that prevents 2-D devices made by mechanical transfer method from finding way in the commercial applications. On the other hand, our devices were synthesized and fabricated with the processes currently used in the semiconductor device industry.
- Our materials are uniform over the entire wafer (presently 1 × 1 cm). As the result, we fabricate large-size devices (over 100 μm in the diameter of the active area) to achieve larger device currents in the vertical geometry. Also the wafer scale of our materials allows to make 50 devices (Fig. 46a) at the same time and study the statistics of the electrical behavior and the trends related to the device sizes. For comparison, typical 2-D devices reported in the literature employ geological material sources and mechanical transfer and are limited to only a few small devices (<100 μm, often ~5 μm) per wafer.[134]

- Both polarities of *pn*-junction diodes are fabricated, *pn* and *np*, which demonstrates the versatility of our approach. Also both polarities are needed for the design of more complex bipolar devices.
- Our 2-D/3-D devices are not affected by the metal proximity because the metal contacts to 2-D are made on the side of the devices and the active 2-D/3-D junctions do not have metal pads on top of 2-D. Therefore, the metal proximity effects (i.e., when the metal/2-D/3-D junction behavior is affected by the metal/3-D junction due to the "electronic transparency" of ultrathin 2-D, as described in Section 6) are eliminated in our devices.
- Lithographical definition of 2-D/3-D microdevices with large contact pads allows the testing of them on a standard probe station without the need of nano-characterization tools, like CAFM or SEM nanoprobes (Sections 5 and 6).
- Vertical device geometry provides the potential for larger testing currents and short electron paths needed for fast operation.

9.3 Three-terminal Device

We described in Section 9.2 the microfabrication steps to produce 2-terminal 2-D/3-D diodes. To make a three-terminal bipolar transistor, we continue processing the chip. SiO_2 pattern is fabricated by EBL with PMMA, ion beam sputtering of SiO_2, and liftoff. Ion beam sputtering process produces dense dielectric films while maintaining a room-temperature deposition needed for the preservation of the EBL resist and 2-D layer, which is an advantage compared to the SiO_2 grown by a PECVD process. This pattern of SiO_2 is needed to serve as a hard mask during a subsequent GaN growth and etch. After the SiO_2 pattern deposition, only the areas are left open where the top layer of GaN is needed to be deposited to serve as the emitter of the HBT.

Next, high-quality GaN (doped *n* via Si or *p* via Mg) for the top third terminal in the HBT is grown by MBE in the Electro-Optics & Photonics Division of CCDC ARL. The MBE growth process is described in the Section 7.2. In order to etch the top GaN emitter above the base contacts, another layer of PMMA is put down. Next, an EBL patterning defines where we need to etch. While PMMA protects the central device area, the GaN at the periphery is etched using an RIE flowing 50 sccm of Cl_2 and 50 sccm of BCl_3 with a power of 500 W. The etch was calibrated with previous tests to provide an etch rate of 7.1 nm/s. SiO_2 under the GaN and above MoS_2 acts like a hard mask during GaN etch only etching approximately

0.02 nm/s, which helps us to accurately etch the correct amount of GaN. The chip is then cleaned with acetone at 50 °C for 1 h.

Another layer of PMMA is deposited to define the Ni/Au contact to the emitter, which is deposited using e-beam evaporation. A liftoff process removes leftover metal and a final layer of PMMA is spun onto the chip. The base contact layer is redefined using EBL, where SiO_2 is washed away from patterned PMMA areas using a buffered oxide wet etch.

An optical image of 3-terminal devices in the middle of the fabrication process are displayed in Fig. 48. The top GaN layer is still to be deposited. The 15 circles in the center will be the MoS_2 active areas of the transistors and the circles on the periphery will be the test structures needed to characterize various material parameters in the device components, such as leakage through dielectric, contact resistances, and so on.

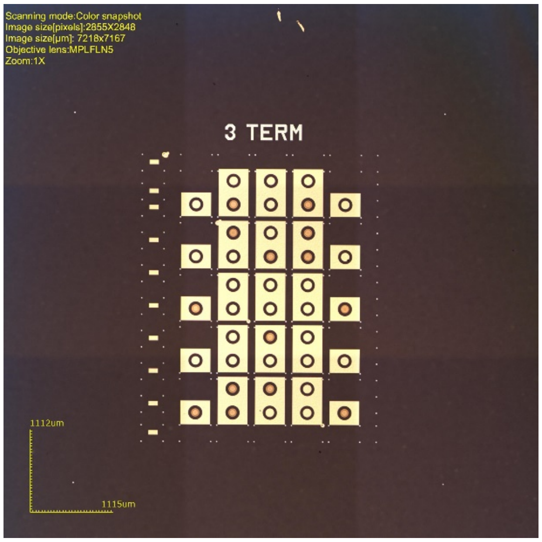

Fig. 48 An optical image of 3-terminal devices at the transitional stage of the fabrication process before the top GaN growth. The double-circled rectangles will contain 15 transistors and the single-circled rectangles are test structures. The horizontal spacing between the centers of circles is 500 µm.

The fabrication of 3-terminal devices is still work in progress and the first complete HBTs are expected to be fabricated in the next months.

9.4 Summary

We have developed a design and microfabrication process for making vertical GaN/MoS_2/GaN HBTs with an ultra-thin base made of 4–5 molecular layer MoS_2. We have validated all major critical aspects of the design, which makes it likely that our design and microfabrication process will produce a working HBT. In particular, 2-D/3-D diode behavior was demonstrated for the all-synthesized heterostructure without mechanical transfer. The np bipolar junctions were successfully implemented with unintentionally doped MoS_2 and *p*-doped GaN. Ohmic contacts to *p*-GaN were tested and carrier reactivation of holes in *p*-GaN was worked out at the process conditions compatible with the 2-D semiconductor. The *pn* bipolar junctions were successfully developed with *n*/*n*+ GaN and *p*-doped MoS_2. The development of the process of the Mg doping of MoS_2 was critical for this type of junctions.

Several properties of 2-D semiconductors were explored that are essential for fabricating complex semiconductor devices. Specifically, we demonstrated that SiO_2 pads can be used to separate the MoS_2 from the GaN substrate in the areas away from the active part, which allows us to create an electrical connection to the MoS_2 base, but not the bottom GaN (collector). Our tests showed that MoS_2 continuously bridges from the GaN substrate up onto the SiO_2 pads without the loss of electrical connection. The SiO_2 pads support the MOCVD growth of MoS_2 and at the same time maintain their integrity as electrical insulators. We have developed several candidate metals for the base contacts that must adhere to the 2-D layer and endure the subsequent MBE growth of GaN.

We have demonstrated the successful MBE growth of the top GaN layer in the trilayer 3-D/2-D/3-D stack (see Section 8). We have developed the doping process for the MBE GaN to produce the carrier density in the emitter desired for the successful operation of the HBT (n = 5E18 cm^{-3} for the *n-p-n* HBT).

Our project has targeted the fabrication of the 3-D/2-D/3-D HBT device. We have fabricated 70% of the devices up to the base layer and contacts. We have worked out most of the critical aspects of the device related to the novelty of this semiconductor system and fabrication process. The first completed HBTs are planned to be fabricated in a month or two, and a few more month would be needed to for the optimization of the HBT device components needed to achieve the amplifying behavior. It is still to be determined whether these new concept HBTs will actually display performance advantages as expected due to their unique qualities over the conventional 3-D semiconductor HBTs.

10. Additional Computational and Theoretical Studies

10.1 Applicability of Large-scale Atomistic Tool for 2-D/3-D Simulation

The epitaxial growth approach implemented for our MoS_2/GaN heterostructure growth is possible mainly due to the small in-plane lattice mismatch (<<2%) between the MoS_2 and GaN layers. This lattice mismatch at the interface and the interlayer vdW force between the layers, collectively, contribute to a small misorientation angle between MoS_2 and GaN during growth. These vdW interactions also contribute to the misorientation of layers during multilayer 2-D material growth. Though the misorientation between 2- and 3-D layers has never been observed in 2-D/3-D heterostructure due to complexity in characterization, we do anticipate a systematic but controllable variation in misorientation angle between the 2- and 3-D layers, a feature common in 2-D/2-D homo- and heterostructures. In the case of the 2-D materials, two lattices stacked with an arbitrary twisting angle form a periodic, or commensurate, structure at particular discrete angles. However, as the length of the periodic lattice vectors of the supercell grows exponentially with decreasing misorientation angle, going from a few 10's to 100's of atoms (angstroms to nanometers) for higher angles to several thousand atoms for smaller angles (multi-nanometer), the physical properties of misoriented heterostructure are sensitive to interfacial commensurability. Though these systems are intriguing for material of choice for both basic and applied applications, a fundamental study, using atomistic modeling, of the twist-angle-dependent features such as layer-to-interaction, band sensitivity, and band alignment are crucial in realizing their full potentials. Nevertheless, the explosive growth in the commensurate supercell size with decreasing misorientation angle limits the theoretical study of these materials with common ab initio codes such as VASP and Quantum Espresso (QE).

One of the key features of 2-D materials, such as MoS_2, WS_2, WSe_2, and so on, is their capability to transition from an indirect bandgap in the bulk to a direct bandgap as the material shrinks to a single layer. This is due to out-of-plane quantum confinement and layer-to-layer coupling. Additionally, these 2-D layered materials exhibit electronic and optical properties that depend upon interlayer vdW interactions brought about by the specific configurations from layer stacking and alignment.

Motivated by these factors, we have conducted a large-scale first-principles study of the electronic properties of the misoriented bilayer 2-D materials using the CP2K program (https://www.cp2k.org/). Using the highly efficient and scalable features of CP2K, the material and device related properties such as lattice parameters, vdW gaps, band levels, band offsets, electron affinity, and WFs as a function of the misorientation angles have been calculated and analyzed. This methodology allows us to apply accurate DFT calculations, as opposed to current state-of-the-art techniques that rely on extrapolation and fitting, to small-angle misoriented layers with thousands of atom unit cells and gives a path to multiscale structural to electrical properties studies necessary for designing materials with desirable electronic properties.

10.1.1 Method/Tools: CP2K

CP2K is an atomistic and molecular simulations tools software for solid, liquid, molecular, and biological systems. It contains a general framework that combines different methods such as DFT using a mixed Gaussian and plane wave approach (GPW) and classical method using many-body potentials. The linear scaling of self-consistent energy and force convergence in this method is achieved by using Quickstep method, which combines the advantages of two representations of the density in terms of Gaussians and plane waves (PWs). The PW implementation, which is also found in other popular tools such as VASP and QE, provides benefit by using a simplified calculation of Hartree potential and efficient conversion of real and reciprocal space representation of the electronic density using FFT. The hybrid approach combining localized and PW method results in reduced number of basis functions required in Kohn–Sham equations, and consequently, sparse Kohn–Shan Matrix, a feature suitable for handling larger systems.

For our study, we employed we employed a 1000 Rydberg energy cutoff, with the MOLOPT basis sets[135] (specifically; Mo: DZVP-MOLOPT-SR-GTH, S: DZVP-MOLOPT-GTH) and GTH pseudopotentials,[136–137] using the revPBE,[68,138] DFT with Grimme's D3,[139–140] and vdW correction. To speed up the simulation, orbital transformation (OT) diagonalization[141] was used. When computing the Fermi energies and molecular orbitals, a 300 K Fermi-Dirac smearing was used with no OT diagonalization. To maintain consistency and avoid any method or parameter dependent discrepancies during comparison, we have also employed similar methods for during VASP and QE simulations. For the VASP and QE simulations, we have employed PAW-PBE functional with Grimme-D2 method for vdW corrections. Convergence tests on energy cutoff, k-points, and screening parameters were performed to identify suitable parameters for our simulations.

10.1.2 Benchmarking

10.1.2.1 Structural Properties of vdW Materials

Structural properties such as lattice constants and vdW gap between the layers are crucial parameters that defines CP2K's applicability into the 2-D materials and their heterostructures domains. In the following sections, we provide a detailed comparison of the structural properties predicted by CP2K against the results from VASP and QE.

10.1.2.1.1 Lattice Parameters

In this study, we compare lattice parameters of single (1L), bilayer (2L), trilayer (3L), and bulk MoS_2 produced by CP2K, VASP, and QE and compare their results with available experimental data. Table 6 summarizes our findings.

Table 6 Lattice parameters comparison of VASP, QE, CP2K and experimental values. Experimental values are taken from Huang et al.[142]

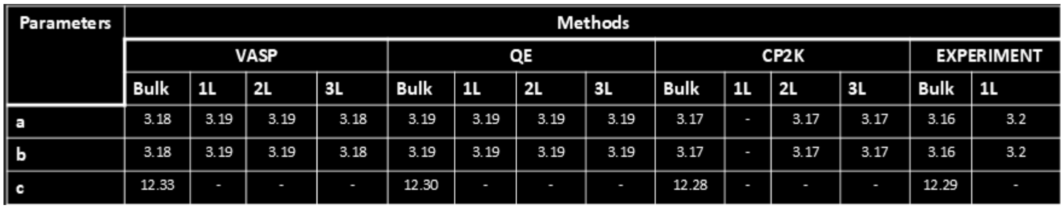

Parameters	Methods													
	VASP				QE				CP2K				EXPERIMENT	
	Bulk	1L	2L	3L	Bulk	1L	2L	3L	Bulk	1L	2L	3L	Bulk	1L
a	3.18	3.19	3.19	3.18	3.19	3.19	3.19	3.19	3.17	-	3.17	3.17	3.16	3.2
b	3.18	3.19	3.19	3.18	3.19	3.19	3.19	3.19	3.17	-	3.17	3.17	3.16	3.2
c	12.33	-	-	-	12.30	-	-	-	12.28	-	-	-	12.29	-

The bulk in-plane lattice constants (a and b) for MoS_2 produced by all three methods are consistent with the available experimental values. Particularly, the CP2K optimized in-plane lattice constants are closer to the experimental values. VASP and QE overpredicted in-plane lattice parameters. Overall, all three methods consistently predicted in-plane lattice parameters within ±1% of the experimental values for the bulk MoS_2. In addition, all the three methods successfully predicted out-of-plane lattice (c) constant within the ±1% of the experimental value. For the 1L system, all the three methods overpredict lattice parameters as compared to the experimental values. Though the experimental data for the multilayer MoS_2 are currently unavailable, it is evident from Table 6 that the CP2K method predicted parameters for these systems are consistent with VASP and QE. In conclusion, the CP2K method is capable predicting lattice parameters for bulk as well as layered 2-D materials.

10.1.2.1.2 vdW Gap

Layered 2-D materials and their heterostructures are characterized by their planar structures held together by strong in-plane covalent bonds and weak out-of-plane vdW forces. Because of their weak out-of-pane bonding, these materials are stacked together to form homogeneous as well as heterogeneous quantum layered system with atomically sharp interfaces between layers. The magnitude and characteristics of this layer-by-layer bonding is defined by the spatial separation between the layers, which is commonly known as vdW gap. Though it is purely a structural property, the vdW gap does influence other fundamental properties such as electronic, optical and transport properties of the multilayered 2-D/2-D, as well as 2-D/3-D, systems and allows researchers to explore novel collective quantum phenomena at the interfaces. So, correct prediction of vdW gap is a crucial requirement in achieving successful modeling of 2-D/2-D and 2-D/3 systems.

To test CP2K's capability in predicting vdW gap in homogeneous and heterogeneous 2-D materials, we have optimized three widely studied bilayer systems: a) bilayer graphene, b) graphene/h-BN, and c) 2L MoS_2 systems (Fig. 49). The simulated models are illustrated in the insets of Fig. 49. The spatial distance between the constituent layers is extracted as the vdW gap between the constituent layers. The resultant vdW gaps predicted by VASP, QE, and CP2K methods are plotted and compared with the available experimental vdW values.

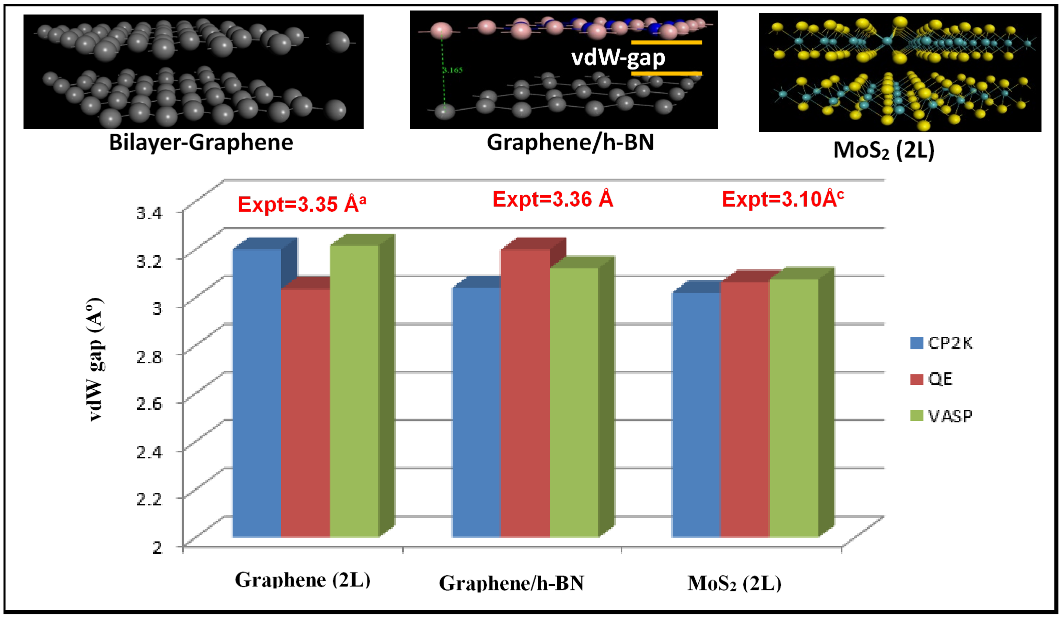

Fig. 49 vdW gaps for 2L, 3L, 4L, and bulk MoS_2 predicted by VASP, QE, and CP2K methods. Experimental values are taken from Zacharia et al.,[143] Pan et al.,[144] and Huang et al.,[142] respectively.

In the layered MoS_2 homogeneous bilayer system, all three methods predict the vdW gaps close to the experimental value. For the bilayer graphene and graphene/h-BN systems, all three methods underpredict the vdW gap, as compared to the available experimental data. For the bilayer graphene system, VASP and CP2K methods yield similar vdW gaps (i.e., ~3.15 Å), which is smaller than the experimental gap. The magnitude of the vdW gap predicted by QE for this system is 3 Å, approximately 10% smaller than the available experimental values. On the contrary, for the graphene/h-BN system, QE predicted vdW gap (3.15 Å) is larger than the gaps predicted by VASP and CP2K and closer to the experimental value of 3.36 Å. In summary, our comparative study of vdW gaps suggest that the CP2K method, which employs hybrid approach combining localized and PW methods, can consistently predict the vdW gaps in the various homogeneous and heterogeneous layered systems.

10.1.2.2 Electronic Properties of vdW Materials

The vdW semiconducting materials such as MoS_2, WS_2, and so on exhibit interesting electronic and optical properties. In particular, these layered materials manifest direct electronic gap, but transition into an indirect electronic gap materials when thinned down from the bulk to the monolayer form. The direct gap between VBE and CBE in the ML form occurs at K-point of the reduced BZ. On the other hand, the indirect gap in the multilayer system occurs between the VBE at Γ-point and CBE at K-point of the BZ. The indirect-to-direct transition of the energy gap characteristics is mainly attributed to the VBE edge movement at the Γ-point. The orbital characteristics of the VBE reveals that the majority of the contribution to the edge states comes from the z-component of *p* orbitals in the S atoms. These out-of-plane orbitals at the VBE extend beyond the surface plane and are quite sensitive to the proximal layer. In addition to the VBE, interlayer interaction also influences the energy gap (E_{gap}), vacuum energy level, and intrinsic Fermi energy level of the multilayered system.

To examine the capability of CP2K in predicting layer-dependent electronic properties of vdW materials, we have calculated self-consistent charges and corresponding electronic states at the Γ-point. Resultant states are then used to extract the VBE, E_{gap}, and work function (Φ), which is defined as the energy difference between the Fermi-level and the vacuum energy level. The VBE and E_{gap} for 1L, 2L, 3L, and 4L MoS_2 are tabulated in Table 7.

Table 7 Layer-dependent VBEs and E_{gap} at Γ-point for MoS_2

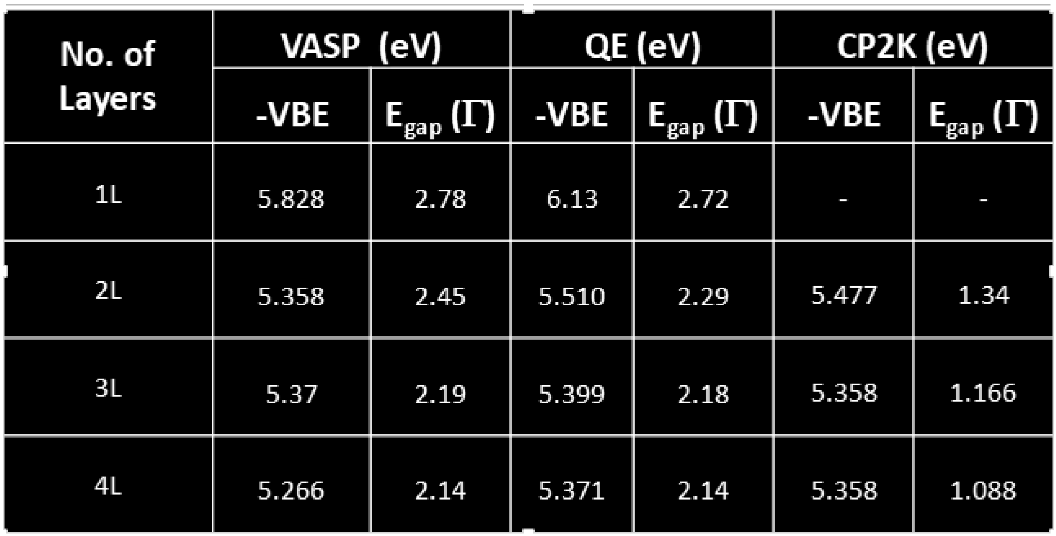

No. of Layers	VASP (eV)		QE (eV)		CP2K (eV)	
	-VBE	E_{gap} (Γ)	-VBE	E_{gap} (Γ)	-VBE	E_{gap} (Γ)
1L	5.828	2.78	6.13	2.72	-	-
2L	5.358	2.45	5.510	2.29	5.477	1.34
3L	5.37	2.19	5.399	2.18	5.358	1.166
4L	5.266	2.14	5.371	2.14	5.358	1.088

It is noted that, due to the limited implementation of the full BZ electronic structure calculation in CP2K, for this comparative study, we are limited to the Γ-point calculation. As stated previously, the CBE at K and VBE at Γ contribute to the fundamental indirect energy gap in the multilayer 2-D materials. Although we can access energy levels only at the Γ-point using the CP2K method, we can approximate the fundamental energy gaps in these systems using the energy difference (ΔCBE) between the CBE at G and K points from our VASP and QE calculations. The ΔCBE remains nearly constant at around 1 eV for all the multilayer system, including the bulk system.

For the 1L MoS_2, the simulations from the CP2K did not result in converged charge during the self-consistent calculation. However, for the VASP and QE resulted in similar values of VBE and E_{gap} at Γ. The quantitative difference in the VBE is mainly due to the difference in the predicted vacuum levels. For multilayer systems, the VBE and E_{gap} decreases with the increasing number of layer mainly due to diminishing out-of-plane confinement. For the VASP and QE, the E_{gap} varies from 2.45 to 2.14 eV and 2.29 to 2.14 eV. Though E_{gap} values initially differs by 0.30 eV for the 2L system, it converges to 2.14 eV for the 4L system. Though similar converging behavior is also observed for the CP2K predicted E_{gap} values, the magnitude of E_{gap} is consistently approximately 1 eV smaller than the VASP and QE predicted values. The lower values of the E_{gap} in CP2K, as compared to VASP and QE values, could be due to lack of full BZ charge integration feature during the electronic structure calculation. Since the electronic structure calculations are limited to G-point, the energy bands from other higher symmetry points, including K-point, fold at the Γ-point. The folded bands interact and repulse at the Γ-point, leading to upshift (downshift) of the VB (CB) energy states, and hence, resulting in the reduced E_{gap} values at the Γ-point.

In addition to the energy gap and VBE calculations, we have also calculated layer-dependent work function, Φ for the multilayer systems. The Φ for solid-state systems are mainly defined by their surface properties, particularly dangling bonds and associated dipoles at the surface. Since these layered systems are inert and lack dangling bonds at the surface, Φ should be independent of the number of layers. As can be seen in Table 8, though the magnitude of the Φ changes with the increasing layer count, the change is nonsystematic. Quantitatively, the Φ values predicted by VASP is higher than the values predicted by both the QE and CP2K methods. Regardless of the methods in use, the Φ varies with the thickness of the surface in these layered multilayer systems and exhibit an oscillatory behavior, similar to the nonlayered semiconducting systems. This is mainly due to the quantum oscillation of the Fermi-level of the systems resulting from the variation of the depth of the "effective potential".[145]

Table 8 Layer-dependent work function, Φ for MoS_2

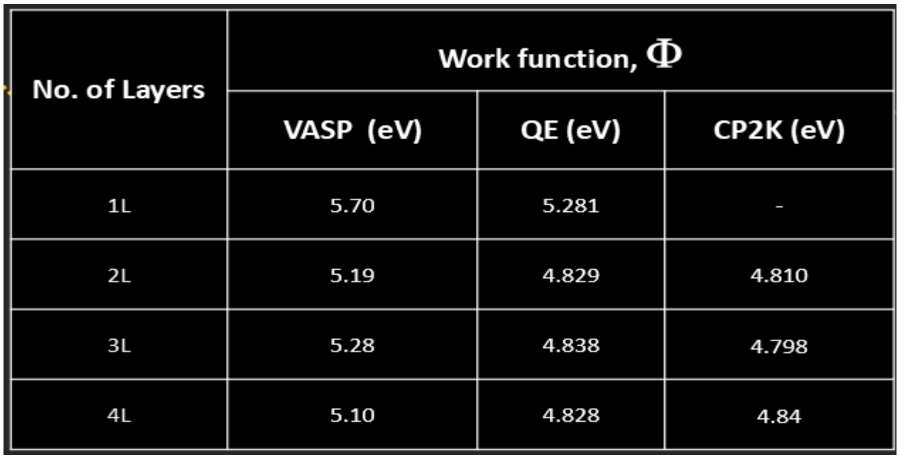

No. of Layers	Work function, Φ		
	VASP (eV)	QE (eV)	CP2K (eV)
1L	5.70	5.281	-
2L	5.19	4.829	4.810
3L	5.28	4.838	4.798
4L	5.10	4.828	4.84

10.1.3 Case Study: Misoriented 2-D Heterostructure

10.1.3.1 Introduction

A feature common among all 2-D materials consisting of a hexagonal lattice structure is that when layers are stacked together, either by mechanical stacking or epitaxial growth, a relative rotation between the layers is introduced due to inter-layer vdW forces. Misorientation between the layers is an additional degree of freedom in assembling vdW heterostructures for our functional needs. The electronic properties of these misoriented heterostructures often sensitively depend on interfacial commensurability. The commensurability between the layers is achieved by twisting layers at particular discrete angles known as magic angles. The size of the commensurate supercell heterostructure is inversely proportional to magnitude of the magic angle. We have designed commensurate misoriented MoS_2 using the method described in[146] and recently used in graphene/graphene[147–148] and graphene/MoS_2 and MoS_2/MoS_2 studies.[149] One of the model misoriented MoS_2 bilayer system used in this study, along with an AB-stacked (oriented) MoS_2 bilayer, is illustrated in Fig. 50. The misoriented angles (total atoms) considered in this study ranges from 2° (2383 atoms) to 27° (78 atoms). Due to the hexagonal lattice symmetry in 2-D materials, the clockwise rotation of 0° to 30° between the layers is analogous to anticlockwise rotation of 60° to 30°. Because of the limited scaling feature and computational efficiency, the simulations with VASP and QE are limited to three angles: 27°, 21°, and 13°, and results from these simulations, are used for comparison against the results from CP2K.

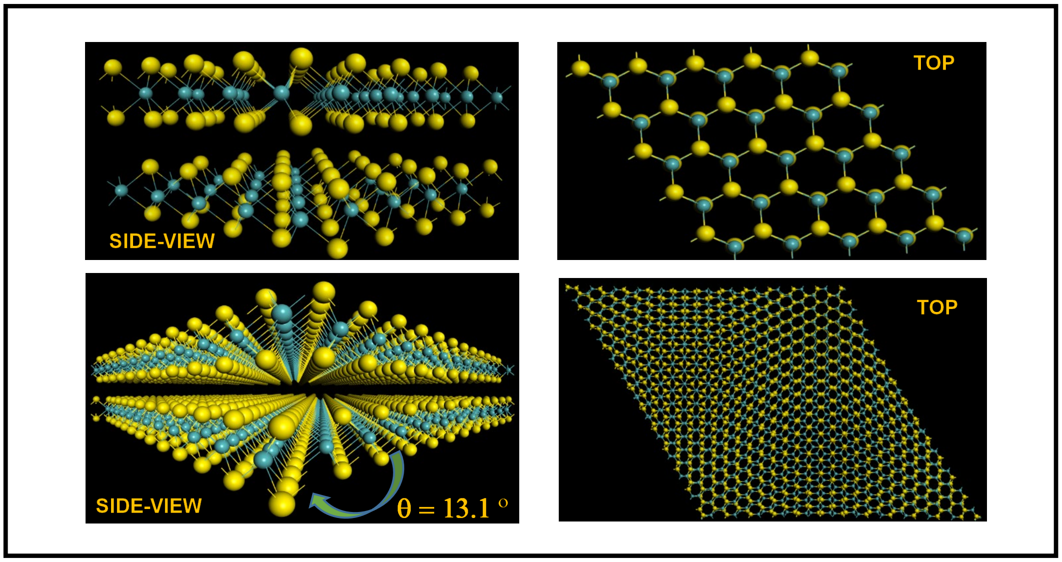

Fig. 50 AB-stacked (oriented) bilayer a and misoriented bilayer MoS_2 models. Side and top views are illustrated side by side for visual clarity.

10.1.3.2 Results

In light of recent experimental report by van Der Zande and group, in their experiment, have attributed the shift in VBE energy levels at Γ to the variation in the fundamental indirect gap of the misoriented MoS_2.[150] Motivated by this, we systematically analyze the fundamental electronic properties (VBE and E_{gap} at Γ-point) of the misoriented MoS_2 bilayer system and make an attempt to establish a theoretical correlation between the misorientation angle and electronic properties. The misoriented angle (θ) dependent electronic properties are tabulated in Table 9. As in the unrotated MoS_2 bilayer system, the edge states contributing to E_{gap} Γ in the misoriented bilayer systems are susceptible to interlayer coupling. For the first three angles, the values of VBE and E_{gap} (Γ) predicted by all three methods are within 1.5 ± 0.1 eV. For the angle that is less than 5°, the E_{gap} (Γ) decreases as a function of the θ, going from 1.435 to 1.282 eV. Recent experimental study attributes this reduction in the E_{gap} (Γ) to the rotation induced reduction of interlayer distance between the layers.[151] Since the distance between the layers is proportional to the magnitude of the interlayer vdW coupling, stronger coupling between the layers results in the band splitting of band edges around Γ-point, and hence the reduction in the E_{gap} (Γ) Furthermore, due to the repeated unit cells in the misoriented models, the bands folds into Γ-point contributing to the further reduction in the direct energy gap at Γ.

Table 9 VBE and energy gap at Γ-point (E_{gap}) as a function of misorientation angle (θ) for the misoriented MoS_2 bilayer systems.

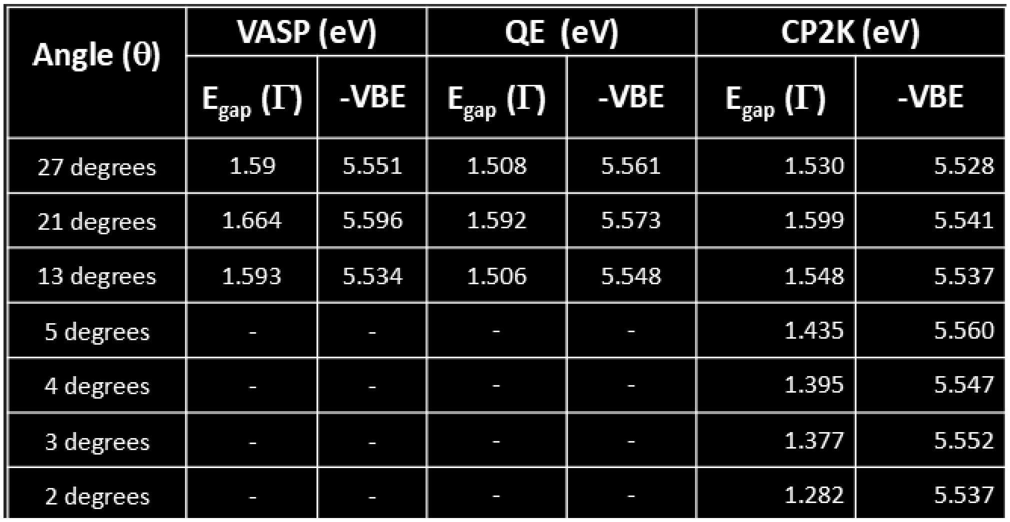

Angle (θ)	VASP (eV)		QE (eV)		CP2K (eV)	
	E_{gap} (Γ)	-VBE	E_{gap} (Γ)	-VBE	E_{gap} (Γ)	-VBE
27 degrees	1.59	5.551	1.508	5.561	1.530	5.528
21 degrees	1.664	5.596	1.592	5.573	1.599	5.541
13 degrees	1.593	5.534	1.506	5.548	1.548	5.537
5 degrees	-	-	-	-	1.435	5.560
4 degrees	-	-	-	-	1.395	5.547
3 degrees	-	-	-	-	1.377	5.552
2 degrees	-	-	-	-	1.282	5.537

For a bilayer MoS_2 system, the VBE states at Γ are derived from out-of-plane p_z and dz^2 orbitals from S and Mo atoms, respectively, and are sensitive to the out-of-plane interlayer coupling. Though the orbital characteristics of the VBE states at Γ in a misoriented MoS_2 bilayer system are similar to that of an unrotated counterpart, the energy levels associated with these states exhibit nonmonotonic fluctuation with the decreasing θ. When the θ is between 10° and 30°, the VBE energy levels remains within 5.5 ± 0.03 eV. However, as the θ decreases below 10°, the VBE energy level decreases with the decreasing angle. This observed nonmonotonic fluctuation of the VBE energy level, with the θ, is consistent with the ARPES and PL measurements by Yeh et al.[152] In this pioneering study, researchers also identified a need for a comprehensive simulation study that can correlate θ to the observed relative shift in VBE, as compared to the unrotated system. Motivated by this, we evaluated the relative shift in VBE (ΔVBE), defined as the energy difference between the VBE energy levels of unrotated and misoriented MoS_2

bilayer systems. The magnitude of the ΔVBE determines the interlayer coupling strength. If the value of ΔVBE is larger, the layer should behave as two isolated layers and preserve their electronic properties. Consequently, smaller ΔVBE indicates strongly coupled layers behaving like an isolated unrotated bilayer system. The obtained values of the ΔVBE as a function of θ is plotted in Fig. 51. The ΔVBE increases linearly with the increasing θ and reaches a maximum value at 0.755 eV at 5.1°, an indication of weakening interlayer coupling between the layers. However, as the θ increases beyond 5.1°, ΔVBE decreases with the decreasing θ and converged to a value closer to the VBE energy level of unrotated bilayer system. Observed bimodal dependency of VBE, as a measure of interlayer coupling, on misorientation angle is consistent with the PL and ARPES measurements on misoriented MoS_2 in Yeh et al.[152]

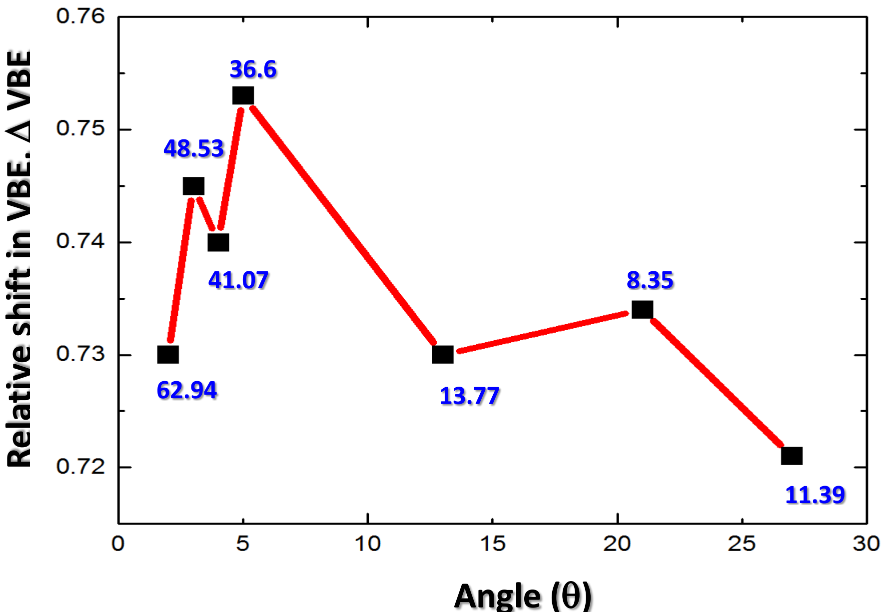

Fig. 51 Relative shift in VBE as a function of misorientation angle (θ) misoriented MoS_2 bilayer systems

In addition to the VBE and E_{gap} (Γ), we have also calculated θ dependent WF Φ of the misoriented MoS_2 bilayer system. The results are in Table 10. As discussed earlier, Φ is mainly influenced by the dipoles resulting from the charge reconfiguration at the surface. In addition to negligible real space strain between the layers in these homogeneous misoriented MoS_2 bilayers systems, the reciprocal space momentum space mismatch between the layers exist due to lattice misorientation, particularly for the larger angles. The coupled effect of minimal strain and momentum mismatch minimizes charge transfer and states hybridization between the layers, leading to minimal dipole fluctuation. The insensitiveness of Φ to the larger interlayer misorientation angle can be inferred from the Table 9.

However, when the θ decreases below 13°, the Φ increases due to the real space momentum mismatch reduction, which prompts charge transfer between the layers.

Table 10 WF (Φ) as a function of misorientation angle, periodic lattice vector, and number of atoms in the supercell for the misoriented MoS_2 bilayer systems

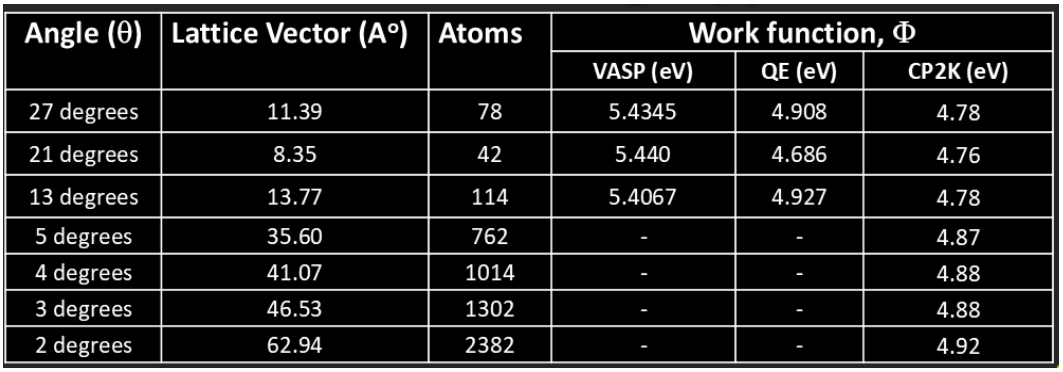

Angle (θ)	Lattice Vector (A°)	Atoms	Work function, Φ		
			VASP (eV)	QE (eV)	CP2K (eV)
27 degrees	11.39	78	5.4345	4.908	4.78
21 degrees	8.35	42	5.440	4.686	4.76
13 degrees	13.77	114	5.4067	4.927	4.78
5 degrees	35.60	762	-	-	4.87
4 degrees	41.07	1014	-	-	4.88
3 degrees	46.53	1302	-	-	4.88
2 degrees	62.94	2382	-	-	4.92

Interestingly, the Φ exhibit weak dependency to the commensurate lattice vector, a real-space distance between the Moire patterns in the commensurate supercell. These Moire patterns in hexagonal bilayer system are formed when two identical atoms from the constituent layers are overlaid with a relative twist and give rise to the periodic charge fluctuation in the surface. Consequently, Moire pattern induced local charge oscillation shifts the vacuum energy level, which in turn results in higher Φ. Furthermore, a larger commensurate lattice vector means sparse Moire patterns and minimal charge fluctuation, and hence large Φ.

10.1.4 Summary and Conclusion

In this study, we have performed a method validation study of large-scale DFT method (i.e., CP2K by analyzing structural and electronic properties of the layered homogeneous and heterogeneous 2-D materials). At first, a comparison of the structural parameters predicted by CP2K method for various 2-D bilayer systems was made against the available experimental data and results from other established theoretical methods, such as VASP and QE. The in-plane lattice parameters predicted by CP2K method were consistent with other methods and were within ±5% of the available experimental parameters. Though the vdW gaps between the layers predicted by all three methods were similar, these values were systematically lower than the experimental values. Following the structural properties study, we have performed layer-dependent study of electronic properties of multilayer MoS_2. Since the k-point implementation of the charge integration in CP2K is limited to the Γ-point, we have limited our study to the analysis of the two key device-related electronic properties, namely VBE and E_{gap} at Γ-point and Φ. All the three methods consistently predicted an oscillatory fluctuation of VBE and Φ, when the thickness of the system varied from a monolayer to a quadlayer. The observed thickness dependent oscillating feature of electronic properties in layered 2-D materials was similar to the one previously reported for conventional semiconducting materials such as Si, gallium arsenide (GaAs), and so on.

Finally, utilizing the scalability feature of CP2K, we have also performed a systematic study of misorientation dependent electronic properties of the experimentally observed misoriented MoS_2 bilayer system. The VBE and E_{gap} at Γ-point exhibit a non- nonmonotonic bimodal characteristics as a function of θ with global minima 0° and local minima between 20° and 30°, an indication of varying interlayer coupling in the misoriented angle range. Similar nonmonotonic dependency of Φ was also observed during the systematic variation of θ between 0° and 30°. We have also established a linear correlation between the length of the commensurate lattice vector and the shift in VBE in the misoriented MoS_2 bilayer system, while ascribing this relationship to the density of Moire pattern induced charge fluctuation at the surface.

In conclusion, the scalable CP2K method is capable of predicting structural properties of 2-D homogeneous and heterogeneous materials within the experimental error margin. In addition to the fundamental lattice parameters of a larger structurer, it is highly suitable for other device related structural properties in 2-D materials systems, such as defect/dopant formation energy, layer binding energy, and layer–substrate interaction energy. However, because of the limited implementation of BZ integration during electronic structure calculation, the electronic properties calculations are only limited to Γ-point of the BZ, limiting its applicability to the parameters, such as band edges at the Γ-point, energy gap at Γ-point, and WF.

10.2 Study on the Effect of GaN Surface Termination in a 2-D/3-D Heterostructure

GaN substrate used as the 3-D layer in a 2-D/3-D heterostructure can be grown using various experimental techniques, such as vapor phase epitaxy (VPE), MBE, and MOCVD. The surface morphology and crystallinity of GaN layers during growth is modified by the experimental growth condition. Regardless of the growth condition, GaN grown planes have a polar configuration (i.e., either Ga or N-polar) based on the surface termination type. A fundamental understanding of the electronic properties of these polar nitride surfaces is crucial for their application into the high-frequency, high-power devices. Furthermore, the surface termination types and degree of surface polarity of GaN surface can have important effects in the structural and electronic properties of the MoS_2/GaN heterostructure. The most common surface types are 1) Ga-terminated GaN (0001) and 2) N-terminated GaN

$(000\bar{1})$. The Ga-terminated GaN (0001) is well understood and widely used in high-power, high-frequency applications because of their interesting properties, such as direct bandgap, high electron mobility, and higher surface conductivity. Though relatively lesser-known, the N-terminated GaN $(000\bar{1})$ also possesses interesting electronic and optical properties.

Over the years, we have demonstrated a successful growth of MoS_2 on Ga-terminated-GaN surface forming MoS_2/GaN epitaxial heterostructures and characterized their structural, electronic, and transport properties. Although MoS_2/GaN is an interesting 2-D/3-D heterostructure system with many possible applications requiring staggered TYPE-II band alignment, the envisioned vertical device geometry requires 3-D/2-D/3-D heterostructure systems that require an additional layer of GaN growth. An additional layer of GaN growth on top of the MoS_2/GaN heterostructure is a complicated process involving complex growth process. Because of the limited information on the interfacial properties of GaN/MoS_2/GaN heterostructure, experimental characterization and theoretical modeling remains a challenge. In general, the sequence layer-by-layer growth during heterostructure growth should not affect overall structural and electronic properties of the resultant heterostructure. However, for the heterostructure system containing polar GaN materials, the growth ordering plays an important role in defining the type of surface termination at the interface. Motivated by these factors, we perform an atomistic study of MoS_2/N-terminated-GaN$(000\bar{1})$ heterostructure, a system analogous to the GaN/MoS_2 component in the GaN/MoS_2/GaN heterostructure and analyze its structural and electronic properties.

10.2.1 Model: Ga- and N-terminated GaN Substrates

The GaN crystal is of wurtzite-type crystal structure and belongs to hexagonal crystal system consists of tetrahedrally coordinated Ga and N atoms that are stacked in ABAB pattern. Using the optimized bulk lattice parameters and discussed in detail in the Section 5.6.1, a Ga- and N-terminated supercell is created by repeating along (0001) and $(000\bar{1})$ directions, respectively. The atomistic models of bare and passivated N-terminated GaN surfaces are illustrated in Fig. 52. Bottom surface of the N-terminated GaN surface is passivated to maintain a valence charge balance and avoid interface states in the energy gap.

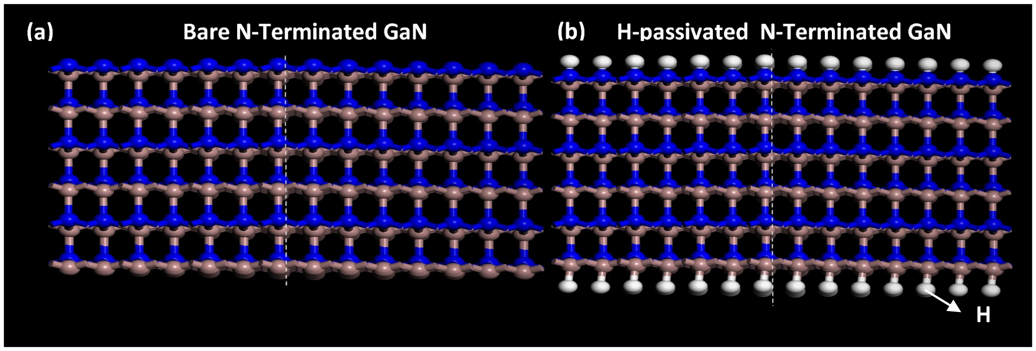

Fig. 52 Models of GaN surfaces. a) Bare N-terminated GaN (000$\bar{1}$) and b) passivated N-terminated GaN (000$\bar{1}$) surfaces models

10.2.2 Method

The dangling bonds at the N-terminated bottom layer were passivated by pseudo-H atoms with a charge of 1.25E in order to prevent an unphysical charge transfer between the top and the bottom slab surfaces. The upper three bilayers of N-terminated GaN (0001) were allowed to relax, while the bottom three bilayers, and saturating H atoms, were fixed to mimic the bulk substrate. A vacuum spacing of 20 Å was added along the *z*-axis for all the structures to minimize spurious interaction due to periodicity. MoS_2/N-terminated GaN model is created using the optimized N-terminated GaN model and combining it with MoS_2 single-layer system by following the procedure discussed in the Section 5. All the VASP (DFT) parameters are similar to the one used in our earlier study on MoS_2/Ga-terminated GaN system.

10.2.3 Results

10.2.3.1 Structural Properties

As part of structural properties study, we have analyzed MoS_2 registry on N-terminated GaN substrate by sliding MoS_2 layer in the in-plane direction and forming three different configurations: a) N-top, b) bridge, and c) Ga-top. These configurations are illustrated in Fig. 53. In the N-top configuration, the S atoms in the MoS_2 layer are directly above the surface N atoms. The bridge configuration is formed when the S atoms in the MoS_2 layer are located in between the surface N atoms and Ga atoms from the second layer. Similarly, for the Ga-top configuration, S atoms in the MoS_2 layer are directly above the Ga atoms from the second layer. Since the chemical composition in each of these configurations remains constant throughout the physical translation from “N-top” to “Ga-top” configuration, the energy contribution to that leads to the variation in the total energy mainly comes from the vdW force (energy) between surface S and N atoms. The MoS_2 layer encounters identical potential energy surface (PES) barriers while transitioning from "N-top" to "bridge" and "bridge" to "Ga-top" configuration on the GaN $(000\overline{1})$ surface. This correlates well with the equidistant physical translation undergone by the MoS_2 layer while transitioning from the "N-top" to "bridge", and finally, to the "Ga-top" configuration. This is an indication that the out-of-plane registry of MoS_2 on GaN substrate is mainly governed by the vdW force between the MoS_2 layer and GaN surface.

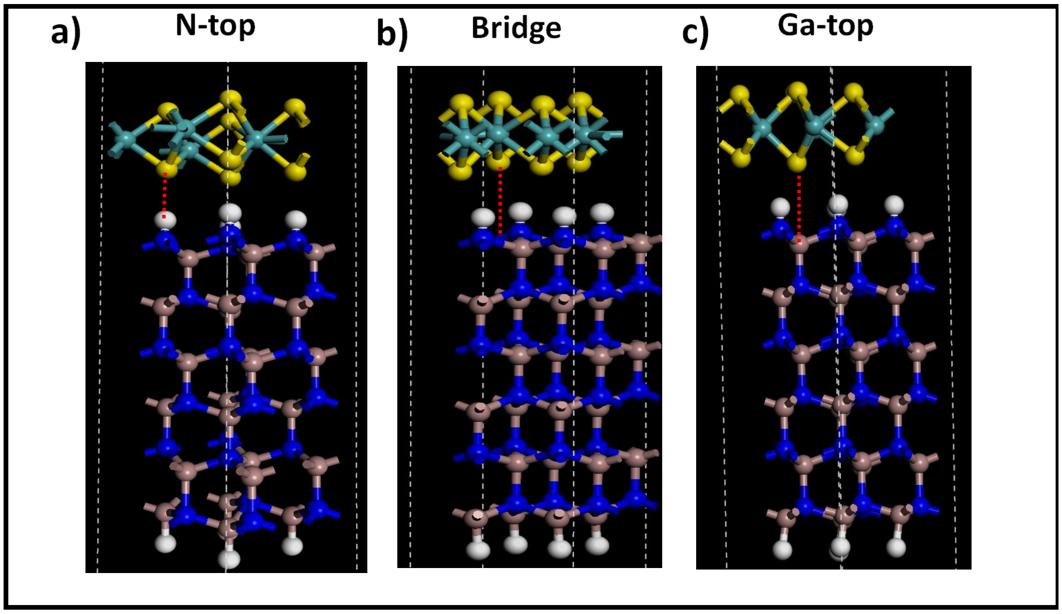

Fig. 53 Out-of-plane registries between the MoS_2 and N-terminated GaN $(000\overline{1})$ surface. a) "N-top" configuration, b) "bridge" configuration, and c) "Ga-top" configuration. Dotted (red) lines indicate vertical registries between S atoms and atoms in the GaN $(000\overline{1})$ surface.

To identify the stable structural configuration and optimized vdW-gap between the MoS_2 and N-terminated GaN substrate, we systematically varied the physical separation between the layers and observed their total energies. The total energies are then normalized to obtain per atom total energies in order to compare these results to the MoS_2/Ga-terminated GaN total energies and plotted in Fig. 53. The per-atom total energies as a function of vdW-gap distance between 2.5 to 3.5 Å for all three configurations are plotted in Fig. 54. For all the vdW distances less than or equal to 2.6 Å, the per-atom total energy for the Ga-top configuration remains lower than the bridge and N-top configurations. The total energies for the N-top configuration remains higher than both the bridge and Ga-top configurations because the N-S interaction is repulsive in nature, contributing to the total energy. Overall, the Ga-top configuration of the MoS_2 layer on N-terminated GaN $(000\overline{1})$ configuration is comparatively stable than the bridge and N-top configurations.

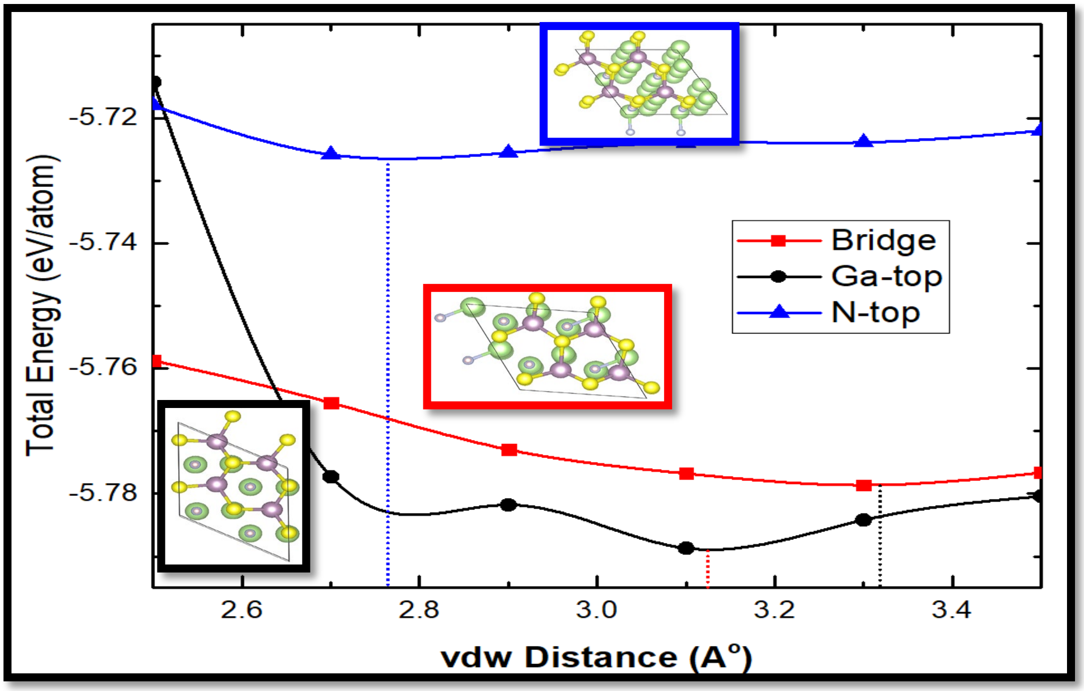

Fig. 54 **Total energies for varying vdW distance (d_{vdW}) between the MoS_2 on N-terminated GaN ($000\bar{1}$) surface for "N-top" (blue), "bridge" (red), and "Ga-top" (black) configurations. Insets illustrate top-down views of these registry configurations. The vertical dotted lines represent the optimized vdW distances at which the total energies are minimum.**

Similar to the MoS_2/Ga-terminated GaN (0001) surfaces, the layer-by-layer epitaxial growth of MoS_2 on N-terminated GaN ($000\bar{1}$), the structural parameters such as lateral spacing and alignment between the layers are mainly defined by the repulsion between the interface atoms mainly caused by the vdW force between interface atoms and their cumulative covalent radii. In our MoS_2/GaN ($000\bar{1}$) heterostructures, S, N, and Ga atoms are the interface atoms with atomic radii of 1.05, 0.71, and 1.22 Å, respectively. Since the sum of radii between S and N atoms is lower than the S and Ga atoms, d_{vdW} for the "N-top" configuration is expected to be lower than the "G-top" configuration. As can be seen in Fig. 54, the d_{vdW} value is slightly larger for the "Ga-top" configuration, as compared to the "bridge" and "N-top" configurations. The quantitative values of d_{vdW} for "N-top", "bridge" and "Ga-top" configurations are 2.77, 3.31, and 3.11 Å, respectively. In conclusion, the larger d_{vdW}, due to the smaller repulsive forces between the interface atoms, between MoS_2 and GaN ($000\bar{1}$) in the "Ga-top" configuration contributes to the stable MoS_2/GaN ($000\bar{1}$) heterostructure, which is consistent with the results from the total energy calculation.

10.2.3.1 Electronic Properties

Using the stable GaN (000$\bar{1}$) surface and MoS$_2$/GaN (000$\bar{1}$) heterostructure, we have performed electronic structure calculations using PBE level of theory. Though the DFT with LDA and PBE exchange correlations are known for their underestimation of the magnitude of the fundamental energy gap in semiconducting systems, these methods successfully capture overall feature of the electronic structure in these systems. The electronic structures predicted by the PBE level of theory for the N-terminated GaN (000$\bar{1}$) and MoS2/GaN (000$\bar{1}$) heterostructure is plotted in Fig. 55.

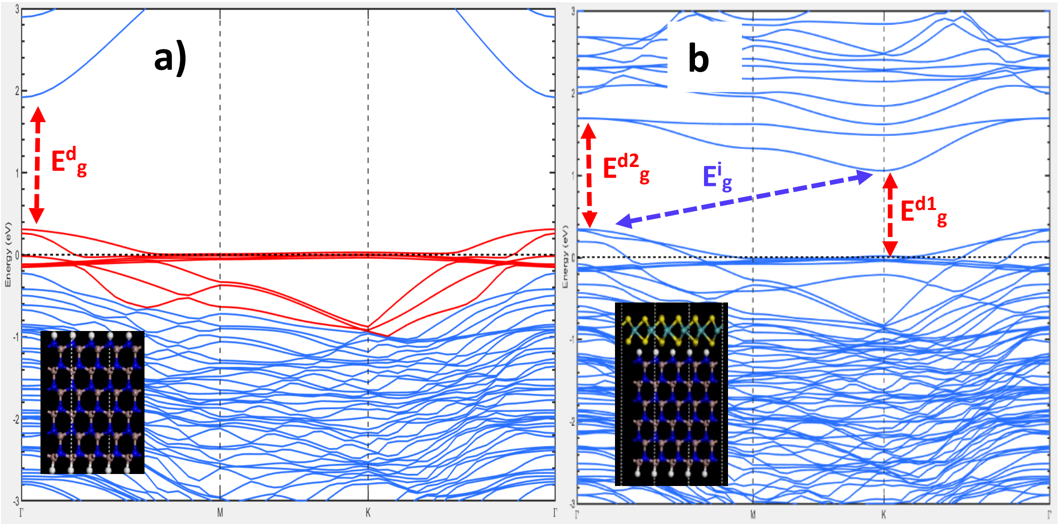

Fig. 55 Electronic structure of the a) N-terminated GaN (000$\bar{1}$) surface and b) MoS$_2$/GaN (000$\bar{1}$) heterostructure. Respective models are shown for reference.

The predicted direct energy gap (E^d_g) for the N-terminated GaN (000$\bar{1}$) is 1.6 eV, which is 0.56 eV smaller than the E^d_g for the Ga-terminated GaN (0001) system. Unlike in the Ga-terminated GaN (0001) system, the overall feature of the electronic structure of the N-terminated GaN ((000$\bar{1}$) is slightly different from the bulk system. In this system, the VBE states are mainly consist of the states from the surface N atoms, and the Fermi level is pinned around these states. Between the M-K points of the BZ, the VBE states are nondispersive. As illustrated in the Fig. 56b, the electronic structure of MoS$_2$/GaN (000$\bar{1}$) heterostructure possess indirect type, where CBE states at the K-point and VBE states at the Γ-point contribute to the energy gap (E^i_g). Quantitatively, the observed direct E^i_g is 0.73 eV and indirect E^{d1}_g (E^{d2}_g) at K (Γ) is 1.11 (1.36) eV. Although the CBE states are mainly dominates by the states from the MoS$_2$ layer, the flattened curvature of the bands, as compared to a single layer MoS$_2$ bands, indicates the increment (decrement) of the carrier effective mass (mobility) in the MoS$_2$ layer. As compared to the MoS$_2$/Ga-terminated GaN (0001) heterostructure, the Fermi level in the

MoS_2/N-terminated GaN $(000\bar{1})$ heterostructure is pinned below the VBE states and the overall system retains the polarity of the GaN $(000\bar{1})$ substrate.

10.3 Knowledge Acquisition

10.3.1 ECON-KG Tool: Electrical Conductivity using DFT

10.3.1.1 Introduction and Motivation

The electrical conductivity of materials is of fundamental interest in a number of research areas, many of which are relevant to current CCDC ARL programs. In the heterogeneous vdW solids like 2-D/3-D heterostructures, the knowledge of the vertical charge transport occurring between layers is critical as it may lead to design and fabrication of devices that are more tunable.

In another CCDC ARL application, the electrical conductivity of the boron carbide armor ceramic, one of the focus materials for the Materials in Extreme Dynamic Environments Collaborative Research Alliance, has been shown to be a function of pressure and carbon content.[2] Similarly, the electrical conductivity of explosive product gases has been shown to depend on carbon content,[3] and electrical conductivity models have become a requirement for input into continuum-level simulations being executed by researchers in the Multi-Threat Armor Branch. Although the increased electrical conductivity observed in detonation products of condensed explosives has received considerable attention experimentally conductivity values corresponding to regular intervals of temperature and pressure are required for accurate interpolation in continuum simulations.

In this effort, a Fortran 90 implementation of the Kubo–Greenwood (KG) formula, for use with the QE[9] software package, is developed and the program is called ECON-KG. This program is currently available at the CCDC ARL Defense Supercomputing Resource Center but can be easily ported to other Department of Defense computing facilities.

10.3.1.2 Technical Detail

In the absence of experimental data, particularly in the case of notional materials that have not yet been synthesized (such as the vdW heterostructures being explored in the aforementioned DSI), the electrical conductivity of materials can be obtained using first-principles quantum mechanical techniques. One approach for computing the conductivity from first principles is based on the KG formalism.[8] In this approach, the frequency (ω)-dependent electrical conductivity is computed as a weighted sum over k-points:

$$\sigma(\omega) = \sum_k \sigma_k(\omega) * W(k)\ , \tag{4}$$

where W(k) is the weighting at integration point k. $\sigma_k(\omega)$ is given by

$$\sigma_k(\omega) = \frac{2\pi e^2\hbar^2}{3m^2\omega\Omega}\sum_{i,j=1}^{n}\sum_{\alpha=1}^{3}\left[F(\varepsilon_{i,k}) - F(\varepsilon_{j,k})\right] \times \left|\langle\Psi_{j,k}|\nabla_\alpha|\Psi_{i,k}\rangle\right|^2 \delta(\varepsilon_{j,k} - \varepsilon_{i,k} - \hbar\omega)\ , \tag{5}$$

where m is the electron mass, Ω is the unit cell volume Φ is the occupation number for bands i and j ε is the band energy, and the index a denotes Cartesian direction for the momentum operator. The KG approach has the advantage that it does not require an estimate of the lifetime or numerical differentiation of band energies, and all requisite quantities can be obtained using quantum mechanical methods without fitting to experiment. The detail on implementation and parameters validation is presented in Taylor.[153]

10.3.1.3 Validation

For the method and tool validation, we have calculated the intrinsic electrical conductivity of a bilayer MoS_2 system using ECKON-KG and compared the results from the KG Electrical Conductivity (KGEC) tool developed by Dr Lazaro Calderin at University of Florida.[154] The results are presented in Fig. 56. It can been that the electrical conductivity predicted by the ECON-KG matches closely to that of KGEC for the considered frequency range. The example results presented in this work were obtained using a single structure extracted from a molecular dynamics trajectory.

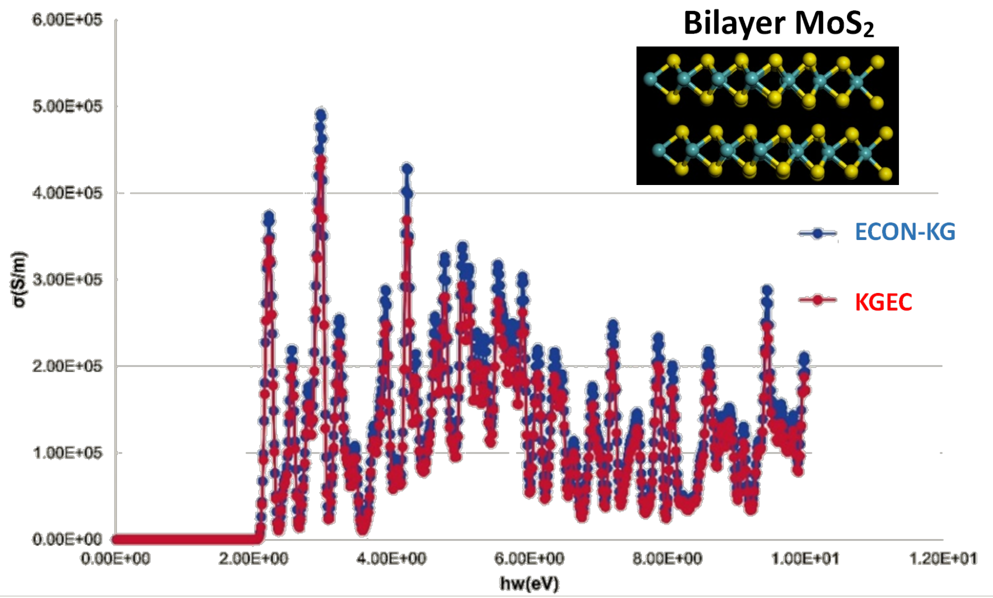

Fig. 56 Electrical conductivity (σ) of a bilayer MoS_2 system predicted by ECON-KG and KGEC Tools. Inset shows a model of bilayer MoS_2.

In practice, one should use multiple structures, with appropriate averaging, to determine the conductivity values. However, for brevity's sake, only a single structure was used for the example application presented in the report. The results in this work are in fairly good agreement with the experiment. However, in the author's experience, the level of agreement can shift dramatically (factor of 10 or more) depending on density functional, system size, and input parameters to ECON-KG. The results can be very sensitive to the number of bands and delta function width, and convergence with respect to these quantities can be challenging.

10.3.2 DFT-VEX Tool: DFT-based Parameter Visualization and Extraction

10.3.2.1 Introduction and Motivation

Over the years, a crucial bottleneck for the DFT calculations has been the availability of computational resources for the large-scale simulation, such as 2-D/2-D heterostructures, 2-D/3-D heterostructures, and metal/2-D/3-D heterostructures. With continuous improvement in the processor speed and innovation of very high throughput networking technology like Infiniband, DFT calculation of a periodic crystal is considered trivial these days. Unfortunately, now the bottleneck is the lack of appropriate tools for visualization and parameter extraction from the available data. Some of the tools like QE and Abinit come with their own postprocessing tools, which are limited in terms of the operating system they can run on. The data generated by the DFT tools are usually structural properties, and electronic band structure and associated projections of the band structures. The usability of these data is based on field of application. For example, for a device physicist the slope of the conduction or valance band of a semiconductor is quite important. Hence, the visualization need for a scientist focusing on materials with device applications can be quite different from that of a scientist focusing on chemical properties of a material. A tool that is field and specialization agnostic is still not available.

DFT-VEX is a visualization and parameter extraction tool for DFT calculations. This code closes the gap between the output data and the decision-making process. The first version of the code can plot band structure, plot ionic and orbital composition of the electronic band structure, and various features of DOS, and can extract effective mass from the band structure. The tool is modularized and object oriented. As a result, this code can be extended to any DFT tool. At this point, the code is capable of visualization and parameter extraction of VASP calculations.

10.3.2.2 Technical Detail

For any calculation, VASP outputs its data in two data formats. In one case, the different data are outputted in separate text files. For example, the band structure, orbital contribution, and the DOS are written into files named EIGENVAL, PROCAR, and DOSCAR files, respectively. Parameters like Fermi level is written into file named OUTCAR. Secondly, all the data for a calculation are also written to a XML file named vasprun.xml. When reading the data for visualization and parameter extraction purpose, a user can use any of the files to read the data. In terms of data collection, using the vasprun.xml file has some advantages, such as a single file for all the calculated data, a structured format, and easier file input/output process, as compared to reading an ASCII file.

The primary language for development of the tool was Matlab. For calculations involving large structure, Matlab can run into memory problems due to the limitation of memory within the virtual Java system on which Matlab runs. To circumvent this problem, a separate XML reader written in Python has been developed. Matlab can be used to call a Python script from its own environment. DFT-VEX calls the appropriate Python functions to read the data. The Python script has a dependency on numpy and scipy. If calling the Python library fails, the code falls back to XML reader written using Matlab. In terms of performance, the Matlab reader is slower compared to its python counterpart, but it enables graceful execution of the code when Python fails. Some of the features of the DFT-VEX tools are the following:

- Band structure visualization
- Ionic/orbital composition of materials visualization
- Total DOS/ionic/orbital breakdown of DOS
- Self-consistent effective mass extraction
- Band-offset in heterogeneous system extraction
- Selective band project and effective mass extraction

One of the unique features of the DFT-VEX tool is a self-consistent effective mass extraction capability. Effective mass (m*) is an intrinsic property of a material that defines slope of the conduction or valance band minima. Electronic transport within a material is strongly dependent on the effective mass of a material. Effective mass can be determined from the band structure. The band edge of a semiconducting material is usually parabolic. This parabolic dispersion can be fitted to a second-order polynomial to extract the effective mass. Effectively the effective mass can be defined as $\frac{1}{m^8} = \frac{1}{\hbar^2}\frac{\partial^2 E}{\partial^2 k}$. To verify the order of the fitted polynomial, the dispersion can be fitted to 4th- or 6th-order polynomial. If the residuals are close to zero, then the dispersion is parabolic. The workflow of the effective mass extraction module is illustrated in Fig. 57. Details on other modules and relevant validations on these modules will be presented in Das and Neupane.[155]

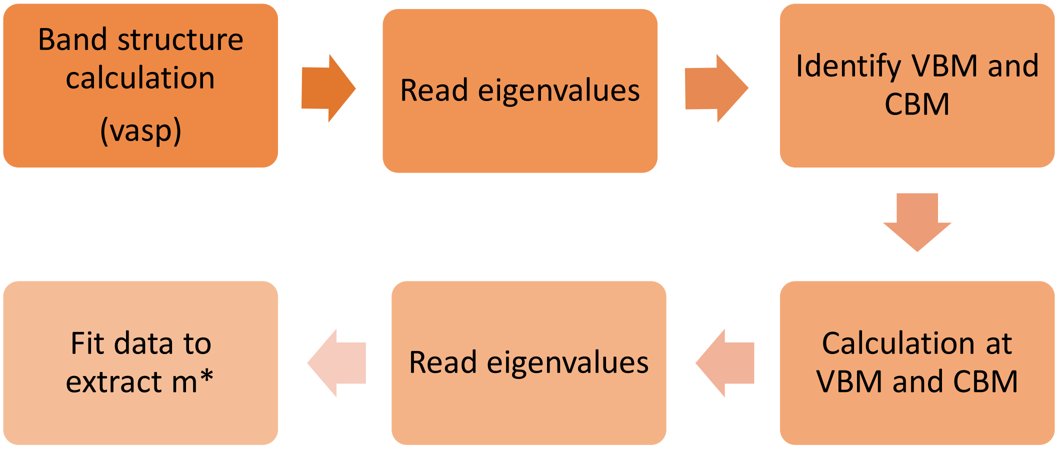

Fig. 57 Workflow for the effective mass extraction module in DFT-VEX tool

10.3.2.3 Validation

Plotting of band structure is the very basic visualization for DFT-based calculation data. While the plotting seems trivial, the data can be in quite different formats based on the theory applied during the calculation. To read the data properly, one needs to identify the level of theory used to generate the data. To read the data properly several cases to be considered. Figure 58 illustrates such two of cases: basic and site-resolved band structure calculations for platinum diselenide ($PtSe_2$) layered 2-D materials.

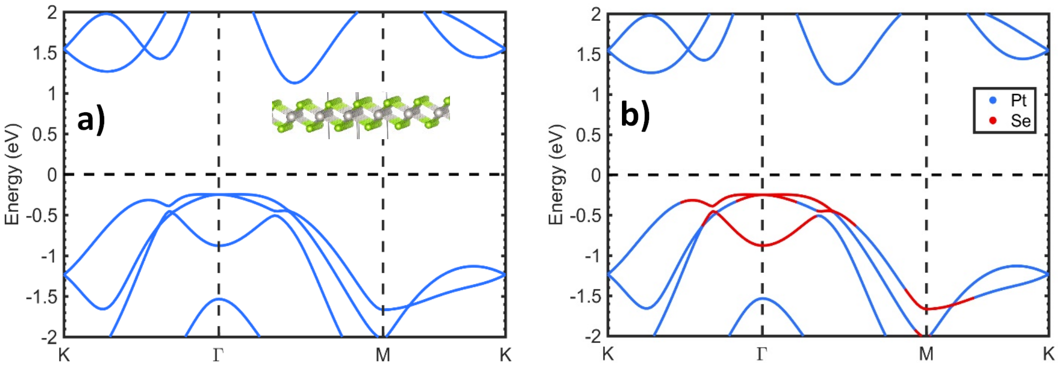

Fig. 58 a) Basic and b) site-resolved band structure for single layer $PtSe_2$ generated by DFT-VEX tool. Inset on a) represents the $PtSe_2$ model used in this calculation.

The basic visualization of band structure in Fig. 58a gives information on band structure type and the location of the band minima in the BZ. In addition to the basic information on band structure, the site-resolved band structure provides information on the atomistic contribution to each bands, which is very useful in designing materials with suitable band structure properties by modifying atomic composition. As can been seen in the Fig. 58b, for the single layer $PtSe_2$, the CB minima states mainly consist of Pt states and VB maxima states composed of hybrid states from Pt and selenium (Se) atoms; however, VBE states are mainly dominated by Se states.

An automated extraction of effective mass from the given band structure enables us to analyze the effect of surface modification, using doping, defect, and heterogeneity, on the device-related parameters such as mobility and carrier densities. To validate the effective mass extraction feature, we have calculated band structure of $MoTe_2/NbSe_2$ heterostructure and plotted in Fig. 59. The site-projected band structure is used to extract the carrier effective mass from a heterogeneous system. The polynomial fitting mechanisms used for the extraction of the carrier effective masses are illustrated in Fig. 60. Since the $NbSe_2$ is a metallic system representing layered metal contact on the semiconducting $MoTe_2$, the modification on the carrier effective masses on $MoTe_2$ is extracted by performing polynomial fit of 2, 4, and 6 orders in longitudinal and transverse directions.

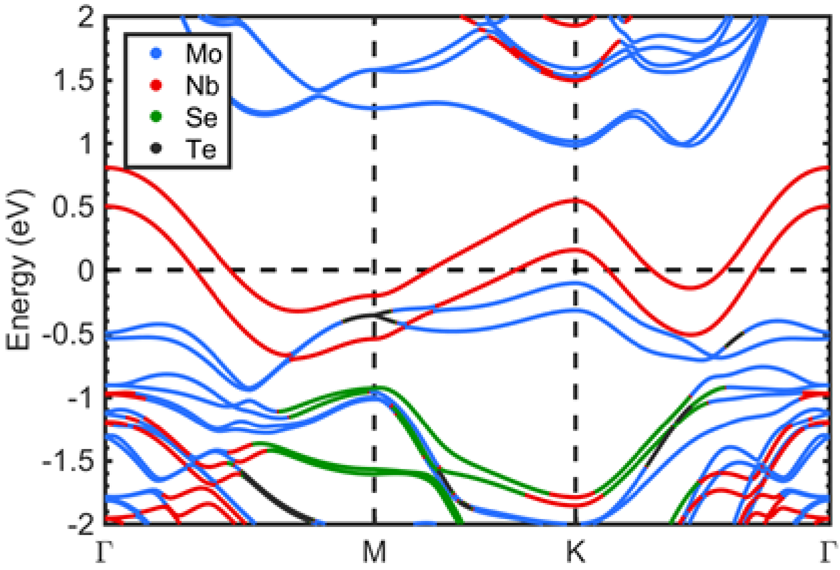

Fig. 59 Site-resolved band structure of the $MoTe_2/NbSe_2$ heterostructure generated by DFT-VEX tool

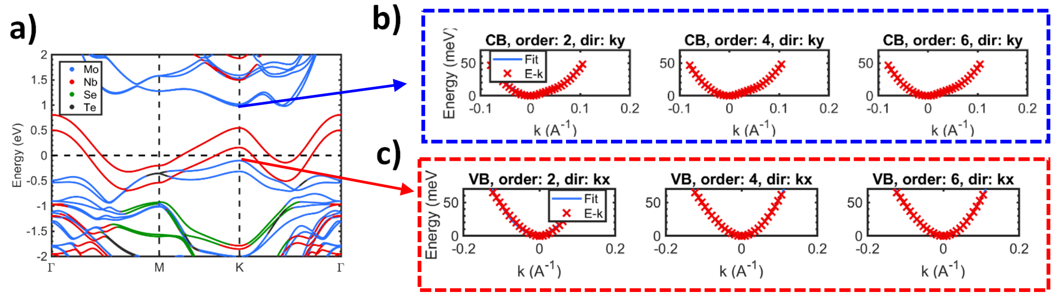

Fig. 60 Illustration of the polynomial fit mechanism used to extract the effective mass extraction from the plotted band structure. a) Site-resolved band structure for the MoTe$_2$/NbSe$_2$ heterostructure, b) polynomial fit for the CB edge band, and c) polynomial fit for the VBE band.

The 6th-degree polynomial fit results in the tight fit to the DFT data. The evaluated effective masses for a single-layer MoTe$_2$ and NbSe$_2$-MoTe$_2$ heterostructures, and relative change in the effective masses are tabulated in Table 11.

Table 11 Extracted effective masses for single-layer MoTe$_2$ and NbSe$_2$-MoTe$_2$

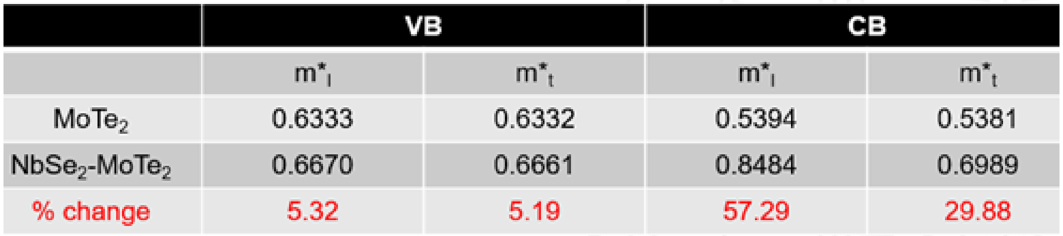

	VB		CB	
	m^*_l	m^*_t	m^*_l	m^*_t
MoTe$_2$	0.6333	0.6332	0.5394	0.5381
NbSe$_2$-MoTe$_2$	0.6670	0.6661	0.8484	0.6989
% change	5.32	5.19	57.29	29.88

Adding metal NbSe$_2$ on top of the semiconducting MoTe$_2$ layer results in the modification of the curvatures of the bands, and hence, the carriers effective masses. The extracted effective masses for the electrons and holes in the NbSe$_2$-MoTe$_2$ heterostructure are modified significantly. For both the longitudinal and transverse effective masses, the hole effective masses of MoTe2 are increased by approximately 5%, due to the states hybridization between MoTe$_2$ and NbSe$_2$ states. The effective of heterogeneity in the electron effective masses of the MoTe$_2$ layer is significant. Quantitatively, the lateral and transverse electron effective masses are increased by approximately 57% and approximately 30%, respectively.

In summary, we have created a modular tool for visualization and parameter extraction from DFT calculations that can visualize data generated by a DFT tool. Visualization of band structure along with projected band structure and DOS are supported. In terms of parameter extraction, the DFT-VEX tool can calculate effective mass from the band structure of a material. This can be done in a generic way from a band structure and in a more precise manner by doing a separate calculation. For a precise calculation of effective mass, input files can be generated using DFT-VEX. Effective mass of a both homogenous and heterogeneous material can be calculated. Right now, the library supports visualization and parameter extraction from VASP calculations. Due to the modular nature of the code, the tool can be extended to any DFT tools in future.

11. Technical Summary/Conclusions and Transition Plan

In this study, by integrating MoS_2 (2-D) with GaN (3-D), we have created a new class of vdW solids to elucidate fundamental understanding of vdW interface science and open up a technological path for 2-D semiconductor integration with 3-D electronics. We have divided our accomplishments into three technological categories: 1) growth and characterization, 2) metrology, device fabrication and electrical characterization, and 3) materials and interface modeling.

Our growth effort was focused on optimization and understanding of PV of MoS_2 on GaN. In particular, we have investigated the impact of MoO_3 nucleation temperature, growth temperature, and growth pressure on the alignment, quality, density, and size of the MoS_2 domains. In the first year, we were able to successfully grow MoS_2 2-D semiconductor on both *n*- and *p*-type GaN due to our improvements in surface preparation of the GaN prior to growth. In the second year, we have successfully doped the MoS_2 *n*-type using rhenium (Re) powder and *p*-type using Nb powder during as sources in the PV growth process. We have also investigated MOCVD as an alternative to PV. Through our PV studies, we have found obtaining uniform coverage to be an issue due to the presence of a MoO_3 during growth. We also determined that ML MoS_2 (1L-MoS_2) only modified the interface and was electronically transparent. Therefore, we needed to transition to a growth technique that would allow us to grow uniform multilayer a stack (several molecular layers) of MoS_2. Finally, we succeeded in growing multilayer MoS_2 utilizing MOCVD.

We have performed a thorough characterization of 2-D/3-D semiconductor heterojunctions with the purpose of developing functional 2-D/3-D bipolar transistors. Our cross-sectional TEM showed 2-D/3-D heterojunctions consisting of MoS_2 single monolayer (1L-MoS_2) and *n*- and *p*-doped GaN. The ML MoS_2 is epitaxial, continuous, and unperturbed on the GaN lattice. The vdW gap size between the 1L-MoS_2 and GaN was measured with TEM, as was the lattice constant of the 1L-MoS_2. The 1L-MoS_2 was proven to be lattice-matched to the GaN substrate, as predicted. An interesting modification of the top two atomic planes of GaN was found only under MoS_2 monolayer. The electrical characteristics of metal/2-D/3-D heterojunctions were investigated in order to develop an understanding of the role of atomically thin semiconductor components in vertical bipolar devices.

In the first approach, the electrical characteristics of MoS_2/GaN heterojunctions for both *n*- and *p*-doped GaN were obtained with CAFM), where the CAFM tip played the role of the metal contact. This approach allowed the characterization of pristine heterojunctions without the exposure to the wet processing. We observed a reversal of the rectification polarity when the GaN substrate was changed from *n* to *p* doping. The analysis of the electrical data led us to an understanding that a single monolayer MoS_2 does not behave as an independent semiconductor in a (CAFM Pt tip)/1L-MoS_2/GaN heterojunctions but rather modifies the tip/GaN SB. Therefore, the 2-D layer in 2-D/3-D heterojunctions has to be above a certain thickness before it exhibits characteristics consistent with a separate semiconductor component in a bipolar transistor.

CAFM was used to electrically characterize multilayer stacks of MoS_2 and WSe_2 grown by MOCVD on GaN. The WSe_2/GaN heterojunctions behaved as *pn*-junctions with WSe_2 being a naturally *p*-type 2-D semiconductor and the GaN substrate chosen to be *n*-doped. In the second approach, permanent metal nanocontacts in the metal/2-D/3-D heterojunctions were fabricated by EBL and I-V measurements were performed with nanoprobes inside an SEM. TEM showed that the heterojunctions of Au/1L-MoS_2/GaN are fully epitaxial, whereas the Au that was grown directly on GaN is not epitaxial. ML MoS_2 is unperturbed in our junction fabrication process and no interdiffusion between Au and 1L-MoS_2 is present according to the TEM analysis. Stable contacts and better electronics (as compared to CAFM) allowed for better quantitative analysis of the electrical behavior of the heterojunctions. Extracted SB data provided insight into the origin of the applied electrical response. In agreement with the CAFM analysis, ML MoS_2 was found to be electronically transparent. This led to Au/1L-MoS_2/*p*-GaN heterojunctions that behave electrically as Au/*p*-GaN junctions that are modified by the 2-D layer presence despite the fact that a distinct separate MoS_2 ML is observed with TEM.

Lastly, we developed a design and microfabrication process for making vertical GaN/MoS_2/GaN HBTs with an ultra-thin base made of 4–5 molecular layer MoS_2. We have validated all major critical aspects of the design, which makes it likely that our design and microfabrication process will produce a working HBT. In particular, 2-D/3-D diode behavior was demonstrated for the all-synthesized heterostructures without mechanical transfer. The STEM and other microstructural analyses confirm that we have synthesized the trilayer 3-D/2-D/3-D semiconductor structure, which can be used for the fabrication of a vertical 2-D/3-D HBT. We believe this is the first demonstration of a 3-D/2-D/3-D semiconductor heterostructure. This is an important step toward the implementation of 2-D crystals in high-speed electronic devices.

Our modeling and theory effort was divided into three subtasks: 1) benchmarking the scalable CP2K first-principles method, 2) design and simulation of 2-D/3-D heterostructures, and 3) formulation of an analytical model for novel devices. In the first task, a case study on the applicability of CP2K was performed by simulating naturally aligned, misoriented 2-D bilayer systems. Our observations indicate that the CP2K, in addition to being highly scalable, can reliably predict fundamental material and structural parameters, and the results are comparable with more established tools such as VASP and QE. However, due to the lack of a full-BZ integration scheme, CP2K has some limitations in predicting electronic properties.

In our second task, we designed and performed structural and electronic structure modeling of 2-D/3-D heterostructures consisting of single layer MoS_2 and GaN bulk-like surfaces, respectively (Fig. 5). Using Grimme's dispersion correction scheme for the vdW forces, the first-principles method implemented in VASP predicted a vdW gap of 3.10 Å between the 1L-MoS_2 and GaN surface, which agrees with the experimentally observed vdW gap. Using the electronic properties of the 2-D/3-D heterostructures and bulk-like metal surfaces (Pt), a band alignment feature for the device characterization and analysis was conceptualized (Fig. 6). Overall, the band alignment between metal/2-D/3-D interfaces predicts the shifts in the SBH due to the interfacial 2-D layer (1L-MoS_2) between metal and 3-D (bulk-GaN) surfaces, consistent with the experimental observation. Additionally, our simulation results also predict 1L-MoS_2 induces suppression of the GaN surface states eluding a new mechanism of passivating GaN surface dangling bonds.

Lastly, we have also developed a model for a metal/2-D/3-D heterostructure and successfully performed numerical simulations on their structural and electronic properties. Structural modeling of an Au contact on a MoS_2/GaN system revealed that the vdW gap between the MoS_2 layer and GaN system is perturbed and increased due to the stronger binding energy between the Au and MoS_2 layers that tend to pull the MoS_2 layer from the GaN substrate, which are consistent with our XTEM observation. In addition, electronic properties of this system results in an atomistic picture of charge depletion across the metal/2-D/3-D junction. The observation of the gap states throughout the GaN and MoS_2 bandgaps is consistent with the substantial band bending due to the FLP observed in the KP measurement, which in turn reduces the effect of the SB and complicates the device design. The functionalization or surface passivation of both the Au and GaN surfaces is a possible solution to minimize the FLP and improve the control on the SB. This study provides quantitative information and insight on the nanostructural and electrical aspects of the interactions of a semiconductor 2-D monolayer with III-V semiconductors, a mainstay of modern high-speed electronics, and metals.

In summary, we have demonstrated in this work the growth of 2-D/3-D and 3-D/2-D/3-D heterojunctions relevant for vertical bipolar devices, gained a better understanding of the physical and electrical interactions of 2- and 3-D materials, and drafted the band alignment for the studied vdW solids. The gained knowledge and experience with 2-D/3-D heterostructures will allow us to transfer our knowledge and skills to the ongoing and future mission-related projects. As part of the technical transition, we also plan to transfer samples and acquired knowledge in the form of this report to our collaborators at Northrop Grumman.

12. References

1. Novoselov KS, Geim AK, Morozov SV, Jiang D, Zhang Y, Dubonos SV, Grigorieva IV, Firsov AA. Electric field effect in atomically thin carbon films. Science. 2004;306:666–669.

2. Geim AK, Grigorieva IV. Van der Waals heterostructures. Nature. 2013;499:419–425.

3. Osada M, Sasaki T. Two-dimensional dielectric nanosheets: novel nanoelectronics from nanocrystal building blocks. Adv Mater. 2012;24:210–228.

4. Britnell L, Ribeiro RM, Eckmann A, Jalil R, Belle BD, Mishchenko A, Kim YJ, Gorbachev RV, Georgiou T, Morozov SV, Grigorenko AN, Geim AK, Casiraghi C, Castro Neto AH, Novoselov KS. Strong light–matter interactions in heterostructures of atomically thin films. Science. 2013;340:1311–1314.

5. Yu WJ, Li Z, Zhou HL, Chen Y, Wang Y, Huang Y, Duan XF. Vertically stacked multi-heterostructures of layered materials for logic transistors and complementary inverters. Nat Mater. 2013;12:246–252.

6. Fang H, Battaglia C, Carraro C, Nemsak S, Ozdol B, Kang JS, Bechtel HA, Desai SB, Kronast F, Unal AA, Conti G, Conlon C, Palsson GK, Martin MC, Minor AM, Fadley CS, Yablonovitch E, Maboudian R, Javey A. Strong interlayer coupling in van der Waals heterostructures built from single-layer chalcogenides. Proc Natl Acad Sci U S A. 2014;111:6198–6202.

7. Wang HT, Yuan HT, Hong SS, Li YB, Cui Y. Physical and chemical tuning of two-dimensional transition metal dichalcogenides. Chem Soc Rev. 2015b;44:2664–2680.

8. Fang H, Tosun M, Seol G, Chang TC, Takei K, Guo J, Javey A. Degenerate n-doping of few-layer transition metal dichalcogenides by potassium. Nano Lett. 2013;13:1991–1995.

9. Ji QQ, Kan M, Zhang Y, Guo Y, Ma DL, Shi JP, Sun Q, Chen Q, Zhang YF, Liu ZF. Unravelling orientation distribution and merging behavior of monolayer MoS_2 domains on sapphire. Nano Lett. 2015;15:198–205.

10. Jeong H, Bang S, Oh HM, Jeong HJ, An SJ, Han GH, Kim H, Kim KK, Park JC, Lee YH, Lerondel G, Jeong MS. Semiconductor-insulator-semiconductor diode consisting of monolayer MoS_2, h-BN, and GaN heterostructure. ACS Nano. 2015a;9:10032–10038.

11. Wang F, Wang ZX, Xu K, Wang FM, Wang QS, Huang Y, Yin L, He J. Tunable GaTe-MoS_2 van der Waals p-n junctions with novel optoelectronic performance. Nano Lett. 2015a;15:7558–7566.

12. Krasnozhon D, Lembke D, Nyffeler C, Leblebici Y, Kis A. MoS_2 transistors operating at gigahertz frequencies. Nano Lett. 2014;14:5905–5911.

13. Radisavljevic B, Whitwick MB, Kis A. Integrated circuits and logic operations based on single-layer MoS_2. ACS Nano. 2011b;5:9934–9938.

14. Radisavljevic B, Radenovic A, Brivio J, Giacometti V, Kis A. Single-layer MoS_2 transistors. Nature Nanotechnology. 2011a;6:147–150.

15. Mak KF, He KL, Shan J, Heinz TF. Control of valley polarization in monolayer MoS_2 by optical helicity. Nature Nanotechnology. 2012;7:494–498.

16. Pu J, Yomogida Y, Liu KK, Li LJ, Iwasa Y, Takenobu T. Highly flexible MoS_2 thin-film transistors with ion gel dielectrics. Nano Lett. 2012;12:4013–4017.

17. Lee GH, Yu YJ, Cui X, Petrone N, Lee CH, Choi MS, Lee DY, Lee C, Yoo WJ, Watanabe K, Taniguchi T, Nuckolls C, Kim P, Hone J. flexible and transparent MoS_2 field-effect transistors on hexagonal boron nitride-graphene heterostructures. ACS Nano. 2013a;7:7931–7936.

18. Varrla E, Backes C, Paton KR, Harvey A, Gholamvand Z, McCauley J, Coleman JN. Large-scale production of size-controlled MoS_2 nanosheets by shear exfoliation. Chem Mat. 2015;27:1129–1139.

19. Dumcenco D, Ovchinnikov D, Marinov K, Lazic P, Gibertini M, Marzari N, Sanchez OL, Kung YC, Krasnozhon D, Chen MW, Bertolazzi S, Gillet P, Morral AFI, Radenovic A, Kis A. Large-area epitaxial monolayer MoS_2. ACS Nano. 2015;9:4611–4620.

20. Kang K, Xie SE, Huang LJ, Han YM, Huang PY, Mak KF, Kim CJ, Muller D, Park J. High-mobility three-atom-thick semiconducting films with wafer-scale homogeneity. Nature. 2015;520:656–660.

21. Serrao CR, Diamond AM, Hsu SL, You L, Gadgil S, Clarkson J, Carraro C, Maboudian R, Hu CM, Salahuddin S. Highly crystalline MoS_2 thin films grown by pulsed laser deposition. Appl Phys Lett. 2015;106:4.

22. Aretouli KE, Tsipas P, Tsoutsou D, Marquez-Velasco J, Xenogiannopoulou E, Giamini SA, Vassalou E, Kelaidis N, Dimoulas A. Two-dimensional semiconductor $HfSe_2$ and $MoSe_2/HfSe_2$ van der Waals heterostructures by molecular beam epitaxy. Appl Phys Lett. 2015;106:5.

23. Xenogiannopoulou E, Tsipas P, Aretouli KE, Tsoutsou D, Giamini SA, Bazioti C, Dimitrakopulos GP, Komninou P, Brems S, Huyghebaert C, Radu IP, Dimoulas A. High-quality, large-area $MoSe_2$ and $MoSe_2/Bi_2Se_3$ heterostructures on AlN(0001)/Si(111) substrates by molecular beam epitaxy. Nanoscale. 2015;7:7896–7905.

24. Gupta P, Rahman AA, Subramanian S, Gupta S, Thamizhavel A, Orlova T, Rouvimov S, Vishwanath S, Protasenko V, Laskar MR, Xing HG, Jena D, Bhattacharya A. Layered transition metal dichalcogenides: promising near–lattice–matched substrates for GaN growth. Sci Rep. 2016a;6:8.

25. Shi YM, Zhou W, Lu AY, Fang WJ, Lee YH, Hsu AL, Kim SM, Kim KK, Yang HY, Li LJ, Idrobo JC, Kong J. van der Waals epitaxy of MoS_2 layers using graphene as growth templates. Nano Lett. 2012;12:2784–2791.

26. Okada M, Sawazaki T, Watanabe K, Taniguch T, Hibino H, Shinohara H, Kitaura R. Direct chemical vapor deposition growth of WS_2 atomic layers on hexagonal boron nitride. ACS Nano. 2014;8:8273–8277.

27. Perry DL. Applications of analytical techniques to the characterization of materials. Boston (MA): Springer US; 1991.

28. Zerweck U, Loppacher C, Otto T, Grafstrom S, Eng LM. Accuracy and resolution limits of Kelvin probe force microscopy. Phys Rev B. 2005;71:9.

29. Jellinek F, Brauer G, Muller H. Molybdenum and niobium sulphides. Nature. 1960;185:376–377.

30. Huang LF, Gong PL, Zeng Z. Correlation between structure, phonon spectra, thermal expansion, and thermomechanics of single-layer MoS_2. Phys Rev B. 2014b;90:7.

31. Leszczynski M, Suski T, Teisseyre H, Perlin P, Grzegory I, Jun J, Porowski S, Moustakas TD. Thermal-expansion of gallium nitride. J Appl Phys. 1994;76:4909–4911.

32. Zhang KH, Feng SM, Wang JJ, Azcatl A, Lu N, Addou R, Wang N, Zhou CJ, Lerach J, Bojan V, Kim MJ, Chen LQ, Wallace RM, Terrones M, Zhu J, Robinson JA. Manganese doping of monolayer MoS_2: the substrate is critical. Nano Lett. 2015;15:6586–6591.

33. Georgieva M, O'Regan T. Identification and mapping of mechanically exfoliated 1H–MoS_2 flakes for field-effect transistors. Aberdeen Proving Ground (MD): Army Research Laboratory (US); 2014. Report no.: ARL-TR-7021.

34. Lee C, Yan H, Brus LE, Heinz TF, Hone J, Ryu S. Anomalous lattice vibrations of single- and few-layer MoS_2. ACS Nano. 2010;4:2695–2700.

35. Li H, Zhang Q, Yap CCR, Tay BK, Edwin THT, Olivier A, Baillargeat D. From bulk to monolayer MoS_2: evolution of raman scattering. Adv Funct Mater. 2012b;22:1385–1390.

36. Zhou KG, Withers F, Cao Y, Hu S, Yu GL, Casiraghi C: Raman Modes of MoS2 Used as fingerprint of van der Waals interactions in 2-D crystal-based heterostructures. ACS Nano. 2014;8:9914–9924.

37. Li YY, Qi ZM, Liu M, Wang YY, Cheng XR, Zhang GB, Sheng LS. Photoluminescence of monolayer MoS_2 on $LaAlO_3$ and $SrTiO_3$ substrates. Nanoscale. 2014b;6:15248–15254.

38. Kim IS, Sangwan VK, Jariwala D, Wood JD, Park S, Chen K-S, Shi F, Ruiz-Zepeda F, Ponce A, Jose-Yacaman M, Dravid VP, Marks TJ, Hersam MC, Lauhon LJ. Influence of stoichiometry on the optical and electrical properties of chemical vapor deposition derived MoS_2. ACS Nano. 2014;8:10551–10558.

39. Sangwan VK, Jariwala D, Kim IS, Chen K-S, Marks TJ, Lauhon LJ, Hersam MC. Gate-tunable memristive phenomena mediated by grain boundaries in single-layer MoS_2. Nat Nanotechnol. 2015;10:403–406.

40. Liu Z, Amani M, Najmaei S, Xu Q, Zou X, Zhou W, Yu T, Qiu C, Birdwell AG, Crowne FJ, Vajtai R, Yakobson BI, Xia Z, Dubey M, Ajayan PM, Lou J. Strain and structure heterogeneity in MoS_2 atomic layers grown by chemical vapour deposition. Nat Commun. 2014;5:5246.

41. Giannazzo F, Fisichella G, Piazza A, Agnello S, Roccaforte F. Nanoscale inhomogeneity of the Schottky barrier and resistivity in MoS_2 multilayers. Phys Rev B. 2015a;92:4.

42. Kaushik V, Varandani D, Mehta BR. Nanoscale mapping of layer-dependent surface potential and junction properties of CVD-grown MoS_2 domains. J Phys Chem C. 2015;119:20136–20142.

43. Dubertret B, Heine T, Terrones M. The rise of two-dimensional materials. Accounts Chem Res. 2015;48:1–2.

44. Lee YH, Yu LL, Wang H, Fang WJ, Ling X, Shi YM, Lin CT, Huang JK, Chang MT, Chang CS, Dresselhaus M, Palacios T, Li LJ, Kong J. Synthesis and transfer of single-layer transition metal disulfides on diverse surfaces. Nano Lett. 2013b;13:1852–1857.

45. Ruzmetov D, Zhang KH, Stan G, Kalanyan B, Bhimanapati GR, Eichfeld SM, Burke RA, Shah PB, O'Regan TP, Crowne FJ, Birdwell AG, Robinson JA, Davydov AV, Ivanov TG. Vertical 2D/3D semiconductor heterostructures based on epitaxial molybdenum disulfide and gallium nitride. ACS Nano. 2016;10:3580–3588.

46. Jung K, Liu C, Kim JD, Choi W, Zhou W, Kuo H, Li X. Large area MoS_2 van der Waals epitaxy on III-Ns and the epitaxial formation of a n-MoS_2/p-InGaN diode; in: 2016 IEEE Photonics Conference (IPC). pp 657–658.

47. Chen Z, Liu H, Chen X, Chu G, Chu S, Zhang H. Wafer-size and single-crystal $MoSe_2$ atomically thin films grown on gan substrate for light emission and harvesting. ACS Applied Materials & Interfaces. 2016;8:20267–20273.

48. Kiraly B, Jacobberger RM, Mannix AJ, Campbell GP, Bedzyk MJ, Arnold MS, Hersam MC, Guisinger NP. Electronic and mechanical properties of graphene–germanium interfaces grown by chemical vapor deposition. Nano Lett. 2015;15:7414–7420.

49. Krishnamoorthy S, Lee EW, Lee CH, Zhang Y, McCulloch WD, Johnson JM, Hwang J, Wu Y, Rajan S. High current density 2D/3D MoS_2/GaN Esaki tunnel diodes. Appl Phys Lett. 2016a;109:183505.

50. Molina–Sanchez A, Wirtz L. Phonons in single-layer and few-layer MoS_2 and WS_2. Phys Rev B. 2011;84:8.

51. Lanzillo NA, Birdwell AG, Amani M, Crowne FJ, Shah PB, Najmaei S, Liu Z, Ajayan PM, Lou J, Dubey M, Nayak SK, O'Regan TP. Temperature-dependent phonon shifts in monolayer MoS_2. Appl Phys Lett. 2013;103:4.

52. Chakraborty B, Bera A, Muthu DVS, Bhowmick S, Waghmare UV, Sood AK. Symmetry-dependent phonon renormalization in monolayer MoS_2 transistor. Phys Rev B. 2012;85:4.

53. Rice C, Young RJ, Zan R, Bangert U, Wolverson D, Georgiou T, Jalil R, Novoselov KS. Raman-scattering measurements and first-principles calculations of strain-induced phonon shifts in monolayer MoS_2. Phys Rev B. 2013;87:5.

54. Mak KF, Lee C, Hone J, Shan J, Heinz TF. Atomically thin MoS_2: a new direct-gap semiconductor. Phys Rev Lett. 2010;105:4.

55. Splendiani A, Sun L, Zhang YB, Li TS, Kim J, Chim CY, Galli G, Wang F. Emerging photoluminescence in monolayer MoS_2. Nano Lett. 2010;10:1271–1275.

56. Li W, Birdwell AG, Amani M, Burke RA, Ling X, Lee YH, Liang XL, Peng LM, Richter CA, Kong J, Gundlach DJ, Nguyen NV. Broadband optical properties of large-area monolayer CVD molybdenum disulfide. Phys Rev B. 2014a;90:8.

57. Ugeda MM, Bradley AJ, Shi SF, da Jornada FH, Zhang Y, Qiu DY, Ruan W, Mo SK, Hussain Z, Shen ZX, Wang F, Louie SG, Crommie MF. Giant bandgap renormalization and excitonic effects in a monolayer transition metal dichalcogenide semiconductor. Nat Mater. 2014;13:1091–1095.

58. Chernikov A, Berkelbach TC, Hill HM, Rigosi A, Li YL, Aslan OB, Reichman DR, Hybertsen MS, Heinz TF. Exciton binding energy and nonhydrogenic rydberg series in monolayer WS_2. Phys Rev Lett. 2014;113:5.

59. Su WT, Dou HL, Li JW, Huo DX, Dai N, Yang L. Tuning photoluminescence of single-layer MoS_2 using H_2O_2. RSC Adv. 2015;5:82924–82929.

60. Yao N, Wang ZL. Handbook of microscopy for nanotechnology. Boston (MA): Springer; 2005.

61. Yu S, Xiong HD, Eshun K, Yuan H, Li QL. Phase transition, effective mass and carrier mobility of MoS_2 monolayer under tensile strain. Appl Surf Sci. 2015;325:27–32.

62. Watkins NJ, Wicks GW, Gao Y. Oxidation study of GaN using X-ray photoemission spectroscopy. Appl Phys Lett. 1999;75:2602–2604.

63. Chou H, Ismach A, Ghosh R, Ruoff RS, Dolocan A. Revealing the planar chemistry of two-dimensional heterostructures at the atomic level. Nat Commun. 2015;6:7482.

64. Taillon JA, Hyuk Yang J, Ahyi CA, Rozen J, Williams JR, Feldman LC, Zheleva TS, Lelis AJ, Salamanca-Riba LG. Systematic structural and chemical characterization of the transition layer at the interface of NO-annealed 4H-SiC/SiO_2 metal-oxide-semiconductor field-effect transistors. J Appl Phys. 2013;113:044517.

65. Petkov V, Billinge SJL, Larson P, Mahanti SD, Vogt T, Rangan KK, Kanatzidis MG. Structure of nanocrystalline materials using atomic pair distribution function analysis: study of $LiMoS_2$. Phys Rev B. 2002a;65:092105.

66. Blochl PE. Projector augmented-wave method. Phys Rev B. 1994;50:17953–17979.

67. Kresse G, Furthmuller J. Efficient iterative schemes for ab initio total-energy calculations using a plane-wave basis set. Phys Rev B. 1996;54:11169–11186.

68. Perdew JP, Burke K, Ernzerhof M. Generalized gradient approximation made simple. Phys Rev Lett. 1996;77:3865–3868.

69. Monkhorst HJ, Pack JD. Special points for Brillouin-zone integrations. Phys Rev B. 1976;13:5188–5192.

70. Grimme S. Semiempirical GGA-type density functional constructed with a long-range dispersion correction. J Comput Chem. 2006;27:1787–1799.

71. Darakchieva V, Monemar B, Usui A. On the lattice parameters of GaN. Appl Phys Lett. 2007;91:3.

72. Schultz T, Schlesinger R, Niederhausen J, Henneberger F, Sadofev S, Blumstengel S, Vollmer A, Bussolotti F, Yang JP, Kera S, Parvez K, Ueno N, Müllen K, Koch N. Tuning the work function of GaN with organic molecular acceptors. Phys Rev B. 2016;93:125309.

73. Tung RT. The physics and chemistry of the Schottky barrier height. Applied Physics Reviews. 2014;1:011304.

74. Walia S, Balendhran S, Wang Y, Kadir RA, Zoolfakar AS, Atkin P, Ou JZ, Sriram S, Kalantar–zadeh K, Bhaskaran M. Characterization of metal contacts for two-dimensional MoS_2 nanoflakes. Appl Phys Lett. 2013;103:232105.

75. Zhong H, Quhe R, Wang Y, Ni Z, Ye M, Song Z, Pan Y, Yang J, Yang L, Lei M, Shi J, Lu J. Interfacial properties of monolayer and bilayer MoS_2 contacts with metals: beyond the energy band calculations. Sci Rep. 2016;6:21786.

76. Torres CM, Lan YW, Zeng CF, Chen JH, Kou XF, Navabi A, Tang JS, Montazeri M, Ademan JR, Lerner MB, Zhong YL, Li LJ, Chen CD, Wang KL. High-current gain two-dimensional MoS_2-base hot-electron transistors. Nano Lett. 2015;15:7905–7912.

77. Song I, Park C, Choi HC. Synthesis and properties of molybdenum disulphide: from bulk to atomic layers. RSC Adv. 2015;5:7495–7514.

78. Rigosi AF, Hill HM, Rim KT, Flynn GW, Heinz TF. Electronic band gaps and exciton binding energies in monolayer Mo_xW_1-xS_2 transition metal dichalcogenide alloys probed by scanning tunneling and optical spectroscopy. Phys Rev B. 2016;94:075440

79. Sze SM. High-speed semiconductor devices; in Sze SM (ed). New York (NY): Wiley-Interscience; 1990.

80. Jariwala D, Marks TJ, Hersam MC. Mixed-dimensional van der Waals heterostructures. Nat Mater. 2017;16:170–181.

81. Fletcher ASA, Nirmal D. A survey of gallium nitride HEMT for RF and high power applications. Superlattices Microstruct. 2017;109:519–537.

82. O'Regan TP, Ruzmetov D, Neupane MR, Burke RA, Herzing AA, Zhang KH, Birdwell AG, Taylor DE, Byrd EFC, Walck SD, Davydov AV, Robinson JA, Ivanov TG. Structural and electrical analysis of epitaxial 2D/3D vertical heterojunctions of monolayer MoS_2 on GaN. Appl Phys Lett. 2017b;111:051602.

83. Lee EW, Lee CH, Paul PK, Ma L, McCulloch WD, Krishnamoorthy S, Wu YY, Arehart AR, Rajan S. Layer-transferred MoS_2/GaN PN diodes. Appl Phys Lett. 2015;107:103505.

84. Tangi M, Mishra P, Ng TK, Hedhili MN, Janjua B, Alias MS, Anjum DH, Tseng CC, Shi YM, Joyce HJ, Li LJ, Ooi BS. Determination of band offsets at GaN/single-layer MoS_2 heterojunction. Appl Phys Lett. 2016b;109:032104.

85. Krishnamoorthy S, Lee EW, Lee CH, Zhang YW, McCulloch WD, Johnson JM, Hwang J, Wu YY, Rajan S. High current density 2D/3D MoS_2/GaN Esaki tunnel diodes. Appl Phys Lett. 2016b;109:183505.

86. Henck H, Ben Aziza Z, Zill O, Pierucci D, Naylor CH, Silly MG, Gogneau N, Oehler F, Collin S, Brault J, Sirotti F, Bertran F, Le Fevre P, Berciaud S, Johnson ATC, Lhuillier E, Rault JE, Ouerghi A. Interface dipole and band bending in the hybrid p-n heterojunction MoS_2/GaN(0001). Phys Rev B. 2017;96:115312.

87. Wan Y, Xiao J, Li JZ, Fang X, Zhang K, Fu L, Li P, Song ZG, Zhang H, Wang YL, Zhao M, Lu J, Tang N, Ran GZ, Zhang X, Ye Y, Dai L. Epitaxial single-layer MoS_2 on GaN with enhanced valley helicity. Adv Mater. 2018;30:1703888.

88. Sze SM. Physics of semiconductor devices. Hoboken (NJ): John Wiley & Sons; 1981.

89. Zhang KH, Jariwala B, Li J, Briggs NC, Wang BM, Ruzmetov D, Burke RA, Lerach JO, Ivanov TG, Haque M, Feenstra RM, Robinson JA. Large-scale 2D/3D hybrids based on gallium nitride and transition metal dichalcogenides. Nanoscale. 2018;10:336–341.

90. Kim C, Moon I, Lee D, Choi MS, Ahmed F, Nam S, Cho Y, Shin HJ, Park S, Yoo WJ. Fermi level pinning at electrical metal contacts of monolayer molybdenum dichalcogenides. ACS Nano. 2017a;11:1588–1596.

91. Kang JH, Liu W, Sarkar D, Jena D, Banerjee K. Computational study of metal contacts to monolayer transition-metal dichalcogenide semiconductors. Phys Rev X. 2014;4:031005.

92. Gong C, Huang CM, Miller J, Cheng LX, Hao YF, Cobden D, Kim J, Ruoff RS, Wallace RM, Cho K, Xu XD, Chabal YJ. Metal contacts on physical vapor deposited monolayer MoS. ACS Nano. 2013;7:11350–11357.

93. Burke RA, et al. Epitaxial growth of molybdenum disulfide on gallium nitride; Aberdeen Proving Ground (MD): CCDC Army Research Laboratory. Forthcoming 2019.

94. Saxler A, Kung P, Zhang X, Walker D, Solomon J, Ahoujja M, Mitchel WC, Vydyanath HR, Razeghi M. GaN doped with sulfur; in Davies G, Nazare MH (eds). Defects in Semiconductors: Icds-19, Pts 1–3. Materials Science Forum. Zurich-Uetikon, Transtec Publications Ltd; 1997, vol. 258–263, p. 1161–1166.

95. Rhoderick EH, Williams RH. Metal–semiconductor contacts. Oxford Science Publications; 1988.

96. Iucolano F, Roccaforte F, Giannazzo F, Raineri V. Temperature behavior of inhomogeneous Pt/GaN Schottky contacts. Appl Phys Lett. 2007;90:092119.

97. Im JS, Moritz A, Steuber F, Harle V, Scholz F, Hangleiter A. Radiative carrier lifetime, momentum matrix element, and hole effective mass in GaN. Appl Phys Lett. 1997;70:631–633.

98. Ke WC, Lee SJ, Chen SL, Kao CY, Houng WC. Effects of growth conditions on the acceptor activation of Mg-doped p-GaN. Mater Chem Phys. 2012;133:1029–1033.

99. Ahmed F, Choi MS, Liu X, Yoo WJ. Carrier transport at the metal–MoS_2 interface. Nanoscale. 2015;7:9222–9228.

100. Card HC, Rhoderick EH. Studies of tunnel mos diodes: 1. interface effects in silicon Schottky diodes. J Phys D–Appl Phys. 1971;4:1589.

101. Yu LS, Qiao D, Jia L, Lau SS, Qi Y, Lau KM. Study of Schottky barrier of Ni on p–GaN. Appl Phys Lett. 2001;79:4536–4538.

102. Pearton SJ, Abernathy CR, Ren F. Gallium nitride processing for electronics, sensors and spintronic. Springer; 2006.

103. Tracy KM, Mecouch WJ, Davis RF, Nemanich RJ. Preparation and characterization of atomically clean, stoichiometric surfaces of n- and p-type GaN(0001). J Appl Phys. 2003;94:3163–3172.

104. Lin SC, Kuo CT, Liu XG, Liang LY, Cheng CH, Lin CH, Tang SJ, Chang LY, Chen CH, Gwo S. Experimental determination of electron affinities for InN and GaN polar surfaces. Appl Phys Express. 2012;5:031003.

105. Bougrov V, Levinshtein M, Rumyantsev S, Zubrilov A. Gallium nitride (GaN). In: Levinshtein ME, Rumyantsev SL, Shur MS (eds). Properties of advanced semiconductor materials: GaN, AlN, InN, BN, SiC, SiGe. Wiley; 2001.

106. Korotkov RY, Gregie JM, Wessels BW. Optical properties of the deep Mn acceptor in GaN : Mn. Appl Phys Lett. 2002;80:1731–1733.

107. Wu CI, Kahn A, Taskar N, Dorman D, Gallagher D. GaN (0001)-(1x1) surfaces: composition and electronic properties. J Appl Phys. 1998;83:4249–4252.

108. O'Regan TP, Ruzmetov D, Neupane MR, Burke RA, Herzing AA, Zhang KH, Birdwell AG, Taylor DE, Byrd EFC, Walck SD, Davydov AV, Robinson JA, Ivanov TG. Structural and electrical analysis of epitaxial 2D/3D vertical heterojunctions of monolayer MoS_2 on GaN. Appl Phys Lett. 2017a;111:5.

109. Lazic P. CellMatch: Combining two unit cells into a common supercell with minimal strain. Comput Phys Commun. 2015;197:324–334.

110. Min KA, Park J, Wallace RM, Cho K, Hong S. Reduction of Fermi level pinning at Au–MoS_2 interfaces by atomic passivation on Au surface. 2D Mater. 2017;4:015019.

111. Kim H, Ovchinnikov D, Deiana D, Unuchek D, Kis A. Suppressing nucleation in metal-organic chemical vapor deposition of MoS_2 monolayers by alkali metal halides. Nano Lett. 2017b;17:5056–5063.

112. Zeng H, Liu GB, Dai J, Yan Y, Zhu B, He R, Xie L, Xu S, Chen X, Yao W, Cui X. Optical signature of symmetry variations and spin-valley coupling in atomically thin tungsten dichalcogenides. Sci Rep. 2013;3:1608.

113. Azcatl A, Kc S, Peng X, Lu N, McDonnell S, Qin X, de Dios F, Addou R, Kim J, Kim MJ, Cho K, Wallace RM. HfO_2 on UV–O_3 exposed transition metal dichalcogenides: interfacial reactions study. 2D Mater. 2015;2:014004.

114. Addou R, McDonnell S, Barrera D, Guo Z, Azcatl A, Wang J, Zhu H, Hinkle CL, Quevedo-Lopez M, Alshareef HN, Colombo L, Hsu JW, Wallace RM.

Impurities and electronic property variations of natural MoS_2 crystal surfaces. ACS Nano. 2015;9:9124–9133.

115. Huang JK, Pu J, Hsu CL, Chiu MH, Juang ZY, Chang YH, Chang WH, Iwasa Y, Takenobu T, Li LJ. Large-area synthesis of highly crystalline $WSe(_2)$ monolayers and device applications. ACS Nano. 2014a;8:923–930.

116. Lee YH, Zhang XQ, Zhang W, Chang MT, Lin CT, Chang KD, Yu YC, Wang JT, Chang CS, Li LJ, Lin TW. Synthesis of large-area MoS_2 atomic layers with chemical vapor deposition. Advanced Materials. 2012;24:2320–2325.

117. Lee G–H, Yu Y–J, Lee C, Dean C, Shepard KL, Kim P, Hone J. Electron tunneling through atomically flat and ultrathin hexagonal boron nitride. Appl Phys Lett. 2011;99:243114.

118. Fowler RH, Nordheim L. Electron emission in intense electric fields. Proc R soc Lond Ser A–Contain Pap Math Phys Character. 1928;119:173–181.

119. Das S, Chen HY, Penumatcha AV, Appenzeller J. High performance multilayer MoS_2 transistors with scandium contacts. Nano Lett. 2013;13:100–105.

120. Tangi M, Mishra P, Tseng CC, Ng TK, Hedhili MN, Anjum DH, Alias MS, We N, Li LJ, Ooi BS. Band alignment at GaN/single-layer WSe_2 interface. ACS Applied Materials & Interfaces. 2017;9:9110–9117.

121. Liu W, Cao W, Kang J, Banerjee K. (Invited) High-performance field-effect transistors on monolayer-WSe_2. ECS Transactions. 2013;58:281–285.

122. Tangi M, Mishra P, Ng TK, Hedhili MN, Janjua B, Alias MS, Anjum DH, Tseng CC, Shi YM, Joyce HJ, Li LJ, Ooi BS. Determination of band offsets at GaN/single-layer MoS_2 heterojunction (vol. 109, 032104 2016). Appl Phys Lett. 2016a;109:079901

123. Nakagawa Y, Haraguchi M, Fukui M, Tanaka S, Sakaki A, Kususe K, Hosokawa N, Takehara T, Morioka Y, Iijima H, Kubota M, Abe M, Mukai T, Takagi H, Shinomiya G. Hydrogen dissociation from Mg-doped GaN. Jpn J Appl Phys Part 1: Regul Pap Brief Commun Rev Pap. 2004;43:23–29.

124. Gelhausen O, Phillips MR, Goldys EM, Paskova T, Monemar B, Strassburg M, Hoffmann A. Dissociation of H-related defect complexes in Mg-doped GaN. Phys Rev B. 2004;69:125210.

125. Kim HK, Adesida I, Seong TY. Interfacial reaction effect on the ohmic properties of a Pt/Pd/Au contact on p-type GaN. J Vac Sci Technol A. 2004;22:1101–1104.

126. Zvanut ME, Uprety Y, Dashdorj J, Moseley M, Doolittle WA: Passivation and activation of Mg acceptors in heavily doped GaN. J Appl Phys. 2011;110:044508.

127. Lin YC, Li J, de la Barrera SC, Eichfeld SM, Nie YF, Addou R, Mende PC, Wallace RM, Cho K, Feenstra RM, Robinson JA. Tuning electronic transport in epitaxial graphene-based van der Waals heterostructures. Nanoscale. 2016;8:8947–8954.

128. Li H, Yin ZY, He QY, Li H, Huang X, Lu G, Fam DWH, Tok AIY, Zhang Q, Zhang H. Fabrication of single- and multilayer MoS_2 film-based field-effect transistors for sensing NO at room temperature. Small. 2012a;8:63–67.

129. Lin YC, Ghosh RK, Addou R, Lu N, Eichfeld SM, Zhu H, Li MY, Peng X, Kim MJ, Li LJ, Wallace RM, Datta S, Robinson JA. Atomically thin resonant tunnel diodes built from synthetic van der Waals heterostructures. Nat Commun. 2015;6:7311

130. Roy T, Tosun M, Cao X, Fang H, Lien DH, Zhao PD, Chen YZ, Chueh YL, Guo J, Javey A. Dual-gated MoS_2/WSe_2 van der Waals tunnel diodes and transistors. ACS Nano. 2015;9:2071–2079.

131. Chipara Aea. Process development for reactive–ion etching of molybdenum (MoS2) utilizing a poly(methyl methacrylate) (PMMA) etch mask. Adelphi (MD); CCDC Army Research Laboratory (US); 2017. Report No.: ARL-TR-8192.

132. Mazzoni A. CCDC ARL, Adelphi, MD. Personal communication, 2019.

133. Davydov AV, Bendersky LA, Boettinger WJ, Josell D, Vaudin MD, Chang KS, Takeuchi I. combinatorial investigation of structural quality of Au/Ni contacts on GaN. Appl Surf Sci. 2004;223:24–29.

134. Huang C-Y, Chang C, Lu G-Z, Huang W-C, Huang C-S, Chen M-L, Lin T-N, Shen J-L, Lin T-Y: Hybrid 2D/3D MoS2/GaN heterostructures for dual functional photoresponse. Applied Physics Letters 2018;112:233106.

135. VandeVondele J, Hutter J. Gaussian basis sets for accurate calculations on molecular systems in gas and condensed phases. J Chem Phys. 2007;127:114105

136. Krack M. Pseudopotentials for H to Kr optimized for gradient-corrected exchange-correlation functionals. Theor Chem Acc. 2005;114:145–152.

137. Goedecker S, Teter M, Hutter J. Separable dual-space Gaussian pseudopotentials. Phys Rev B. 1996;54:1703–1710.

138. Zhang YK, Yang WT. Comment on “Generalized gradient approximation made simple”. Phys Rev Lett. 1998;80:890–890.

139. Grimme S, Ehrlich S, Goerigk L. Effect of the damping function in dispersion corrected density functional theory. J Comput Chem. 2011;32:1456–1465.

140. Grimme S, Antony J, Ehrlich S, Krieg H. A consistent and accurate ab initio parametrization of density functional dispersion correction (DFT-D) for the 94 elements H–Pu. J Chem Phys. 2010;132:154104.

141. VandeVondele J, Hutter J. An efficient orbital transformation method for electronic structure calculations. J Chem Phys. 2003;118:4365–4369.

142. Huang YL, Chen Y, Zhang W, Quek SY, Chen C-H, Li L-J, Hsu W-T, Chang W-H, Zheng YJ, Chen W, Wee ATS. Bandgap tunability at single-layer molybdenum disulphide grain boundaries. Nat Commun. 2015;6:6298.

143. Zacharia R, Ulbricht H, Hertel T. Interlayer cohesive energy of graphite from thermal desorption of polyaromatic hydrocarbons. Phys Rev B. 2004;69:155406.

144. Pan MH, Liang LB, Lin WZ, Kim SM, Li Q, Kong J, Dresselhaus MS, Meunier V. Modification of the electronic properties of hexagonal boron-nitride in BN/graphene vertical heterostructures. 2D Mater. 2016;3:045002.

145. Kim J, Qin S, Yao W, Niu Q, Chou MY, Shih C-K. Quantum size effects on the work function of metallic thin film nanostructures. Proceedings of the National Academy of Sciences. 2010;107:12761–12765.

146. Shallcross S, Sharma S, Kandelaki E, Pankratov OA. Electronic structure of turbostratic graphene. Phys Rev B. 2010;81:165105.

147. Habib KMM, Sylvia SS, Ge S, Neupane M, Lake RK. The coherent interlayer resistance of a single, rotated interface between two stacks of AB graphite. Appl Phys Lett. 2013;103:243114.

148. Ramnani P, Neupane MR, Ge S, Balandin AA, Lake RK, Mulchandani A. Raman spectra of twisted CVD bilayer graphene. Carbon. 2017;123:302–306.

149. Wang Z, Chen Q, Wang J. Electronic Structure of twisted bilayers of graphene/ MoS_2 and MoS_2/MoS_2. The Journal of Physical Chemistry C. 2015c;119:4752–4758.

150. van der Zande AM, Kunstmann J, Chernikov A, Chenet DA, You Y, Zhang X, Huang PY, Berkelbach TC, Wang L, Zhang F, Hybertsen MS, Muller DA,

Reichman DR, Heinz TF, Hone JC. Tailoring the electronic structure in bilayer molybdenum disulfide via interlayer twist. Nano Lett. 2014;14:3869–3875.

152. Huang S, Ling X, Liang L, Kong J, Terrones H, Meunier V, Dresselhaus MS. Probing the interlayer coupling of twisted bilayer MoS_2 using photoluminescence spectroscopy. Nano Lett. 2014c;14:5500–5508.

152. Yeh P–C, Jin W, Zaki N, Kunstmann J, Chenet D, Arefe G, Sadowski JT, Dadap JI, Sutter P, Hone J, Osgood RM. Direct measurement of the tunable electronic structure of bilayer MoS_2 by interlayer twist. Nano Lett. 2016;16:953–959.

153. Taylor DE, Econ–KG. A code for computation of electrical conductivity using density functional theory. Aberdeen Proving Ground (MD): Army Research Laboratory (US); 2017 Oct.

154. Calderín L, Karasiev VV, Trickey SB. Kubo–Greenwood electrical conductivity formulation and implementation for projector augmented wave datasets. Comput Phys Commun. 2017;221:118–142.

155. Das P, Neupane MR. CCDC ARL, Adelphi, MD. DFT-VEX: an automated toolkit for device parameters extractions from first principle simulation. Personal communication, 2019.

Appendix. Metrics

This appendix appears in its original form, without editorial change.

A-1 Publications

1. D. Ruzmetov, K. Zhang, G. Stan, B. Kalanyan, G. R. Bhimanapati, S. M. Eichfeld, R. A. Burke, P. B. Shah, T. P. O'Regan, F. J. Crowne, A. G. Birdwell, J. A. Robinson, A. V. Davydov, and T. Ivanov. "*Vertical 2D/3D Semiconductor Heterostructures Based on Epitaxial Molybdenum Disulfide and Gallium Nitride*." **ACS Nano 10, 3580, 2016.**
2. S. Najmaei, L. Sidong, R. Burke, G. Anthony, P. Ajayan, A. Franklin, J. Lou, and M. Dubey, "*Enabling ultra-sensitive photo-detection through control of interface properties in molybdenum disulfide atomic layers*." **Nature Scientific Reports 6, 39465, 2016**.
3. Hi Tian, Bingchen Deng, Matthew L. Chin, Xiaodong Yan, Hao Jiang, Vivian Sun, Qiangfei Xia, Madan Dubey, Fengnian Xia, and Han Wang. "*A dynamically reconfigurable ambipolar black phosphorus memory device.*" **ACS Nano 10, 10428, 2016.**
4. T. P. O'Regan, D. Ruzmetov, M. R. Neupane, R. A. Burke, A.A. Herzing, K. Zhang, A. G. Birdwell, DeCarlos Taylor, Edward Byrd, S.D. Walck, A. V. Davydov, J. A. Robinson, and T. G. Ivanov, *"Structural and electrical analysis of epitaxial 2D/3D vertical heterojunctions of monolayer MoS$_2$ on GaN."* **Applied Physics Letters 111, 051602, 2017**.
5. P. R. Ramnani M. R. Neupane, S. Ge, A. A. Balandin, R. K. Lake and A. Mulchandani, "*Raman spectra of twisted CVD bilayer graphene."* **Carbon 123, 302, 2017**.
6. Y. Luo, J. Xu, T. Zhu, G. Wu, E. J. McCormick, W. Zhan, M. R. Neupane, and R. K. Kawakami, "*Opto-valleytronic spin injection in MoS$_2$/graphene hybrid spin valves.*" **Nano Letters 17, 3877, 2017**.
7. D. Rhodes, D.A. Chenet, B.E. Janicek, C. Nyby, Y. Lin, W. Jin, D. Edelberg, E. Mannebach, N. Finney, A. Antony, T. Schiros, T. Klarr, A. Mazzoni, M. Chin, Y.-c Chiu, W. Zheng, Q.R. Zhang, F. Ernst, J.I. Dadap, X. Tong, J. Ma, R. Lou, S. Wang, T. Qian, H. Ding, R.M. Osgood Jr., D.W. Paley, A.M. Lindenberg, P.Y. Huang, A.N. Pasupathy, M. Dubey, J. Hone, and L. Balicas. "*Engineering the structural and electrical phases of MoTe$_2$ through W substitution*." **Nano Letters 17, 1616, 2017.**
8. T.L. Atallah, J. Wang, M. Bosch, D. Seo, R.A. Burke, O. Moneer, J. Zhu, M. Theibault, L.E. Brus, J. Hone, and X.-Y. Zhu. "Electrostatic screening of charged defects in monolayer MoS$_2$." **Journal of Physical Chemistry Letters 8, 2148 (2017).**
9. C.N. Eads, D. Bandak, M.R. Neupane, D. Nordlund, O.L.A. Monti. "*Anisotropic Attosecond Charge Carrier Dynamics and Layer Decoupling in Quasi-2D Layered SnS$_2$.*" ***Nature Communications*** **8, No. 1369, 2017**.
10. B. Debnath, Y. Barlas, D. Wickramaratne, M.R. Neupane, R.K. Lake. "*Exciton Condensate in Bilayer Transition Metal Dichalcogenides: Strong Coupling Regime*." ***Physical Review B*** **96, No. 174504, 2017**.

11. DeCarlos Taylor**, "***Econ-kg: A Code for Computation of Electrical Conductivity Using Density Functional Theory*." **ARL-TR-8196, 2017**
12. D. Ruzmetov, M. R. Neupane, A. Herzing, T. P. O'Regan, A. Mazzoni, M. L. Chin, R. A. Burke, F. J. Crowne, A. G. Birdwell, D. E. Taylor, A. Kolmakov, K. Zhang, J. A. Robinson, A. V. Davydov, T. G. Ivanov. "*Van der Waals interfaces in epitaxial vertical metal/2D/3D semiconductor heterojunctions of monolayer* MoS_2 *and GaN*." **2D Materials, Vol.5, No. 4, 2018**
13. Mahesh R. Neupane, Dmitry Ruzmetov, Robert Burke, A. Glen Birdwell, Decarlos Taylor, Matthew Chin, Terrance O'Regan, Frank Crowne, Barbara Nichols, Pankaj Shah, Edward Byrd, Tony Ivanov. "*Challenges and opportunities in integration of 2D materials on 3D substrates: Materials and device perspectives*." **76th Device Research Conference Proceeding, 18071263 , No. 1-2, 2018**
14. Tung Pham, Pankaj Ramnani, Claudia C Villarreal, Jhoann Lopez, Protik Das, Ilkeun Lee, Mahesh R Neupane, Youngwoo Rheem, and Ashok Mulchandani. "MoS_2*-Graphene Heterostructures as efficient organic compounds sensing 2D materials."* ***Carbon*** **123, Pg. 302, 2018**
15. Chenyang Li, Bishwajit Debnath, Xiaojian Tan, Shanshan Su, Kui Xu, Supeng Ge, Mahesh R. Neupane, and Roger K. Lake. "*Commensurate lattice constant dependent thermal conductivity of misoriented bilayer graphene*." **Carbon, Vol.138, No. 451-457, 2018.**
16. S. Najmaei, M.R. Neupane, B.M. Nichols, R.A. Burke, A.L. Mazzoni, M.L. Chin, D.A. Rhodes, L. Balicas, A.D. Franklin, and M. Dubey. "*Cross-Plane Carrier Transport in Van der Waals Layered Materials*." ***Small*** **14, No. 1703808, 2018**.
17. P.B. Shah. "*Semiconductor Electron Device Formed Of 2-D Van Der Waals Material Whose Free Charge Carrier Concentration Is Determined By Adjacent Semiconductor's Polarization."* **US Patent 9,893,155, 2018.**
18. K. Zhang, B. Jariwala, J. Li, N.C. Briggs, B. Wang, D. Ruzmetov, R.A. Burke, J.O. Lerach, T.G. Ivanov, M. Haque, R.M. Feenstra, J.A. Robinson, "*Large Scale 2D/3D Hybrids Based on Gallium Nitride and Transition Metal Dichalcogenides."* ***Nanoscale*** **10, Pg. 336, 2018**.
19. S.B. Cronin, R. Dhall, R. Lake, Z. Li, M. Neupane, D. Wickramaratne. "*Bulk Direct Gap* MoS_2 *by Plasma Induced Layer Decoupling*." ***US Patent 15/536,628*****, 2018**.

A-2 Presentations (Talks and Posters)

1. Mahesh R. Neupane, Dmitry Ruzmetov, Robert Burke, A. Glen Birdwell, Decarlos Taylor, Matthew Chin, Terrance O'Regan, Frank Crowne, Barbara Nichols, Pankaj Shah, Edward Byrd, Tony Ivanov, "*Challenges and opportunities in integration of 2D materials on 3D substrates: Materials and device perspective.* **76th Device Research Conference**, Santa Barbara, June 26-28, 2018 (**invited**)

2. Mahesh Neupane, DeCarlos Taylor, Dmitry Ruzmetov, Robert Burke, A Birdwell, Andrew Herzing, Terrance O'Regan, Edward Byrd, Tony Ivanov, Role of GaN surface Termination on Structural and Electronic Properties of 2D/GaN and Metal/2D/GaN Heterostructures.*”* contributed talk, 2018 **APS March meeting**, Los Angeles, CA.
3. Sergey Rudin, Greg Rupper, Gregory Garrett, Chelsea Haughn, Mahesh Neupane*, “Excitonic Effects and Mott Transition in Semiconductor Heterostructures.”* contributed talk, 2018 **APS March meeting**, Los Angeles, CA.
4. M. Neupane, D. Taylor, E. Byrd, D. Ruzmetov, T. O'Regan, T. Ivanov, *"Effect of surface relaxation and inter-layer interaction on electronic properties of lattice-matched 2D/3D Heterostructures: A first-principles study."* contributed talk, 2017 **APS March meeting**, New Orleans, LA.
5. D. Taylor, M. Neupane, E. Byrd, Supeng Ge, Roger Lake, “*A first principle study of the naturally aligned bilayer two dimensional (2D) materials."* contributed talk, 2017 **APS March meeting**, New Orleans, LA.
6. D. Ruzmetov, T. P. O'Regan, A. Mazzoni, *et al. "Electrical transport and structural characterization of epitaxial monolayer MoS2 /n- and p-doped GaN vertical lattice-matched heterojunctions."* contributed talk, 2017 **APS March meeting**, New Orleans, LA.
7. D. Taylor, M. Neupane, E. Byrd, T. O’Regan, “*Large Scale Density Functional Theory Calculations of Homogeneous and Heterogeneous Two-Dimensional (2D) Materials"* contributed talk, 2017 **MRS Spring meeting**, Phoenix, AZ.
8. M.R. Neupane, *"2D/2D and 2D/3D heterostructures for future applications: Materials and Device perspectives."* (**Invited**), Department of Chemistry and Biochemistry Physical **Seminar** Series, University of Arizona, Tucson, Arizona, April 17, 2017.
9. R. Burke, K. Zhang, D. Ruzmetov, A. Herzing, G. Birdwell, M. Neupane, T. O’Regan, B. Nichols, M. Chin, A. Mazzoni, A. Davydov, J. Robinson, M. Dubey, and T. Ivanov. “*Epitaxial growth of molybdenum disulfide on gallium nitride*.” **ACCGE-21/OMVPE-18.** Santa Fe, NM, July 31, 2017.
10. M. R. Neupane, D. E. Taylor, and E. F. Byrd, “*A first principle study of the naturally aligned bilayer 2D materials: A materials and device perspective*.” **Two Dimensional Electronics Beyond Graphene. Gordon Research Conference, 2016**.
11. R. A. Burke, D. A. Ruzmetov, K. Zhang, T. P. O’Regan, S. D. Walck, L. Giri, A. A. Herzing, I. Levi, M. R. Neupane, D. E. Taylor, E. F. Byrd., A. V. Davydov, J. A. Robinson, and T. G. Ivanov, “*CVD growth of* MoS_2 *on GaN: Sample Preparation, TEM, and Modeling*.” **Two Dimensional Electronics Beyond Graphene. Gordon Research Conference, 2016**.

12. M. Chin, A. Mazzoni, R. Burke, S. Najmaei, B. Nichols, and M. Dubey. "*Exploring the effects of metal-*MoS_2 *interfaces and lateral cross-sectional area on contact resistance and electrical conduction*." 2016 **MRS Fall Meeting,** Boston, MA.
13. R.A. Burke, K. Zhang, D.A. Ruzmetov, A.A. Herzing, M.R. Neupane, A.G. Birdwell, G. Stan, T.P. O'Regan, D.E. Taylor, E.F. Byrd, M.L. Chin, A. Mazzoni, B.M. Nichols, S.D. Walck, M. Dubey, A.V. Davydov, J.A. Robinson, and T.G. Ivanov. "*Epitaxial growth of molybdenum disulfide on gallium nitride*." **Graphene and Beyond: From Atoms to Application.** State College, PA, May 10, 2017.

List of Symbols, Abbreviations, and Acronyms

2-D	two-dimensional
2ML	two monolayer
3-D	three-dimensional
AFM	atomic force microscopy
Al	aluminum
AM-AFM	amplitude modulation AFM
ARL	Army Research Laboratory
BB	band bending
BEP	beam equivalent pressure
BZ	Brillouin zone
C	carbon
CAFM	conductive atomic force microscopy
CBE	conduction band edges
CBED	convergent-beam electron diffraction
CBO	conduction band offset
CCDC	US Army Combat Capabilities Development Command
CG	conjugated gradient
CVD	chemical vapor deposition
DES	diethyl sulfide
DFT	density functional theory
DOS	densities of state
DSI	Director's Strategic Initiative
EBID	Electron Beam Induced Deposition
EBL	Electron Beam Lithography
EBSD	electron backscatter diffraction

EDS	energy dispersive spectroscopy
EELS	electron energy loss spectroscopy
EG	epitaxial graphene
FETs	field-effect transistors
FFT	fast Fourier transform
FIB	focused ion beam
FL	few layer
FLP	Fermi-level pinning
FWHM	full-width half-maximum
Ga	gallium
GaN	gallium nitride
GGA	generalized gradient approximation
H	hydrogen
HAADF	High-Angle Annular Dark-Field
HBT	heterojunction bipolar transistor
HR(S)TEM	high resolution (scanning) transmission electron microscopy (
IBID	ion beam induced deposition
I-V	current-voltage
KG	Kubo–Greenwood
KGEC	Kubo–Greenwood Electrical Conductivity
KP	Kelvin probe
KPFM	Kelvin probe force microscopy
LEEM/LEER	Low Energy Electron Microscopy/Reflectivity
MBE	molecular beam epitaxy
ME	mechanically exfoliated
MIBK	methyl isobutyl ketone
ML	monolayer

Mo	molybdenum
MOCVD	metalorganic chemical vapor deposition
Mo	molybdenum
MoO_3	molybdenum trioxide
MoS_2	molybdenum disulfide
MS	metal-semiconductor
Nb	niobium
NDR	negative differential resistance
PA-MBE	plasma-assisted molecular beam epitaxy
PAW	projector augmented wave
PBE	Perdew–Burke and Ernzerhof
Pd	palladium
PDOS	projected density of states
PECVD	plasma enhanced chemical vapor deposition
PES	potential energy surface
PL	photoluminescence
PLD	pulsed laser deposition
PV	powder vaporization
PVD	physical vapor deposition
QE	Quantum Espresso
Re	rhenium
RF	radio frequency
RIE	reactive ion etch
S	sulfur
Si	silicon
SiC	silicon carbide
SiO_2	silicon dioxide

SB	Schottky barrier
SBHs	Schottky barriers heights
Se	selenium
SEDD	Sensors and Electron Devices Directorate
SEM	scanning electron microscopy
SML	single-molecular layer
SP	surface potential
STEM	scanning transmission electron microscope
Te	tellurium
TEM	transmission electron microscopy
Ti	titanium
TMDs	transition metal dichalcogenides
TOF-SIMS	time-of-flight secondary ion mass spectrometry
TUNA	Tunneling Atomic Force Microscopy
VASP	Vienna Ab-initio Simulation package
VB	valence band
VBE	valence band edge
VBM	valence band maximum
VBO	valence band offset
vdW	van der Waals
VPE	vapor phase epitaxy
W	tungsten
WF	Work Function
WMRD	Weapons and Materials Research Directorate
Xe	xenon
XC	exchange-correlation
XEDS	X-ray energy dispersive spectroscopy

XPS	X-ray photoelectron spectroscopy
XTEM	cross-sectional transmission electron microscopy

1 DEFENSE TECHNICAL
(PDF) INFORMATION CTR
DTIC OCA

2 CCDC ARL
(PDF) FCDD RLD CL
TECH LIB

7 CCDC ARL
(PDF) FCDD RLS RE
M NEUPANE
D RUZMETOV
AG BIRDWELL
R ENCK
M CHIN
T IVANOV
FCDD RLW LB
E BYRD